Aus dem Institut für Prophylaxe und Epidemiologie der Kreislaufkrankheiten
(IPEK)

Klinikum der Ludwig-Maximilians-Universität München

Direktor: Prof. Dr. med. Christian Weber

Chemokin-Interaktionen bei der Chemotaxis von Leukozyten

Dissertation

zum Erwerb des Doktorgrades der Medizin

an der Medizinischen Fakultät der

Ludwig-Maximilians-Universität zu München

vorgelegt von

Veit Eckardt

aus

Zürich

Jahr

2021

Mit Genehmigung der Medizinischen Fakultät

der Universität München

Berichterstatter: Univ.-Prof. Dr. med. Christian Weber

Mitberichterstatter: Univ.-Prof. Dr. rer. nat. Jürgen Bernhagen

                                Priv. Doz. Dr. rer. nat. Andreas Herbst

                                Priv. Doz. Dr. Claudia Nußbaum

Mitbetreuung durch den

promovierten Mitarbeiter: Dr. med. Philipp von Hundelshausen

Dekan: Prof. Dr. med. dent. Reinhard Hickel

Tag der mündlichen Prüfung: 25.02.2021

Affidavit

I hereby declare, that the submitted thesis entitled

Chemokine interactions in the recruitment of leukocytes

is my own work. I have only used the sources indicated and have not made unauthorized use of services of a third party. Where the work of others has been quoted or reproduced, the source is always given.
I further declare that the submitted thesis or parts thereof have not been presented as part of an examination degree to any other university.

München, 26.02.2021   Veit Eckardt

_____   _____

Place, date   Signature doctoral candidate

Content

1. Abbreviations

CANTOS:	Canakinumab Antiinflammatory Thrombosis Outcome Study
CKBP:	Chemokine-binding protein
CRD:	Carbohydrate recognition domain
CRP:	C-reactive protein
GAG:	Glycosaminoglycan
Gal-1/3:	Galectin-1/3
GPCR:	G protein-coupled receptor
GWAS:	Genome-wide association study
HMGB1:	High mobility group box 1
HNP-1:	Human neutrophil peptide 1
IL-1β:	Interleukin-1β
IL1R:	Interleukin-1 receptor
LoDoCo:	Low-Dose Colchicine
Mac-2:	Macrophage-2 antigen
MDS:	Molecular dynamics simulation
MHC II:	Major histocompatibility complex class II
MIF:	Macrophage migration inhibitory factor
NMR:	Nuclear magnetic resonance
OPRAH:	Obligate PF4-RANTES heterodimer
ORATH:	Obligate RANTES-TARC heterodimer
OxLDL:	Oxidized low-density lipoprotein
PCSK9:	Proprotein convertase subtilisin/kexin type 9
PDB:	Protein data bank
PROVE IT-TIMI 22:	Pravastatin or Atorvastatin Evaluation and Infection Therapy-Thrombolysis in Myocardial Infarction 22
SPR:	Surface plasmon resonance
TCR:	T-cell receptor
Th1/2 cell:	Type 1/2 T helper cell
TLR:	Toll-like receptor
Treg cell:	Regulatory T cell
TSG-6:	Tumor necrosis factor-stimulated gene 6 protein

2. Publications

Project 1

P. von Hundelshausen, S. M. Agten, **V. Eckardt**, X. Blanchet, M. M. Schmitt, H. Ippel, C. Neideck, K. Bidzhekov, J. Leberzammer, K. Wichapong, A. Faussner, M. Drechsler, J. Grommes, J. P. van Geffen, H. Li, A. Ortega-Gomez, R. T. A. Megens, R. Naumann, I. Dijkgraaf, G. A. F. Nicolaes, Y. Döring, O. Soehnlein, E. Lutgens, J. W. M. Heemskerk, R. R. Koenen, K. H. Mayo, T. M. Hackeng, C. Weber, Chemokine interactome mapping enables tailored intervention in acute and chronic inflammation. *Sci. Transl. Med.* **9**, eaah6650 (2017).

Journal impact factor in 2017: 16.7

Percentile in *Medicine, Research & Experimental* in 2017: 98.9

Percentile in *Cell Biology* in 2017: 95.5

Project 2

V. Eckardt, M. C. Miller, X. Blanchet, R. Duan, J. Leberzammer, J. Duchene, O. Soehnlein, R. T. A. Megens, A.-K. Ludwig, A. Dregni, A. Faussner, K. Wichapong, H. Ippel, I. Dijkgraaf, H. Kaltner, Y. Döring, K. Bidzhekov, T. M. Hackeng, C. Weber, H.-J. Gabius, P. von Hundelshausen, K. H. Mayo, Chemokines and galectins form heterodimers to modulate inflammation. *EMBO Rep.* **21**, e47852 (2020).

Journal impact factor in 2018 (most recent): 8.4

Percentile in *Biochemistry & Molecular Biology* in 2018: 91.8

Percentile in *Cell Biology* in 2018: 86.8[1]

---

[1] All journal statistics according to InCites Journal Citation Reports, Clarivate Analytics, Boston, MA, USA

3. Introduction

Complex chronic inflammatory diseases, including atherosclerosis, are major global health issues. However, treatment options are limited. Modern systems biology postulates that the precise and comprehensive identification and characterization of structural and functional protein networks yields targets for effective and specific pharmacological intervention. Chemokines constitute a family of approximately 50 inflammatory cytokines that regulate leukocyte migration which represents a ubiquitous feature of all inflammatory processes. It has been shown that several chemokines form functionally active heterodimers. However, a comprehensive interactome of all currently known chemokines has not been developed. We have therefore performed an extensive study of chemokine/chemokine interactions and expanded the concept to another molecular entity to demonstrate a broader scale of the chemokine interactome. In **project 1**, we generated a chart of all heterodimeric chemokine interactions by means of biochemical and biophysical assays and validated their functional relevance by cellular and animal experiments. In **project 2**, we extended the concept of chemokine interactions to the family of galectins. An extensive understanding of chemokine interactions may help to specifically interfere with inflammatory processes, such as the progression of atherosclerotic plaques, while preserving host defense.

3.1 Protein/protein interactions in health and disease

Medical molecular biology was traditionally based on a focused and reductionist one gene-one disease model which implied that a single genetic mutation directly generates a clinical phenotype. Hence, scientific problems were approached causally, or vertically, by studying a few molecules with different experimental tools

to interfere with an assumed chain of action. This approach was well suited to test focused scientific hypotheses, but lacked efficiency in generating experimental data, sensitivity in identifying preclinical disease and specificity in classifying clinical disease (*1*).

Consequently, diseases were increasingly defined as changes in large datasets (*2*). In a more global, horizontal, strategy multiple molecules were identified and characterized using high-throughput tools under different experimental conditions (*3*). For example, genomics and proteomics (the suffix -ome designates an entirety of some sort) attempt to describe the entire human genome and proteome and catalogue their variants. However, it became clear that the pathophysiological role of a gene depends on the position of the protein in a complex structural and functional network with other genetic and environmental factors (*4*). Therefore, even with detailed and comprehensive information on genes and proteins at hand, the assignment of context and function to proteins in clinical disorders remained challenging (*3, 4*).

Modern systems biology attempts to combine the traditional vertical hypothesis-driven science with the more recent horizontal discovery science in an integrative manner. It seeks to entirely characterize all the components of a particular system by multiple high-throughput methods, to experimentally perturb and monitor the components in a systematic manner, to reconcile the experimental outcome with model hypotheses on their structural and functional relations, and eventually to interfere with the system based on the generated hypotheses (*5*).

The protein/protein interactome (and also the protein/glycan interactome that will be referred to and the protein/nucleic acid interactome that will not be discussed) plays an important role in the precise molecular characterization of human diseases (*1, 6*). For instance, disease variants are multiple fold more likely to

perturb protein interactions than nondisease variants (*7*). And difference and extent of the perturbation account for a disease phenotype (*7*). This applies to simple diseases characterized by a single failure of the system (e.g. primary immunodeficiency disorders) and particularly to the more common complex systemic diseases (e.g. chronic inflammatory diseases such as atherosclerosis) (*4*). The identification and characterization of structure and function of protein/protein pairs remains methodologically challenging. However, the disruption or imitation of protein/protein interactions is a promising concept for the design of effective single-target, multi-target low-dose and multi-stage therapies with limited toxicity (*2, 4*).

3.2 Chemokine/chemokine interactions

Chemokines are extracellular proteins with a molecular weight ranging between 8 and 12 kDa. Whereas their amino acid sequence may differ widely, their secondary and tertiary structure is highly conserved. All chemokines exhibit a flexible N-terminal segment, followed by a three-stranded antiparallel β-sheet and a C-terminal α-helix folded onto the β-sheet (*8*). In almost all cases, their structure is stabilized by two disulfide bridges. With approximately 50 members, the group of chemokines constitutes the largest entity of cytokines. Chemokines are classified in four groups, the two most common types being a CC-type with the first two cysteine residues being adjacent and a CXC-type with the cysteines being separated by a non-conserved amino acid (Table1). Their nomenclature is derived from the chemokine type, followed by the letter "L" for "ligand" and a number which specifies their order of discovery. Each chemokine binds to and activates one or several of 18 G protein-coupled chemokine receptors (GPCRs) with its core domain and N-terminus. The receptors are named after the chemokine type they bind to followed by the letter "R" for "receptor" and a number which specifies their

order of discovery. Each receptor may bind to several chemokines (Table 2). Chemokines must be immobilized on cell surface glycosaminoglycans (GAGs) to elicit their function *in vivo* (*9*).

The primary role of chemokines is the mediation of leukocyte trafficking into lymphoid organs and peripheral tissue in homeostasis and during innate and adaptive immune responses in acute and chronic inflammation (*10, 11*). However, they may also be involved in other immunoregulatory processes such as immune cell activation, differentiation and proliferation and nonleukocytic cell activation and migration in angiogenesis or thrombosis (*12, 13*). Virtually all diseases involve chemokines. Disease models in which chemokines are particularly relevant include atherosclerosis leading to myocardial infarction and stroke (*14-16*), rheumatoid arthritis (*17*), allergic asthma (*18*), HIV (*19*) and cancer (*20*). Due to their central functional role, chemokine expression and activity is tightly regulated. Mechanisms of adaptation include the control of their transcription and translation (e.g. by miRNA), splice variation, posttranslational modifications (e.g. by proteolytic cleavage) and chemokine degradation (*21*). In addition, oligomerization of chemokines and chemokine receptors (Table 1 and 2) (*8, 22*), chemokine receptor recycling and biased signaling, receptor antagonism (*23*) and scavenging by atypical decoy receptors (*24*) (Table 2), chemokine interaction with cell surface GAGs (*9*), chemokine-binding proteins (e.g. high mobility group box 1 (HMGB1)) and atypical chemokines (e.g. macrophage migration inhibitory factor (MIF)) (*25*) affect chemokine activity (Table 2). Given the shear number of chemokines and chemokine receptors, and their promiscuous interactions, a high level of redundancy has initially been attributed to the system. However, chemokine/chemokine interactions and also chemokine interactions with GAGs (which foster chemokine oligomerization), seem to render the chemokine system highly specific (*8*).

Chemokines homodimerize in elongated end-to-end CC-type dimers in a two-stranded antiparallel β-sheet formed between their N-termini, and globular CXC-type dimers with antiparallel α-helices on top of an extended β-sheet (Table 1) (*8*). Dimerization alters chemokine function (*21*). Since complex pathophysiological conditions, particularly inflammation, most often involve multiple chemokines, structural and functional similarities between different chemokines prompted the investigation of their heterodimerization. Initial reports suggested that the combination of chemokines may enhance or inhibit their function, with chemokines in subfunctional concentrations exerting a synergistic effect when combined (*26-29*). Since then, several studies demonstrated that chemokine heterodimers are functionally implicated in disease models such as atherosclerosis and cancer and may be targeted by small peptide inhibitors (Fig. 1) (*15, 30, 31*). However, a comprehensive interactome of all chemokines which may provide a basis for better understanding the suitability of chemokine interactions as targets for systems-based therapeutic approaches has not been determined.

3.3 Chemokine-binding proteins

When functional chemokine heterodimers were first described, it had already been discovered that other species express many chemokine-binding proteins (CKBPs) and exploit their immunomodulatory potential for host evasion. For instance, it had been demonstrated that chemokines interact broadly with many viral proteins (*32*). Later it was shown that chemokines interact selectively with tick-specific evasins (*33*). In most instances, these CKBPs inhibit chemokine function by blocking GPCR binding, alter their tertiary or quaternary structure and affect their bioavailability for example by modifying their GAG-binding capacity (*32*).

Considering the relatively abundant occurrence of CKBPs in other species, it is noteworthy that only three endogenous soluble CKBPs have been described so far in humans. The damage-associated molecular pattern HMGB1 interacts specifically with CXCL12 and potentiates CXCL12 activity by forming a complex with two chemokine molecules and two chemokine receptor molecules on the cell surface (*25*). The GAG-binding protein tumor necrosis factor-stimulated gene 6 protein (TSG-6) interacts with several chemokines (*34*) and inhibits their activity by preventing the interaction of chemokines with endothelial GAGs. And the neutrophil-derived defensin human neutrophil peptide 1 (HNP-1) interacts with CCL5 from platelets to foster monocyte recruitment to inflamed endothelium (*35*).
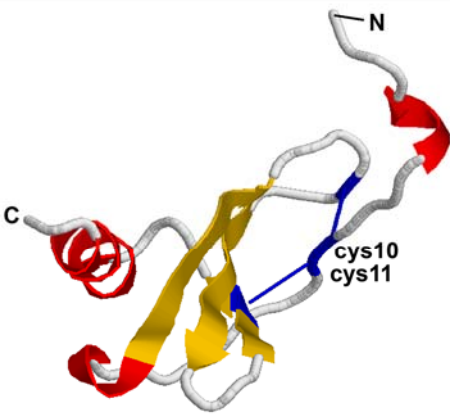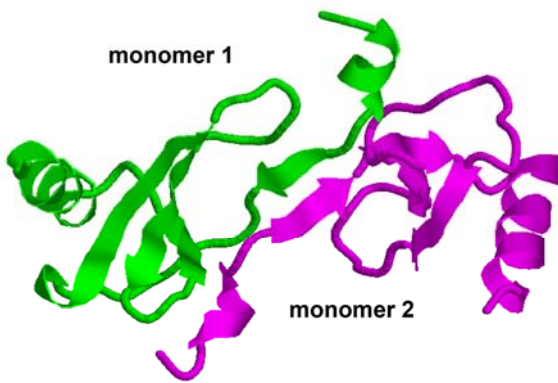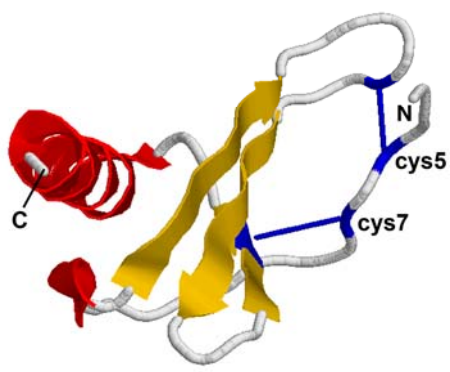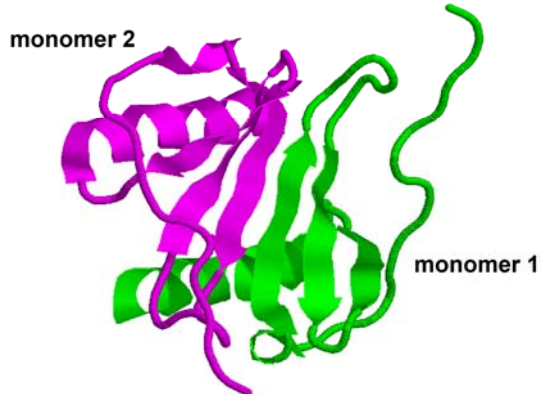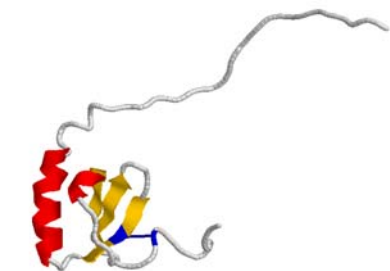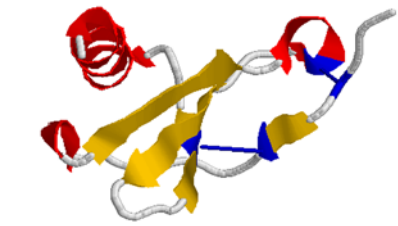
Table 1. Structures of the chemokine subtypes. The tertiary (monomer) and quarternary (homooligomer) structure of the different chemokine subtypes are shown. The CC-type was derived from the structure of CCL2 ((*36*), protein data bank (PDB) access codes 1DOL and 1DOK), the CXC-type from CXCL8 ((*37*), PDB access codes 5D14 and 1IL8), the XC-type shows XCL1 ((*38*),(*39*), PDB access codes 1J9O and 2N54) and the only CX3C-type is CX3CL1 ((*40*), PDB access code 1F2L). β-sheets are displayed in yellow, helices in red, cysteine residues and disulfide bridges in blue. In the quarternary structures monomers are presented in green and magenta, pink and purple. Structures were modified with RasWin Molecular Graphics, Windows Version 2.7.5.2.

Table 2. The chemokine system. Data from several references were combined for this table (*10-13, 21-25, 33, 41-45*).

4. Results

4.1 A comprehensive chemokine/chemokine interactome

In **project 1**, we systematically evaluated the binary interaction of all human chemokines by solid-phase assays. In total, we found approximately 200 of 1250 possible interactions. We then confirmed our results by surface plasmon resonance (SPR). Mostly inflammatory/nonhomeostatic chemokines interact (Fig. 2, A and B). By means of nuclear magnetic resonance (NMR) spectroscopy and molecular dynamics simulations (MDSs), we could show that CCL5 and CCL2, CCL17 and CXCL4 form CC-type heterodimers whereas CCL5 and CXCL12 form CXC-type heterodimers. We confirmed that CC-type interactions are synergistic in cell signaling, transmigration with activated human T cells and endothelial arrest assays with T cells and monocytes. Synergistic effects may be differentially mediated to increase the potency of the targeted chemokines by receptor heteromerization or the efficacy by receptor retention (via auxiliary GAG binding). However, CXC-type heterodimers are inhibitory (Fig. 3). Their effect is mediated by conformational changes in the targeted chemokine and chemokine receptors. To confirm our functional results and evaluate their therapeutic potential, we utilized our structural findings to design specific CCL5-derived inhibitory peptides which disrupt or mimic chemokine interactions. Cyclic CAN and CKEY which constitute different parts of the interfaces with CCL17 and CXCL4 disrupt the interaction between CCL5 and CCL17 and CCL5 and CXCL4 respectively to abrogate synergisms. Linear VREY and its cyclic multiple [VREY]^4 mimic parts of the interface with CCL5 and interact with CXCL12 to imitate the inhibitory effect of CCL5. Furthermore, we designed obligate CCL5/CCL17 (obligate RANTES-TARC heterodimer (ORATH)) and CCL5/CXCL4 (obligate PF4-RANTES heterodimer (OPRAH)) heterodimers. ORATH shows increased potency and efficacy in T cell

arrest compared to CCL5 and CCL17 combined. OPRAH exhibits increased potency and efficacy in T cell migration and monocyte arrest compared to CCL5 and CXCL4 combined. To demonstrate the incidence of the uncovered chemokine interactions *in vivo*, we detected endogenous CCL5/CCL17 heterodimers in murine lymph nodes by a proximity ligation assay. We then validated the relevance of our concept in murine models of acute and chronic inflammation. In a model of LPS-induced acute lung injury in which neutrophil recruitment is triggered by platelet chemokines, CKEY reduces neutrophil infiltration in the lung. In a model of diet-induced atherosclerosis, CAN reduces aortic lesion size possibly by limiting the CCL17-dependent recruitment of naive T cells in which conversion to regulatory T (Treg) cells is suppressed. Of note, we found CCL5/CCL17 heteromers in the aortic root of diseased mice, in plaque of human coronary arteries but not in healthy coronaries. Replacing CXCL4 with an interaction-deficient CXCL4 variant reduces lesion size with the same efficiency than a CXCL4 knockout. This effect was attributed to a reduction in plaque macrophages. OPRAH restores lesion size and plaque macrophage count in CCL5$^{-/-}$CXCL4$^{-/-}$ mice. Interestingly, whereas CCL5/CCL17 heterodimers are detected in the aortic root, the size of lesions in the aortic root is not affected by CXCL4 knockout/CXCL4 variant knockin. Furthermore, [VERY][4] inhibits CXCL12-dependent aggregation of murine and human platelets relevant to atherothrombosis.

4.2 A chemokine/galectin interactome

In **project 2,** we extended the chemokine interactome to another molecular entity. We demonstrated that chemokines interact with galectins, a family of β-galactoside-binding proteins (nine in humans) which are structurally and functionally similar to chemokines. All galectins comprise a β-sandwich structure that constitutes their carbohydrate recognition domain (CRD). The opposing faces

of this structure are termed S-face (or sugar-binding face) and F-face (*46*).
Interestingly, it has been shown that galectins can form homodimers,
homooligomers and heterodimers (*47, 48*). Galectins regulate immune cell
recruitment in inflammatory conditions such as atherosclerosis (*49*). Using solid-
phase assays and SPR, we showed that many chemokines interact specifically
with galectin-1 and -3 (Gal-1/-3) (Fig. 4 and 5). We then focused on CXCL12 and
Gal-3 to investigate the mechanism of their interaction by NMR spectroscopy. To
test the relevance of our findings *in vivo*, we detected CXCL12/Gal-3 heterodimers
in murine lymph nodes by means of a proximity ligation assay. Furthermore, we
showed that Gal-3 inhibits CXCL12-induced immune cell recruitment in
transmigration assays with different leukocyte subsets and a murine model of
peritoneal inflammation. Gal-3 impairs CXCL12-induced CXCR4 signaling without
interfering with receptor internalization. Based on cell binding studies and MDSs,
we suggested that Gal-3 inhibits CXCL12 signaling by forming a ternary complex
with the chemokine and its receptor CXCR4.
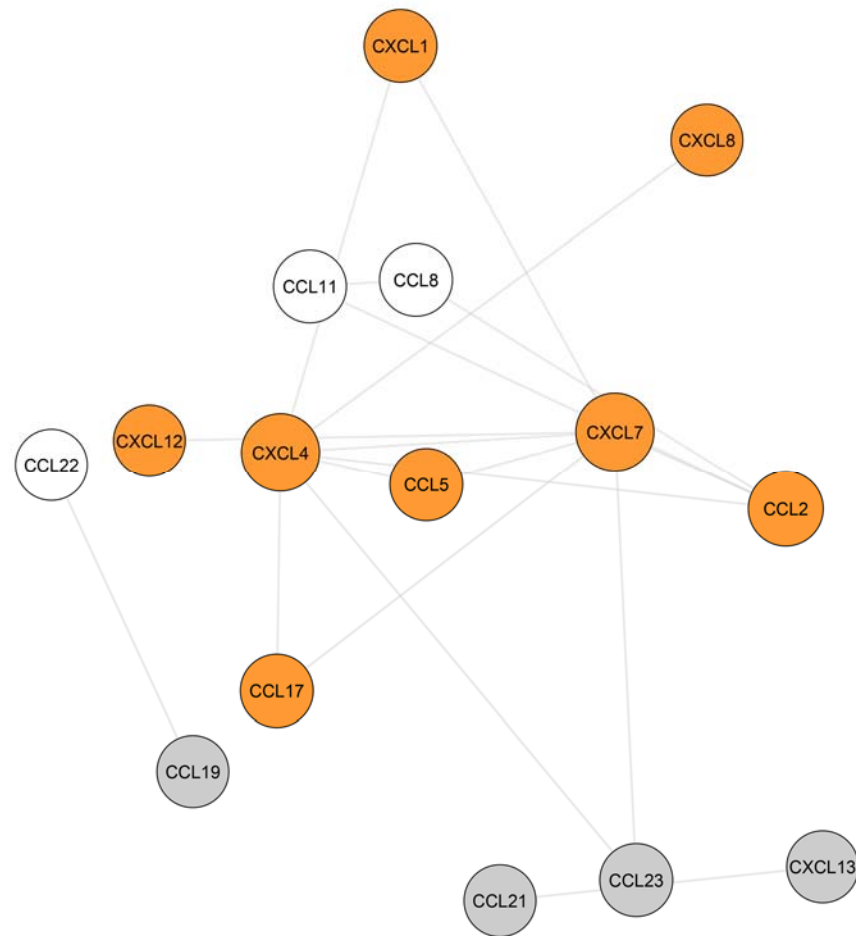
Fig. 1. Chemokine interactions as documented by previous publications. Interactions are depicted as a node-edge model where nodes represent proteins and edges represent physical interactions (*50, 51*). Atherogenic chemokines are shown in orange (*14, 15, 52*). Homeostatic chemokines in gray (*11*). The figure was generated with Cytoscape 3.7.2. An organic layout was chosen.

Fig. 2A. The new chemokine interactome. Known interactions are shown in gray. New interactions are shown in blue (confirmed by both ligand blot and SPR, in pink found only on ligand blot, in green found only in SPR). The size of each node indicates the degree of interaction of the protein.
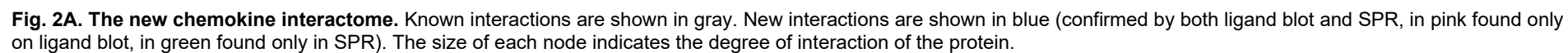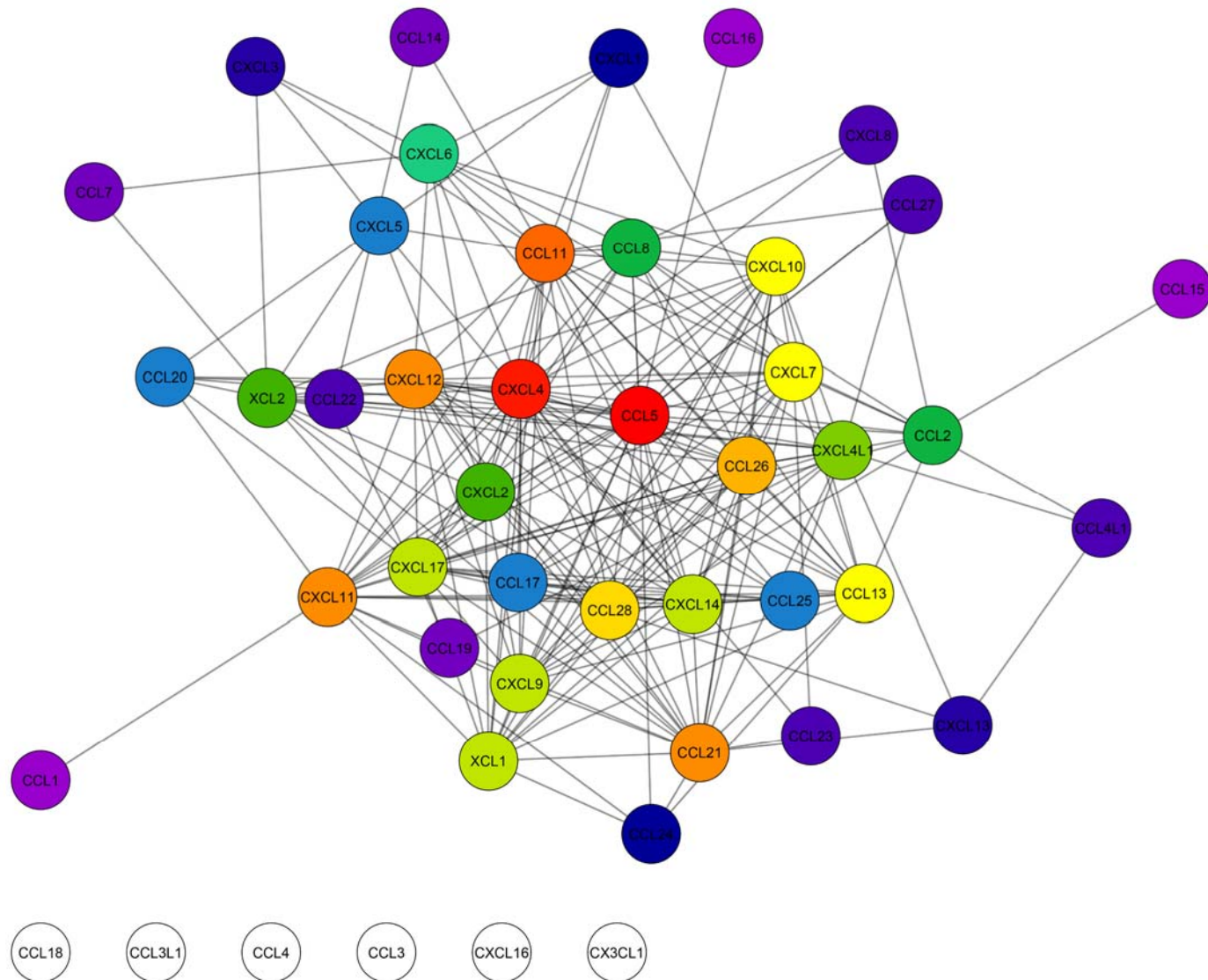
Fig. 2B. The new chemokine interactome. As in Figure 2. The color of each node indicates the degree of interaction of the protein from purple (1 interaction) to red (25 interactions).
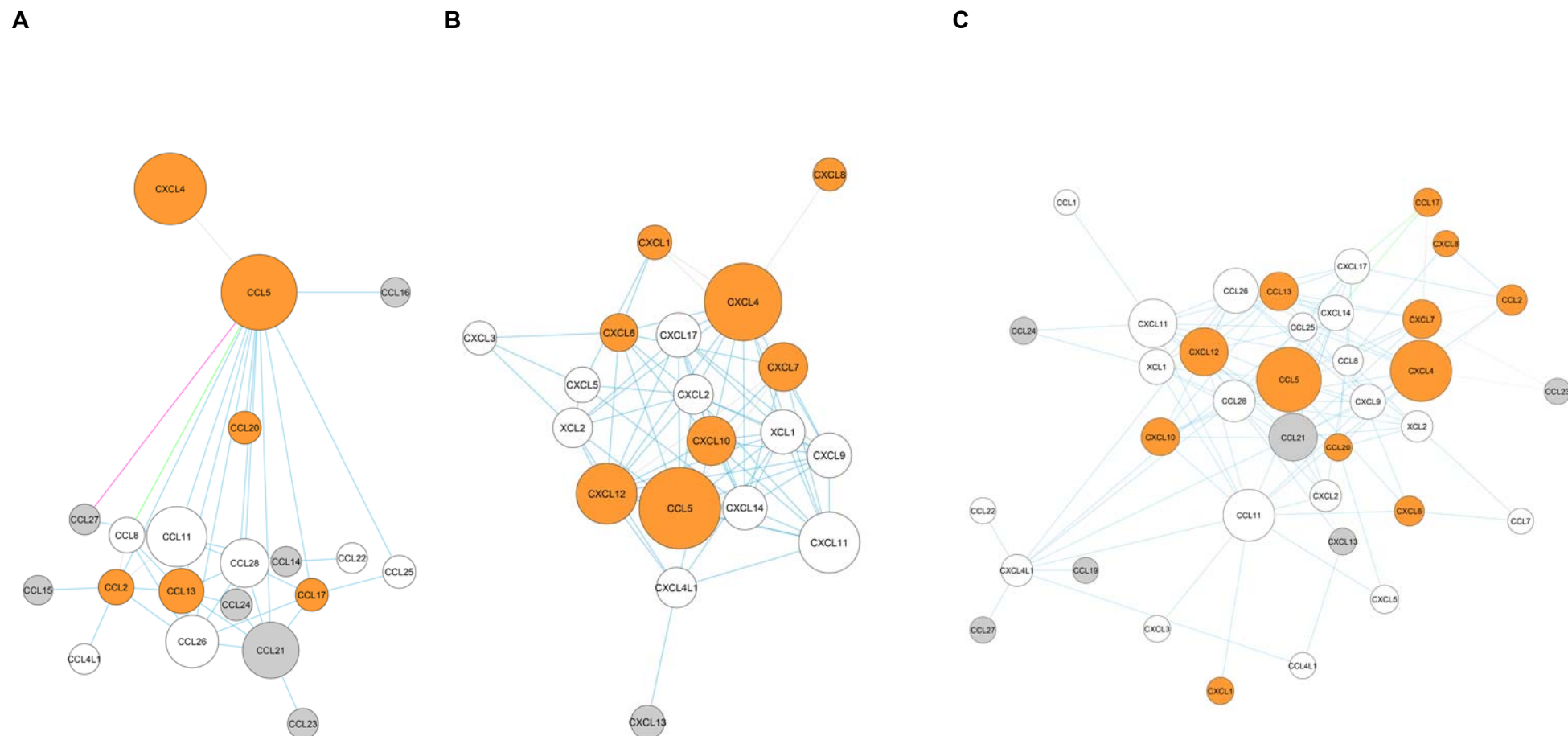
Fig. 3. The functional implications of the new chemokine interactome. (**A**) Known or presumably synergistic CC-type interactions are shown. (**B**) Known or presumably inhibitory CXC-type interactions are shown. (**C**) The function of these interactions is unknown. An organic layout was chosen.
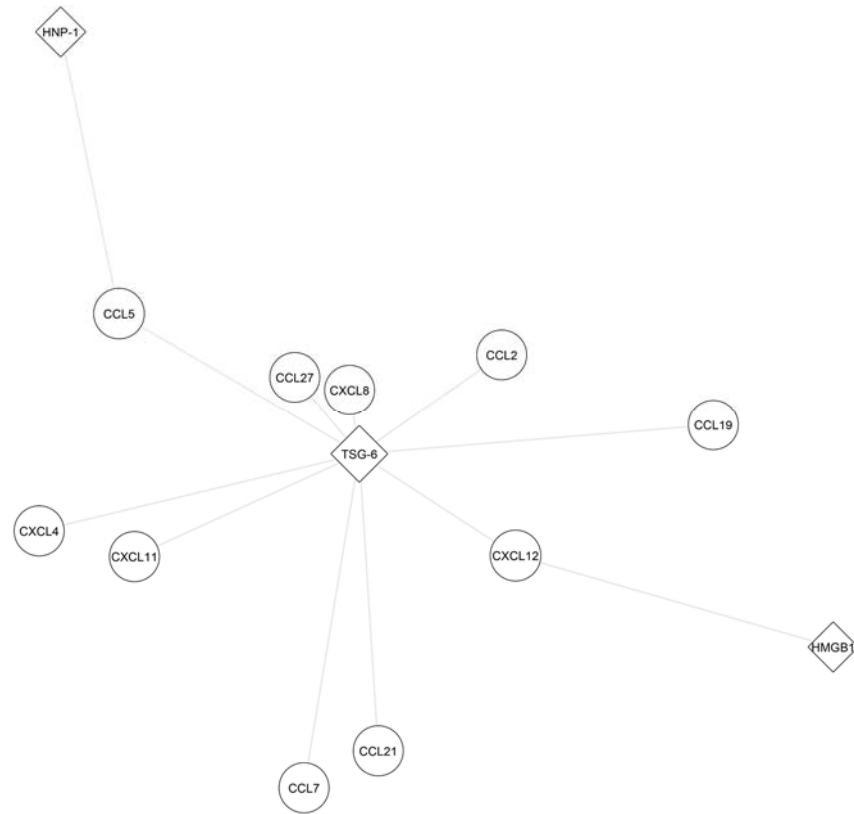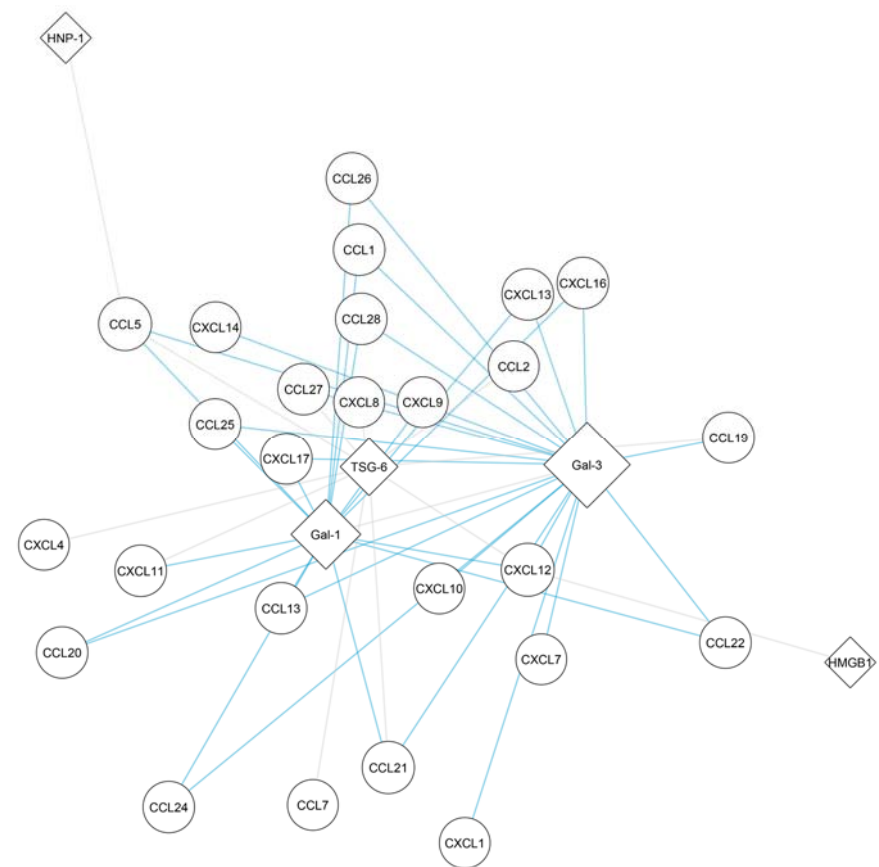
Fig. 4. Known and new interactions of chemokines with other cytokines. (**A**) Known interactions of chemokines with high mobility group box 1 (HMGB1), human neutrophil peptide 1 (HNP-1) and tumor necrosis factor-stimulated gene 6 protein (TSG-6) are shown in gray. Nonchemokine cytokines are depicted as diamonds. (**B**) New interactions of chemokines with galectin-1 (Gal-1) and galectin-3 (Gal-3) are displayed in blue in addition to the known interactions in A.
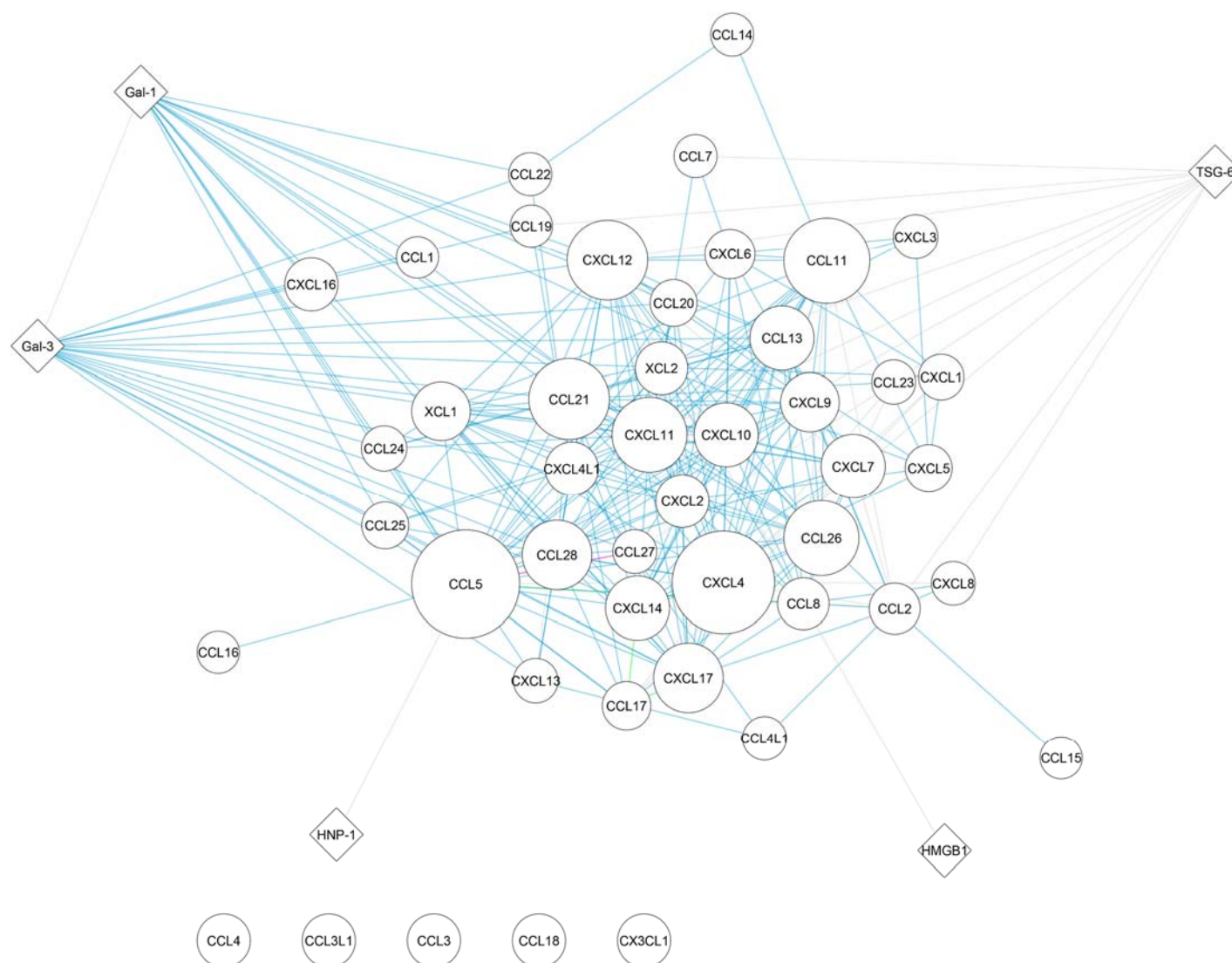
Fig. 5. Previously found and new chemokine interactions.

5. Discussion: Potential pharmacological implications

Our findings may have therapeutic implications. Despite the recognized importance of chemokines for the mediation of inflammation, primarily two reasons preclude targeting chemokines for therapeutic interventions. First, the function of single chemokines may be redundant or, conversely, restricted, and therefore resistant to pharmacological intervention. Second, given that the chemokine system constitutes an important part of the immune system, long-term treatments may impair host defense. Hence, despite overwhelming evidence for their involvement in the pathophysiology of many diseases, strategies to effectively and specifically target the chemokine system are lagging behind.

Chemokine heterodimers may pose limits to redundancy and robustness while increasing the specificity of the system, and may therefore lend themselves to pharmacological intervention. For example, two chemokines A and B may activate the same chemokine receptor so are presumably redundant. Targeting chemokine A alone would not be effective because chemokine B may take over its function. However, the two chemokines may interact with other chemokines which alter their function. Therefore targeting chemokine A by interrupting or mimicking interactions with these chemokines (e.g. with small peptide/molecule inhibitors) may well represent an effective treatment option. It may also be that chemokines A and B play a restricted role but regulate the system in a complex interplay. Targeting chemokine A or chemokine B alone would not affect the system sufficiently. Well-designed interference with shared interactions of both chemokines may constitute an effective pharmacological option. Furthermore, targeting a chemokine which has a predominant role in a system A (e.g. with specific antibodies) may be accompanied by undesired side effects if this chemokine is also involved in a

process B. By contrast, interfering with specific interactions of this chemokine may under certain conditions represent a means to specifically target an adverse process A without interfering with a beneficial process B, in which the same chemokine is also involved. Of note, our findings suggest that mostly inflammatory chemokines form heterodimers which may increase the specificity of pharmacological interventions. Furthermore, chemokine-derived peptides, polyantagonistic peptide bundles or monomolecular polyantagonists are well suited to meet therapeutic requirements.

Our results are particularly relevant to systemic chronic diseases with a strong inflammatory pathogenesis. Atherosclerosis is a chronic inflammatory disease of large and medium-size arteries defined by endothelial dysfunction and subendothelial deposition and modification of lipoproteins. Modified lipoproteins then foster the recruitment of inflammatory cells of the innate and adaptive immune response in a feed-forward loop. Cell migration into, out of and within atherosclerotic lesions constitutes a preeminent driver of the disease (Fig. 6A) (*14, 15*). This inflammatory response generates atherosclerotic plaques that narrow, or occlude vessels after plaque rupture. Atherosclerosis constitutes the underlying pathology of most cardiovascular diseases, including myocardial infarction, stroke, peripheral artery disease and aneurisms and is involved in complications of hypertension or diabetes. It is estimated that the United States will spend more than 1 trillion dollars on direct and indirect costs related to cardiovascular diseases by 2030, which will constitute almost 5% of their GDP by then (*53*).

Although the inflammatory pathogenesis of the disease has long been documented, traditional therapeutic approaches have been based on lipid-lowering agents (statins, ezetimibe, proprotein convertase subtilisin/kexin type 9 (PCSK9) inhibitors), together with blood pressure, hemostatic and metabolic control. Many

patients suffer cardiovascular events despite recommended treatment. For example, one study evaluated the effect of moderate and intensive statin therapy on cardiovascular events in patients with a recent acute coronary syndrome. Even with intensive therapy which effectively reduced low-density lipoprotein (LDL) cholesterol levels, approximately 20% of the patients still suffered cardiovascular events or death from any cause (see e.g. the Pravastatin or Atorvastatin Evaluation and Infection Therapy - Thrombolysis in Myocardial Infarction 22 (PROVE IT-TIMI 22) study (*54*)). These cardiovascular events may be mostly attributed to residual inflammation as measured by increased C-reactive protein (CRP) levels that independently predict recurrent mycocardial infarction or death of coronary cause more strongly than LDL cholesterol levels (*55*). Recent anti-inflammatory approaches have been successful in decreasing this inflammatory risk. The monoclonal interleukin-1β (IL-1β) antibody Canakinumab reduced cardiovascular events by approximately 15% compared to placebo in patients after myocardial infarction with increased high-sensitivity CRP levels on lipid-lowering therapy. This effect was independent of lipid-level lowering (see the Canakinumab Antiinflammatory Thrombosis Outcome Study (CANTOS) trial (*56*)). Colchicine, an anti-inflammatory inhibitor of microtubule formation, reduced cardiovascular events by approximately 70% compared to placebo in patients with stable coronary artery disease under statin (see the Low-Dose Colchicine (LoDoCo) trial (*57*)). However, side effects in these trials where common. For example, patients in the CANTOS trial exhibited an increase in fatal infections and sepsis that counteracted the reduction in cardiovascular events to a net equal all-cause mortality compared to placebo (*56*). Therefore, more specific interference with inflammatory pathways is necessary. The complexity of the immune system may allow to target specific immune cell types, lesion stages and regions if targets and their mechanisms of action are thoroughly characterized (*14*).

Chemokines may constitute targets for efficient anti-inflammatory intervention as shown for CCR2 agonists (*58-60*). In fact, a specific chemokine may have a precise cell type-specific function at a specific disease stage. For example, CCL5 can be detected in atherosclerotic lesions but not in healthy arteries particularly in the initial phase of the disease (*61*). It is involved in the recruitment of T cells and monocytes mediating inflammatory monocyte and T cell arrest on the endothelium (Fig. 6A) (*15*). The polymorphism G403A near the CCL5 gene has been correlated with an enhanced risk for coronary artery disease (*62*). Other chemokines such as CXCL12 are expressed in atherosclerotic plaques but not in healthy vessels particularly at later stages of the disease. Genome-wide association studies (GWASs) attributed a proatherogenic role to endothelial CXCL12 (*63*).

Although initial studies have shown that CCL5 and CXCL12 interact with other chemokines (CXCL4/CXCL7 and CXCL7 respectively) and chemokine-binding proteins (HNP1/TSG-6 and HMGB1/TSG-6 respectively) (Fig. 1 and 4A), our studies extend the spectrum of their interactions to more than 20 other chemokines and, in addition, to the two galectins Gal-1 and Gal-3 (Fig. 2, A and B, 4B and 5). Of note, Gal-3 has a proatherogenic role, is a marker for macrophages (Mac-2) and attracts monocytes and macrophages (Fig. 6A) (*49*). Provided that temporal expression profiles of interacting chemokines and other inflammatory mediators in the plaque overlap, it may now be possible to characterize the disease stage or location of an atherosclerotic plaque based on chemokine interactions (Fig. 6B). For example, in **project 1**, we observed CCL5/CC17 heterodimer formation in diseased human coronaries but not in healthy vessels. Furthermore, we could show differences between the vascular regions of plaque progression. We provided evidence that functionally active CCL5/CXCL4 heterodimers form in the aorta and aortic arch, but not the aortic root where CCL5/CCL17 can be detected. These specific interactions may than be targeted without interfering with host defense. Of note, combined blockade of chemokine receptors in atherosclerosis

has proven very successful in the past (*64*). This approach may integrate detailed knowledge on the function of specific chemokines with the comprehensive analysis of their interactions paving the way for effective and specific therapeutics against atherosclerosis in accordance with modern systems biology.

A

INITIAL STAGE   EARLY LESION   ADVANCED PLAQUE

Vascular lumen

Th2/Treg cell
Th1 cell
Monocyte
Platelet
CCR8
CCR2
CXCL4
CXCR3
CCL5
CCR7
CCR6
CCR5
CXCL12
CXCR2
Endothelial cell
CX3CR1
CX3CL1
LDL
GAGs
Smooth muscle cell

Tunica intima

oxLDL
CCL19/21
CCL1
CCL2
CCL20
CCL17
CXCL10
CCR4
TLR,IL1R etc.
CXCL1
TCR↔MHC II
IL-1β
Gal-3 (Mac-2)
Scavenger receptor
Th2/Treg cell
Th1 cell
Inflammatory macrophage
Foam cell
?

Tunica media

B

CCL1 CCL2 CCL5 CCL17 CCL19 CCL20 CCL21 CXCL4 CXCL10 CXCL12

CCL1 CCL2 CCL5 CCL17 CCL19 CCL20 CCL21 CXCL1 CXCL4 CXCL10 CXCL12

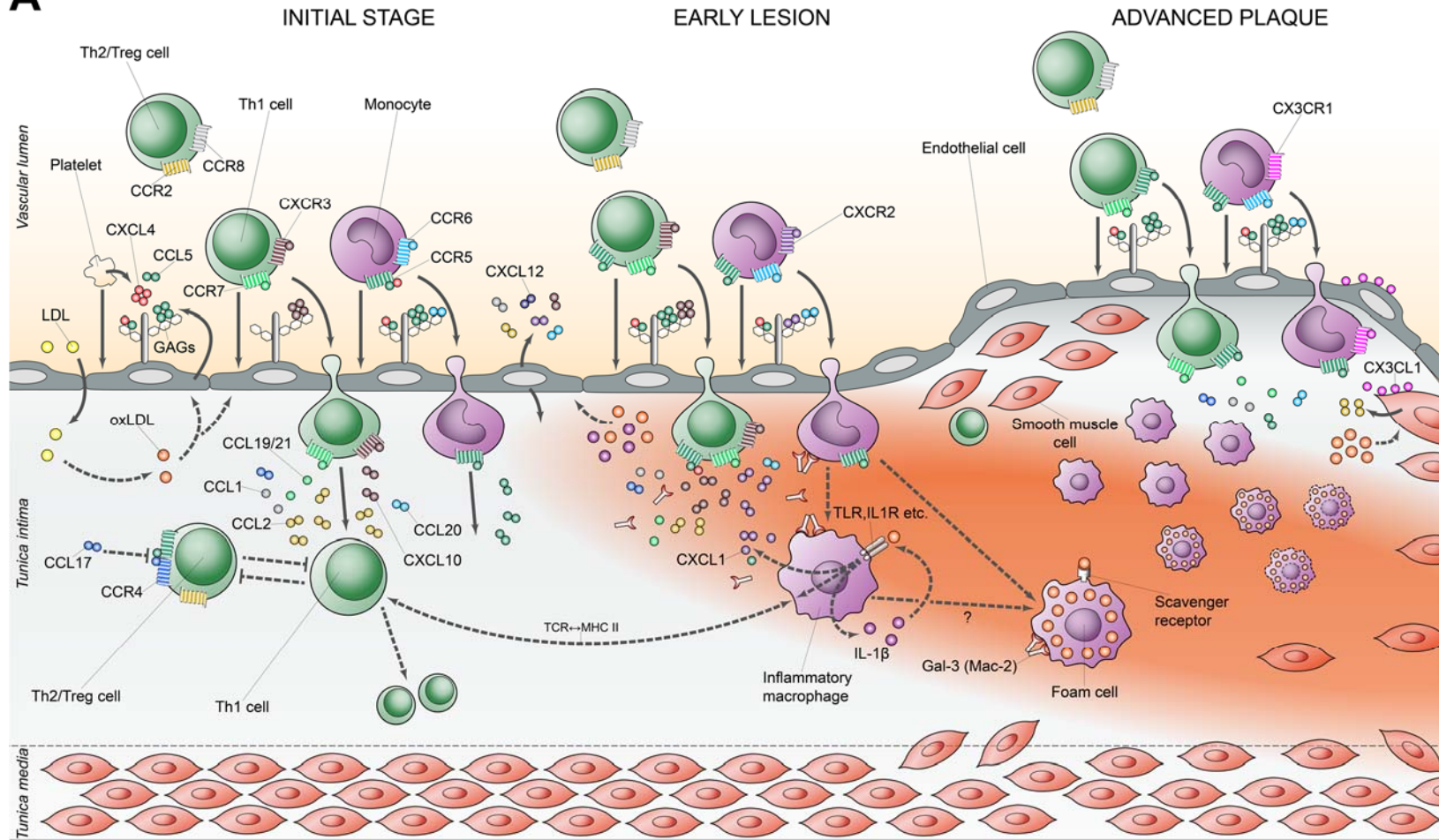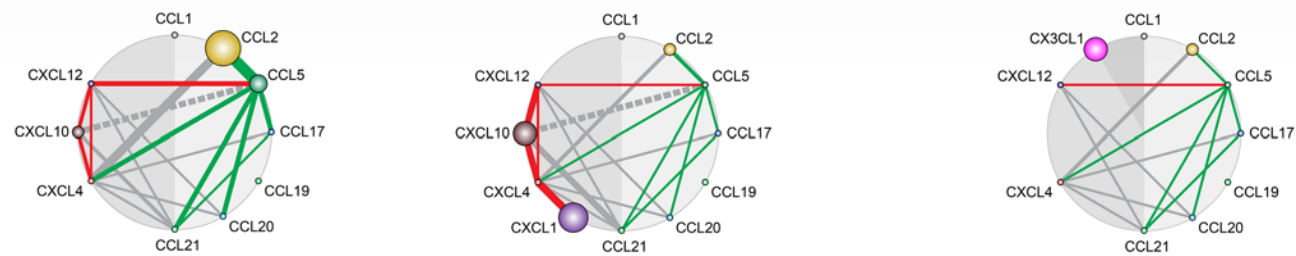CX3CL1 CCL1 CCL2 CCL5 CCL17 CCL19 CCL20 CCL21 CXCL4 CXCL12

Fig. 6. Chemokines and chemokine interactions in the progression of atherosclerotic plaque. (**A**, from left to right) This figure is a highly simplified depiction of the pathophysiological processes leading to atherosclerotic plaque from its initiation, over the early lesion or fatty streak, to the advanced plaque (*14, 15, 51, 61, 65-68*). Risk factors for atherosclerosis (e.g. high blood pressure) induce endothelial injury (not shown). This injury facilitates the entry of low-density lipoproteins (LDLs) from the blood stream into the vascular tunica intima. LDLs are oxidized (oxLDLs) and stimulate endothelial cells to express adhesion molecules (not shown) and chemokines. Consequently, platelets and blood leukocytes, most importantly T cells and monocytes, adhere to the inflamed endothelium. Platelets deposit chemokines on endothelial glycosaminoglycans (GAGs) which facilitate their oligomerization as homooligomers or heterodimers. Leukocytes transmigrate through the endothelium to the tunica intima. The recruitment of leukocytes is mediated by various chemokines and their respective heptahelical G protein-coupled receptors (GPCRs). We showed in **project 1** that a CCL5/CXCL4 heterodimer promotes monocyte adhesion to the inflamed endothelium and T cell migration synergistically by retaining the CCL5 receptor CCR5 on the cell surface. Type 2 T helper (Th2) cells and regulatory T (Treg) cells control the more abundant type 1 T helper (Th1) cells. In **project 1**, we demonstrated that a CCL5/CCL17 heterodimer inhibits the generation of Treg cells synergistically. Naive T cells are either activated within the plaque by oxLDL-particle presenting dendritic cells (not shown) or migrate to secondary lymphatic organs through the tunica media for activation (not shown). Inflammatory macrophages evolve from migrated monocytes and take up oxLDL via Toll-like receptors (TLRs). They produce chemokines and other inflammatory cytokines (e.g. interleukin-1β (IL-1β)) which active them in an autocrine manner (e.g. via the interleukin-1 receptor (IL1R)). Th1 cells and inflammatory macrophages stimulate each other via an interaction between the T-cell receptor (TCR) on the T cell and the oxLDL particle-presenting major histocompatibility complex class II (MHC II) on the macrophage. Monocytes also develop into anti-inflammatory foam cells that clear oxLDL via scavenger receptors. Galectin-3 (Gal-3 or macrophage-2 antigen (Mac-2)) is a proatherogenic macrophage marker. In **project 2**, we suggested that it may also exert an antiatherogenic function by interacting with several chemokines to inhibit T cell and monocyte migration. Apoptotic foam cells (dashed outline) constitute a necrotic core of cellular debris and cholesterol (orange). Smooth muscle cells from the tunica media migrate into the developing plaque. They are activated by oxLDL to express chemokines but also produce extracellular matrix in a fibrotic cap to stabilize the plaque (gray). (**B**) We demonstrate in **project 1** that chemokines act in a complex network of heterodimeric interactions (gray circles). Depending on the type of interaction, chemokine heterodimers may be synergistic (green connecting line) or inhibitory (red connecting line, gray line if the type of interaction is unknown, dashed line if the heterodimer is functionally neutral). These networks may be combined with intraplaque expression data of relevant chemokines (in this figure according to the literature, see e.g. (*67, 68*), visualized by the different size of the chemokines and the different width of their connecting lines). We envision that these chemokine networks are in dynamic chemical equilibrium depending on the affinity of the chemokines to each other (not shown). Hence, the networks may be specific in terms of disease progression and location of a plaque within the vasculature. More importantly, they may allow to discriminate the inflammatory processes within atherosclerotic plaque from other inflammatory processes. Therefore, they may lend themselves to precise pharmacological intervention.

6. Summary

Chemokines play a central role in many inflammatory diseases, including atherosclerosis. Their function is tightly regulated. Exemplary studies had shown that chemokines interact with other chemokines and CKBPs. However, the validity of a comprehensive chemokine interactome as regulatory mechanism and therapeutic target had not been investigated. In **project 1**, we tested all human chemokines for heterodimeric interactions by solid-phase assays and SPR and structurally analyzed the interaction of example pairs by NMR spectroscopy. We then investigated the function of these pairs by transmigration and endothelial arrest assays. We confirmed that CC-chemokines form synergistic CC-type heterodimers, whereas CXC-chemokines form inhibitory CXC-type dimers. We then designed small peptide inhibitors to disrupt chemokine heterodimers and covalently linked obligate chemokine heterodimers to prove the validity of the chemokine interactome in mouse models of acute lung injury and atherosclerosis. In **project 2**, we extended the chemokine interactome to another molecular entity, glycan-binding galectins. We found that Gal-1 and 3 interact specifically with several chemokines. We established the structural model of a CXCL12/Gal-3 heterodimer by NMR spectroscopy and showed that Gal-3 inhibits CXCL12-induced immune cell recruitment *in vitro* and *in vivo*. Both studies support the concept of the chemokine interactome as a general principle in immunoregulation. The data may provide the basis for the design of powerful and specific therapies for chronic inflammatory diseases such as atherosclerosis.

7. Zusammenfassung

Chemokine sind entscheidend an der Entstehung entzündlicher Erkrankungen wie Atherosklerose beteiligt. Sie unterliegen genauen regulatorischen Mechanismen. Einige Studien konnten beispielhaft zeigen, dass Chemokine mit anderen Chemokinen und Chemokin-bindenden Proteinen interagieren. Allerdings wurde bisher nicht nachgewiesen, dass diese Interaktionen Teil eines regulatorischen Mechanismus für die Mehrzahl der Chemokine im Sinne eines Chemokin-Interaktoms sind und damit einen Therapieansatz darstellen. In **Projekt 1** untersuchten wir alle menschlichen Chemokine mit Hilfe von Festphasen-Immunassays und Oberflächenplasmonresonanz auf die Bildung von Chemokin-Heterodimeren hin und analysierten einige Paare mit Kernspinresonanzspektroskopie strukturell. Darüber hinaus untersuchten wir die funktionellen Auswirkungen der Paarbildung in Transmigrationsversuchen und endothelialen Arrestassays. Wir bestätigten, dass CC-Chemokine funktionell synergistische Heterodimere vom CC-Typ, CXC-Chemokine hingegen inhibitorische Dimere vom CXC-Typ bilden. Wir entwickelten Inhibitoren auf Peptidbasis, die die Bildung von Chemokin-Heterodimeren verhindern, und kovalent verknüpfte obligate Chemokin-Heterodimere, um die Wirkung von Chemokin-Heterodimeren *in vivo* anhand von Mausmodellen des akuten Lungenversagens und der Atherosklerose zu beweisen. In **Projekt 2** erweiterten wir das Chemokin-Interaktom um die Gruppe der glykan-bindenden Galektine. Wir fanden heraus, dass Gal-1 und Gal-3 spezifisch mit einer Reihe von Chemokinen interagieren. Wir entwarfen ein Strukturmodell der Interaktion von CXCL12 und Gal-3 mit Hilfe von Kernspinresonanzspektroskopie und konnten zeigen, dass Gal-3 die CXCL12-vermittelte Chemotaxis von Leukozyten *in vitro* und *in vivo* hemmt. Beide Arbeiten unterstützen die Hypothese, dass das Chemokin-Interaktom ein allgemeingültiger Mechanismus zur Immunregulation ist. Unsere Ergebnisse

könnten grundsätzlich zur Entwicklung von effektiven und spezifisch wirksamen

Therapien für chronisch-entzündliche Erkrankungen wie Atherosklerose beitragen.

8. Personal contributions

In **project 1**, I planned, executed and interpreted results of solid-phase experiments, transmigration and endothelial arrest assays. This included the generation of a T cell model to test numerous chemokine interactions using only one cell type. I presented my data regularly in lab meetings and was involved in discussions on project progress and planning.

In **project 2**, I planned, executed and interpreted results of solid-phase experiments, SPR experiments, transmigration assays and mouse experiments, signaling and cell binding studies, proximity ligation experiments, cell aggregation experiments and cell viability studies. I contributed significantly to project planning and wrote the manuscript.

9. References

1. A. L. Barabasi, N. Gulbahce, J. Loscalzo, Network medicine: A network-based approach to human disease. *Nat. Rev. Genet.* **12**, 56-68 (2011).

2. J. van der Greef, R. N. McBurney, Innovation: Rescuing drug discovery: In vivo systems pathology and systems pharmacology. *Nat. Rev. Drug Discov.* **4**, 961-967 (2005).

3. M. Vidal, A biological atlas of functional maps. *Cell* **104**, 333-339 (2001).

4. E. E. Schadt, S. H. Friend, D. A. Shaywitz, A network view of disease and compound screening. *Nat. Rev. Drug Discov.* **8**, 286-295 (2009).

5. T. Ideker, T. Galitski, L. Hood, A new approach to decoding life: Systems biology. *Annu. Rev. Genomics Hum. Genet.* **2**, 343-372 (2001).

6. J. Loscalzo, I. Kohane, A. L. Barabasi, Human disease classification in the postgenomic era: A complex systems approach to human pathobiology. *Mol. Syst. Biol.* **3**, 124 (2007).

7. K. Luck, G. M. Sheynkman, I. Zhang, M. Vidal, Proteome-scale human interactomics. *Trends Biochem. Sci.* **42**, 342-354 (2017).

8. M. C. Miller, K. H. Mayo, Chemokines from a structural perspective. *Int. J. Mol. Sci.* **18**, E2088 (2017).

9. G. J. Graham, T. M. Handel, A. E. I. Proudfoot, Leukocyte adhesion: Reconceptualizing chemokine presentation by glycosaminoglycans. *Trends Immunol.* **40**, 472-481 (2019).

10. J. W. Griffith, C. L. Sokol, A. D. Luster, Chemokines and chemokine receptors: Positioning cells for host defense and immunity. *Annu. Rev. Immunol.* **32**, 659-702 (2014).

11. A. Zlotnik, O. Yoshie, The chemokine superfamily revisited. *Immunity* **36**, 705-716 (2012).

12. C. E. Hughes, R. J. B. Nibbs, A guide to chemokines and their receptors. *FEBS J.* **285**, 2944-2971 (2018).

13. P. Lopez-Cotarelo, C. Gomez-Moreira, O. Criado-Garcia, L. Sanchez, J. L. Rodriguez-Fernandez, Beyond chemoattraction: Multifunctionality of chemokine receptors in leukocytes. *Trends Immunol.* **38**, 927-941 (2017).

14. E. Lutgens, D. Atzler, Y. Döring, J. Duchene, S. Steffens, C. Weber, Immunotherapy for cardiovascular disease. *Eur. Heart J.* **40**, 3937-3946 (2019).

15. H. Noels, C. Weber, R. R. Koenen, Chemokines as therapeutic targets in cardiovascular disease. *Arterioscler. Thromb. Vasc. Biol.* **39**, 583-592 (2019).

16. V. Eckardt, C. Weber, P. von Hundelshausen, Glycans and glycan-binding proteins in atherosclerosis. *Thromb. Haemost.* **119**, 1265-1273 (2019).

17. Z. Szekanecz, A. E. Koch, Successes and failures of chemokine-pathway targeting in rheumatoid arthritis. *Nat. Rev. Rheumatol.* **12**, 5-13 (2016).

18. P. J. Barnes, Targeting cytokines to treat asthma and chronic obstructive pulmonary disease. *Nat. Rev. Immunol.* **18**, 454-466 (2018).

19. Z. Wang, H. Shang, Y. Jiang, Chemokines and chemokine receptors: Accomplices for Human immunodeficiency virus infection and latency. *Front. Immunol.* **8**, 1274 (2017).

20. N. Nagarsheth, M. S. Wicha, W. Zou, Chemokines in the cancer microenvironment and their relevance in cancer immunotherapy. *Nat. Rev. Immunol.* **17**, 559-572 (2017).

21. M. J. Stone, J. A. Hayward, C. Huang, E. H. Z, J. Sanchez, Mechanisms of regulation of the chemokine-receptor network. *Int. J. Mol. Sci.* **18**, E342 (2017).

22. L. Martinez-Munoz, R. Villares, J. L. Rodriguez-Fernandez, J. M. Rodriguez-Frade, M. Mellado, Remodeling our concept of chemokine receptor function: From monomers to oligomers. *J. Leukoc. Biol.* **104**, 323-331 (2018).

23. A. J. Zweemer, J. Toraskar, L. H. Heitman, A. P. Ijzerman, Bias in chemokine receptor signalling. *Trends Immunol.* **35**, 243-252 (2014).

24. S. Gencer, E. P. C. van der Vorst, M. Aslani, C. Weber, Y. Döring, J. Duchene, Atypical chemokine receptors in cardiovascular disease. *Thromb. Haemost.* **119**, 534-541 (2019).

25. A. Kapurniotu, O. Gokce, J. Bernhagen, The multitasking potential of alarmins and atypical chemokines. *Front. Med. (Lausanne)* **6**, 3 (2019).

26. B. Vanbervliet, N. Bendriss-Vermare, C. Massacrier, B. Homey, O. de Bouteiller, F. Briere, G. Trinchieri, C. Caux, The inducible CXCR3 ligands control plasmacytoid dendritic cell responsiveness to the constitutive chemokine Stromal cell-derived factor 1 (SDF-1)/CXCL12. *J. Exp. Med.* **198**, 823-830 (2003).

27. M. Gouwy, S. Struyf, F. Mahieu, W. Put, P. Proost, J. Van Damme, The unique property of the CC chemokine Regakine-1 to synergize with other plasma-derived inflammatory mediators in neutrophil chemotaxis does not reside in its NH2-terminal structure. *Mol. Pharmacol.* **62**, 173-180 (2002).

28. A. Krug, R. Uppaluri, F. Facchetti, B. G. Dorner, K. C. Sheehan, R. D. Schreiber, M. Cella, M. Colonna, IFN-producing cells respond to CXCR3 ligands in the presence of CXCL12 and secrete inflammatory chemokines upon activation. *J. Immunol.* **169**, 6079-6083 (2002).

29. A. Z. Dudek, I. Nesmelova, K. Mayo, C. M. Verfaillie, S. Pitchford, A. Slungaard, Platelet factor 4 promotes adhesion of hematopoietic progenitor cells and binds IL-8: Novel mechanisms for modulation of hematopoiesis. *Blood* **101**, 4687-4694 (2003).

30. G. D'Agostino, V. Cecchinato, M. Uguccioni, Chemokine heterocomplexes and cancer: A novel chapter to be written in tumor immunity. *Front. Immunol.* **9**, 2185 (2018).

31. R. R. Koenen, P. von Hundelshausen, I. V. Nesmelova, A. Zernecke, E. A. Liehn, A. Sarabi, B. K. Kramp, A. M. Piccinini, S. R. Paludan, M. A. Kowalska, A. J. Kungl, T. M. Hackeng, K. H. Mayo, C. Weber, Disrupting functional interactions between platelet chemokines inhibits atherosclerosis in hyperlipidemic mice. *Nat. Med.* **15**, 97-103 (2009).

32. H. Heidarieh, B. Hernaez, A. Alcami, Immune modulation by virus-encoded secreted chemokine binding proteins. *Virus Res.* **209**, 67-75 (2015).

33. R. P. Bhusal, J. R. O. Eaton, S. T. Chowdhury, C. A. Power, A. E. I. Proudfoot, M. J. Stone, S. Bhattacharya, Evasins: Tick salivary proteins that inhibit mammalian chemokines. *Trends Biochem. Sci.* **45**, 108-122 (2020).

34. A. J. Day, C. M. Milner, TSG-6: A multifunctional protein with anti-inflammatory and tissue-protective properties. *Matrix Biol.* **78-79**, 60-83 (2019).

35. J. E. Alard, A. Ortega-Gomez, K. Wichapong, D. Bongiovanni, M. Horckmans, R. T. Megens, G. Leoni, B. Ferraro, J. Rossaint, N. Paulin, J. Ng, H. Ippel, D. Suylen, R. Hinkel, X. Blanchet, F. Gaillard, M. D'Amico, P. von Hundelshausen, A. Zarbock, C. Scheiermann, T. M. Hackeng, S. Steffens, C. Kupatt, G. A. Nicolaes, C. Weber, O. Soehnlein, Recruitment of classical monocytes can be inhibited by disturbing heteromers of neutrophil HNP1 and platelet CCL5. *Sci. Transl. Med.* **7**, 317ra196 (2015).

36. J. Lubkowski, G. Bujacz, L. Boque, P. J. Domaille, T. M. Handel, A. Wlodawer, The structure of MCP-1 in two crystal forms provides a rare example of variable quaternary interactions. *Nat. Struct. Biol.* **4**, 64-69 (1997).

37. G. M. Clore, E. Appella, M. Yamada, K. Matsushima, A. M. Gronenborn, Three-dimensional structure of interleukin 8 in solution. *Biochemistry* **29**, 1689-1696 (1990).

38. E. S. Kuloglu, D. R. McCaslin, M. Kitabwalla, C. D. Pauza, J. L. Markley, B. F. Volkman, Monomeric solution structure of the prototypical 'C' chemokine Lymphotactin. *Biochemistry* **40**, 12486-12496 (2001).

39. J. C. Fox, R. C. Tyler, C. Guzzo, R. L. Tuinstra, F. C. Peterson, P. Lusso, B. F. Volkman, Engineering metamorphic chemokine Lymphotactin/XCL1 into the GAG-binding, HIV-inhibitory dimer conformation. *ACS Chem. Biol.* **10**, 2580-2588 (2015).

40. D. M. Hoover, L. S. Mizoue, T. M. Handel, J. Lubkowski, The crystal structure of the chemokine domain of Fractalkine shows a novel quaternary arrangement. *J. Biol. Chem.* **275**, 23187-23193 (2000).

41. F. Bachelerie, G. J. Graham, M. Locati, A. Mantovani, P. M. Murphy, R. Nibbs, A. Rot, S. Sozzani, M. Thelen, New nomenclature for atypical chemokine receptors. *Nat. Immunol.* **15**, 207-208 (2014).

42. F. Bachelerie, A. Ben-Baruch, A. M. Burkhardt, C. Combadiere, J. M. Farber, G. J. Graham, R. Horuk, A. H. Sparre-Ulrich, M. Locati, A. D. Luster, A. Mantovani, K. Matsushima, P. M. Murphy, R. Nibbs, H. Nomiyama, C. A. Power, A. E. Proudfoot, M. M. Rosenkilde, A. Rot, S. Sozzani, M. Thelen, O. Yoshie, A. Zlotnik, International Union of Basic and Clinical Pharmacology. [corrected]. LXXXIX. Update on the extended family of chemokine receptors and introducing a new nomenclature for atypical chemokine receptors. *Pharmacol. Rev.* **66**, 1-79 (2014).

43. X. Blanchet, M. Langer, C. Weber, R. R. Koenen, P. von Hundelshausen, Touch of chemokines. *Front. Immunol.* **3**, 175 (2012).

44. C. A. Hansell, C. E. Hurson, R. J. Nibbs, DARC and D6: Silent partners in chemokine regulation? *Immunol. Cell Biol.* **89**, 197-206 (2011).

45. A. Mantovani, R. Bonecchi, M. Locati, Tuning inflammation and immunity by chemokine sequestration: Decoys and more. *Nat. Rev. Immunol.* **6**, 907-918 (2006).

46. R. D. Cummings, F. T. Liu, G. R. Vasta, "Galectins" in Essentials of Glycobiology (Cold Spring Harbor Laboratory Press, Cold Spring Harbor, ed. 3, 2015), pp. 469-480.

47. M. C. Miller, A. K. Ludwig, K. Wichapong, H. Kaltner, J. Kopitz, H. J. Gabius, K. H. Mayo, Adhesion/growth-regulatory galectins tested in combination: Evidence for formation of hybrids as heterodimers. *Biochem. J.* **475**, 1003-1018 (2018).

48. J. Kopitz, S. Vertesy, S. Andre, S. Fiedler, M. Schnolzer, H. J. Gabius, Human chimera-type galectin-3: Defining the critical tail length for high-affinity glycoprotein/cell surface binding and functional competition with galectin-1 in neuroblastoma cell growth regulation. *Biochimie* **104**, 90-99 (2014).

49. M. Nachtigal, A. Ghaffar, E. P. Mayer, Galectin-3 gene inactivation reduces atherosclerotic lesions and adventitial inflammation in ApoE-deficient mice. *Am. J. Pathol.* **172**, 247-255 (2008).

50. J. Carlson, S. A. Baxter, D. Dreau, I. V. Nesmelova, The heterodimerization of platelet-derived chemokines. *Biochim. Biophys. Acta* **1834**, 158-168 (2013).

51. R. R. Koenen, C. Weber, Therapeutic targeting of chemokine interactions in atherosclerosis. *Nat. Rev. Drug Discov.* **9**, 141-153 (2010).

52. J. Duchene, P. von Hundelshausen, Platelet-derived chemokines in atherosclerosis. *Hamostaseologie* **35**, 137-141 (2015).

53. P. A. Heidenreich, J. G. Trogdon, O. A. Khavjou, J. Butler, K. Dracup, M. D. Ezekowitz, E. A. Finkelstein, Y. Hong, S. C. Johnston, A. Khera, D. M. Lloyd-Jones, S. A. Nelson, G. Nichol, D. Orenstein, P. W. Wilson, Y. J. Woo, on behalf of the American Heart Association Advocacy Coordinating Committee, Stroke Council, Council on Cardiovascular Radiology and Intervention, Council on Clinical Cardiology, Council on Epidemiology and Prevention, Council on Atherosclerosis, Thrombosis and Vascular Biology, Council on Cardiopulmonary, Critical Care, Perioperative and Resuscitation, Council on Cardiovascular Nursing, Council on the Kidney in Cardiovascular Disease, Council on Cardiovascular Surgery and Anesthesia, and Interdisciplinary Council on Quality of Care and Outcomes Research, Forecasting the future ofheind cardiovascular disease in the United States: A policy statement from the American Heart Association. Circulation 123, 933-944 (2011).

54. C. P. Cannon, E. Braunwald, C. H. McCabe, D. J. Rader, J. L. Rouleau, R. Belder, S. V. Joyal, K. A. Hill, M. A. Pfeffer, A. M. Skene, for the Pravastatin or Atorvastatin Evaluation and Infection Therapy-Thrombolysis in Myocardial Infarction 22 Investigators, Intensive versus moderate lipid lowering with statins after acute coronary syndromes. N. Engl. J. Med. 350, 1495-1504 (2004).

55. P. M. Ridker, C. P. Cannon, D. Morrow, N. Rifai, L. M. Rose, C. H. McCabe, M. A. Pfeffer, E. Braunwald, for the Pravastatin or Atorvastatin Evaluation and Infection Therapy-Thrombolysis in Myocardial Infarction 22 (PROVE IT-TIMI 22) Investigators, C-reactive protein levels and outcomes after statin therapy. N. Engl. J. Med. 352, 20-28 (2005).

56. P. M. Ridker, B. M. Everett, T. Thuren, J. G. MacFadyen, W. H. Chang, C. Ballantyne, F. Fonseca, J. Nicolau, W. Koenig, S. D. Anker, J. J. P. Kastelein, J. H. Cornel, P. Pais, D. Pella, J. Genest, R. Cifkova, A. Lorenzatti, T. Forster, Z. Kobalava, L. Vida-Simiti, M. Flather, H. Shimokawa, H. Ogawa, M. Dellborg, P. R. F. Rossi, R. P. T. Troquay, P. Libby, R. J. Glynn, for the CANTOS Trial Group, Antiinflammatory therapy with Canakinumab for atherosclerotic disease. N. Engl. J. Med. 377, 1119-1131 (2017).

57.   S. M. Nidorf, J. W. Eikelboom, C. A. Budgeon, P. L. Thompson, Low-dose Colchicine for secondary prevention of cardiovascular disease. *J. Am. Coll. Cardiol.* **61**, 404-410 (2013).

58.   A. W. Aday, P. M. Ridker, Targeting residual inflammatory risk: A shifting paradigm for atherosclerotic disease. *Front. Cardiovasc. Med.* **6**, 16 (2019).

59.   J. Gilbert, J. Lekstrom-Himes, D. Donaldson, Y. Lee, M. Hu, J. Xu, T. Wyant, M. Davidson, for the MLN1202 Study Group, Effect of CC chemokine receptor 2 CCR2 blockade on serum C-reactive protein in individuals at atherosclerotic risk and with a single nucleotide polymorphism of the Monocyte chemoattractant protein-1 promoter region. Am. J. Cardiol. 107, 906-911 (2011).

60.   J. A. de Lemos, D. A. Morrow, M. S. Sabatine, S. A. Murphy, C. M. Gibson, E. M. Antman, C. H. McCabe, C. P. Cannon, E. Braunwald, Association between plasma levels of Monocyte chemoattractant protein-1 and long-term clinical outcomes in patients with acute coronary syndromes. *Circulation* **107**, 690-695 (2003).

61.   C. Weber, H. Noels, Atherosclerosis: Current pathogenesis and therapeutic options. *Nat. Med.* **17**, 1410-1422 (2011).

62.   E. Simeoni, B. R. Winkelmann, M. M. Hoffmann, S. Fleury, J. Ruiz, L. Kappenberger, W. Marz, G. Vassalli, Association of RANTES G-403A gene polymorphism with increased risk of coronary arteriosclerosis. *Eur. Heart J.* **25**, 1438-1446 (2004).

63.   Y. Döring, E. P. C. van der Vorst, J. Duchene, Y. Jansen, S. Gencer, K. Bidzhekov, D. Atzler, D. Santovito, D. J. Rader, D. Saleheen, C. Weber, CXCL12 derived from endothelial cells promotes atherosclerosis to drive coronary artery disease. *Circulation* **139**, 1338-1340 (2019).

64.   C. Combadiere, S. Potteaux, M. Rodero, T. Simon, A. Pezard, B. Esposito, R. Merval, A. Proudfoot, A. Tedgui, Z. Mallat, Combined inhibition of CCL2, CX3CR1, and CCR5 abrogates Ly6C(hi) and Ly6C(lo) monocytosis and almost abolishes atherosclerosis in hypercholesterolemic mice. *Circulation* **117**, 1649-1657 (2008).

65.   J. W. Williams, L. H. Huang, G. J. Randolph, Cytokine circuits in cardiovascular disease. *Immunity* **50**, 941-954 (2019).

66.   R. R. Koenen, C. Weber, Chemokines: Established and novel targets in atherosclerosis. *EMBO Mol. Med.* **3**, 713-725 (2011).

67.   C. Cheng, D. Tempel, R. van Haperen, H. C. de Boer, D. Segers, M. Huisman, A. J. van Zonneveld, P. J. Leenen, A. van der Steen, P. W. Serruys, R. de Crom, R. Krams, Shear stress-induced changes in atherosclerotic plaque composition are modulated by chemokines. *J. Clin. Invest.* **117**, 616-626 (2007).

68.   E. Lutgens, B. Faber, K. Schapira, C. T. Evelo, R. van Haaften, S. Heeneman, K. B. Cleutjens, A. P. Bijnens, L. Beckers, J. G. Porter, C. R. Mackay, P. Rennert, V. Bailly, M. Jarpe, B. Dolinski, V. Koteliansky, T. de Fougerolles, M. J. Daemen, Gene profiling in atherosclerosis reveals a key role for small inducible cytokines: Validation using a novel Monocyte chemoattractant protein monoclonal antibody. *Circulation* **111**, 3443-3452 (2005).

INFLAMMATION

Chemokine interactome mapping enables tailored intervention in acute and chronic inflammation

Philipp von Hundelshausen,[1,2] Stijn M. Agten,[3]* Veit Eckardt,[1]* Xavier Blanchet,[1]*
Martin M. Schmitt,[1]* Hans Ippel,[3]* Carlos Neideck,[1]* Kiril Bidzhekov,[1]* Julian Leberzammer,[1]
Kanin Wichapong,[3] Alexander Faussner,[1] Maik Drechsler,[1] Jochen Grommes,[4]
Johanna P. van Geffen,[3] He Li,[1] Almudena Ortega-Gomez,[1] Remco T. A. Megens,[1]
Ronald Naumann,[5] Ingrid Dijkgraaf,[3] Gerry A. F. Nicolaes,[3] Yvonne Döring,[1,2] Oliver Soehnlein,[1,2,6]
Esther Lutgens,[1,2,7] Johan W. M. Heemskerk,[2] Rory R. Koenen,[1,3] Kevin H. Mayo,[3,8]
Tilman M. Hackeng,[3] Christian Weber[1,2,3]†

Chemokines orchestrate leukocyte trafficking and function in health and disease. Heterophilic interactions between chemokines in a given microenvironment may amplify, inhibit, or modulate their activity; however, a systematic evaluation of the chemokine interactome has not been performed. We used immunoligand blotting and surface plasmon resonance to obtain a comprehensive map of chemokine-chemokine interactions and to confirm their specificity. Structure-function analyses revealed that chemokine activity can be enhanced by CC-type heterodimers but inhibited by CXC-type heterodimers. Functional synergism was achieved through receptor heteromerization induced by CCL5-CCL17 or receptor retention at the cell surface via auxiliary proteoglycan binding of CCL5-CXCL4. In contrast, inhibitory activity relied on conformational changes (in CXCL12), affecting receptor signaling. Obligate CC-type heterodimers showed high efficacy and potency and drove acute lung injury and atherosclerosis, processes abrogated by specific CCL5-derived peptide inhibitors or knock-in of an interaction-deficient CXCL4 variant. Atheroprotective effects of CCL17 deficiency were phenocopied by a CCL5-derived peptide disrupting CCL5-CCL17 heterodimers, whereas a CCL5 α-helix peptide mimicked inhibitory effects on CXCL12-driven platelet aggregation. Thus, formation of specific chemokine heterodimers differentially dictates functional activity and can be exploited for therapeutic targeting.

INTRODUCTION

Chemokines regulate leukocyte activation and coordinate their trafficking to sites of inflammation or during immune surveillance. The G protein–coupled receptor (GPCR) binding and function of chemokines are governed by their interaction with cell surface proteoglycans, oligomer formation, naturally occurring antagonists, and proteolytic processing (1, 2). Recent studies unveiled that heteromeric interactions between chemokines modify their biological activities and provide structural insight into underlying mechanisms. Consequently, we hypothesized that a functional chemokine interactome composed of pairwise heteromeric interactions could inform how signals conferred by individual chemokines can be integrated to control leukocyte responses (3, 4).

Many chemokines form homodimers or oligomers based on two modes to support interfaces: CC-type or CXC-type (5). Dimerization in a CC-type occurs via interaction of the flexible N termini to form a two-stranded antiparallel β-sheet, whereas in a CXC-type, chemokines interact by antiparallel extension of preformed β-strands (5). In addition, their structural similarity allows chemokines to form unique heterodimers to shape the overall signaling response of their

receptors, and homo- and heteromerization of some chemokines are linked to glycosaminoglycan (GAG) binding (4–7). Molecular dynamics simulation (MDS) for selected chemokine homo- and heterodimer pairs predicts that association of free energies depend upon the particular chemokine combination and dimer-type (CC or CXC), some of which are energetically favored over others (8). MDS suggests that CC chemokines preferably engage in CC-type interactions and that CXC chemokines favor a CXC-type, whereas both interactions can occur in mixed CC-CXC heteromers. Preferred modes of interaction have been validated experimentally for some chemokine pairs but have not been extensively explored or linked to differential functions. Nuclear magnetic resonance (NMR) analyses revealed that CC chemokine receptor 2 (CCR2) ligands form CC-type heteromers and that CCL5 forms a mixed CC-type heteromer with the CXC chemokine CXCL4 (6, 7). The CXC-type heterodimer CXCL4-CXCL8 inhibits CXCL8-mediated endothelial cell activation and proliferation, binding CXCR2 less strongly than CXCL8 alone (9, 10). Peptide-mediated disruption of the CCL5-CXCL4 heteromer revealed that this interaction enhances CCL5-mediated leukocyte recruitment, acute lung injury, and atherosclerosis in mouse models (7, 11); however, other heteromers have not been evaluated in disease models.

Among the interactions between platelet-derived chemokines identified by mass spectrometry, MDS revealed that CXCL4 can undergo conformational changes to align its α-helix with that of CXCL12 to form a CXC-type dimer (12). Without providing clues toward the type of interaction, screening for synergistic effects on leukocytes showed that combinations of CCR7 agonists with some nonagonist chemokines led to formation of heteromers that enhance T cell migration and CCR2 ligand activity in monocytes (13, 14). Such evidence of functional synergy implied that heteromers may act as amplifiers in

[1]Institute for Cardiovascular Prevention (IPEK), Ludwig-Maximilians-Universität München, Munich, Germany. [2]German Center for Cardiovascular Research (DZHK), Partner Site Munich Heart Alliance, Munich, Germany. [3]Cardiovascular Research Institute Maastricht, Maastricht University, Maastricht, Netherlands. [4]Department of Vascular Surgery, RWTH Aachen University, Aachen, Germany. [5]Max Planck Institute of Molecular Cell Biology and Genetics, Dresden, Germany. [6]Department of Physiology and Pharmacology, Karolinksa Institutet, Stockholm, Sweden. [7]Department of Medical Biochemistry, AMC, Amsterdam, Netherlands. [8]Department of Biochemistry, Molecular Biology and Biophysics, University of Minnesota, Minneapolis, MN, USA.
*These are co-second authors.
†Corresponding author. Email: chweber@med.lmu.de

chemokine-rich tissues; however, a systematic and in-depth approach to map interactions between chemokines and to verify their functional specificity has not been undertaken. Here, we have established the chemokine interactome comprising all heterophilic chemokine-chemokine interactions. We further show that CC-type heterodimers mediate functional synergism, whereas CXC-type heterodimers cause inhibitory effects, both of which can be targeted by specific peptides in models of inflammation and atherosclerosis.

RESULTS

Mapping the chemokine interactome

Unbiased bidirectional immunoblot chemokine screening, in which one partner was immobilized on a nitrocellulose membrane and the other remained in solution (fig. S1), identified heteromeric interactions between pairwise combinations of all known human chemokines. Interactions were considered positive when they exceeded a densitometry threshold of 5% (on average) relative to positive controls in either direction (Fig. 1A and table S1). The full interactome matrix revealed hotspots of heteromeric interactions (mostly for inflammatory pairs) and large areas devoid of interactions (Fig. 1A). Neither CC chemokines that adopt unusual polymeric or unique monomer states (CCL3, CCL4, and CCL18) (15, 16) nor transmembrane chemokines (CX3CL1 and CXCL16) formed heteromers. With the exception of CCR7 ligands, only a few nonmucosal homeostatic chemokines or plasma chemokines activated by N-terminal cleavage (1) engaged in interactions.

In pursuit of disease-specific therapeutic targets, we focused on chemokines involved in atherosclerosis. CCL2 interacted with CCL5, CXCL8, and other CCR2 ligands (Fig. 1A). The atherogenic CCR1/3/5 agonist CCL5 was the most promiscuous chemokine, forming heteromers with 24 partners (Fig. 1A). Various CXCR2 and CXCR3 ligands (2) interacted with each other and with CCL2, CCL5, or CCL11. We did not consider CCR7 ligands because of their inconclusive role in atherosclerosis models (17). The atypical chemokine CXCL4 interacted with CXCL12 and many atherogenic chemokines. CXCL4L1, a CXCL4 variant that differs at three C-terminal residues (18, 19), primarily interacted with CCL19/21/25/27 and CXCL12 but not with CCL5, thus displaying a more homeostatic profile. An explanation as to why CXCL4L1 does not interact with CCL5 is that the changes in the C-terminal helix lead to a larger angle formed with the central β-sheet and exposure of residues within the core that are usually covered by the helix (19). Because heterodimer formation of CCL5-CXCL4 requires residues from the β-sheet of CXCL4 (7), this alteration may critically interfere with the binding of CCL5.

The multiple interactions observed for CCL5 and CXCL4 were validated by surface plasmon resonance (SPR), which also confirmed the interactions of atheroprotective CXCL12 with CCL5 or CXCL4 and a more selective interaction pattern of CCL17 (Fig. 1, B to E). Thresholds for SPR and densitometry were defined so as to minimize the number of nonvalidated interactions. In addition to observing positive signals in ligand blots and/or in previous assays, interactions were considered bona fide when they passed these thresholds or had good affinity [dissociation constant (K_d) < 10^{-6} M] despite subthreshold SPR responses (Fig. 1, A to E, and table S2).

To elaborate interactions of interest, we performed kinetics analyses, for example, using native CCL5 and CCL5^{E66S} (to obtain equilibrium binding at higher concentrations) on CCL17-conjugated

chips (fig. S2). Equilibrium K_ds revealed that CCL5 and CCL5^{E66S} had equivalent affinity for CCL17 and CXCL4 (K_d < 10^{-8} M), intermediate affinity for CCL2 and CXCL7 (K_d < 10^{-7} M), and lower affinity for CXCL12 (table S2). The affinities of CCL5 for CXCL4, CXCL4^{K50E}, and the CXCL4$^{R>Q}$ mutant with abolished heparin binding (20) were moderately reduced or similar, whereas CXCL4L1 did not bind CCL5 but retained affinity for CXCL12. Conversely, CCL5 and the mutant CCL5^{E66S} had high affinity for CXCL4, whereas mutation of the basic BBXB cluster (CCL5^{44AANA47}) or E26 (CCL5^{E26A}) resulted in no or impaired binding, identifying residues critical for the interaction. CCL5 and CCL5^{E66S} showed similar affinities for CCL17 and CXCL12. Monomeric CCL5^{MT7} (N-methylated T7) did not bind CXCL4 and bound CCL17 with 17-fold lower affinity, consistent with a role of the CCL5 N terminus in CC-type interactions. CCL5^{E26A} but not CCL5^{44AANA47} had high affinity for CCL17, implying a specific role of E26 in binding to CXCL4, with the BBXB motif also involved in binding to CCL17.

Formation of different types of chemokine heterodimers

We focused our NMR structural studies on CCL5 and partners selected for their range of interactions and inflammatory relevance. To avoid higher-order aggregation (21) and poor spectral characteristics of native CCL5 (22), we used CCL5^{E66S}. The CXCL4^{K50E} mutant was applied to attenuate CXCL4 tetramer formation and to allay concerns about broadening of NMR spectra due to chemical exchange (23). Heteronuclear single-quantum coherence (HSQC) with ^{15}N-enriched CCL5^{E66S} is exemplified by CXCL4^{K50E} and CCL17 (Fig. 2, A and B; see full spectra in fig. S3). Substantial resonance broadening and minimal chemical shift ($\Delta\delta$) changes indicated heteromeric interactions in the intermediate exchange regime. Changes in resonance intensity (Δintensity) and $\Delta\delta$ of the CCL5^{E66S} monomer were plotted versus its sequence (Fig. 2, C to F). Because CCL5^{E66S} dimer resonances were much less perturbed (fig. S4, A to D), we concluded that heteromeric interactions with CCL5^{E66S} occur between monomers and not dimers. This was supported by comparing $\Delta\delta$ and Δintensity changes for native CXCL4 interactions with monomeric and dimeric CCL5^{E66S} (fig. S4, E to H) and for CXCL4^{K50E} interactions with ^{15}N-enriched wild-type CCL5 at low concentrations (fig. S5). Relative amounts of heterodimer depend on the presence of various homooligomer states and their respective equilibrium constants. Nevertheless, our subsequent results with the obligate CCL5^{MT7} monomer and the noninteracting CXCL4L1 variant that show a lack of functional synergy make off-target effects and altered monomer activity unlikely. Moderate changes in $\Delta\delta$ and homodimers suggest that NMR-deduced binding constants for the heterodimer are higher than those obtained by SPR. Such differences in the affinity range between NMR and SPR are to be expected, primarily because NMR studies require the use of lower pH values and higher protein concentrations than those present under physiological conditions that are better mimicked by SPR using surface-immobilized binding partners.

The type of heterodimer formed (CC or CXC) was elucidated by analyzing spectral changes ($\Delta\delta$ and Δintensity). The most perturbed CCL5^{E66S} monomer resonances belong to residues (7 to 14, 30 to 33, and 47 to 50) involved in CC-type dimers (Fig. 2, C to F, and fig. S4, E and F). In both heteropairs, residues 7 to 11 at the primary CC-type dimer interface displayed relatively large changes. In CCL5^{E66S}, residues 47 to 50 (corresponding to β-strand 3) were more perturbed by interactions with CCL17, whereas residues 30 to 33 were more affected by interactions with CXCL4^{K50E} or CXCL4. As compared to CCL17,

von Hundelshausen et al., Sci. Transl. Med. 9, eaah6650 (2017)   5 April 2017

50

Fig. 1. Mapping of the chemokine interactome. (**A**) Chemokine-chemokine interactions were detected by bidirectional immunoligand blotting. Known atherogenic chemokines are highlighted in orange, and nonmucosal homeostatic chemokines are shaded in gray. No interaction for nonmucosal homeostatic chemokines (gray square) or all other chemokines (white square) is shown. Black squares indicate that antibody binding indistinguishably detects both immobilized and soluble (complexed) chemokine. Chemokine interactions were considered positive (blue) if the densitometric signal exceeded that of the positive control by 5% (on average) on either side of the blot (n = 2 to 4 independent experiments). Chemokine interactions previously identified and experimentally confirmed by other techniques are indicated in dark blue. (**B** to **E**) Binding of soluble chemokines (100 nM) to immobilized CCL5 (B), CXCL4 (C), CXCL12 (D), and CCL17 (E) was assessed by SPR. Mass equivalent response units (RU) were compared after the association phase. SPR thresholds (as indicated by dotted lines) optimally delineating binders (black bars) and nonbinders (white bars) were based on median values derived from all tested interactions of CCL5, CXCL4, and CXCL12 (B to D) or were set at 300 RU by interpolation with immunoblotting for CCL17. Data represent means ± SEM (n = 3 to 5 independent experiments).

smaller spectral effects for CXCL4 indicate slightly weaker interactions with CCL5[E66S], confirming that heterodimer stability depends on residue composition and subunit orientation at the interface (8). Although the coexistence of monomeric, homooligomeric, and heterodimeric conformations and formation of both heterodimer types may occur with varying molar ratios (fig. S6), these two chemokine pairs prefer to form CC-type heterodimers (Fig. 2, G and H).

As evidenced by CCL5[E66S]-induced ^{15}N-CXCL12 spectral changes that reflect intermediate exchange, CXCL12 and CCL5 also form heterodimers (fig. S7, A and B). The most perturbed ^{15}N-CXCL12 resonances belong to residues in β-strand 1 and the C-terminal helix, which are involved in the CXC-type dimer interface. Combining ^{15}N-CCL5[E66S] and unlabeled CXCL12 was also indicative of an interaction but inconclusive in terms of heterodimer-type formed (fig. S7, C and D). Other chemokines, for example, CXCL10, induced relatively nonspecific and moderate spectral changes that are likely attributable to their propensity for homoaggregation, as seen for CXCL10 tetramers (24), and increased viscosity at higher concentrations (fig. S7E). Weighted averaging of Δintensity changes and MDS-based in silico modeling supported the idea that CXCL12 prefers to form CXC-type interactions with CCL5 and
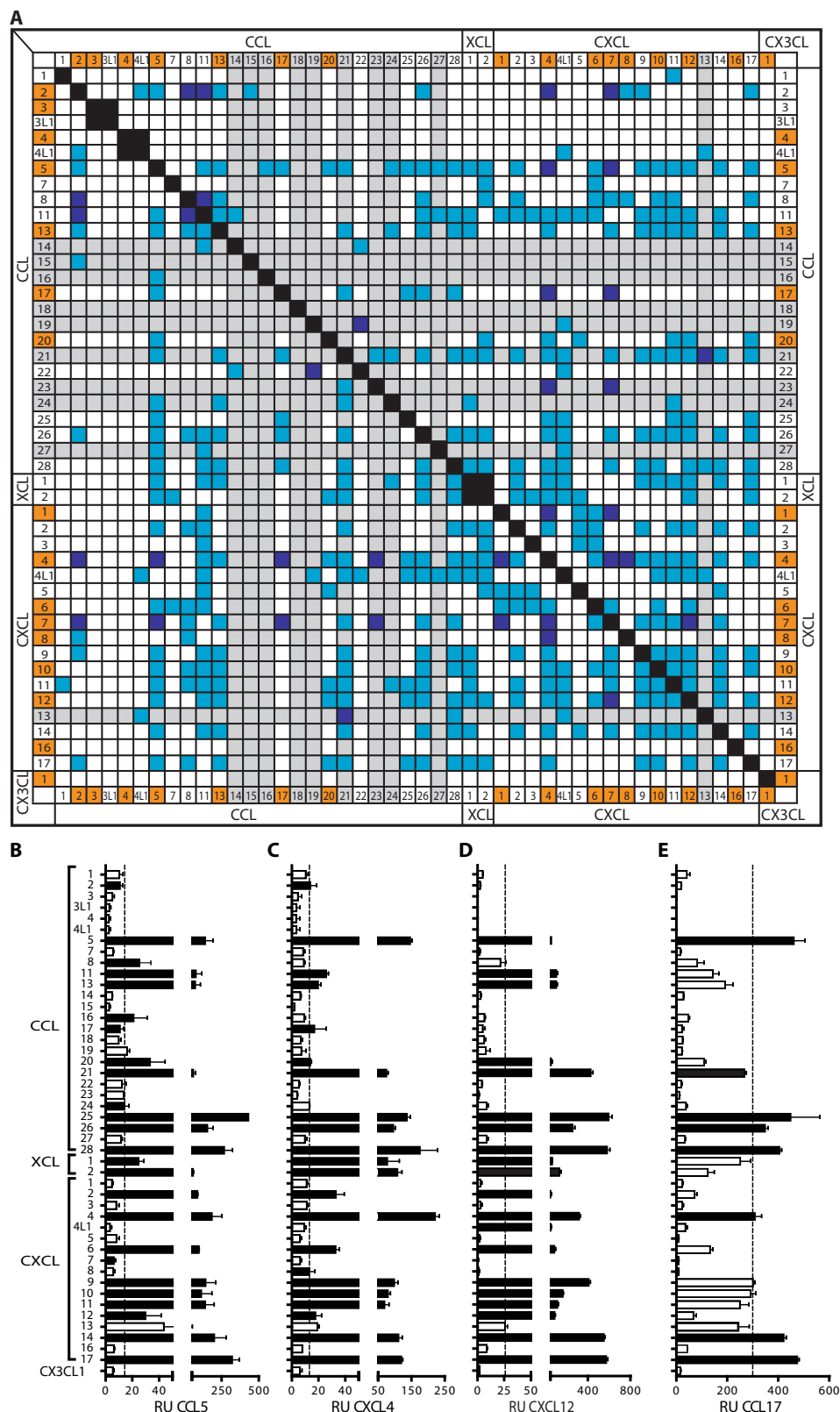
von Hundelshausen et al., Sci. Transl. Med. **9**, eaah6650 (2017)   5 April 2017

51
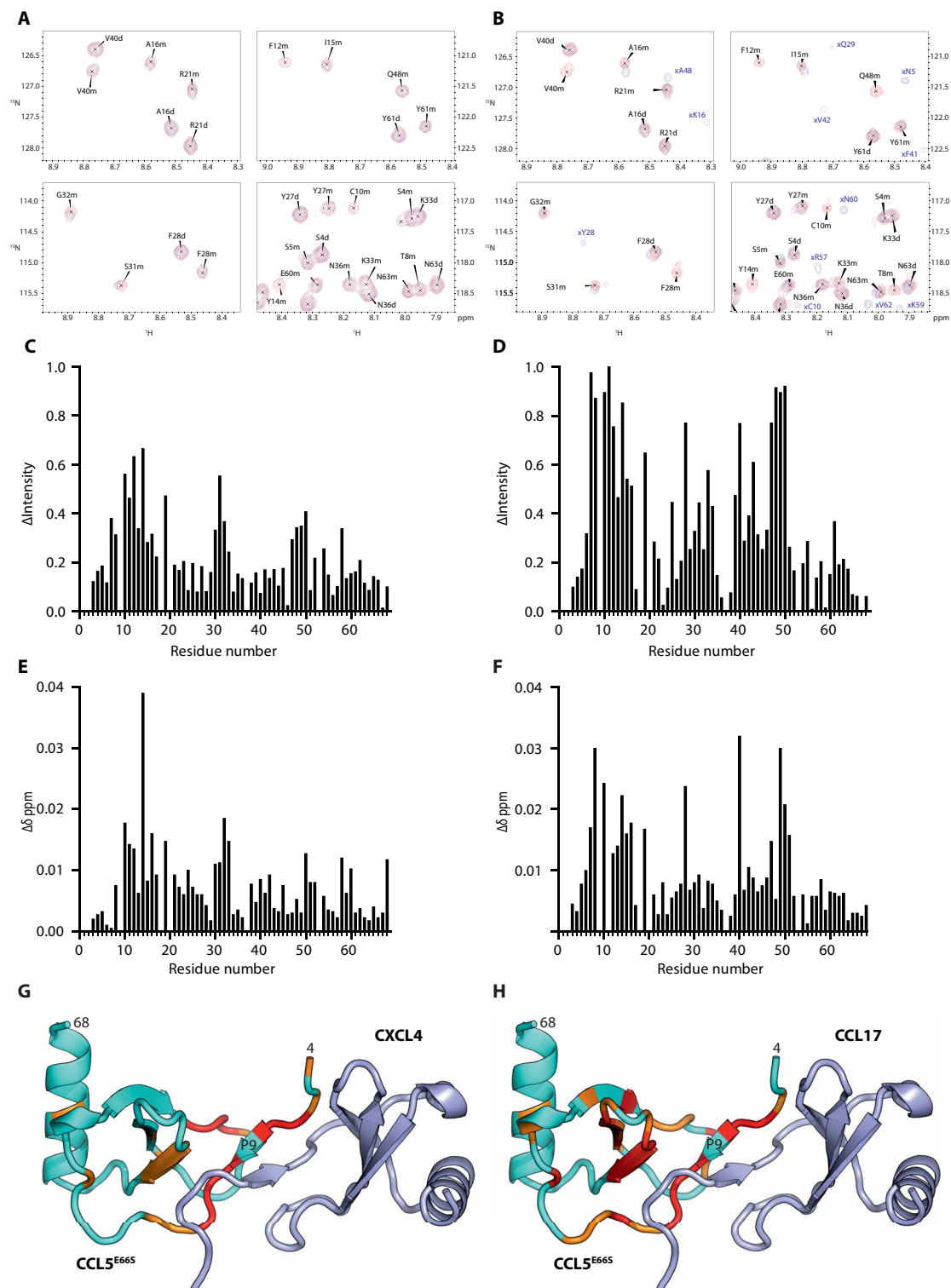
Fig. 2. Characterization of chemokine interactions by NMR spectroscopy. (**A** to **F**) ^{1}H-^{15}N HSQC spectra were acquired with 128 scans per transient and sweep widths of 16 parts per million (ppm) in the ^{1}H (2000 points) dimension and 22 ppm in the ^{15}N (200 points) dimension. Expansions are shown for ^{15}N-CCL5^{E66S}, either alone (red) or in the presence of unlabeled CXCL4 (blue) (A) or unlabeled CCL17 (blue) (B); the molar ratios of CCL17/CCL5^{E66S} (^{1}H; 850 MHz) and CXCL4/CCL5^{E66S} (^{1}H; 700 MHz) were 33:1 (20 μM CCL5^{E66S}) and 20:1 (30 μM CCL5^{E66S}), respectively. Labels indicate monomers (m), dimers (d), and ^{15}N bleed-through from CCL17 (x). The changes in intensity (Δintensity) and chemical shift (Δδ) for the ^{15}N-CCL5^{E66S} monomer resonances upon binding to CXCL4 (C and E) and CCL17 (D and F) versus those of CCL5^{E66S} are shown. (**G** and **H**) Primary CCL5^{E66S} residues binding CXCL4 (G) and CCL17 (H) heterodimer subunits are indicated on the basis of the native CCL5 homodimer structure (Protein Data Bank 1U4L). The broadest resonances within a single subunit are in red (>2 SD above average), orange (between 1 and 2 SD), and blue (<1 SD). Full-view HSQC spectra are displayed in fig. S3.

CXCL4, whereas CCL2, CCL17, and CXCL4 favor formation of CC-type heterodimers with CCL5 (table S3).

To exploit our structural models for the design of peptide-based inhibitors, we generated CCL5-derived peptides (CKEY, CAN and VREY), which form part of the heterodimer interfaces with CXCL4, CCL17, and CXCL12, respectively (table S4). Modeled CCL5-CCL17 (CC-type) and CCL5-CXCL12 (CXC-type) heterodimers are illustrated in fig. S8 (A and B). Cyclic CKEY, containing N-loop and β-sheet 2 with residues K25 to R44 (7), reversed CXCL4-induced changes in $\Delta\delta$ and broadening of ^{15}N-CCL5^{E66S} monomer, but not homodimer, resonances (fig. S9, A and B). Cyclic CAN comprising CCL5 β-sheet 3 (residues K33 to N52) interacted with CCL17 (fig. S10) and partially reversed CCL17-induced changes in $\Delta\delta$ and broadening of ^{15}N-CCL5^{E66S} monomer resonances (fig. S11, A and B). Perturbations at the binding interfaces reflect a specific disruption of both CC-type heterodimers. Linear VREY (α-helix residues E54 to S68) mimicked heterodimer interactions of CCL5 with ^{15}N-CXCL12 as similar resonances at the dimer interface were chemically shifted. To improve solubility and conformational stability (25), we generated a four-helix template-assembled synthetic protein (TASP) version of VREY ([VREY]^4; fig. S12A). Changes in $\Delta\delta$ and a structural perturbation plot (fig. S12, B to D) indicated that [VREY]^4 interacts with ^{15}N-CXCL12 and attenuates its homo- or heterodimer state, as evidenced by relevant shifts at the interface (fig. S12E).

We validated these findings using SPR, where CKEY inhibited the interaction of CCL5 with CXCL4 but not with CCL17 or CXCL12; this effect was abrogated in the variant CKEY^{RE} by substitutions at key residues R44 and E26, crucial for heterodimerization (table S5). Conversely, CAN inhibited the interaction of CCL5 with CCL17 but not with CXCL4 or CXCL12, whereas the N-terminal peptide CCL5$^{1-33}$ blocked both CC-type interactions of CCL5 with CXCL4 or CCL17 (table S5). Finally, [VREY]^4 competed with CCL5 for binding to CXCL12 but not to CCL17 or CXCL4 (table S5). These data suggest that chemokine heterodimers can be specifically disrupted by peptides to target their activity.

Differential function and disruption of heterodimers

To assess the functional effects of chemokine heterodimers, we studied chemotaxis of activated human T cells, which display a large chemokine-receptor repertoire (fig. S13A) and differentially respond to various chemokines (fig. S13, B to G). Whereas CCL5 plus CCL17 or CXCL4 (CC-type), but not interaction-deficient CXCL4L1, acted synergistically to enhance chemotaxis (Fig. 3, A to D, and fig. S14, A to C), combination with CCL5, CXCL4, or CXCL4L1 (CXC-type) inhibited CXCL12-induced chemotaxis (fig. S14, D to F). Consistent with a lack of specific interactions, CCL5 plus CCL3 or CXCL10 resulted in functionally neutral, that is, neither synergistic nor inhibitory, effects (fig. S14, G and H). Furthermore, combinations preferentially forming CC-type heterodimers (CCL5 plus CXCL4, CCL2, or CCL17) acted synergistically to increase monocyte and/or T cell arrest (Fig. 3, E and F, and fig. S15A). By contrast, combinations forming CXC-type heterodimers, such as CXCL4 and CXCL8 or CCL5 and CXCL12, exerted inhibitory or less than additive effects (fig. S15, B and C). Overall, different types of heterodimeric interactions can have opposite functional consequences, namely, all CC-type interactions identified and functionally tested were synergistic, whereas all CXC-type interactions identified and functionally tested were inhibitory.

In the chemotactic dose-response curve, a left shift demonstrated that CCL5 increased the potency of CCL17 (Fig. 3A), indicating

increased affinity or receptor heteromerization. Synergistic effects of CCL5-CCL17 involved both the CCL17 receptor (CCR4) and CCL5 receptors (CCR1 or CCR5), as shown by inhibition with the CCR4 antagonist C021 and the CCL5 receptor antagonist Met-RANTES (fig. S15D). By contrast, CXCL4 increased the efficacy of CCL5 over the entire dose range (Fig. 3B). This effect was blocked by Met-RANTES but not by an antibody to the low-affinity CXCL4 receptor CXCR3 (fig. S15E). These data imply that different modes of synergy (affecting potency or efficacy) occur through distinct mechanisms.

Notably, monomeric CCL5^{MT7} did not form strong heterodimers or support functional synergy with CCL17 or CXCL4, whereas the N-terminal peptide CCL5$^{1-33}$ blocked synergistic effects of CCL5 with CXCL4, CCL17, or CCL2, indicating that N-terminal motifs are required for CC-type heterodimer formation and activity (Fig. 3, C, D, G, and H). Consistent with SPR results, CKEY but not CKEY^{RE} specifically inhibited CCL5-CXCL4 synergy, and CAN specifically inhibited CCL5-CCL17 (Fig. 3, C, D, G, and H, and fig. S15, F and G). Peptide targeting of heterodimer interfaces encompassing β-strands 2 or 3 with adjacent loops thus confers specificity for functional inhibition. Mimicking the effects of CCL5, [VREY]^4 but not the other peptides inhibited CXCL12 activity in chemotaxis and arrest (fig. S15, C and H). Along with our NMR data, this indicates that CCL5 and [VREY]^4 induce structural changes in the CXCL12 dimer, thereby inhibiting CXCL12 activity.

On the basis of modeling (Fig. 2G), we generated a covalently linked CC-type CXCL4-CCL5 heterodimer termed OPRAH (obligate PF4-RANTES heterodimer; Fig. 3I) by introducing an oxime linker between N-terminal residues of CCL5 (T7) and CXCL4 (L8). The efficacy and potency of OPRAH in triggering monocyte arrest and T cell chemotaxis were greater than those of CCL5 alone or in combination with CXCL4 at concentrations favoring heterodimer formation (Fig. 3J and fig. S15I). By contrast, OPRAH with the N termini tethered at the first residues (nOPRAH) failed to enhance function (Fig. 3J), showing an importance of freely available N termini. CKEY did not inhibit the effects of OPRAH (Fig. 3K). An obligate CCL5-CCL17 heterodimer, ORATH (obligate RANTES TARC heterodimer), induced T cell arrest with higher potency and efficacy than CCL5 and CCL17 combined (fig. S15J), establishing that heterodimers are responsible for the synergistic effects.

To address underlying mechanisms for synergy, we used an in situ proximity ligation assay (26) reporting protein interactions that detect the presence of CCL5-CCL17 heterodimers formed on activated endothelial cells after incubation with both chemokines or with Met-RANTES (fig. S16, A and B). Endogenous heterodimers could be detected in mouse lymph nodes (fig. S16, C and D). In dendritic cells (DCs), which express both CCR4 and CCR5, CCL5-CCL17 heterodimers assembled on the cell surface when adding both chemokines, whereas CCR4-CCR5 complexes were constitutively present (Fig. 4A). The increase in CCL5-CCL17 heterodimers was inhibited by CAN (Fig. 4B), revealing that heterodimers can be disrupted by peptides in a cellular context. Notably, the number of CCR4-CCR5 complexes was increased by combining CCL5 and CCL17 but not by either alone (Fig. 4C), as were ligand-receptor cross-interactions (fig. S17, A to D). This effect was impaired by CAN, thus being mediated by CCL5-CCL17 heterodimers, and disrupted by CCR5-derived peptides spanning transmembrane 1 and 4 motifs (Fig. 4C), as seen for CCR5 homodimers (27). Peptide-based disruption of CCL5-CCL17 or CCR5-CCR4 impeded synergy in T cell chemotaxis (Fig. 4D and fig. S17E), substantiating a role of ligand-induced receptor heteromer
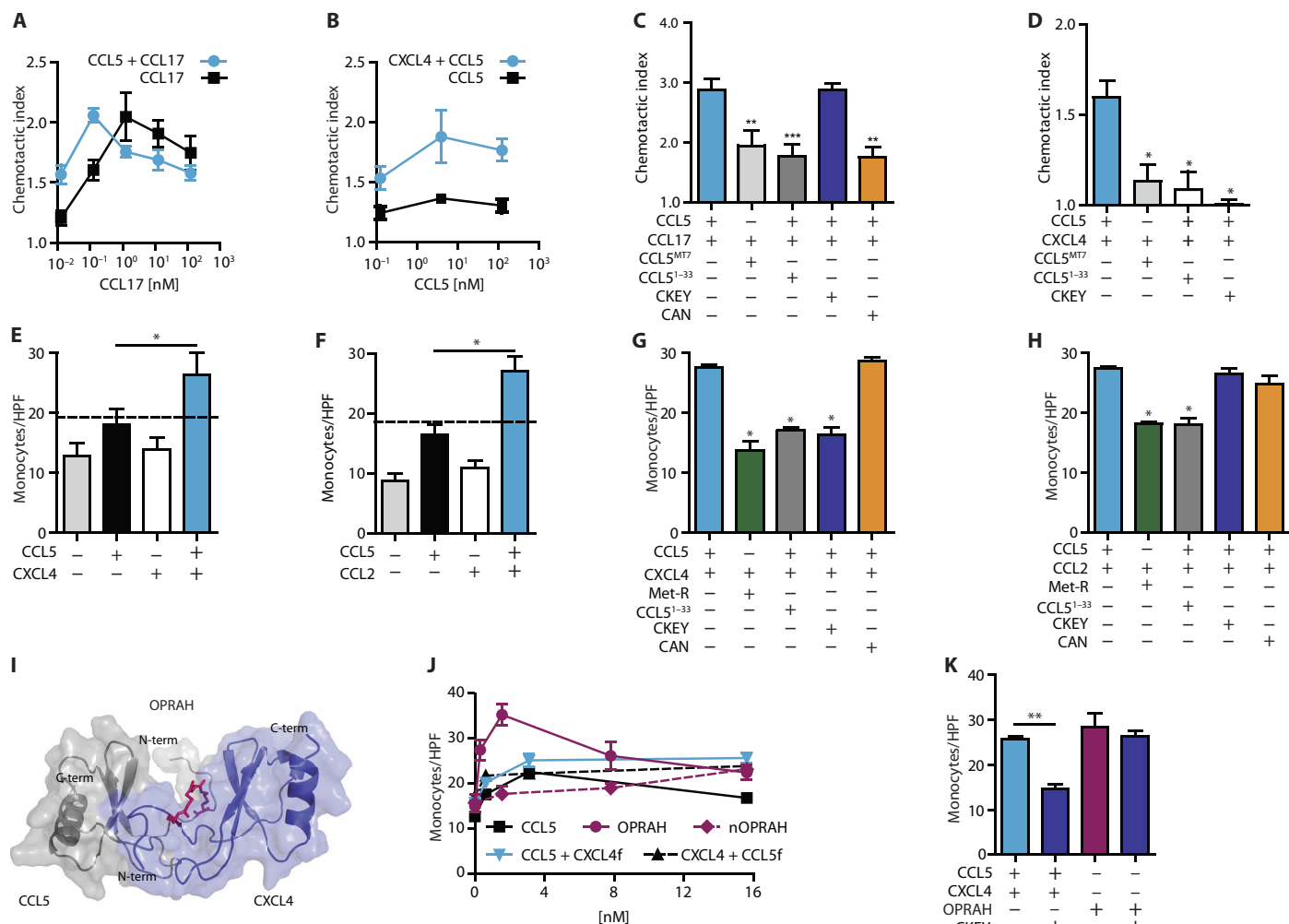
Fig. 3. Differential function and specific inhibition of chemokine combinations. (**A** to **D**) Transwell filter chemotaxis assays were performed using interleukin-2 (IL-2)–activated and CD3/C28-activated human T cells. The chemotactic index was determined as the ratio of chemokine-induced versus unstimulated migration by counting the cells in the bottom chamber. Combinations of CCL5 (1 nM) plus CCL17 at the indicated concentrations ($n = 7$) (A), CXCL4 (4 nM) plus CCL5 at the indicated concentrations (B) ($n = 6$), CCL5 or CCL5^{MT7} (both 1 nM) plus CCL17 (0.1 nM; $n = 9$) (C), and CCL5 plus CXCL4 (both 4 nM) or obligate platelet factor 4 (PF4)–RANTES heterodimer (OPRAH; 0.4 nM) ($n = 6$) (D) were added to the bottom chamber. The CCL5 peptides CCL5$^{1-33}$ (N-terminal), CAN (CCL5-CCL17 interface), and CKEY (CCL5-CXCL4 interface) were added at 10-fold molar excess. (**E** to **K**) Isolated human blood monocytes were perfused over IL-1β–activated human aortic endothelial cells (HAoECs) preincubated with chemokines, and numbers of adherent cells per high-power field (HPF) were counted. HAoECs were incubated with CCL5 and/or CXCL4 (40 nM each) (E and G) and with CCL5 and/or CCL2 (4 nM each; $n = 17$) (F and H). Dashed lines indicate virtually calculated additive effects. Monocytes were preincubated with the CCL5 receptor antagonist Met-RANTES (Met-R; 40 nM), and CCL5$^{1-33}$, CKEY, or CAN (40 nM each) was combined with CCL5 plus CXCL4 (G) or CCL5 plus CCL2 (H) for pretreating HAoECs ($n = 3$). (I) Energy-minimized structure model depicting the CC-type interaction of CCL5 (gray) and CXCL4 (blue) trapped via a covalent oxime linkage (magenta), yielding an obligate PF4-RANTES heterodimer (OPRAH). (J) HAoECs were pretreated with the indicated concentrations of CCL5 plus CXCL4 fixed at 4 nM (CCL5 + CXCL4f), indicated concentrations of CXCL4 plus CCL5 fixed at 4 nM (CXCL4 + CCL5f), or indicated concentrations of OPRAH or nOPRAH (N-terminally tethered OPRAH) ($n = 3$ to 6). (K) HAoECs were pretreated with CCL5 plus CXCL4 or OPRAH (all 4 nM) with or without CKEY (40 nM; $n = 5$). Data represent means ± SEM from the indicated numbers of independent experiments. *$P \leq 0.05$, **$P \leq 0.01$, ***$P \leq 0.001$ versus chemokine combinations (cyan), as analyzed by one-way analysis of variance (ANOVA) (C, E, and F) or Kruskal-Wallis test (D, G, H, and K).

complexes. Binding competition assays revealed that the affinity of CCL17 for CCR4 was higher when adding CCL5 but not CXCL1, to promote heterodimer formation (Fig. 4E and fig. S17F). To test whether CCL5-CCL17 can elicit receptor heteromer activity distinct from its monomers, we used GloSensor transfectants expressing CCR4 or CCR4 and CCR5 to assess cyclic adenosine monophosphate (cAMP) signaling. Our data show that CCR4 and CCR5 together mediate the synergistic effects of CCL5-CCL17 on G$_i$-mediated inhibition of cAMP formation (fig. S17G). In contrast, transfectants expressing CCR1 only

efficiently responded to OPRAH (fig. S18A). As for a combination of CCL2 and CCL5 favoring CCR2-CCR5 heterodimerization to enhance cell arrest (28), phosphatidylinositol 3-kinase signaling was also addressed by CCR4-CCR5 heteromers, in that combining CCL5 and CCL17 induced its sustained activation (fig. S18, B and C).

To identify mechanisms underlying CXCL4-mediated synergy, we used the GAG binding–impaired mutant CXCL4$^{R>Q}$, which forms heterodimers with CCL5 (table S2). This mutant did not enhance CCL5-induced monocyte arrest, suggesting that GAG binding through
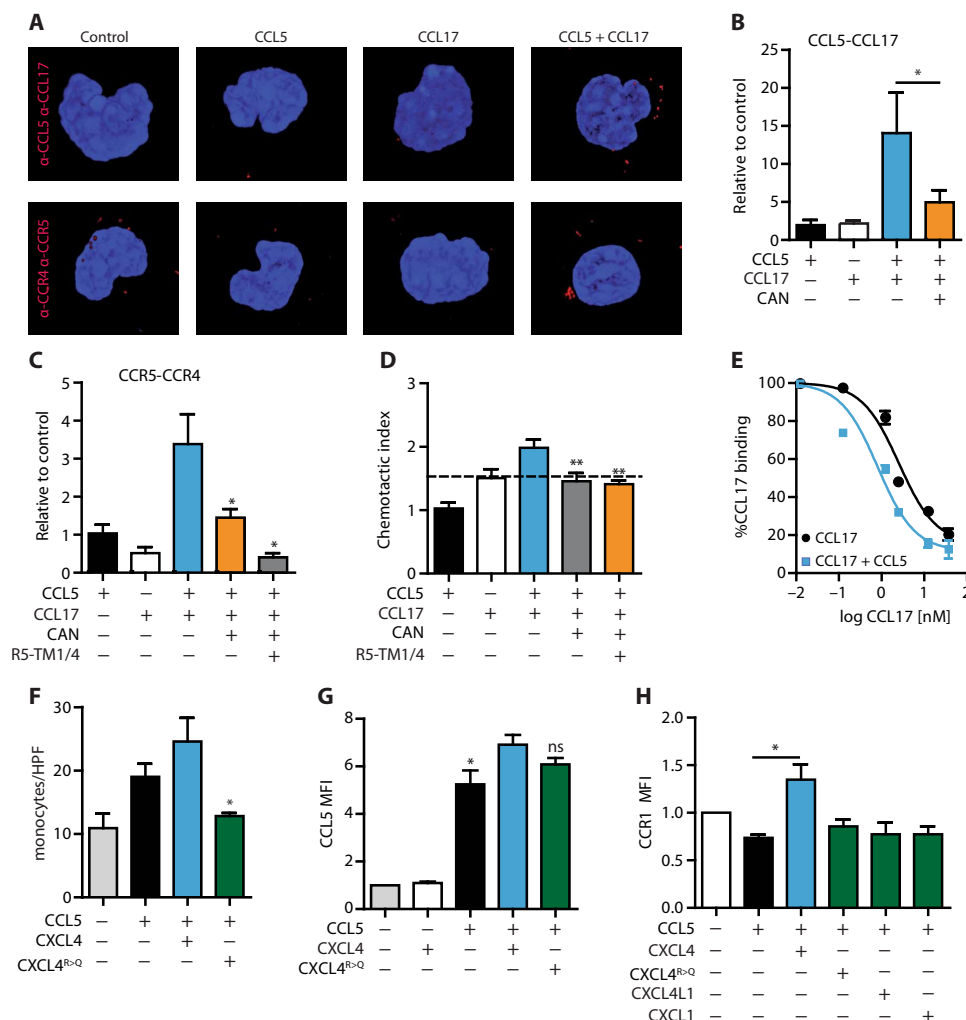
von Hundelshausen et al., Sci. Transl. Med. 9, eaah6650 (2017) 5 April 2017

54

Fig. 4. Mechanisms for the synergistic effects of chemokine heterodimers. (**A** to **C**) Interactions between murine CCL5, CCL17, CCR4, and CCR5 were detected on the surface of adherent DCs using a proximity ligation assay after the cells were incubated with CCL5, CCL17, or both (6 nM each) in the presence/absence of CAN (60 nM) or transmembrane (TM) 1/4 CCR5 peptides (50 μg/ml) known to inhibit CCR5 dimerization. Representative images depict the presence of CCL5-CCL17 and CCR4-CCR5 heterodimers (red dots) on the DC surface (A). Proximity ligation signals generated by interactions of CCL5-CCL17 ($n = 8$) (B) and CCR5-CCR4 ($n = 5$) (C) were quantified relative to CCL5 alone (control). (**D**) Transwell filter chemotaxis assays were performed using CD3/CD28-activated primary mouse T cells ($n = 8$). Chemotactic index was determined as the ratio of chemokine-induced versus unstimulated migration by counting the cells in the bottom chamber. Migration toward CCL5 and/or CCL17 (6 nM each) in the bottom chamber was analyzed in the presence/absence of CAN (60 nM) or TM1/4 peptides (50 μg/ml). (**E**) Binding competition assay; CCL17–Alexa Fluor 647 (2.5 nM) bound to CCR4-expressing human embryonic kidney (HEK) 293 transfectants was displaced by unlabeled CCL17 in the presence or absence of CCL5 (1 nM; $n = 6$). (**F**) Isolated human monocytes were perfused over IL-1β–activated HAoECs pretreated with CCL5 and CXCL4 or the GAG binding–deficient mutant CXCL4$^{R>Q}$ (all 4 nM), and numbers of adherent cells per HPF were counted ($n = 4$). (**G**) Deposition of exogenous CCL5, alone or in combination with CXCL4 or CXCL4$^{R>Q}$ (all 100 nM) on the surface of primary human monocytes, was detected by flow cytometry and reported as specific mean fluorescence intensity (MFI) ($n = 3$). ns, not significant. (**H**) CCR1 surface expression on monocytes was detected by flow cytometry after treatment with CCL5 (4 nM), alone or in combination with CXCL4, CXCL4$^{R>Q}$, or CXCL1 (all 40 nM; $n = 4$). Data represent means ± SEM from the indicated numbers of independent experiments. *$P < 0.05$, **$P < 0.01$ versus chemokine combinations (cyan), as analyzed by one-way ANOVA (B and D), Kruskal-Wallis test (C), or Mann-Whitney test (F and G).

CXCL4 may improve presentation of CCL5 to its arrest-triggering receptors (Fig. 4F). CXCL4 but not CXCL4$^{R>Q}$ increased surface binding of CCL5 to monocytes, indicating that this was mediated by GAG binding via CXCL4 (Fig. 4G). As a consequence, CXCL4 but not CXCL4$^{R>Q}$ prevented CCR1 internalization by CCL5 (Fig. 4H), without altering the affinity of CCL5 for CCR1 or CCR5 (fig. S18, D and E). This effect was also observed using primary mouse monocytes adherent in carotid arteries perfused ex vivo (fig. S18F). CXCL1 and CXCL4L1, which neither specifically interact with CCL5 nor activate CCR1, but bind to GAGs, did not recapitulate the effect on CCR1 internalization

observed with CXCL4, indicating that this is dependent on heterodimer formation with CCL5 (Fig. 4H). SPR on a low–molecular weight heparin-conjugated chip revealed binding of CXCL4L1 but not of CXCL4$^{R>Q}$, and combination with wild-type CXCL4 but not with CXCL4L1 or CXCL4$^{R>Q}$ supported strong binding of CCL5^{E66S} on immobilized heparin (fig. S19A). Such GAG-mediated binding of CCL5-containing heterodimers was confirmed by binding of OPRAH to heparin with similar affinity as CCL5^{E66S} (fig. S19, B and C). Thus, the GAG-binding capacity of CCL5-CXCL4 heterodimers limits receptor internalization from the cell surface, where it is retained for continuous

von Hundelshausen et al., Sci. Transl. Med. **9**, eaah6650 (2017)   5 April 2017

55

G protein signaling, as seen for GPCR families lacking β-arrestin recruitment for endosomal targeting (29). Experiments using HEK293 transfectants coexpressing C-terminally tagged CCR5-RlucII and enhanced yellow fluorescent protein–tagged arrestin 1/2 to analyze bioluminescence resonance energy transfer events confirmed that the presence of CXCL4 inhibited the CCL5-induced association of arrestin with CCR5 (fig. S19D), reflecting a prolonged signaling cycle.

Specific targeting of heterodimers in inflammatory disease models

To confirm a role of heterodimer formation in vivo, we used a short-term model of lipopolysaccharide (LPS)–induced acute lung injury, which relies on platelet chemokines mediating neutrophil recruitment and subsequent extravasation (11). Treatment with CKEY (but not with CKEY^{RE}) dose-dependently reduced infiltration in the lung, as evidenced by lower intravascular, interstitial, bronchoalveolar, and total neutrophil counts (Fig. 5A and fig. S20, A to C). Conversely, reconstitution of mice carrying $Ccl5^{-/-}Cxcl4^{-/-}$ bone marrow (deficient in the heterodimer pair) with OPRAH but not with CCL5 exacerbated lung infiltration, as reflected in higher intravascular neutrophil numbers and a trend toward higher total counts (Fig. 5B and fig. S20D).

To demonstrate the biological relevance of heterodimer interactions, we generated $Cxcl4^{L1/L1}$ mice with a CXCL4 knockout and knock-in of the CXCL4L1 variant (which neither exists in mice nor forms heterodimers with CCL5) to study diet-induced atherosclerosis on an $Apoe^{-/-}$ background (fig. S21). Notably, $Cxcl4^{L1/L1}$ mice showed a marked reduction of atherosclerotic lesion size in the aorta and the aortic arch, comparable to that in CXCL4-deficient mice (Fig. 5, C and D, and fig. S22, A and B). Heterozygous $Cxcl4^{L1/+}$ mice displayed an intermediate gene-dosing effect. Lesion size in the aortic root was attenuated in $Cxcl4^{-/-}$ mice but not in $Cxcl4^{L1/L1}$ mice (fig. S22, C and D), implying regional differences unrelated to heterodimerization. Except for lower macrophage content in $Cxcl4^{L1/L1}$ mice, plaque composition (that is, phenotype classification, smooth muscle cells, necrotic core, and T cell content), lipid profiles, body weight, and blood cell counts did not differ among all groups (Fig. 5E, fig. S23, and table S6). Platelet-specific expression of a CXCL4L1 transgene in $Apoe^{-/-}$ mice did not alter lesion size, indicating that its effects are not dominant negative but are due to a lack of interaction (Fig. 5F). Treatment with mouse OPRAH restored lesion formation in the aorta including the arch and increased macrophage content in aortic root plaques but did not change other parameters in $Ccl5^{-/-}Cxcl4^{-/-}Apoe^{-/-}$ mice and heterozygous $Cxcl4^{L1/wt}Apoe^{-/-}$ mice expressing noninteracting CXCL4L1 (Fig. 5, G and H, fig. S24, and table S7).

The atheroprotective homeostasis of regulatory T cells (T$_{regs}$) is suppressed by DC-derived CCL17, a phenotype not replicated in $Ccr4$-deficient mice (3, 30, 31), possibly implicating other chemokine receptors or heterodimers. We detected CCL5-CCL17 heteromers in aortic root lesions of $Apoe^{-/-}$ mice (Fig. 6A), in the intima and adventitia of human coronary arteries with advanced atherosclerosis but not in undiseased vessels or segments (Fig. 6B). Notably, combined interference with CCR4-CCR5 using the CCR5 antagonist DAPTA in CCR4-deficient $Apoe^{-/-}$ mice increased T$_{reg}$ numbers in the paraaortic lymph nodes and, marginally, in peripheral blood (Fig. 6, C and D). Similar results were obtained by treatment with CAN (for 6 weeks), which also reduced lesion size in the aortic root (Fig. 6, C to F), phenocopying the effects of CCL17 deficiency (30). These findings may be due to limiting CCL17-mediated recruitment of naïve CD3$^+$ T cells, in which T$_{reg}$ conversion or maintenance is

suppressed via subsequent CCL17-dependent pathways involving other receptors.

To exploit inhibitory interactions exemplified by the CXC-type heterodimer CCL5-CXCL12, we tested whether [VREY]^4 inhibits CXCL12-depedent platelet aggregation, as relevant to atherothrombosis. Notably, CXCL12 facilitated platelet aggregation as deletion of $Cxcl12$ in blood of $CreER^{T2}Cxcl12^{fl/fl}Apoe^{-/-}$ mice showed reduced multiparameter platelet activity and thrombus scores ex vivo (Fig. 6, G and H). Treating $Apoe^{-/-}$ mice with [VREY]^4 afforded a similar inhibition of platelet activity (Fig. 6, G and H). Likewise, [VREY]^4 inhibited CXCL12-induced human platelet aggregation and CXCR4 activation in HEK293 cells, likely due to conformational effects on CXCL12 (Fig. 6, I and J).

DISCUSSION

The comprehensive map of all heteromeric chemokine interactions obtained by immunoligand blotting and SPR contributes to the completion of the binary human protein interactome network (32). We found that inflammatory and nonhomeostatic chemokines, for example, platelet-derived atherogenic CCL5 and CXCL4, favor interactions, whereas homeostatic chemokines are generally less interactive. This may correspond to the need to amplify, fine-tune, and resolve chemokine activity at inflammatory sites through heteromeric interactions, whereas the stand-alone functions of noninteracting chemokines appear sufficient for organogenesis, immune architecture, and surveillance or antimicrobial activity. For example, CXCL4-deficient mice have no overt phenotype and show unaltered immune responses in the absence of challenge, whereas CXCL12 deficiency entails embryonic lethality, and CXCL13 deficiency shows its essential role for lymph node development and natural immunity (33, 34).

Structure-function analysis revealed an interesting dichotomous pattern wherein CC-type heterodimers promote synergy and CXC-type heterodimers cause inhibition. The use of obligate heterodimers such as OPRAH provided conclusive proof that CC-type heterodimers mediate functional synergy. Functional inhibition with a CCL5-derived N-terminal peptide supports a more general role of the N terminus in CC-type heterodimer formation and synergy. The spacing and shapes adopted by CC-type homodimers can vary with minimal changes in N-terminal sequence (16). Functional synergy indeed involved flexible N termini, as illustrated by a tethered version of the obligate heterodimer OPRAH, and could be ascribed to addressing receptor heteromers (increasing potency of CCL5-CCL17) or to auxiliary GAG binding and impaired receptor internalization (increasing efficacy of CCL5-CXCL4).

Chemokine-receptor activation follows a two-site binding mechanism involving interactions of the chemokine N-loop/core with the receptor N terminus (site I) and of the chemokine N terminus with extracellular/transmembrane residues (site II). The modeled structure for binding of the atypical CC chemokine vMIP-II to CXCR4 appears to support findings that CC chemokine homodimers cannot bind or activate receptors because the dimerization interface largely coincides with an intermediate recognition site (35–37); however, this may not extend to all chemokine-receptor interactions because N-terminal and core structures in a CC-type heterodimer, for example, OPRAH, may be differently presented to receptors. Instead, binding may involve receptor complexes enabling synergy. Concomitant peptide-based disruption of CCL5-CCL17 and CCR4-CCR5 formation/function supported the concept that CC-type heterodimers can
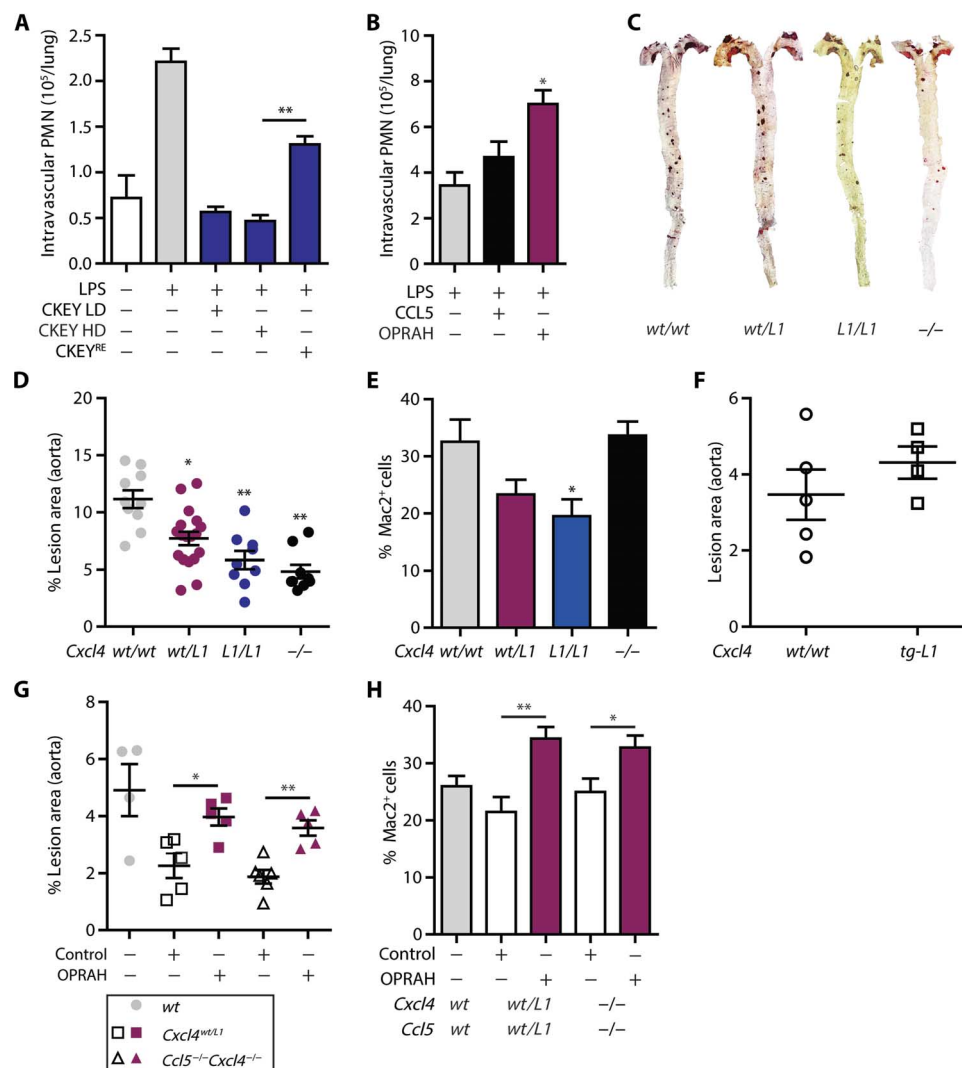
Fig. 5. Inflammatory effects of CCL5-CXCL4 in vivo require heterodimer formation. (**A** and **B**) Acute lung injury in C57/BL6 mice was induced by LPS inhalation. Intravascular neutrophil accumulation was detected by intravenous injection of a fluorescein isothiocyanate–GR1 antibody before lung explantation. (A) Mice were injected intraperitoneally with CKEY at a low dose (LD; 1 mg/kg) or high dose (HD; 10 mg/kg) or with CKEY^{RE} at high dose before LPS challenge ($n = 5$ to 6). PMN, polymorphonuclear neutrophil. (B) Bone marrow of $Ccl5^{-/-}Cxcl4^{-/-}$ chimeric mice were intravenously injected with CCL5 (150 μg/kg) or OPRAH (300 μg/kg) or vehicle (ctrl) before LPS challenge. (**C** to **E**) Atherosclerosis was analyzed in wild-type (wt) $Cxcl4^{wt/wt}$ mice, homozygous $Cxcl4^{L1/L1}$ mice with a $Cxcl4$ knockout and knockin of a mouse variant of human CXCL4L1, heterozygous $Cxcl4^{wt/L1}$ mice, and CXCL4-deficient $Cxcl4^{-/-}$ mice on an $Apoe^{-/-}$ background after 12 weeks of high-fat diet (HFD). Representative images of the aorta stained with Oil Red O are shown (C). The area of the aorta showing Oil Red O–positive lesions (D) and the area of Mac2-positive cells in the aortic arch (E) were quantified and expressed as percentage of the total area ($n = 4$ to 11). (**F**) The lesion area in the aorta of $Apoe^{-/-}$ mice expressing a human CXCL4L1 transgene (tg-L1) in addition to CXCL4 was analyzed after 12 weeks of HFD. (**G** and **H**) $Cxcl4^{wt/L1}Apoe^{-/-}$ and $Ccl5^{-/-}Cxcl4^{-/-}Apoe^{-/-}$ mice were treated (intraperitoneally) with OPRAH (10 μg, twice a week) while on HFD for 6 weeks. The Oil Red O–positive lesion area (G) and Mac2-positive area in the aortic arch (H) were quantified and expressed as percentage of the total area ($n = 6$ to 13). Data represent means ± SEM from the indicated numbers of mice. *$P < 0.05$, **$P < 0.01$, as analyzed by Kruskal-Wallis test (B, D, and E) or Mann-Whitney test (A, G, and H).

prompt the formation of corresponding receptor complexes, requiring CCR5 transmembrane regions. Furthermore, because chemokine N-terminal residues play an important role in receptor activation, they may also affect the mechanisms of action for heterodimers. For instance, N-terminal sequence variations may cause differences in N-terminal orientation and/or accessibility between CCL17-CCL5 heterodimers and CCL5 homodimers to affect receptor binding and activation. As evidenced from a disulfide-trapped CCL4 variant, dissociation of CCL4 homodimers may be required to accomplish receptor binding and activation by a monomer (37). This may also hold true

for chemokine heterodimers, namely, CCL5-CCL17, when addressing respective heterodimers.

The conserved GP motif in CXCL8 can couple sites I and II, dictating both substrates and cross-talk between sites to control receptor activity (38). Conformational coupling was corroborated by a CC mutant of CXCL8 that retained binding via N-loop–site I interactions for CXCR1 activation (39). Moreover, a disulfide-trapped CXCL8 dimer had reduced affinity for CXCR1 due to perturbed binding at N-loop residues, giving rise to a model where binding of a CXC-type dimer triggers conformational changes, leading to release and high-affinity

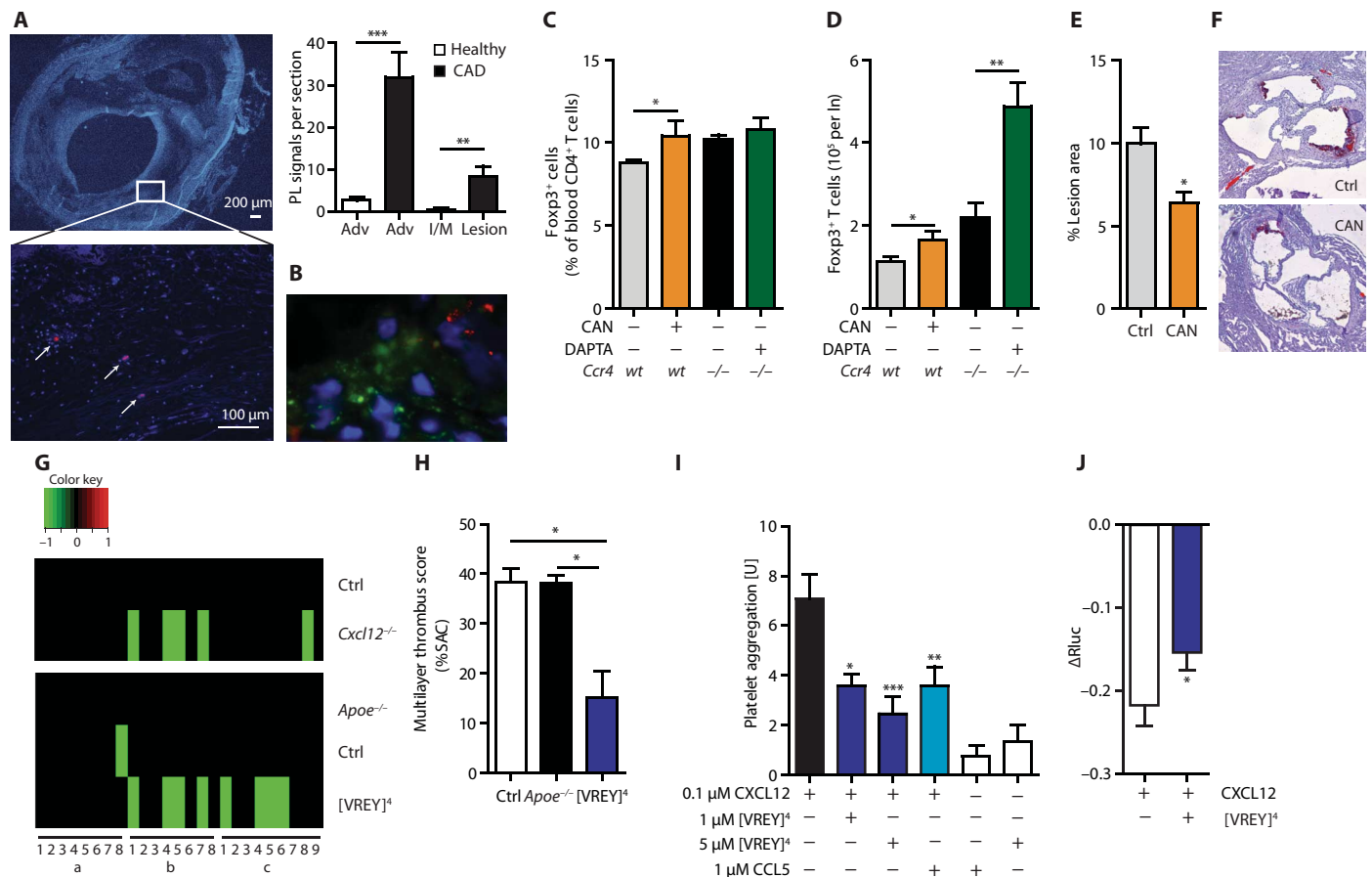**Fig. 6. Specific peptides inhibit atherogenic CCL5-CCL17 and CXCL12-driven platelet activity.** (**A** and **B**) Interactions of CCL5-CCL17 (left; red dots indicated by arrows in the representative image) were detected in the adventitia (adv) and intima/media (I/M) of human coronary arteries with (diseased) or without (healthy) atherosclerotic lesions [representative image with inset (left) and quantification (right); $n = 9$ to 14] (A) or in aortic root sections from $Apoe^{-/-}$ mice fed an HFD for 12 weeks (B) using a proximity ligation assay. PL, proximity ligation. (**C** and **D**) Wild-type or bone marrow from $Ccr4^{-/-}$ chimeric $Apoe^{-/-}$ mice were injected intraperitoneally with the CCR5 inhibitor DAPTA or CAN (each at 1 mg/kg, three times a week) for 2 weeks, and the number of Foxp3+CD4+ T_{regs} in peripheral blood (relative to CD4+ T cells; $n = 6$ to 8) (C) and paraaortic lymph nodes [per lymph node (ln); $n = 8$ to 9] (D) was determined by flow cytometry. (**E** and **F**) $Apoe^{-/-}$ mice were injected (intraperitoneally) with CAN (1 mg/kg, three times per week) while on HFD for 2 weeks. Oil Red O–positive lesion areas in the aortic root were quantified and expressed as percentage of the total area ($n = 9$ to 10) (E). Representative images of aortic roots stained with Oil Red O are shown (F). (**G** and **H**) Blood from $CreER^{T2-}Cxcl12^{fl/fl}$ (ctrl) or $CreER^{T2+}Cxcl12^{fl/fl}Apoe^{-/-}$ mice ($Cxcl12^{-/-}$) after tamoxifen treatment for $Cxcl12$ deletion (top) and from $Apoe^{-/-}$ mice treated with or without the CCL5 peptide [VREY]^4 or vehicle (ctrl; bottom) was perfused over collagen for 4 min at 1000 s^{-1} ($n = 5$ to 10). (G) Multiparameter assessment of thrombus formation using distinct surfaces (a, vWF-BP + laminin; b, vWF-BP + laminin + rhodocytin; c, collagen I) was performed and depicted in a heat map. Parameters were assessed by bright-field and subsequent tricolor fluorescence microscopy as follows: 1, morphological score; 2, platelet deposition [surface area coverage (SAC)]; 3, thrombus contraction score; 4, multilayer thrombus score; 5, multilayered thrombus (% SAC); 6/7, phosphatidylserine exposure (% SAC or platelet count/field); 8, CD62P expression (% SAC); and 9, αIIbβ3 activation (% SAC). Heat maps for all microspots (normalized per parameter) and genotype/perturbation were colored as increased (red) or decreased (green) based on statistical significance versus controls. The multilayered thrombus score is exemplified in (H). (**I**) Platelet aggregation in human blood treated with combinations of CXCL12 (100 nM), [VREY]^4 (500 nM), and CCL5 (1 μM) was measured by impedance using a Multiplate analyzer ($n = 12$; CCL5 alone, $n = 3$). (**J**) cAMP signaling, expressed as decrease of the specific Rluc signal, was analyzed in GloSensor and CXCR4-transfected HEK293 cells 15 min after stimulation with CXCL12 (40 nM) in the presence or absence of [VREY]^4 (100 nM) ($n = 8$). Data represent means ± SEM from the indicated numbers of mice or independent experiments. *$P < 0.05$, **$P < 0.01$, ***$P < 0.001$, as analyzed by Mann-Whitney test (A to C), unpaired t test (D, E, and J), or Kruskal-Wallis test (H and I).

receptor binding of a monomer (40). Whether this applies to CC-type heterodimers is unclear; however, findings with OPRAH indicate that dissociation may not be essential for function. Conversely, some receptors, for example, CXCR2, are permissive for dimer binding (41). Macrophage migration inhibitory factor (resembling a CXCL8 dimer) features sites I and II binding to CXCR2 without typical N termini (42, 43). Thus, N termini may not need to fit fully into the site II pocket.

The increased efficacy of CCL5-bearing heterodimers may be explained by several aspects. CCR5 antagonists inhibited both CCL5-

CXCL4– and CCL5-CCL17–induced arrest. Thus, CC-type heterodimers can modulate CCR5 functionality, converting it into an arrest receptor such as CCR1 (requiring CCL5 oligomers and extracellular loop 3 for sensing) (44–46). As revealed by GAG binding–impaired CXCL4, synergy with CCL5 relies on elevated cell surface presentation, impeding CCR1 internalization to sustain its signaling activity. Formation of chemokine homo- and heterodimers can be affected by GAGs, which may foster or prevent an association of chemokines (6), implying that there is not a single entity of chemokine-chemokine

von Hundelshausen et al., Sci. Transl. Med. **9**, eaah6650 (2017)   5 April 2017

58

interactions but rather that the interactome may vary depending on the presence of soluble or membrane-bound GAGs. Binding of CXCL4 to surface-bound heparin allowed for an additive, likely heteromeric, association of CCL5. The structural basis for CCL5 oligomerization and GAG binding has been elaborated (47). Polymerization creates distinctive grooves that increase GAG avidity; besides the BBXB motif, CCL5 uses another positively charged motif, KKWVR, which supports CCR5 function (44). Models further predict that CXCL4 can assemble heterooligomers with CCL5 featuring an altered surface charge distribution that facilitates GAG binding (47).

Regarding the inhibitory effects of CXC-type heterodimers, it is remarkable that a constitutively homodimeric CXCL12 variant bridged by N-terminal CXCR4 peptides induces calcium signals but inhibits chemotaxis, whereas a monomeric variant remains chemotactic, indicating that dimerization limits monomer-induced chemotaxis (48). Related mechanisms may apply to CXC-type heterodimers, whereby functional activity is impeded by more stable β-sheet interactions attenuating monomer release. Alternatively, CXC-type heterodimeric interactions may cause conformational alterations, for example, by aligning the α-helices (12). Consistent with spectral changes, α-helical peptide [VREY][4] inhibited CXCL12 function, mimicking the effects of full-length CCL5.

When assessing the stoichiometry of chemokines, it is reasonable to also consider the role of receptor stoichiometry. Although we detected chemokine receptor heteromers (CCR4-CCR5), the stoichiometry of this association currently remains unknown. Chemokine receptors can cluster in arrays, thereby influencing their surface expression, ligand levels, and function (49). The functional effects observed herein are mediated by distinct mechanisms, depending on which chemokine heterodimer is actually formed, and can involve one agonist receptor or receptor heterodimers. Similar principles may apply to the heterodimerization of chemokines, as for their homooligomerization. In particular, inhibition by CXC-type chemokine heterodimers may favor a 2:1 receptor/chemokine model as a feasible explanation for negative binding cooperativity and transinhibition between chemokine receptor heterodimers (50).

We should point out that the models proposed herein, for instance, with regard to underlying mechanisms by which chemokine heterodimers address their respective receptors, are elaborated to best explain our data but still await direct structural evidence. In addition, we could functionally test and validate only a selected number of chemokine heterodimers but not all possible combinations. Hence, we cannot exclude that some heterodimer pairs may not comply with the functional dichotomy observed for CC- and CXC-type heterodimers.

Several lines of evidence support a functional relevance of heteromer formation in disease models. First, obligate CC-type heterodimers show high efficacy and potency in recruitment assays, namely, OPRAH-exacerbated LPS-induced acute lung injury and chronic macrophage-laden atherosclerosis. Second, knocking in of CXCL4L1 (not interacting with CCL5) was similarly effective in protecting from atherosclerosis as CXCL4 deficiency, indicating that heterodimer formation with CCL5 was essential for atherogenic activity of CXCL4. Finally, the inhibition of T_{reg}-dependent atherosclerosis by CAN extends findings that CKEY limits atherosclerosis and acute lung injury (7, 11) by interfering with residues crucial for heterodimerization.

Notably, structural information regarding the type of interaction and precise location of the interface can be exploited to design peptide inhibitors selectively blocking CC-type heterodimers (as exemplified by CKEY targeting CCL5-CXCL4 and CAN targeting CCL5-CCL17). By

contrast, [VREY][4] mimics the inhibitory effects of CXC-type interactions between CCL5 and CXCL12 and attenuates CXCL12-mediated platelet aggregation. Therefore, such CXCL12-targeting peptides could serve as alternative antiplatelet therapeutics. Our paradigms illustrate strategies for specific targeting of heterodimer-mediated functions in the chemokine interactome and may allow for multivalent interference with a diversity of responses in disease-related chemokine microenvironments (fig. S25). The TASP scaffolding used for [VREY][4] may also be applicable to bundle different peptides in a polyantagonist approach. Alternatively, sequence hybridization could be used to generate monomolecular polyantagonists, as described for peptide triagonists (51). Our data enable the development of peptide therapeutics based on endogenous sequences that are selective in modulating heteromeric but not primary receptor interactions of chemokines and could thus lack many adverse effects associated with direct receptor-ligand antagonism.

MATERIALS AND METHODS
Study design
The overall objective of this study was to establish a comprehensive map of the chemokine interactome and to identify the structure-function relationship of different chemokine heterodimer types. Subsequent objectives were the design of specific peptides to disrupt functional synergy or to mimic the inhibitory effects of heterodimers and their validation in models of inflammation and atherosclerosis. For mouse studies, a power analysis was performed using BiAS software (version 11.02). We assumed a detectable biological difference of at least 50% among up to four groups with an SD of <15%, an α of 0.05, and a resultant power of 0.8. On the basis of these assumptions, at least four mice were included in each group. The number of biological replicates for each data point is included in the figure legends. All data were included (no outliers were excluded).

Ligand blots
Chemokines (1 μg) were spotted on a nitrocellulose membrane, which was immersed overnight with the soluble chemokine (1 to 5 μg/ml), and reacted with biotinylated antibodies and streptavidin-conjugated horseradish peroxidase and enhanced chemiluminescence substrate (Thermo Fisher Scientific) essentially as described (52). The chemiluminescence signal was digitally recorded and analyzed by the luminescence image analyzer LAS-3000 and Multi Gauge software (Fuji Photo Film).

Surface plasmon resonance
SPR was performed using a Biacore X100 instrument (GE Healthcare Europe GmbH) and neutravidin-modified C1 sensor chips (52). Biotinylated chemokines were immobilized on flow cells to 0.3×10^3 to 1.3×10^3 RU. Screening of chemokine binding was performed at 100 nM in HBS-EP+ buffer at 90 μl/min after 20 s. Apparent affinities were calculated from on and off rates after fitting of the curves obtained from increasing analyte concentrations using a 1:1 Langmuir interaction model (BIAevaluation software). To assess the inhibitory capacity of peptides, we recorded the binding of chemokines (20 nM) incubated with increasing peptide concentrations and calculated the percentage inhibition. Half-maximal inhibitory concentrations (IC_{50}) were determined by four-parameter logistic nonlinear regression (GraphPad version 5.0).

NMR spectroscopy
NMR samples were prepared in Wilmad 3-mm NMR tubes (160 μl). Typically, chemokine samples were buffer-exchanged and concentrated

into 25 mM sodium acetate-d₃ (pH 4.5) containing 0.1 mM EDTA and 0.2 mM sodium azide, through five ultracentrifugation steps over Amicon Ultra-4 3-kDa filter devices (Merck Millipore). Concentrations of final stock solutions were determined using a NanoDrop 2000 spectrophotometer (Thermo Fisher Scientific). Mixtures of chemokines at defined molar ratios were prepared from these stock solutions, and 5% (v/v) D_2O was added for field locking, together with a trace of DSS (4,4-dimethyl-4-silapentane-1-sulfonic acid) as internal chemical shift standard. NMR spectra [^{1}H-^{15}N HSQC with flip-back pulse, DIPSI (decoupling in the presence of scalar interactions), and NOESY (nuclear Overhauser effect spectroscopy)] were recorded at 37°C on Bruker Avance III HD 700- and 850-MHz spectrometers equipped with cryogenically cooled TCI probes. Spectra were processed and analyzed using Bruker TopSpin 3.2 and Sparky 3.114 software (T. D. Goddard, D. G. Kneller, SPARKY 3, and the University of California, San Francisco).

Resonance assignments of CCL5^{E66S} and CXCL12 were performed by two-dimensional (2D) NOESY and 3D-edited NOESY spectra. Because CCL5^{E66S} show homodimers and monomers that are in slow exchange on the NMR chemical shift time scale, resonances for both dimers and monomers are observed and well resolved in HSQC spectra, allowing assessment of effects on both states (22). Chemical shift differences ($\Delta\delta$) induced upon binding were calculated as follows: $[(\Delta^1H)^2]^{1/2} + [(0.25\Delta^{15}N)^2]^{1/2}$ (in ^{1}H ppm). ΔIntensity was calculated as follows: $1 - \text{Int}_i/\text{Int}_o$, where Int_i is the resonance intensity of CCL5^{E66S} or CXCL12 resonances in the presence of the other chemokine, and Int_o is the intensity of CCL5^{E66S} or CXCL12 resonances in its absence.

Statistical analysis

Data are expressed as means ± SEM unless otherwise specified. If D'Agostino-Pearson omnibus and/or Shapiro-Wilk normality test indicated Gaussian distribution, an unpaired t test for side-by-side comparisons or one-way ANOVA with Newman-Keuls posttest for multiple comparisons was performed. Otherwise, Mann-Whitney tests for side-by-side comparisons and Kruskal-Wallis test with Dunn's posttest for multiple comparisons were performed using GraphPad Prism version 5.04 for Windows (GraphPad Software).

For all other Materials and Methods, please see Supplementary Materials.

SUPPLEMENTARY MATERIALS

www.sciencetranslationalmedicine.org/cgi/content/full/9/384/eaah6650/DC1

Materials and Methods

REFERENCES AND NOTES

1. A. Zlotnik, O. Yoshie, The chemokine superfamily revisited. *Immunity* **36**, 705–716 (2012).
2. F. Bachelerie, A. Ben-Baruch, A. M. Burkhardt, C. Combadiere, J. M. Farber, G. J. Graham, R. Horuk, A. H. Sparre-Ulrich, M. Locati, A. D. Luster, A. Mantovani, K. Matsushima, P. M. Murphy, R. Nibbs, H. Nomiyama, C. A. Power, A. E. I. Proudfoot, M. M. Rosenkilde, A. Rot, S. Sozzani, M. Thelen, O. Yoshie, A. Zlotnik, International Union of Basic and Clinical Pharmacology. LXXXIX. Update on the extended family of chemokine receptors and introducing a new nomenclature for atypical chemokine receptors. *Pharmacol. Rev.* **66**, 1–79 (2014).
3. C. Weber, H. Noels, Atherosclerosis: Current pathogenesis and therapeutic options. *Nat. Med.* **17**, 1410–1422 (2011).
4. R. R. Koenen, C. Weber, Therapeutic targeting of chemokine interactions in atherosclerosis. *Nat. Rev. Drug Discov.* **9**, 141–153 (2010).
5. E. J. Fernandez, E. Lolis, Structure, function, and inhibition of chemokines. *Annu. Rev. Pharmacol. Toxicol.* **42**, 469–499 (2002).
6. S. E. Crown, Y. Yu, M. D. Sweeney, J. A. Leary, T. M. Handel, Heterodimerization of CCR2 chemokines and regulation by glycosaminoglycan binding. *J. Biol. Chem.* **281**, 25438–25446 (2006).
7. R. R. Koenen, P. von Hundelshausen, I. V. Nesmelova, A. Zernecke, E. A. Liehn, A. Sarabi, B. K. Kramp, A. M. Piccinini, S. R. Paludan, M. A. Kowalska, A. J. Kungl, T. M. Hackeng, K. H. Mayo, C. Weber, Disrupting functional interactions between platelet chemokines inhibits atherosclerosis in hyperlipidemic mice. *Nat. Med.* **15**, 97–103 (2009).
8. I. V. Nesmelova, Y. Sham, J. Gao, K. H. Mayo, CXC and CC chemokines form mixed heterodimers: Association free energies from molecular dynamics simulations and experimental correlations. *J. Biol. Chem.* **283**, 24155–24166 (2008).
9. A. Z. Dudek, I. Nesmelova, K. Mayo, C. M. Verfaillie, S. Pitchford, A. Slungaard, Platelet factor 4 promotes adhesion of hematopoietic progenitor cells and binds IL-8: Novel mechanisms for modulation of hematopoiesis. *Blood* **101**, 4687–4694 (2003).
10. I. V. Nesmelova, Y. Sham, A. Z. Dudek, L. I. van Eijk, G. Wu, A. Slungaard, F. Mortari, A. W. Griffioen, K. H. Mayo, Platelet factor 4 and interleukin-8 CXC chemokine heterodimer formation modulates function at the quaternary structural level. *J. Biol. Chem.* **280**, 4948–4958 (2005).
11. J. Grommes, J. E. Alard, M. Drechsler, S. Wantha, M. Morgelin, W. M. Kuebler, M. Jacobs, P. von Hundelshausen, P. Markart, M. Wygrecka, K. T. Preissner, T. M. Hackeng, R. R. Koenen, C. Weber, O. Soehnlein, Disruption of platelet-derived chemokine heteromers prevents neutrophil extravasation in acute lung injury. *Am. J. Respir. Crit. Care Med.* **185**, 628–636 (2012).
12. J. Carlson, S. A. Baxter, D. Dréau, I. V. Nesmelova, The heterodimerization of platelet-derived chemokines. *Biochim. Biophys. Acta* **1834**, 158–168 (2013).
13. S. Sebastiani, G. Danelon, B. Gerber, M. Uguccioni, CCL22-induced responses are powerfully enhanced by synergy inducing chemokines via CCR4: Evidence for the involvement of first β-strand of chemokine. *Eur. J. Immunol.* **35**, 746–756 (2005).
14. K. Kuscher, G. Danelon, S. Paoletti, L. Stefano, M. Schiraldi, V. Petkovic, M. Locati, B. O. Gerber, M. Uguccioni, Synergy-inducing chemokines enhance CCR2 ligand activities on monocytes. *Eur. J. Immunol.* **39**, 1118–1128 (2009).
15. M. Ren, Q. Guo, L. Guo, M. Lenz, F. Qian, R. R. Koenen, H. Xu, A. B. Schilling, C. Weber, R. D. Ye, A. R. Dinner, W.-J. Tang, Polymerization of MIP-1 chemokine (CCL3 and CCL4) and clearance of MIP-1 by insulin-degrading enzyme. *EMBO J.* **29**, 3952–3966 (2010).
16. W. G. Liang, M. Ren, F. Zhao, W.-J. Tang, Structures of human CCL18, CCL3, and CCL4 reveal molecular determinants for quaternary structures and sensitivity to insulin-degrading enzyme. *J. Mol. Biol.* **427**, 1345–1358 (2015).
17. A. Zernecke, C. Weber, Chemokines in atherosclerosis: Proceedings resumed. *Arterioscler. Thromb. Vasc. Biol.* **34**, 742–750 (2014).
18. S. Struyf, M. D. Burdick, P. Proost, J. Van Damme, R. M. Strieter, Platelets release CXCL4L1, a nonallelic variant of the chemokine platelet factor-4/CXCL4 and potent inhibitor of angiogenesis. *Circ. Res.* **95**, 855–857 (2004).

19. J.-H. Kuo, Y. P. Chen, J.-S. Liu, A. Dubrac, C. Quemener, H. Prats, A. Bikfalvi, W.-g. Wu, S.-C. Sue, Alternative C-terminal helix orientation alters chemokine function: Structure of the anti-angiogenic chemokine, CXCL4L1. *J. Biol. Chem.* **288**, 13522–13533 (2013).

20. K. H. Mayo, E. Ilyina, V. Roongta, M. Dundas, J. Joseph, C. K. Lai, T. Maione, T. J. Daly, Heparin binding to platelet factor-4. An NMR and site-directed mutagenesis study: Arginine residues are crucial for binding. *Biochem. J.* **312** (Pt. 2), 357–365 (1995).

21. L. G. Czaplewski, J. McKeating, C. J. Craven, L. D. Higgins, V. Appay, A. Brown, T. Dudgeon, L. A. Howard, T. Meyers, J. Owen, S. R. Palan, P. Tan, G. Wilson, N. R. Woods, C. M. Heyworth, B. I. Lord, D. Brotherton, R. Christison, S. Craig, S. Cribbes, R. M. Edwards, S. J. Evans, R. Gilbert, P. Morgan, E. Randle, N. Schofield, P. G. Varley, J. Fisher, J. P. Waltho, M. G. Hunter, Identification of amino acid residues critical for aggregation of human CC chemokines macrophage inflammatory protein (MIP)-1α, MIP-1β, and RANTES. Characterization of active disaggregated chemokine variants. *J. Biol. Chem.* **274**, 16077–16084 (1999).

22. T. M. Handel, P. J. Domaille, Heteronuclear (¹H, ¹³C, ¹⁵N) NMR assignments and solution structure of the monocyte chemoattractant protein-1 (MCP-1) dimer. *Biochemistry* **35**, 6569–6584 (1996).

23. K. H. Mayo, M. J. Chen, Human platelet factor 4 monomer-dimer-tetramer equilibria investigated by 1H NMR spectroscopy. *Biochemistry* **28**, 9469–9478 (1989).

24. A. D. Luster, S. M. Greenberg, P. Leder, The IP-10 chemokine binds to a specific cell surface heparan sulfate site shared with platelet factor 4 and inhibits endothelial cell proliferation. *J. Exp. Med.* **182**, 219–231 (1995).

25. P. E. Dawson, S. B. H. Kent, Convenient total synthesis of a 4-helix template-assembled synthetic protein (TASP) molecule by chemoselective ligation. *J. Am. Chem. Soc.* **115**, 7263–7266 (1993).

26. O. Söderberg, M. Gullberg, M. Jarvius, K. Ridderstråle, K.-J. Leuchowius, J. Jarvius, K. Wester, P. Hydbring, F. Bahram, L.-G. Larsson, U. Landegren, Direct observation of individual endogenous protein complexes in situ by proximity ligation. *Nat. Methods* **3**, 995–1000 (2006).

27. P. Hernanz-Falcón, J. M. Rodríguez-Frade, A. Serrano, D. Juan, A. del Sol, S. F. Soriano, F. Roncal, L. Gomez, A. Valencia, A. C. Martínez-A, M. Mellado, Identification of amino acid residues crucial for chemokine receptor dimerization. *Nat. Immunol.* **5**, 216–223 (2004).

28. M. Mellado, J. M. Rodríguez-Frade, A. J. Vila-Coro, S. Fernández, A. Martín de Ana, D. R. Jones, J. L. Torán, A. C. Martínez-A, Chemokine receptor homo- or heterodimerization activates distinct signaling pathways. *EMBO J.* **20**, 2497–2507 (2001).

29. G. E. Callander, W. G. Thomas, R. A. Bathgate, Prolonged RXFP1 and RXFP2 signaling can be explained by poor internalization and a lack of β-arrestin recruitment. *Am. J. Physiol. Cell Physiol.* **296**, C1058–C1066 (2009).

30. C. Weber, S. Meiler, Y. Döring, M. Koch, M. Drechsler, R. T. A. Megens, Z. Rowinska, K. Bidzhekov, C. Fecher, E. Ribechini, M. A. M. J. van Zandvoort, C. J. Binder, I. Jelinek, M. Hristov, L. Boon, S. Jung, T. Korn, M. B. Lutz, I. Forster, M. Zenke, T. Hieronymus, T. Junt, A. Zernecke, CCL17-expressing dendritic cells drive atherosclerosis by restraining regulatory T cell homeostasis in mice. *J. Clin. Invest.* **121**, 2898–2910 (2011).

31. D. F. J. Ketelhuth, G. K. Hansson, Adaptive response of T and B cells in atherosclerosis. *Circ. Res.* **118**, 668–678 (2016).

32. M. Vidal, How much of the human protein interactome remains to be mapped? *Sci. Signal.* **9**, eg7 (2016).

33. K. M. Ansel, V. N. Ngo, P. L. Hyman, S. A. Luther, R. Forster, J. D. Sedgwick, J. L. Browning, M. Lipp, J. G. Cyster, A chemokine-driven positive feedback loop organizes lymphoid follicles. *Nature* **406**, 309–314 (2000).

34. K. M. Ansel, R. B. S. Harris, J. G. Cyster, CXCL13 is required for B1 cell homing, natural antibody production, and body cavity immunity. *Immunity* **16**, 67–76 (2002).

35. L. Qin, I. Kufareva, L. G. Holden, C. Wang, Y. Zheng, C. Zhao, G. Fenalti, H. Wu, G. W. Han, V. Cherezov, R. Abagyan, R. C. Stevens, T. M. Handel, Crystal structure of the chemokine receptor CXCR4 in complex with a viral chemokine. *Science* **347**, 1117–1122 (2015).

36. L. J. Drury, J. J. Ziarek, S. Gravel, C. T. Veldkamp, T. Takekoshi, S. T. Hwang, N. Heveker, B. F. Volkman, M. B. Dwinell, Monomeric and dimeric CXCL12 inhibit metastasis through distinct CXCR4 interactions and signaling pathways. *Proc. Natl. Acad. Sci. U.S.A.* **108**, 17655–17660 (2011).

37. H. Jin, X. Shen, B. R. Baggett, X. Kong, P. J. LiWang, The human CC chemokine MIP-1β dimer is not competent to bind to the CCR5 receptor. *J. Biol. Chem.* **282**, 27976–27983 (2007).

38. P. R. B. Joseph, K. V. Sawant, A. Isley, M. Pedroza, R. P. Garofalo, R. M. Richardson, K. Rajarathnam, Dynamic conformational switching in the chemokine ligand is essential for G-protein-coupled receptor activation. *Biochem. J.* **456**, 241–251 (2013).

39. K. Rajarathnam, G. N. Prado, H. Fernando, I. Clark-Lewis, J. Navarro, Probing receptor binding activity of interleukin-8 dimer using a disulfide trap. *Biochemistry* **45**, 7882–7888 (2006).

40. A. Ravindran, P. R. B. Joseph, K. Rajarathnam, Structural basis for differential binding of the interleukin-8 monomer and dimer to the CXCR1 N-domain: Role of coupled interactions and dynamics. *Biochemistry* **48**, 8795–8805 (2009).

41. A. Ravindran, K. V. Sawant, J. Sarmiento, J. Navarro, K. Rajarathnam, Chemokine CXCL1 dimer is a potent agonist for the CXCR2 receptor. *J. Biol. Chem.* **288**, 12244–12252 (2013).

42. S. Kraemer, H. Lue, A. Zernecke, A. Kapurniotu, E. Andreetto, R. Frank, B. Lennartz, C. Weber, J. Bernhagen, MIF-chemokine receptor interactions in atherogenesis are dependent on an N-loop-based 2-site binding mechanism. *FASEB J.* **25**, 894–906 (2011).

43. L. Xu, Y. Li, D. Li, P. Xu, S. Tian, H. Sun, H. Liu, T. Hou, Exploring the binding mechanisms of MIF to CXCR2 using theoretical approaches. *Phys. Chem. Chem. Phys.* **17**, 3370–3382 (2015).

44. B. K. Kramp, R. T. Megens, A. Sarabi, S. Winkler, D. Projahn, C. Weber, R. R. Koenen, P. von Hundelshausen, Exchange of extracellular domains of CCR1 and CCR5 reveals confined functions in CCL5-mediated cell recruitment. *Thromb. Haemost.* **110**, 795–806 (2013).

45. C. Weber, K. S. Weber, C. Klier, S. Gu, R. Wank, R. Horuk, P. J. Nelson, Specialized roles of the chemokine receptors CCR1 and CCR5 in the recruitment of monocytes and T$_H$1-like/ CD45RO⁺ T cells. *Blood* **97**, 1144–1146 (2001).

46. T. Baltus, K. S. Weber, Z. Johnson, A. E. I. Proudfoot, C. Weber, Oligomerization of RANTES is required for CCR1-mediated arrest but not CCR5-mediated transmigration of leukocytes on inflamed endothelium. *Blood* **102**, 1985–1988 (2003).

47. W. G. Liang, C. G. Triandafillou, T. Y. Huang, M. M. L. Zulueta, S. Banerjee, A. R. Dinner, S. C. Hung, W.-J. Tang, Structural basis for oligomerization and glycosaminoglycan binding of CCL5 and CCL3. *Proc. Natl. Acad. Sci. U.S.A.* **113**, 5000–5005 (2016).

48. C. T. Veldkamp, C. Seibert, F. C. Peterson, N. B. De la Cruz, J. C. Haugner III, H. Basnet, T. P. Sakmar, B. F. Volkman, Structural basis of CXCR4 sulfotyrosine recognition by the chemokine SDF-1/CXCL12. *Sci. Signal.* **1**, ra4 (2008).

49. M. Thelen, L. M. Munoz, J. M. Rodríguez-Frade, M. Mellado, Chemokine receptor oligomerization: Functional considerations. *Curr. Opin. Pharmacol.* **10**, 38–43 (2010).

50. P. Cutolo, N. Basdevant, G. Bernadat, F. Bachelerie, T. Ha-Duong, Interaction of chemokine receptor CXCR4 in monomeric and dimeric state with its endogenous ligand CXCL12: Coarse-grained simulations identify differences. *J. Biomol. Struct. Dyn.* **35**, 399–412 (2017).

51. B. Finan, B. Yang, N. Ottaway, D. L. Smiley, T. Ma, C. Clemmensen, J. Chabenne, L. Zhang, K. M. Habegger, K. Fischer, J. E. Campbell, D. Sandoval, R. J. Seeley, K. Bleicher, S. Uhles, W. Riboulet, J. Funk, C. Hertel, S. Belli, E. Sebokova, K. Conde-Knape, A. Konkar, D. J. Drucker, V. Gelfanov, P. T. Pfluger, T. D. Muller, D. Perez-Tilve, R. D. DiMarchi, M. H. Tschöp, A rationally designed monomeric peptide triagonist corrects obesity and diabetes in rodents. *Nat. Med.* **21**, 27–36 (2015).

52. P. von Hundelshausen, R. R. Koenen, M. Sack, S. F. Mause, W. Adriaens, A. E. I. Proudfoot, T. M. Hackeng, C. Weber, Heterophilic interactions of platelet factor 4 and RANTES promote monocyte arrest on endothelium. *Blood* **105**, 924–930 (2005).

53. J. Feierler, M. Wirth, B. Welte, S. Schussler, M. Jochum, A. Faussner, Helix 8 plays a crucial role in bradykinin B$_2$ receptor trafficking and signaling. *J. Biol. Chem.* **286**, 43282–43293 (2011).

54. A. E. I. Proudfoot, F. Borlat, Purification of recombinant chemokines from *E. coli*. *Methods Mol. Biol.* **138**, 75–87 (2000).

55. A. E. I. Proudfoot, T. M. Handel, Z. Johnson, E. K. Lau, P. LiWang, I. Clark-Lewis, F. Borlat, T. N. C. Wells, M. H. Kosco-Vilbois, Glycosaminoglycan binding and oligomerization are essential for the in vivo activity of certain chemokines. *Proc. Natl. Acad. Sci. U.S.A.* **100**, 1885–1890 (2003).

56. T. M. Hackeng, J. H. Griffin, P. E. Dawson, Protein synthesis by native chemical ligation: Expanded scope by using straightforward methodology. *Proc. Natl. Acad. Sci. U.S.A.* **96**, 10068–10073 (1999).

57. P. E. Dawson, T. W. Muir, I. Clark-Lewis, S. B. Kent, Synthesis of proteins by native chemical ligation. *Science* **266**, 776–779 (1994).

58. S. M. Agten, D. Suylen, H. Ippel, M. Kokozidou, G. Tans, P. van de Vijver, R. R. Koenen, T. M. Hackeng, Chemoselective oxime reactions in proteins and peptides by using an optimized oxime strategy: The demise of levulinic acid. *ChemBioChem* **14**, 2431–2434 (2013).

59. S. M. Agten, R. R. Koenen, H. Ippel, V. Eckardt, P. von Hundelshausen, K. H. Mayo, C. Weber, T. M. Hackeng, Probing functional heteromeric chemokine protein-protein interactions through conformation-assisted oxime ligation. *Angew. Chem. Int. Ed. Engl.* **55**, 14963–14966 (2016).

60. J.-E. Alard, A. Ortega-Gomez, K. Wichapong, D. Bongiovanni, M. Horckmans, R. T. Megens, G. Leoni, B. Ferraro, J. Rossaint, N. Paulin, J. Ng, H. Ippel, D. Suylen, R. Hinkel, X. Blanchet, F. Gaillard, M. D'Amico, P. von Hundelshausen, A. Zarbock, C. Scheiermann, T. M. Hackeng, S. Steffens, C. Kupatt, G. A. F. Nicolaes, C. Weber, O. Soehnlein, Recruitment of classical monocytes can be inhibited by disturbing heteromers of neutrophil HNP1 and platelet CCL5. *Sci. Transl. Med.* **7**, 317ra196 (2015).

61. K. Wichapong, J.-E. Alard, A. Ortega-Gomez, C. Weber, T. M. Hackeng, O. Soehnlein, G. A. F. Nicolaes, Structure-based design of peptidic inhibitors of the interaction between

CC chemokine ligand 5 (CCL5) and human neutrophil peptides 1 (HNP1). *J. Med. Chem.* **59**, 4289–4301 (2016).

62. R. Van Kruchten, J. M. E. M. Cosemans, J. W. M. Heemskerk, Measurement of whole blood thrombus formation using parallel-plate flow chambers—A practical guide. *Platelets* **23**, 229–242 (2012).

63. S. M. de Witt, F. Swieringa, R. Cavill, M. M. Lamers, R. van Kruchten, T. Mastenbroek, C. Baaten, S. Coort, N. Pugh, A. Schulz, I. Scharrer, K. Jurk, B. Zieger, K. J. Clemetson, R. W. Farndale, J. W. Heemskerk, J. M. Cosemans, Identification of platelet function defects by multi-parameter assessment of thrombus formation. *Nat. Commun.* **5**, 4257 (2014).

Citation: P. von Hundelshausen, S. M. Agten, V. Eckardt, X. Blanchet, M. M. Schmitt, H. Ippel, C. Neideck, K. Bidzhekov, J. Leberzammer, K. Wichapong, A. Faussner, M. Drechsler, J. Grommes, J. P. van Geffen, H. Li, A. Ortega-Gomez, R. T. A. Megens, R. Naumann, I. Dijkgraaf, G. A. F. Nicolaes, Y. Döring, O. Soehnlein, E. Lutgens, J. W. M. Heemskerk, R. R. Koenen, K. H. Mayo, T. M. Hackeng, C. Weber, Chemokine interactome mapping enables tailored intervention in acute and chronic inflammation. *Sci. Transl. Med.* **9**, eaah6650 (2017).

von Hundelshausen *et al.*, *Sci. Transl. Med.* **9**, eaah6650 (2017)   5 April 2017

62

Science Translational Medicine

Chemokine interactome mapping enables tailored intervention in acute and chronic inflammation

Philipp von Hundelshausen, Stijn M. Agten, Veit Eckardt, Xavier Blanchet, Martin M. Schmitt, Hans Ippel, Carlos Neideck, Kiril Bidzhekov, Julian Leberzammer, Kanin Wichapong, Alexander Faussner, Maik Drechsler, Jochen Grommes, Johanna P. van Geffen, He Li, Almudena Ortega-Gomez, Remco T. A. Megens, Ronald Naumann, Ingrid Dijkgraaf, Gerry A. F. Nicolaes, Yvonne Döring, Oliver Soehnlein, Esther Lutgens, Johan W. M. Heemskerk, Rory R. Koenen, Kevin H. Mayo, Tilman M. Hackeng and Christian Weber

Hampering heterodimers interrupts inflammation

Inflammation is dependent on the recruitment of cells responding to chemokines. Von Hundelshausen *et al.* cataloged how human chemokines interact with each other and found that certain kinds of chemokine pairs can activate or inhibit receptor signaling. These chemokine heterodimers were shown to be active in mouse models of acute and chronic inflammation, which were ameliorated by treatment with a peptide designed to disrupt the chemokine pairing. Patients suffering from inflammatory conditions such as atherosclerosis could benefit from these kinds of therapeutics.

ARTICLE TOOLS	http://stm.sciencemag.org/content/9/384/eaah6650
SUPPLEMENTARY MATERIALS	http://stm.sciencemag.org/content/suppl/2017/04/03/9.384.eaah6650.DC1
RELATED CONTENT	http://stm.sciencemag.org/content/scitransmed/9/399/eaal3322.full http://stke.sciencemag.org/content/sigtrans/10/480/eaai8529.full http://stke.sciencemag.org/content/sigtrans/11/529/eaal2869.full http://stke.sciencemag.org/content/sigtrans/11/552/eaat2214.full http://stke.sciencemag.org/content/sigtrans/12/597/eaat4128.full
REFERENCES	This article cites 63 articles, 30 of which you can access for free http://stm.sciencemag.org/content/9/384/eaah6650#BIBL
PERMISSIONS	http://www.sciencemag.org/help/reprints-and-permissions

Use of this article is subject to the Terms of Service

Science
Translational
Medicine
AAAS

Supplementary Materials for

Chemokine interactome mapping enables tailored intervention in acute and chronic inflammation

Philipp von Hundelshausen, Stijn M. Agten, Veit Eckardt, Xavier Blanchet,
Martin M. Schmitt, Hans Ippel, Carlos Neideck, Kiril Bidzhekov, Julian Leberzammer,
Kanin Wichapong, Alexander Faussner, Maik Drechsler, Jochen Grommes,
Johanna P. van Geffen, He Li, Almudena Ortega-Gomez, Remco T. A. Megens,
Ronald Naumann, Ingrid Dijkgraaf, Gerry A. F. Nicolaes, Yvonne Döring,
Oliver Soehnlein, Esther Lutgens, Johan W. M. Heemskerk, Rory R. Koenen,
Kevin H. Mayo, Tilman M. Hackeng, Christian Weber*

*Corresponding author. Email: chweber@med.lmu.de

This PDF file includes:

Fig. S16. Microscopy of chemokine interactions at the cell surface.
Fig. S17. Mechanisms for synergy of chemokine heterodimers.
Fig. S18. Effect of heterodimers on signaling pathways, receptor affinity, and internalization.
Fig. S19. CCL5-CXCL4 heterodimers bind to heparin and prevent arrestin recruitment.
Fig. S20. Relevance of chemokine heterodimer formation in acute lung injury.
Fig. S21. Generation of mice deficient in *Cxcl4* or *Cxcl12* or carrying *Cxcl4* variants.
Fig. S22. Analysis of atherosclerotic lesion in mice expressing Cxcl4 or its variant.
Fig. S23. Composition of aortic root lesions in mice expressing Cxcl4 or its variant.
Fig. S24. Obligate chemokine heterodimers mimic natural heterodimers.
Fig. S25. Summary scheme.
Table S1. Densitometry analysis of bidirectional immunoligand blotting.
Table S2. Kinetic analysis of chemokine binding by SPR.
Table S3. Weighted averaging of Δintensity changes and MDS-based in silico modeling.
Table S4. Sequence and origin of peptide inhibitors.
Table S5. CCL5-derived peptides specifically inhibit heterodimer formation.
Table S6. Lipid parameters and peripheral blood counts of different CXCL4 genotypes.
Table S7. Effect of OPRAH on lipid parameters and peripheral blood counts.
References (*53–63*)

Supplementary Materials

Materials and Methods

Cells and cell culture

Human CD4 T cells were isolated from whole blood of healthy volunteers after separating peripheral blood mononuclear cells (PBMCs) with Biocoll (Biochrom, Merck Millipore using the Dynabeads Untouched Human CD4 T Cells kit, stimulated with Dynabeads Human T-Activator CD3/CD28 (both Thermo Fisher Scientific) for 3 days and expanded in the presence of Dynabeads with hIL-2 (30 U/mL) for another 3 days. Human monocytes were isolated from PBMCs, and purified by negative selection using the "Monocyte Isolation Kit II" (Miltenyi Biotec). Mouse CD4 T cells were isolated from spleens of mice with indicated genotypes using Dynabeads Untouched mouse CD4 Cells Kit and activated using Dynabeads Mouse T-Activator, Thermo Fisher Scientific), as described for human cells. Mouse dendritic cells were isolated from spleens by positive and negative selection using magnetic beads (Pan DC MicroBeads, mouse, Miltenyi Biotec). Human aortic endothelial cells (HAoECs) were from PromoCell. Oligonucleotides were synthesized at MWG-Biotech.

The Flp-In system and Flp-In™ TREx-293 (HEK293) cells were from Invitrogen. Plasmids harboring sequences for CCR1, CCR4, CCR5 and CXCR4 were from Missouri S&T cDNA Resource Center (www.cdna.org). The pGloSensor™-20F-vector and luciferin-EF were from Promega. The sequence of the luciferase-cAMP binding site fusion protein from the pGloSensor™-20F-vector was amplified and ligated into a bicistronic pIRESneo vector (Clontech) to obtain the reporter gene plasmid. The pcDNA5/FRT/TO vector (Invitrogen) was used to express receptor constructs carrying an N-terminal hemagglutinin-tag or enhanced yellow fluorescent protein (eYFP) (*53*). HEK293 cells were transfected with the reporter gene vector using Eco-Transfect (OZBioscience), stable clones were selected as host cell lines for expressing receptor constructs using the Flp-In system (*53*), and re-selected with G418 and hygromycin B.

Chemokines and peptides

CCL5, CXCL4 and CXCL12 were recombinantly expressed using codon-optimized genes (Genscript, NJ, USA), and pET-24a(+), -32a(+) or -43.1a(+) vectors, respectively, in E.coli BL21(DE3) cells and purified, essentially as described (*54*). To generate ^{15}N-labeled chemokines, we used Spectra M9 medium (Cambridge Isotope Laboratories). Mass and disulfide bond

integrity were examined by UPLC-QTOF mass spectroscopy. Biotinylation of chemokines was performed while bound to heparin columns. Purified CCL5^{E26A} and the synthesized CCL5^{MT7} variant were kindly provided by Dr. A. Proudfoot (*55*). Other chemokines were purchased from Peprotech or R&D Systems. CCL5 and CCL17 C-terminally-conjugated with AF647 were from ALMAC science.

The peptides CAN and CKEY were synthetized by Bachem AG. All other peptides (Table S4) were synthesized manually by SPPS on PAM resin or thioester (COSR) generating resin using *in situ* neutralization/HCTU activation for tBoc chemistry (*56*). Semi-preparative HPLC was performed using Vydac C18 or C4 HPLC columns using a Waters Deltaprep system. Peptide analysis was performed on a Waters UPLC XEVO-G2QTOF system. The peptide monomer VREY was extended at the N-terminus by introducing a glycine spacer to which (Boc-aminooxy) acetic acid (AO) was coupled (AO-G-EKKWVREYINSLEMS-COOH). A modified cyclic backbone TASP template was used to obtain a parallel 4-helix bundle (H$_2$N-CPKGKGPGKGKG-COSR) (*25*). TASP-lysines were modified to present a ketone group using 4-acetylbutyric acid (*56*). TASP was cyclized by native chemical ligation (NCL) (*25*) and the free cysteine was alkylated to prevent dimer formation. Ketone-derivatized TASP and a 2.5-fold excess of aminooxy-VREY were reacted to obtain [VREY]^4 through oxime linkage.

The total chemical synthesis of OPRAH (obligate PF4-RANTES heterodimer), nOPRAH (n-terminally tethered OPRAH), mOPRAH (mouseOPRAH using the murine orthologs) and ORATH (obligate RANTES-TARC heterodimer) comprised the individual synthesis of CCL5, CXCL4 or CCL17, which were subsequently folded and coupled by oxime chemistry. The individual chemokines were synthesized in three parts that were joined by NCL and folded by oxidation (*57*). CCL5 N-termini were modified to introduce aminooxy moieties for oxime ligation. For both human and mouse CCL5$^{1-10}$, Lys(ε-amino-Alloc) was introduced at position T7 to allow for on-resin aminooxy modification. As counterparts in the oxime ligation reactions, ketones (4-acetylbutyric acid) were added in the chemokine N-termini by introducing Lys(ε-amino-Alloc) at position L8 of human CXCL4, at position L13 of mouse CXCL4, and at position G7 of human CCL17 (*58*). The folded N-terminally ketone-derivatized chemokines were reacted with a 2-fold excess of aminooxy-CCL5. The mixture was placed at -20°C for 1 h to complete the reaction. The covalent heterodimer product was purified using HPLC. Detailed information about the synthesis of the heterodimers is available (*59*).

Molecular dynamics (MD) simulation and binding free energy calculations

Chemokine structures were downloaded from the Protein Data Bank (PDB): codes 1DOK (CCL2), 2L9H (CCL5), 1NR4 (CCL17), 1F9Q (CXCL4), 4UAI (CXCL12). Dimer complexes (CC or CXC type) were manually assembled by superimposition onto the CC-conformation of CCL5 or the CXC-conformation of CXCL4. The different chemokine complexes were subjected to MD simulations as described (*60, 61*), except applying Amber12SB force field and TIP4P-Ew water model. Free MD simulations were performed for 100 ns and accelerated molecular dynamics were employed for another 30 ns. Snapshots between 100-130 ns were extracted for binding free energy calculation using molecular mechanics/generalized Born surface area (MM/GBSA) approach and the binding free energies were approximated from enthalpy values (*61*). Default parameters were applied for binding free energy calculation, except using generalized Born model 8 to compute the free energy of solvation.

Transmigration assays

Transmigration assays were performed using Transwell-96 Permeable Support (Corning) with 5.0 µm (human T cells) or 3.0 µm (mouse T cells) pore size (*45*). Chemokines were added to the bottom chambers and 10^4 activated T cells were allowed to migrate for 2 h from the top chamber. Receptor antagonists were added to top chambers, while compounds modulating chemokine interactions were added to bottom chambers at 10x molar excess relative to chemokine. The number of cells migrated was analyzed by flow cytometry (FACSCanto II, BD Biosciences) and FlowJo v.10 software (Tree Star Inc.). The chemotactic index was calculated as the ratio of chemokine-stimulated to unstimulated migration.

Arrest assays

Confluent HAoEC monolayers were activated with IL-1β for 4 h before incubation with chemokines, synthetic obligate chemokine heterodimers and/or peptides for 30 min. Monocytes or T cells (0.7×10^6/ml) pretreated with receptor antagonists (C021, DAPTA, Met-RANTES) were perfused over activated HAoECs in a laminar flow chamber at a shear stress of 1.5 dyn/cm^2 for 2 min. Cells were visualized and recorded by video microscopy (Olympus IX 50, Shinjuku, Japan, 20x objective). Firmly adherent leukocytes were counted in 10 high-power fields (HPF) per plate.

Proximity Ligation Assay

Proximity ligation was performed using the Duolink In Situ Red Kit Goat/Rabbit on PFA-fixed cryo-sections of aortic roots or lymph nodes of *Apoe*$^{-/-}$ mice, using primary polyclonal antibodies

to mouse CCL17 (R&D, AF529), mouse CCL5 (Acris, AP20618PU-N) according to the manufacturer's instructions. Mouse dendritic cells and SV40-transformed endothelial cells (SVECs) cultured on collagen-coated cover slips were pre-incubated with mouse CCL5, CXCL4 and CCL17 (Biolegend) alone or in combination with CAN or CCR5-derived transmembrane peptides TM1 and TM4 known to inhibit CCR5 dimerization (*27*). The same kit was used on paraffin sections of human coronary arteries using polyclonal antibodies to human CCL5 (AF278-NA, R&D Systems) and CCL17 (ab182793, Abcam). Imaging was performed using fluorescence microscopy (Leica DM4000) after which deconvolution algorithms for wide field microscopy were applied to improve overall image quality (Huygens professional 16.10; SVI). The number of Duolink-detected interactions was determined in the processed images using the Leica LAS 4.2 analyses software. In order to more accurately resolve the interactions detected with Duolink, representative dendritic cell samples of each condition were also visualized with a Leica SP8 3X microscope using a combination of 3D confocal microscopy (DAPI) and 3D STED nanoscopy (Duolink Red). Image processing and deconvolution of the resultant 3D datasets was performed using the Leica LAS X and Huygens professional software packages. The study was approved by the Ethics Committee of the Academic Medical Centre at the University of Amsterdam. Anonymous post-mortem coronary artery specimen did not require informed consent.

Flow cytometry

Whole blood obtained from the retro-orbital plexus of mice was EDTA-buffered and subjected to red blood-cell lysis. Lymph nodes and spleens were mechanically disrupted and passed through a cell strainer. Leukocytes were counted and analyzed by the following antibody cocktail: anti-CD45, anti-CD115, anti-Gr1, anti-CD11b, anti-CD19 (eBioscience, clone MB19-1) and anti-CD3 (eBioscience, clone 145-2C11). Leukocyte subsets were defined using FlowJo software: neutrophils ($CD45^+CD115\text{-}Gr1^{high}$), monocytes ($CD45^+CD115^+$), classical monocytes ($CD45^+CD115^+Gr1^{high}$), non-classical monocytes ($CD45^+CD115^+Gr1^{low}$) and lymphocytes ($CD45^+CD3^+$ and $CD45^+CD19^+$). Chemokine receptors were analyzed using FITC-anti-Ccr1 (R&D, FAB5986F), AF647-anti-Ccr3 (BioLegend, clone TG14/Ccr3), PE-anti-Ccr5 (eBioscience, clone HM-CCR5) and PE-anti-Ccr2 (R&D Systems).

Mice

All animal experimental procedures were designed and conducted in agreement with the German Animal Welfare Legislation, and were reviewed and approved by the local authorities (Regierung von Oberbayern, Munich, Germany). All mice were housed in IVC units and maintained on

a 12-h dark/12-h light cycle. B6.129P2-Apoe/J ($Apoe^{-/-}$) and B6.129P2-Ccl5^{tm1Hso}/J ($Ccl5^{-/-}$) mice were obtained from The Jackson Laboratory, C57BL/6J mice were from Janvier and tamoxifen-inducible general Cre-deleter C57BL/6-$Gt(ROSA)26Sor^{tm9(Cre/ESR1)Arte}$ (CreERT2) mice were from Taconic (TaconicArtemis GmbH).

$Cxcl4^{L1/L1}$, $Cxcl4^{tg-L1}$ and $Cxcl12^{-/-}$ mice were generated by laser-assisted (XY-Clone Hamilton Thorne) injection of R1/E(129/Sv) cells into 8-cell stage C57Bl/6NCrl embryos. Embryo recipients were Crl:CD1(ICR) mice (Charles River). All manipulations were carried out in the Transgenic Core Facility (TCF) of the MPI-CBG, Dresden. Chimeras were crossed to C57Bl/6NCrl mice and their offspring were screened for germline transmission. Details of the targeting constructs used to induce homologous recombination and knock-in into the Rosa locus are depicted in Fig. S21.

Bone marrow transplantation

$Apoe^{-/-}$ mice underwent lethally whole body irradiation (2x5Gy) and were reconstituted with donor bone marrow cells from $Apoe^{-/-}Ccr4^{-/-}$ or $Apoe^{-/-}Ccl5^{-/-}Cxcl4^{-/-}$ mice, essentially as described (*7*). After 4 weeks, animals were injected i.p. with the CCR5 antagonist DAPTA (TOCRIS) or CAN peptide every second day for 2 weeks.

Atherosclerotic lesion formation, quantification and histological analysis

To induce lesions, 8 week old $Apoe^{-/-}$ mice fed a high-fat diet (HFD, 21% fat, 19.5 % casein, 0.15% cholesterol, ssniff) for 2 weeks (bone-marrow chimeras) for 6 weeks (OPRAH injection) or 12 weeks (analysis of Cxcl4-deficient and knock-in strains). Mice were anesthetized with ketamine (80 mg/kg) and xylazine (10 mg/kg) and EDTA-anticoagulated blood was retroorbitally collected. Cell counts were determined using an automated hematology analyzer (scil Animal Care). Plasma was used to detect cholesterol and triglyceride levels (CHOD-PAP or GPO-PAP kit, Roche). After complete bleeding, *in situ* perfusion fixation was performed using 4% buffered formaldehyde (Carl Roth) and the heart and entire aorta were excised. The aorta was longitudinally opened and stained *en face* with Oil-Red-O to visualize lipid deposition. The lesion area was calculated as percentage of the Oil-Red-O$^+$ stained area normalized to the respective aortic area (arch, thoracoabdominal, inner curvature, outer curvature). After paraffin-embedding and cutting into 4 µm transverse sections for aortic roots or 6 µm longitudinal sections for aortic arches, atherosclerotic lesion size was measured after Elastica-van Gieson (EVG) staining (Baacklab). In aortic roots, the percentage of lesion area of the aortic valves normalized to the area of the internal lumen was determined. In aortic arches, total lesion size was quantified in the

inner curvature and the three branches. Cellular content was analyzed by immunofluorescence staining for macrophages, CD3$^+$ T cells and smooth muscle cells (SMCs) using anti-Mac-2 (Cedarlane Labs), anti-CD3 and anti-αSMA antibodies (Dako). Nuclei were counterstained with DAPI (Vector Laboratories). Primary antibodies were visualized using DyLight-488, -550 and -650–conjugated secondary antibodies (Abcam). Images were recorded with a DM 6000B fluorescence microscope (Leica, Solms), connected to a monochrome digital camera (DFC 365FX) for fluorescent imaging or a DFC425C camera for bright-field microscopy. Mac-2-, CD3- and αSMA cells were manually quantified as positive cells per plaque area. Stages of atherosclerotic lesions were determined in EVG-stained aortic root sections according to the Virmani classification. Necrotic cores were quantified as anuclear crystal-laden areas of lesions and normalized to the lesion area.

Acute lung injury

The acute lung injury (ALI) model was performed as described (*11*). ALI was induced in 8 weeks-old male C57BL/6 mice (Janvier) or *Ccl5$^{-/-}$CXCL4$^{-/-}$* bone marrow chimeric mice by exposure to aerosolized LPS (500 µg/ml) from Salmonella enteritidis (Sigma) for 30 min. Peptides, chemokines or mOPRAH were injected i.v. at indicated doses. Alveolar, interstitial, and intravascular neutrophils were analyzed after 4 h. To label intravascular neutrophils, FITC-Ly-6G (Gr1) (clone RB6-8L5, eBioscience) was applied by tail vein injection 30 min before sacrifice. Broncho-alveolar lavage (BAL) fluid was obtained by repeated injection and withdrawal of PBS. The pulmonary vasculature was rinsed with PBS 0.5 mM EDTA. Lungs were removed, minced and digested with liberase (Roche), passed through a cell strainer and neutrophils were analyzed by labeling with anti-mouse PerCP-Cy5.5-Ly-6G, PE-CD115, APC-Cy7-CD45 antibodies (eBioscience).

Competitive chemokine receptor-ligand binding

HEK293 transfectants expressing CCR1, CCR4 or CCR5 were incubated with AF647-labeled CCL5 or CCL17 (2.5 nM) in presence or absence of unlabeled CCL5 or CCL17 (at increasing concentrations) for 1 h at 4°C. After washing, fluorescence intensity was measured by flow cytometry (FACSCantoII) and analyzed using FlowJo v.10 software (Tree Star Inc.).

Chemokine binding to monocytes

Monocytes were incubated with CCL5 in combination with CXCL4 or CXCL4$^{R>Q}$ (each 100 nM) for 1 h at 4°C. CCL5-binding was reacted with a CCL5-antibody (5 µg/ml, Abcam AB9679) and detected with an AF488-conjugated secondary antibody (2 µg/ml, Thermo Fisher Scientific).

Chemokine receptor internalization

CCR1-, CCR4- or CCR5-expressing HEK293 transfectants were incubated for 1 h at 4°C with AF647- labeled CCL5 or CCL17 (2.5 nM) in presence of increasing concentrations of unlabeled chemokines. Cells were then washed with cold PBS and fluorescence intensity was analyzed by flow cytometry.

CCR1 surface expression on adherent arterial leukocytes

Carotid arteries of wild-type mice (C57BL/6) were carefully mounted in custom-made perfusion chambers and set at a physiological pressure of 80 mmHg. A syringe pump (Harvard apparatus PHD ULTRA) was connected to the common carotid side of the artery while a water column was attached to the bifurcation side, in order to maintain physiological pressure under flow. The artery was placed on the microscope stage in a climate chamber (37°C). Bone marrow-derived leukocytes from these mice were fluorescently labeled with cell tracker red CMTPX (Thermo Scientific) and stimulated with or without CCL5 (30 ng/ml) alone or combined with CXCL4 or $CXCL4^{R>Q}$ (300 ng/ml each) in Hanks Balanced Salt Solution (HBSS) containing Ca^{++} and Mg^{++} for 45 min at 37°C. After staining with a FITC-conjugated antibody to CCR1 (Biorbyt), leukocytes (10^6/ml) were perfused in the mounted carotid artery at an arterial flow rate of 0.54 ml/min, the endothelium was stained with an Alexa Fluor 450®-conjugated antibody against CD31 (eBioscience), and after 10 min, the artery was flushed with 2 ml HBSS. Subsequently, two-photon laser scanning microscopy was performed to visualize the luminal area within the artery using a Leica SP5MPII system with a pulsed Ti:Sapphire laser (Spectra Physics MaiTai DeepSee) tuned at 800 nm and a 20×NA1.00 water immersion objective. Adherent leukocytes were imaged at 1024*1024 pixels and three-fold line and frame average, in Z-stacks of 2.5 μm intervals. To quantify cell surface CCR1, images were processed using LAS AF 3.0 software (Leica), and 3D cropping of single cells adhering to the endothelium was performed. Standard background noise reduction and thresholding of CCR1 signal was equally applied to every image. Mean Intensity Fluorescence (MFI) of single cells was quantified.

Cyclic AMP signaling

Levels of cyclic adenosine monophosphate (cAMP) were measured in confluent HEK293 chemokine receptor transfectants after stimulation with chemokines using Glosensor technology over up to 30 min. After incubation with luciferin-EF (2.5 mM) at RT for 2 h, cells were stimulated with CXCL12 in the presence or absence of [VREY][4] and luminescence indicating the reduction

of cAMP was recorded. Likewise, HEK293 cells were transfected with CCR4 or with CCR4 and CCR5 and stimulated with CCL5, CCL17 or both. CCR1 transfectants were stimulated by concentrations of OPRAH as indicated.

Bioluminescence resonance energy transfer (BRET)

Transfection of HEK293 cells with 0.05 µg of a plasmid harboring the CCR5-RlucII construct and 0.2 µg of a plasmid containing the eYFP-arrestin-1/2 constructs or a mock plasmid was performed in 24-wells using 0.5 µl of EcoTransfect. After 24 h, cells were transferred into black 96-well plates with clear bottom, and 72 h after transfection cells were washed and further incubated in HBSS (30 µl) at 21°C. Fluorescence was measured in a plate reader (excitation 480, emission 530). HBSS (10 µl) containing coelenterazine H (5 µM) was added to each well, a white sticker attached to the bottom and total luminescence measured for 5 min. Then, HBSS (10 µl) with and without stimulus (CCL5, CXCL4 or both) was added and the BRET signal (ratio 530/480 nm) determined for 1 s intervals over 20 min. Net-BRET was calculated as the BRET ratio in the presence of the respective eYFP-construct minus BRET ratio obtained with the mock plasmid.

Platelet aggregometry and ex vivo thrombus formation

Human venous blood was collected in hirudin-precoated tubes (Sarstedt,). Informed consent was obtained as approved by the Ethics Committee of the Faculty of Medicine, LMU Munich. Platelet aggregation in blood was determined by multiple electrode aggregometry (MEA) using the Multiplate® device (Roche Diagnostics). Whole blood was diluted with NaCl 1:1 and CXCL12, CCL5 or [VREY]^4 were added, stirring was started and the increase in electrical impedance was recorded continuously for 5 min. The mean value of two independent determinations is expressed as area under the curve in arbitrary units (U).

The multi-parameter assessment of thrombus formation has been described in detail for human blood (*62, 63*). Mouse blood was collected into 0.1 volume of saline with a final concentration of 4 µM PPACK, 4 U/ml fragmin and 5 U/ml heparin. Microspot-coated coverslips, coated as described with three distinct surfaces (a: VWF + laminin. b: VWF + laminin + CLEC-2 ligand. c: collagen type I, Horm), were mounted onto a parallel-plate flow chamber and a shear rate of 1000 s^{-1} was applied. In thrombi, platelets were stained with monoclonal antibodies against CD62P (FITC), activated integrin $\alpha_{IIb}\beta_3$ (PE-JON/A)t, and AF647-annexin-A5. Parameters were assessed by bright-field and sub-sequent tri-color fluorescence microscopy.

Supplementary Figures

A

CCL1	CCL2	CCL3	CCL3L1	CCL4	CCL4L1	CCL5	CCL7	CCL8	CCL11
CCL13	CCL14	CCL15	CCL16	CCL17	CCL18	CCL19	CCL20	CCL21	CCL22
CCL23	CCL24	CCL25	CCL26	CCL27	CCL28	XCL1	CXCL1	CXCL2	CXCL3
CXCL4	CXCL5	CXCL6	CXCL7	CXCL8	CXCL9	CXCL10	CXCL11	CXCL12a	CXCL12b
CXCL13	CXCL14	CXCL16	CXCL17	CXCL4L1	CX3CL1				

B

C
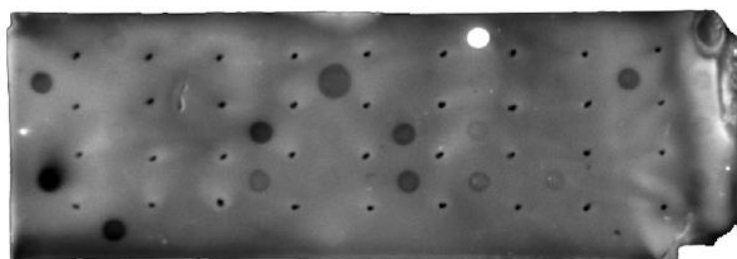
D

0.0000	0.0751	0.0293	0.0000	0.0000	0.0000	1.0000	0.0000	0.0000	0.0000
0.1960	0.0000	0.0000	0.0000	0.3420	0.0000	0.0000	0.0000	0.1533	0.0074
0.0000	0.0000	0.0000	0.2205	0.0000	0.1891	0.0280	0.0000	0.0000	0.0766
0.2908	0.0000	0.0000	0.0957	0.0000	0.1509	0.0000	0.0306	0.0689	0.0218
0.0000	0.1484	0.0000	0.0000	0.0038					

Fig. S1. Representative ligand blot and densitometric values.
(**A**) Chemokines were spotted on a nitrocellulose membrane (1 µl, 1 ng) as indicated. In this example, CCL5 served as the positive control (orange). (**B** and **C**) The membrane was left untreated to test for antibody specificity (B) or incubated overnight at 4°C with 100 nM CCL5 (**C**). CCL5 partners were detected using a biotinylated antibody to CCL5 and a HRP-conjugated secondary antibody (**C**). (**D**) The absolute luminescence signal (area and density) was digitally recorded, background was subtracted and expressed relative to the signal of the positive control (CCL5).
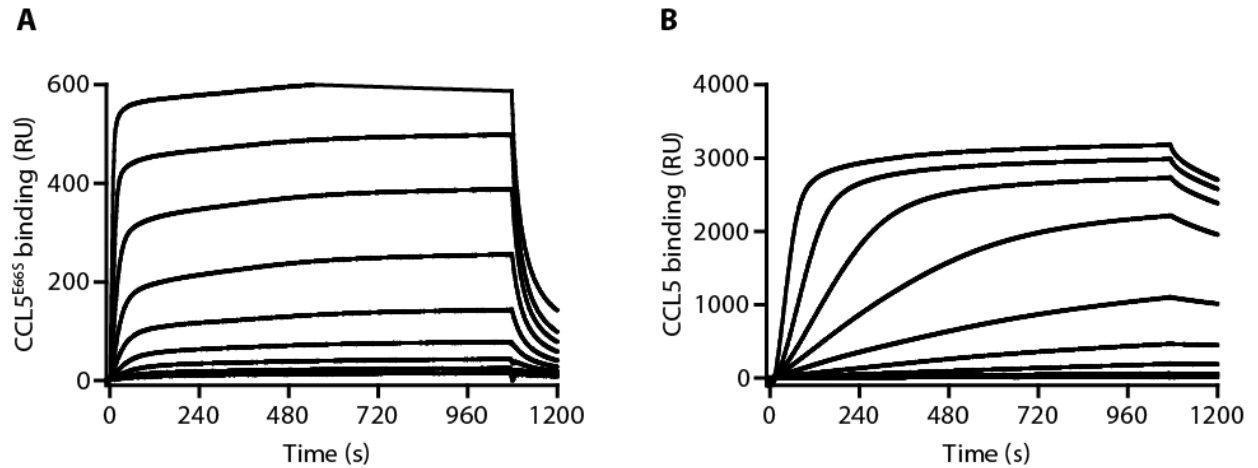
Fig. S2. Interaction of CCL5 and CCL5^{E66S} with CCL17 analyzed by SPR.
To validate chemokine interactions of interest, we performed kinetics analyses of their binding curves using surface plasmon resonance (SPR). Apparent affinities were calculated from on-rates (k_a) and off-rates (k_d) obtained by fitting the curves using BIAevaluation with the 1:1 interaction model (Langmuir). In this example, CCL17 was biotinylated and immobilized onto a neu-travidin-coated sensor chip C1 (BIAcore). (**A**) CCL5^{E66S} was perfused at 2, 4, 8, 16, 32, 64, 128, 256, and 512 nM, and (**B**) CCL5 was perfused at 1.6, 3.1, 6.3, 12.5, 25, 50, 100, 20, 400 and 800 nM, at 5 µl/min in running buffer (HBS-EP+, pH 7.4) and regenerated with 100 mM NaOH, 0.05% SDS and 30% acetonitrile. K_D was calculated to be 93 nM for CCL5^{E66S} and 65 nM for native CCL5.
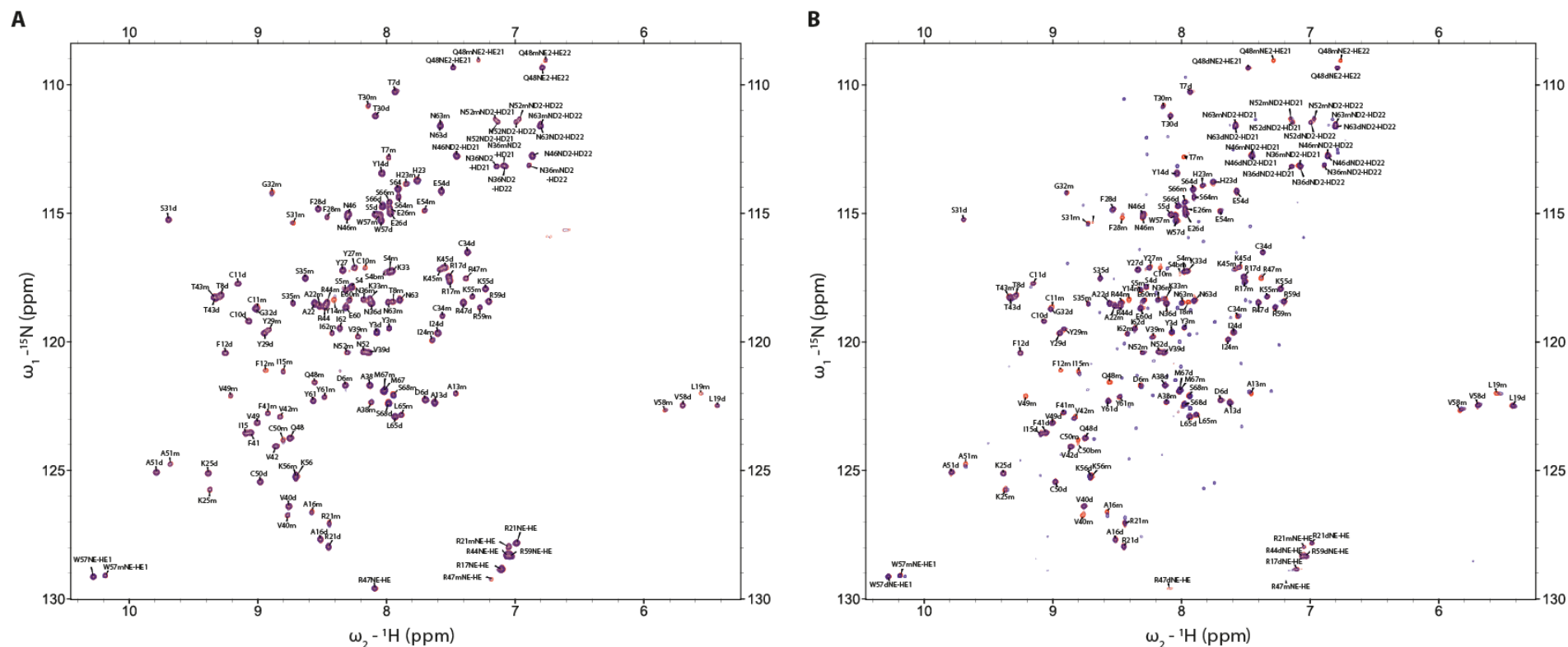
Fig. S3. CXCL4^{K50E}- and CCL17-induced changes in the HSQC spectrum of CCL5^{E66S}.
(**A** and **B**) ^{15}N-^{1}H heteronuclear single quantum coherence (HSQC) spectra (^{1}H frequency of 700 MHz) obtained by nuclear magnetic resonance (NMR) are shown for 30 μM ^{15}N-labeled CCL5^{E66S} in the presence of 600 μM CXCL4^{K50E} (**A**) and 20 μM ^{15}N-labeled CCL5^{E66S} in the presence of 650 μM CCL17 (**B**). In both spectra, free CCL5^{E66S} cross-peaks are in red, and CCL5^{E66S} cross-peaks in presence of CXCL4^{K50E} or CCL17 are in blue. We denote CCL5^{E66S} dimers with "d" and CCL5^{E66S} monomers with the prefix "m", Arginine NE sidechain peaks are folded in the ^{15}N dimension. Solution conditions were 25 mM Na-acetate-d^{3} buffer (95% H$_2$O; 5% D$_2$O), pH 4.5, 37°C. Expanded regions taken from these two HSQC spectral overlays are displayed in Fig. 2A and B.
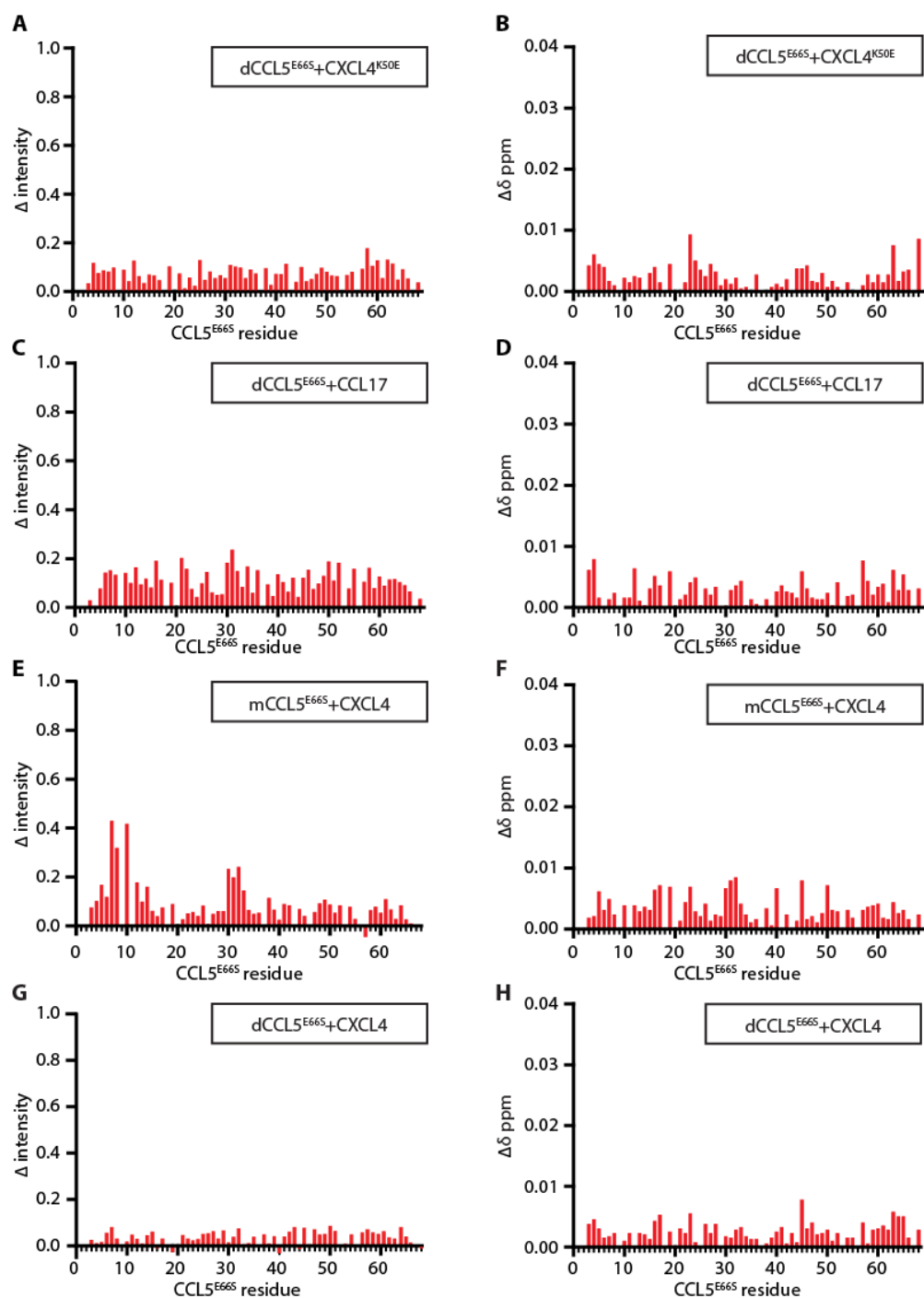
Fig. S4. Chemical shift and resonance intensity changes of CCL5[E66S] residues.
Chemical shift (δΔ) and resonance intensity (ΔIntensity) changes for ^{15}N-labeled CCL5[E66S] (30 μM) in the presence of CXCL4[K50E] or CXCL4 (600 μM) or for ^{15}N-labeled CCL5[E66S] (20 μM) in the presence of CCL17 (650 μM) were quantified and plotted vs the CCL5 amino acid sequence. We denote CCL5[E66S] dimers with "d" and CCL5[E66S] monomers with the prefix "m". (**A**) ΔIntensity values for dCCL5[E66S] plus CXCL4[K50E]; (**B**) δΔ values for dCCL5[E66S] plus CXCL4[K50E]; (**C**) ΔIntensity values for dCCL5[E66S] plus CCL17; (**D**) δΔ values for dCCL5[E66S] plus CCL17; (**E**) ΔIntensity values for mCCL5[E66S] plus CXCL4; (**F**) δΔ values for mCCL5[E66S] plus CXCL4; (**G**) ΔIntensity values for dCCL5[E66S] plus CXCL4; (**H**) δΔ values for dCCL5[E66S] plus CXCL4. Solution conditions were 25 mM Na-acetate-d[3] buffer (95% H_2O; 5% D_2O), pH 4.5, 37°C.

A

B
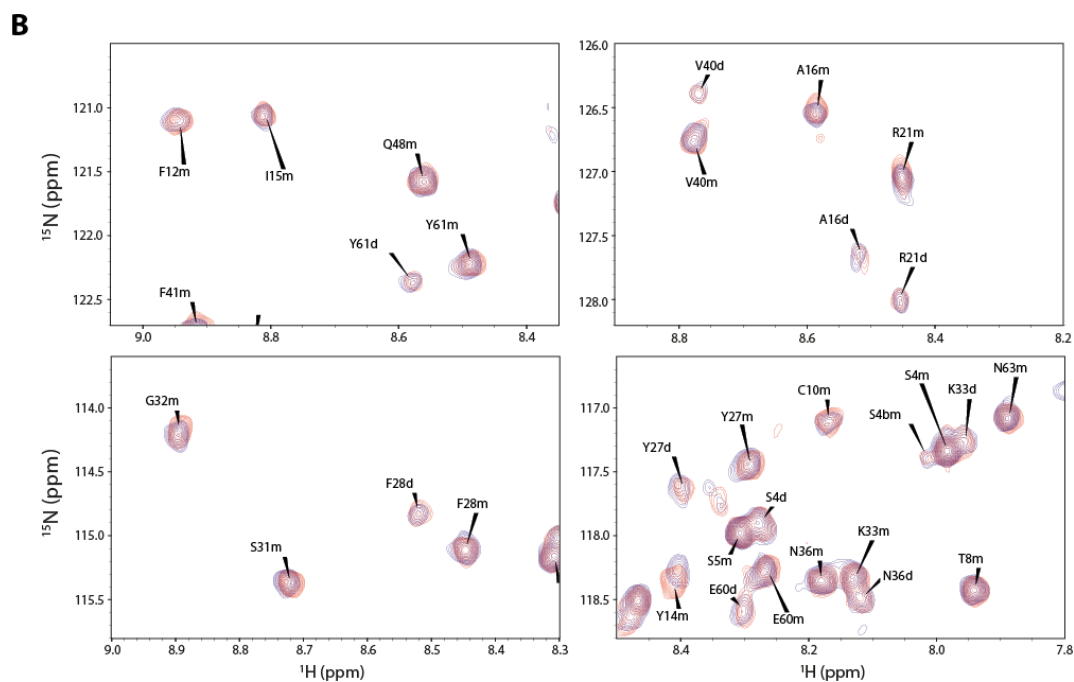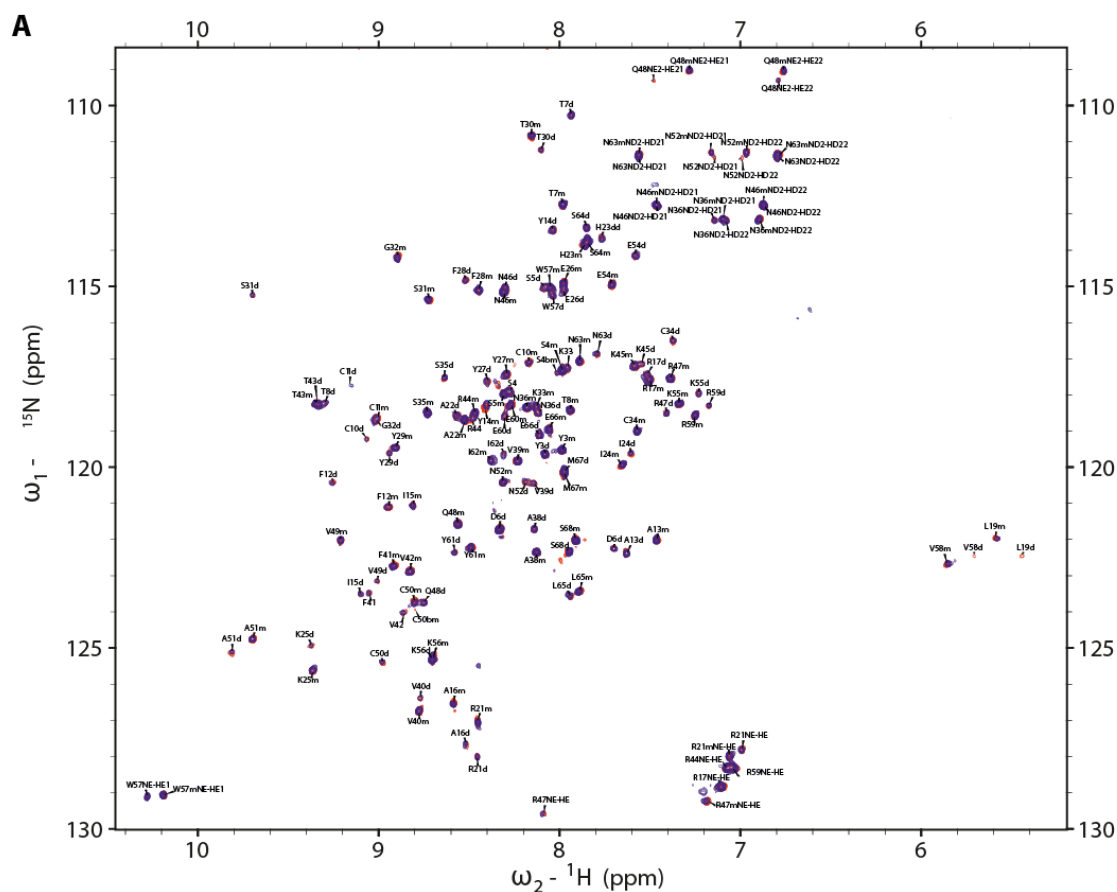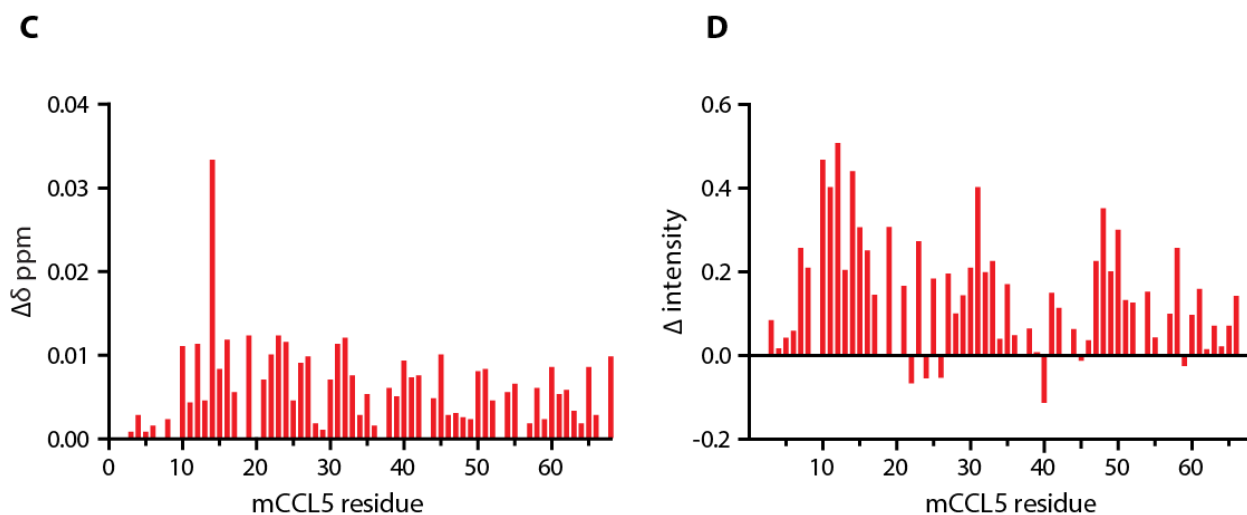
Fig. S5. CXCL4[K50E]-induced changes in the HSQC spectrum of CCL5.
[15]N-^{1}H heteronuclear single quantum coherence (HSQC) spectra were acquired with 128 scans per transient and sweep widths of 16 ppm in the 1H (2k points) dimension and 22 ppm in the 15N (200 points) dimension. Shown are full spectra (**A**) and expansions (**B**) of wildtype ^{15}N-CCL5 (5 µM) either alone (red) or in the presence of unlabeled 400 µM CXCL4[K50E] (blue). Values for δΔ (**C**) and ΔIntensity (**D**) (calculated as described in the legend to Fig. S4) are plotted versus the amino acid sequence of CCL5.
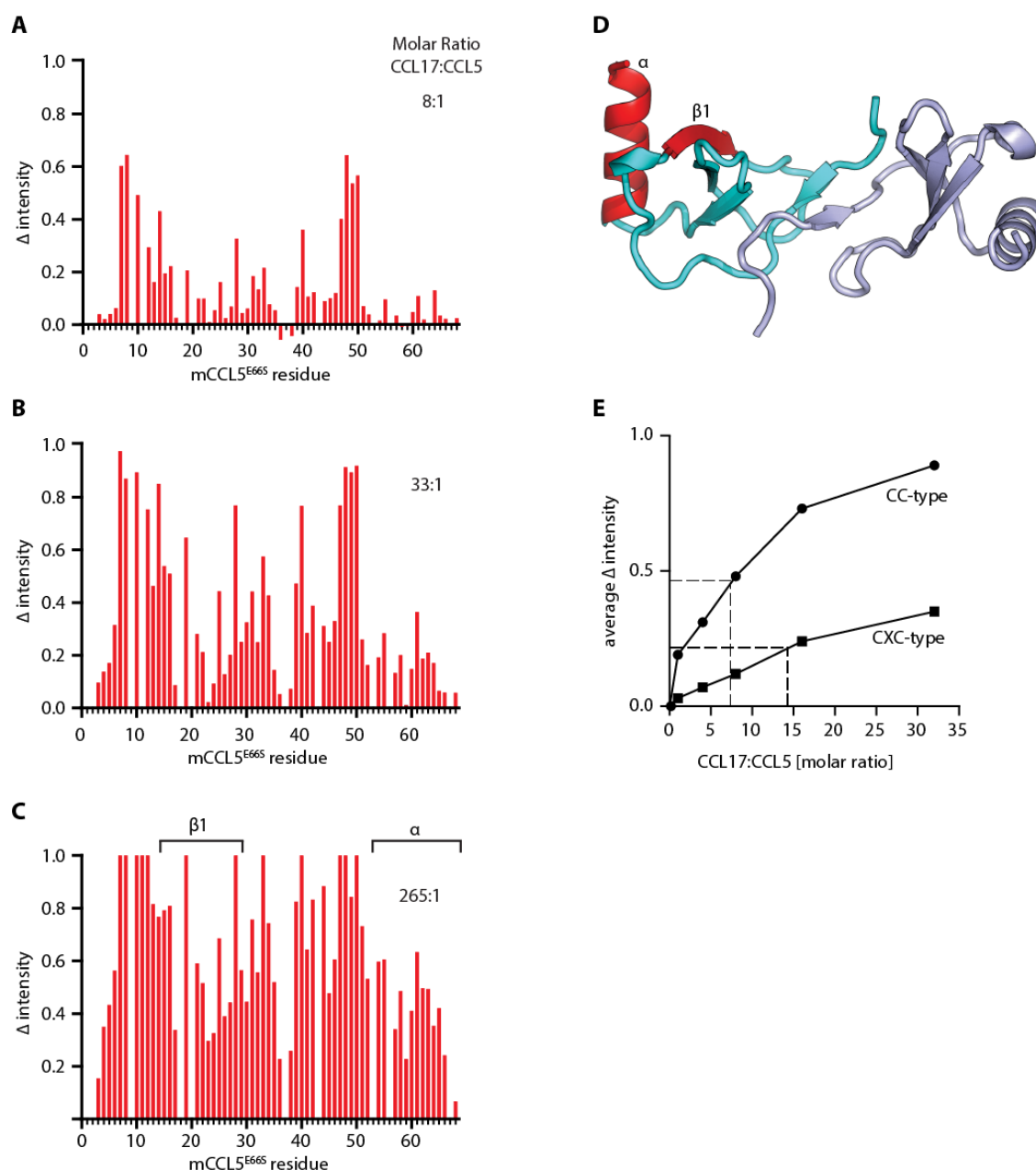
Fig. S6. Concentration-dependent formation of CC- versus CXC-type heterodimers.
Changes in resonance intensity (ΔIntensity) for ^{15}N-labeled CCL5[E66S] monomer resonances in the presence of increasing concentrations of CCL17 are plotted vs the amino acid sequence of CCL5. The final CCL17:CCL5[E66S] molar ratios were 8:1 (**A**), 33:1 (**B**) and 265:1 (**C**), as indicated. The total concentration of CCL5[E66S] was 20 μM at the two lowest ratios and 10 μM at the 265:1 ratio. ΔIntensity was calculated as in Fig. S4. Solution conditions were 25 mM Na-acetate-d[3] buffer (95% H_2O; 5% D_2O), pH 4.5, 37°C. (**D**) ΔIntensity values increasing the most by the highest CCL17 concentration are highlighted in red on the X-ray crystal structure of CCL5 (PDB code 1U4L). (**E**) ΔIntensity values averaged over residues at the CC-type (residues 3-16; 30-35, 46-50) or CXC-type (residues 24-30, 53-68) heterodimer interfaces are plotted *vs* the CCL17:CCL5[E66S] molar ratio.
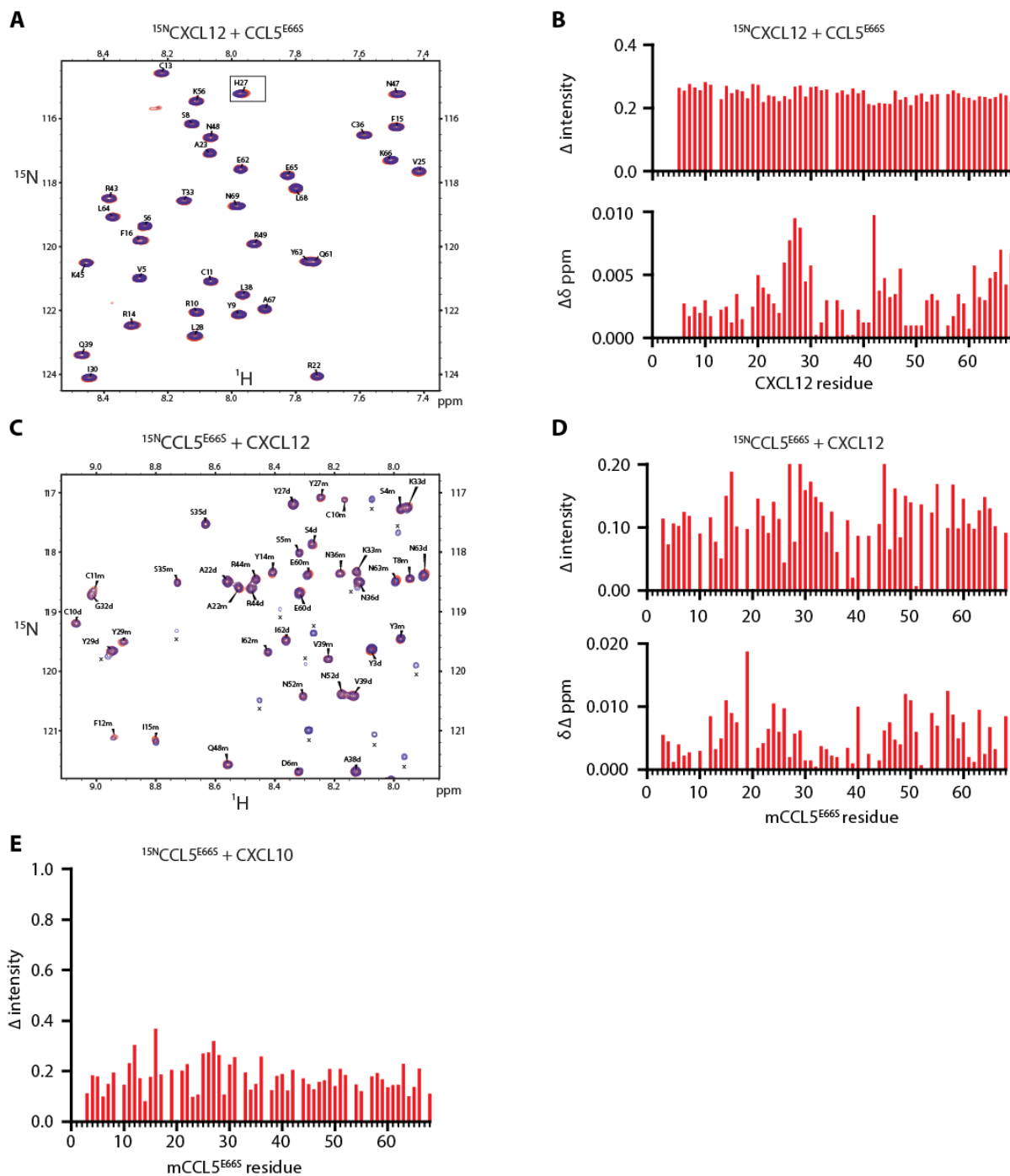
Fig. S7. CCL5-induced changes in HSQC spectra of CXCL12.

(**A**) ^{15}N-^{1}H heteronuclear single quantum coherence (HSQC) spectra (^{1}H frequency of 700 MHz) for ^{15}N-labeled CXCL12 (30 µM) in the absence (red contours) and presence (blue contours) of CCL5^{E66S} (315 µM) are overlaid. (**B**) From the HSQC spectra shown in **A**, δΔ and ΔIntensity values (calculated as in Fig. S4) are plotted vs the amino acid sequence of CXCL12. (**C**) ^{15}N-^{1}H HSQC spectra (^{1}H frequency of 700 MHz) for ^{15}N-labeled CCL5^{E66S} (20 µM) in the absence (red contours) and presence (blue contours) of CXCL12 (770 µM) are overlaid. (**D**) From the HSQC spectra shown in **C**, δΔ and ΔIntensity values (calculated as described in the legend to Fig. S4) are plotted versus the amino acid sequence of CCL5. (**E**) From ^{15}N-^{1}H HSQC spectra of ^{15}N-CCL5^{E66S} (20 µM) in the absence and presence of CXCL10 (1.0 mM), ΔIntensity values (calculated as in Fig. S4) are plotted vs the amino acid sequence of CCL5. Solution conditions were 25 mM Na-acetate-d^{3} buffer (95% H$_2$O; 5% D$_2$O), pH 4.5, 37°C.
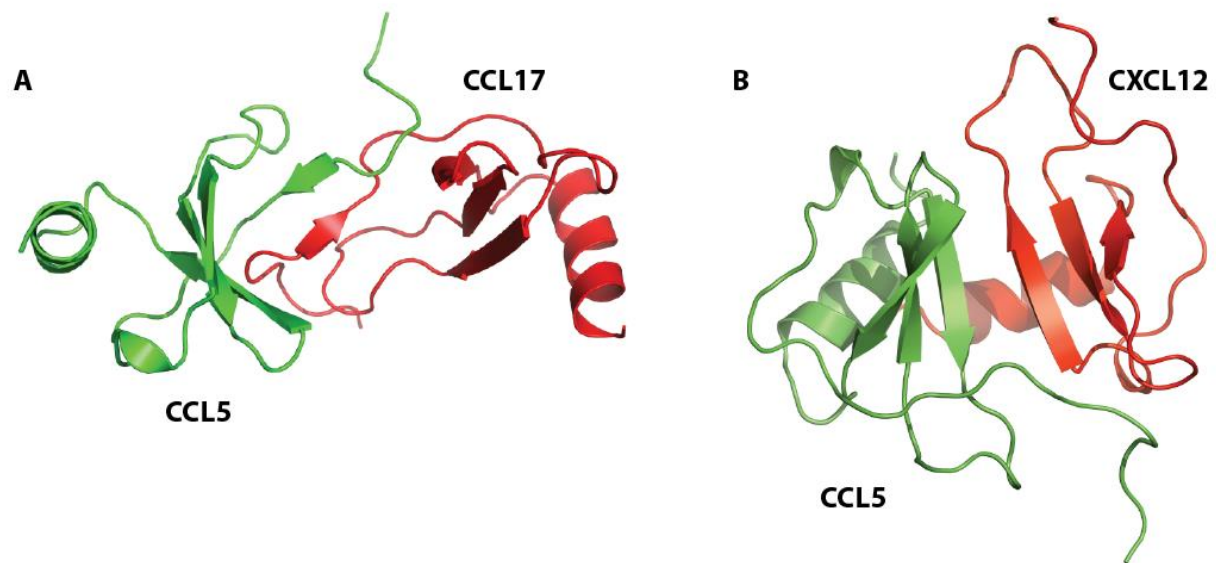
Fig. S8. Structural models of CC-type and CXC-type heterodimers.
Structures of CCL5-CCL17 (CC-type, **A**) and CCL5-CXCL12 (CXC-type, **B**) modelled following molecular dynamics simulation plus minimization (CCL5 in green, CCL17 and CXCL12 in red, respectively) are illustrated.
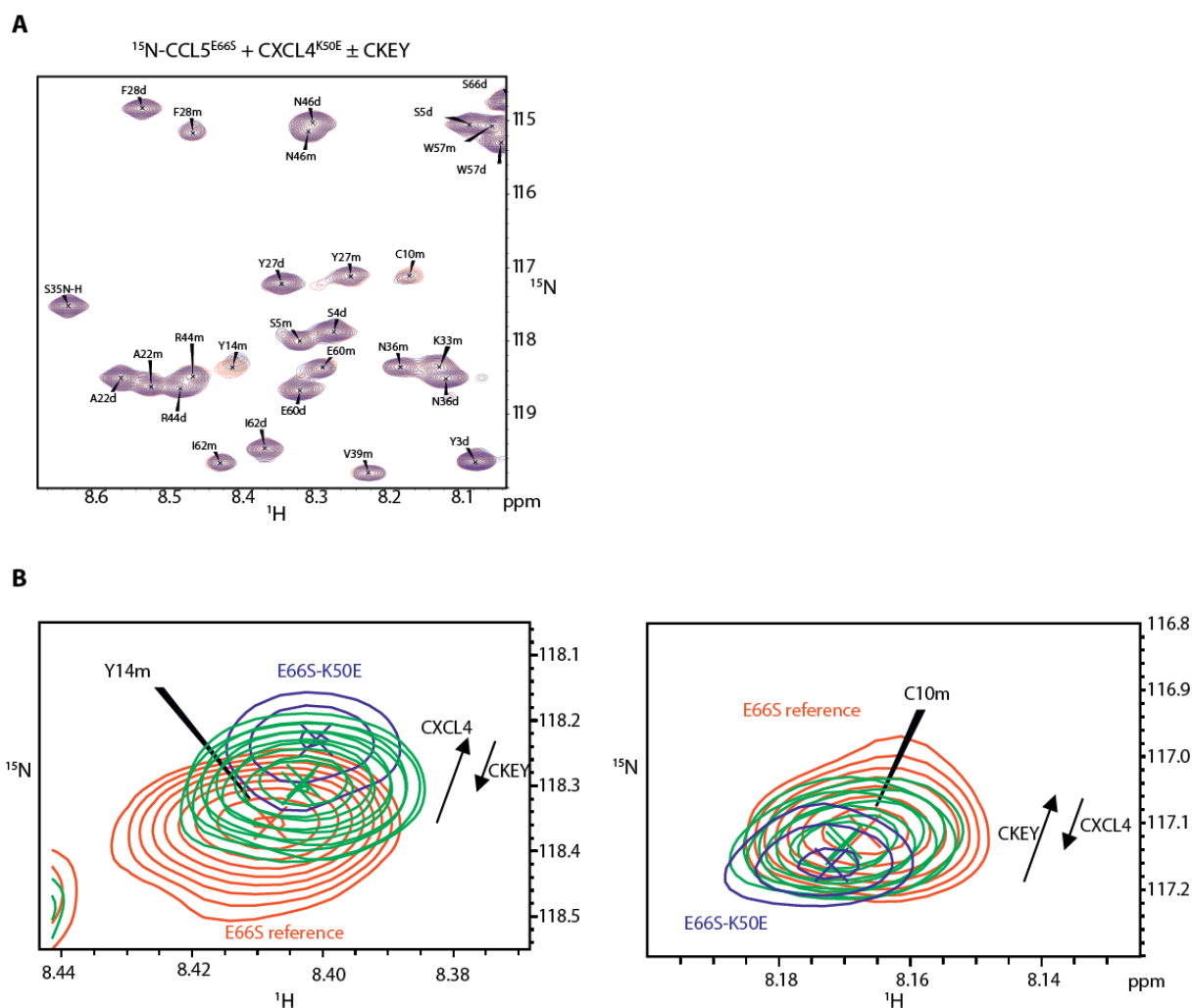
Fig. S9. Targeting of CCL5-CXCL4 heterodimer by CKEY.

^{15}N-^{1}H heteronuclear single quantum coherence (HSQC) spectra (**A**) and spectral expansions for mCCL5^{E66S} residues C10 and Y14 (**B**) at the heterodimer interface are shown to exemplify the inhibitory effect that increasing concentrations of CKEY peptide has on the formation of ^{15}N-CCL5^{E66S}-CXCL4^{K50E} heterodimers. Red contour lines show relatively sharp resonances of free CCL5^{E66S} monomer peaks, blue contours indicate the corresponding broadened peak caused by heterodimer formation with CXCL4^{K50E}, while green contours show reverse trends in linewidth and chemical shift on CCL5^{E66S} heterodimer peaks caused by the competitive binding of CKEY.
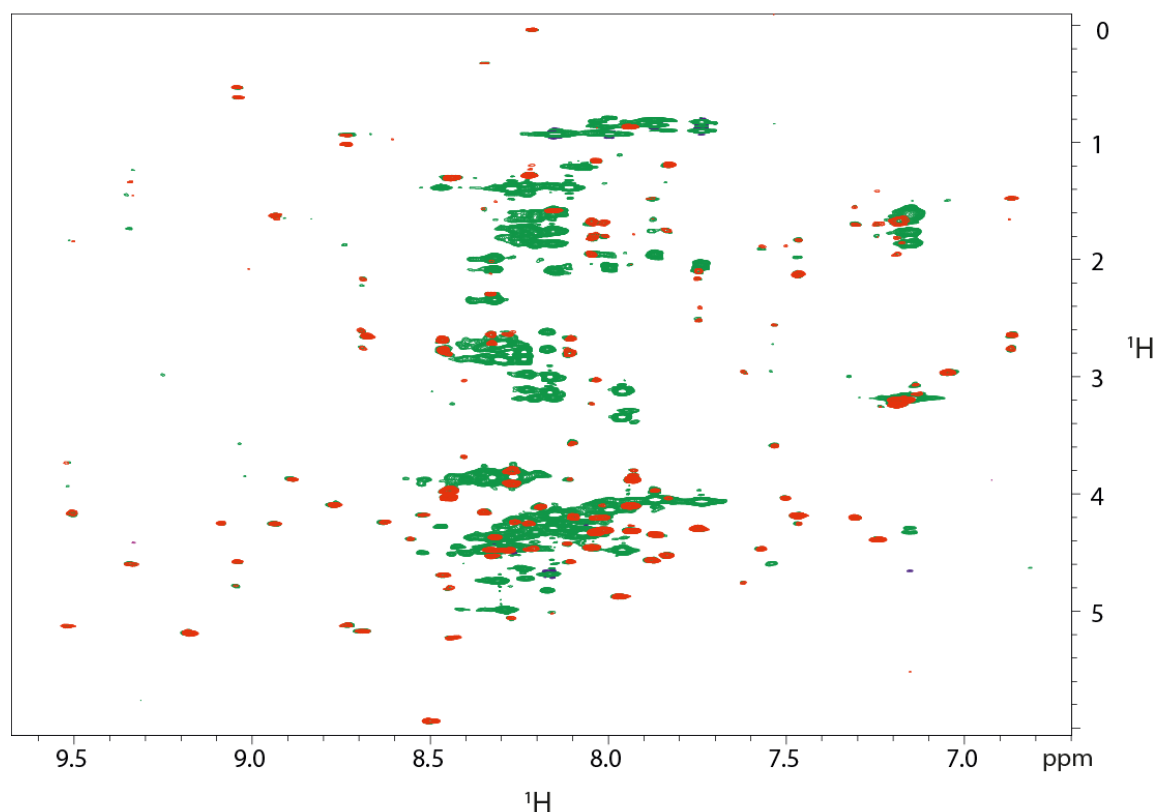
Fig. S10. Interaction of CAN with CCL17.
The amide region of DIPSI spectra of unlabeled CCL17 (20 µM) in the absence (red peaks) and presence of CAN peptide (200 µM, green peaks) recorded at 37°C and pH 4.5 are overlaid. Resonances arising from CCL17 are dispersed and defined, indicating a well-folded protein. On the other hand, resonances from the CAN peptide are generally broad and less disper-sed, most likely reflecting highly interconverting conformations and random coil states expected for a short linear peptide. Although many CCL17 and CAN resonances overlap, a number of CCL17 resonances are chemically shifted and broadened by the 10-fold molar excess of CAN.

A
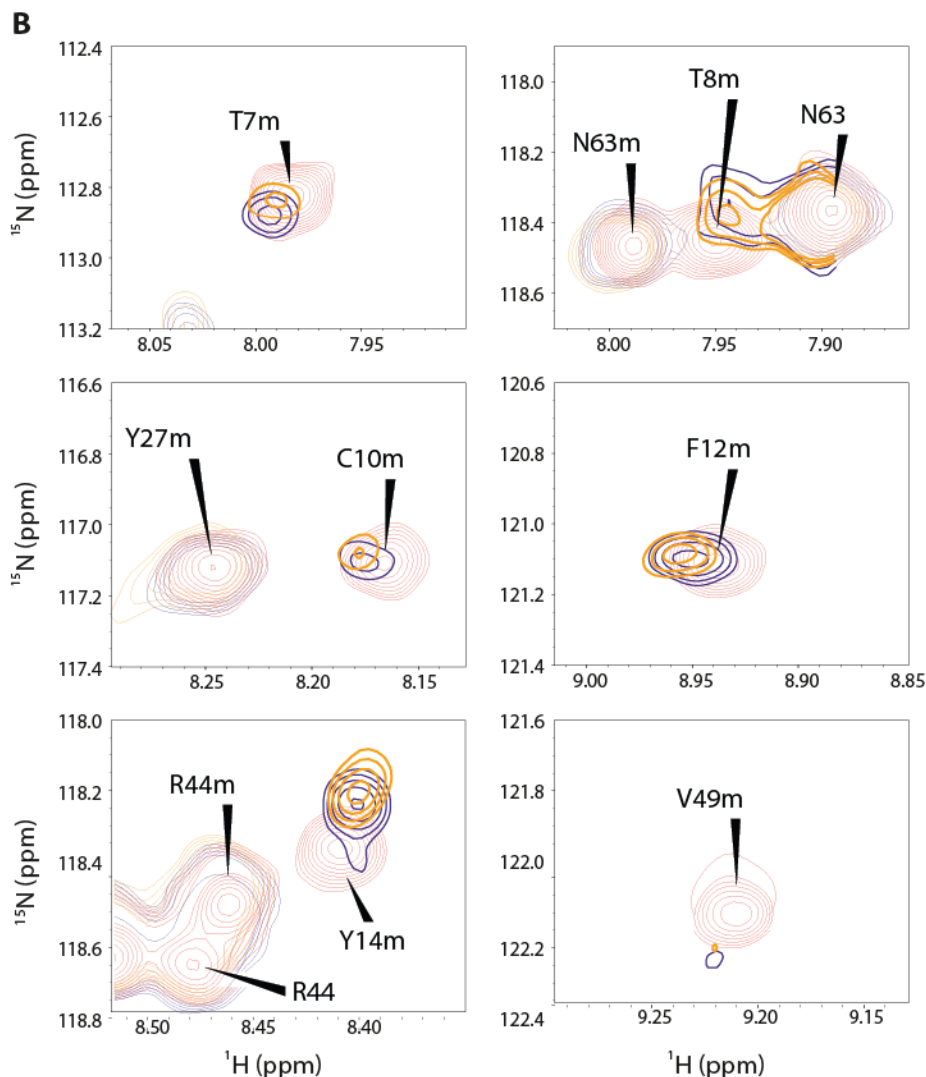
Fig. S11. Targeting of CCL5-CCL17 heterodimer by CAN.

(**A**) ^{15}N-^{1}H heteronuclear single quantum coherence (HSQC) spectra of ^{15}N-labeled CCL5^{E66S} (20 µM) in the absence (red peaks) and presence of CCL17 (320 µM, orange peaks) and upon addition of CAN peptide (640 µM, blue peaks) are overlaid. (**B**) ^{15}N-^{1}H HSQC spectral expansions for residues at the heterodimer interface are shown to exemplify inhibitory effects of CAN on the formation of ^{15}N-CCL5^{E66S}-CCL17 heterodimers. Residues T7 and T8 are centrally positioned at the CC-type dimer interface in CCL5^{E66S} homodimers and CCL17-CCL5^{E66S} heterodimers. Note that presence of CCL17 (orange peaks) substantially shifts T7 and T8 resonances, and addition of CAN (blue peaks) partially shifts those resonances back towards the CCL5^{E66S} monomer state, whereas resonances of C10, F12, Y14 and V49 do not show such a reversal.

Fig. S12. Efficient targeting of CCL5-CXCL12 heterodimer by [VREY]⁴.
(**A**) Chemical structure of 4 VREY molecules on a TASP scaffold resulting in [VREY]⁴. (**B**) Overlays of ^{15}N-^{1}H heteronuclear single quantum coherence (HSQC) spectral expansions of 10 µM monomeric ^{15}N-CXCL12 in the absence (red contours) and presence (blue contours) of 40 µM [VREY]⁴ peptide. (**C**) Using these HSQC data, δΔ values (calculated as in Fig. S4) are plotted versus the amino acid sequence of CXCL12. (**D**) Structural perturbation plot of CXCL12 (monomeric) induced by [VREY]⁴, as taken from the experimentally derived delta ppm values. (**E**) ^{15}N-^{1}H HSQC spectral expansions for five residues at the heterodimer interface are shown to exemplify the inhibitory effect that [VREY]⁴ has on the formation of ^{15}N-CXCL12-CCL5 heterodimers. Solution conditions were 25 mM potassium phosphate buffer (95% H_2O; 5% D_2O), pH 7.1, 25°C. Poor solubility of [VREY]⁴ at pH values lower than 7 prevents the study of heterodimer formation at standard pH 4.5 buffer conditions.

Fig. S13. Dose dependency of T cell chemotaxis elicited by single chemokines.
Membrane expression of chemokine receptors was detected by antibodies directly conjugated to a fluorophores and expressed as percentage of positively stained human T cells (**A**). (**B–G**) Chemotaxis assays were performed using IL-2- and CD3/C28-activated human T cells in 3 µm Transwell-filter plates. Chemokines were added to the bottom chamber at indicated concentrations: CCL5 (**B**), CCL17 (**C**), CXCL12 (**D**), CXCL4 (**E**), CXCL4L1 (**F**), CXCL10 (**G**). The chemotactic index was calculated as the ratio of chemokine-induced versus unstimulated migration, as determined by counting cells in the bottom chamber. Data represent mean±SEM of n=5-20 independent experiments.
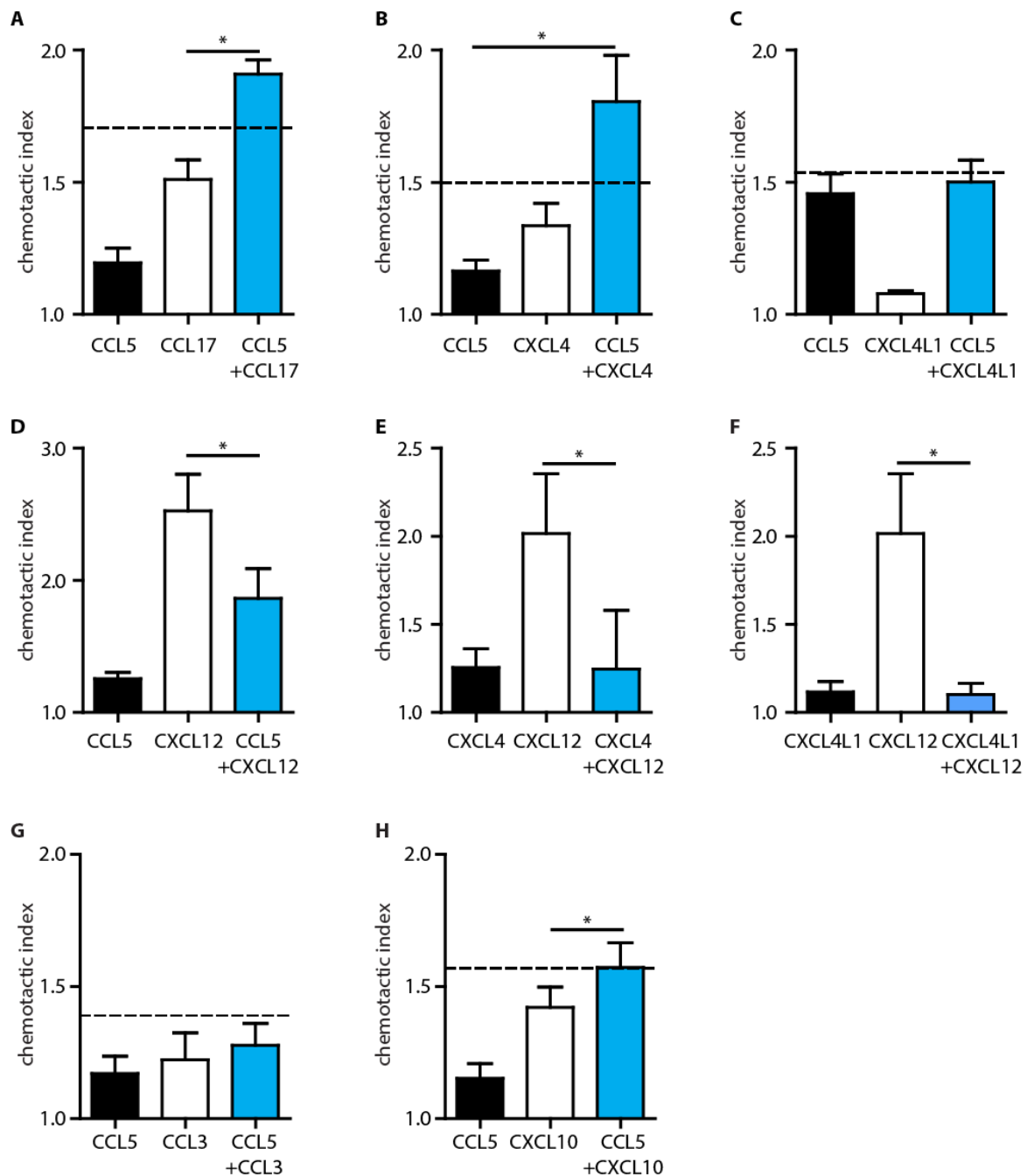
Fig. S14. Differential effects of chemokine combinations on T cell chemotaxis.
(**A-H**) Chemotaxis assays were performed using IL-2- and CD3/C28-activated human T cells in Transwell-filter plates. Combinations of CCL5 (1 nM) with CCL17 (0.1 nM) (**A,** n=14), of CXCL4 (n=5) or CXCL4L1 (n=6) with CCL5 (all at 4 nM) (**B,C**), of CXCL12 with CCL5 (n=14), CXCL4 (n=9), or CXCL4L1 (n=9) (all at 40 nM) (**D–F**) and of CCL5 (1 nM) with CCL3 (n=3) or CXCL10 (n=4) (both at 100 nM), (**G,H**) were added to the bottom chamber. The chemotactic index was calculated as the ratio of chemokine-induced versus unstimulated migration. Dashed lines indicate virtually calculated additive effects (**A-C, G,H**). Data represent mean±SEM from the indicated number of independent experiments. *p<0.05, as analyzed by Kruskal-Wallis-test.
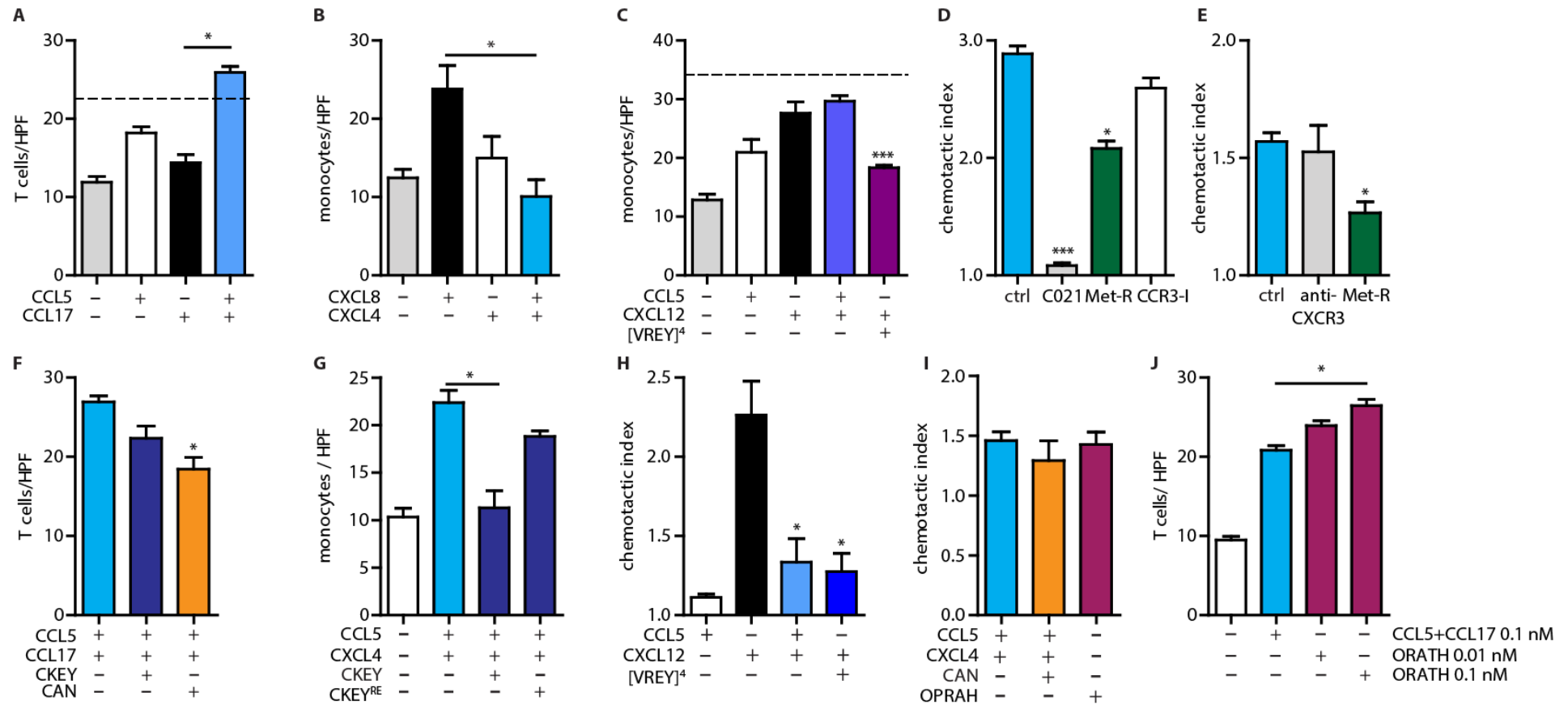
Fig. S15. Differential effects of chemokine heterodimerization on leukocyte recruitment.
(**A–I**) The firm arrest of IL-2- and CD3/C28-activated human T cells (**A, F, I, J**) or isolated monocytes (**B, C, G**) perfused over IL-1β-stimulated human aortic endothelial cells (HAoECs) at 1.5 dyne/cm^2 was analyzed by counting high-power fields (HPF) and chemotaxis assays were performed using IL-2- and CD3/C28-activated human T cells in Transwell-filter plates (**D, E**). For T-cell arrest, CCL5 (1 nM) and CCL17 (0.1 nM) were immobilized on HAoECs in combination with CAN or CKEY (both 10 nM) (**A**, n=5; **F**, n=3). For monocyte arrest, HAoECs were pre-incubated with CXCL8 and/or CXCL4 (**B**, n=4) and with CCL5 and/or CXCL12 (all at 40 nM) in combination with a 10-fold excess of [VREY]^4 (**C**, n=6). The effect of CCL5 (1 nM) plus CCL17 (0.1 nM) on T-cell chemotaxis was inhibited by blocking CCR4 (C021) or CCL5 receptors with Met-RANTES (Met-R) (**D**, n=5). The effect of CCL5 plus CXCL4 (both 4 nM) on T-cell chemotaxis was inhibited by blocking CCL5 receptors with Met-R (**E**, n=8). Isolated

human blood monocytes were perfused on IL-1β-activated HAoECs pre-incubated with CCL5 (4 nM) plus CXCL4 (40 nM) and CKEY or CKEY[RE] with the substitutions R44A and E26A (both 400 nM), and arrest was quantified (**G**, n=5). A combination of CXCL12 with or without CCL5 (both 40 nM) and a 10-fold excess of [VREY][4] were added to the bottom chamber to assess T-cell chemotaxis (**H**, n=5). Combinations of CCL5, CXCL4 (4 nM) plus CAN (40 nM) or obligate platelet factor 4-RANTES heterodimer (OPRAH, 4 nM) were added to the bottom chamber and T-cell chemotaxis was evaluated (**I**, n=3). Arrest of activated T cells on IL-1β -stimulated HAoECs pre-incubated with CCL5 (1 nM) plus CCL17 (0.1 nM) or with covalently bound CCL5-CCL17 heterodimer ORATH (Obligate RAntes Tarc Heterodimer) at indicated concentrations (**J**, n=3). Dashed lines indicate virtually calculated additive effects (**A, C**). Data represent mean±SEM from the indicated number of independent experiments. *p<0.05, **p<0.01, ***p<0.001, as analyzed by Kruskal-Wallis-test (**A–D, F–I**) or one-way ANOVA (**E, I**), or Mann-Whitney-test (**J**).
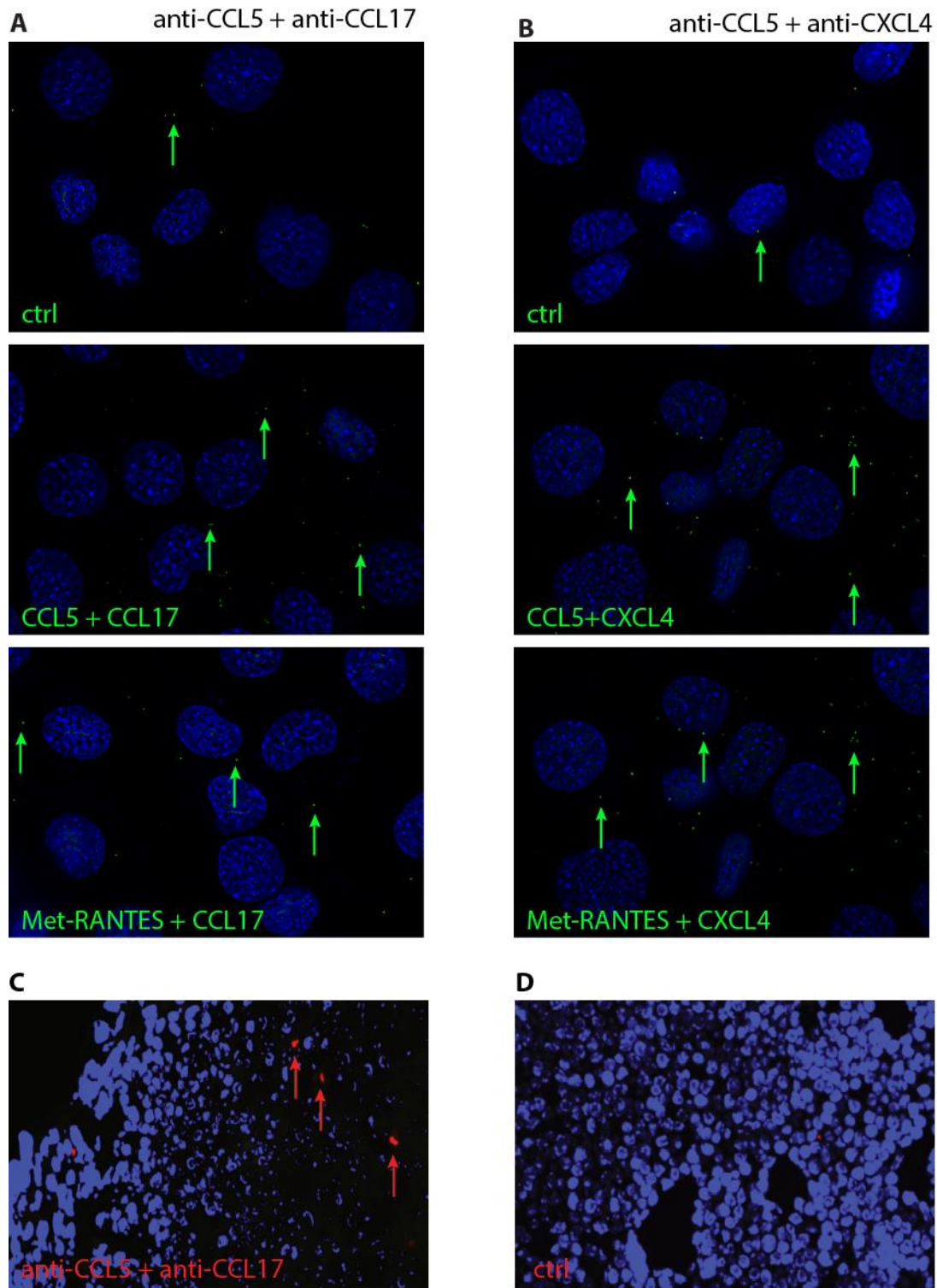
Fig. S16. Microscopy of chemokine interactions at the cell surface.
(**A–D**) Interactions of murine CCL5 with CCL17 or CXCL4 were analyzed using an antibody-based proximity-ligation assay. (**A, B**) Signals indicative of interaction (green, as indicated by arrows) were detected on the surface of mouse Simian-virus 40-transformed endothelial cells (SVECs) without (ctrl) or after incubation with CCL5 or Met-RANTES in combination with CCL17 (**A**) or CXCL4 (**B**) (6 nM each) by fluorescence microscopy. The endogenous presence of CCL5-CCL17 (red signals, as indicated by arrows) was detected by proximity ligation in frozen sections of murine para-aortic lymph nodes (**C**) but not in controls (ctrl) (**D**).
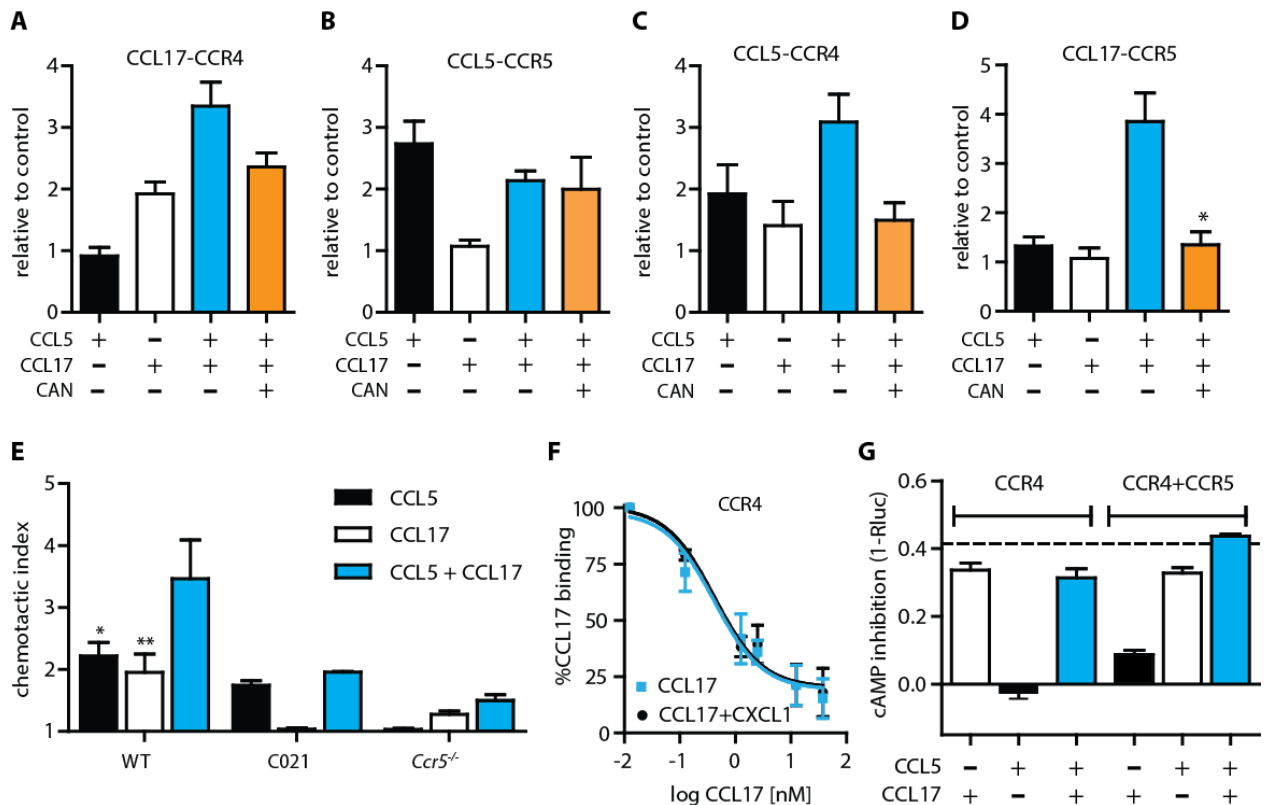
Fig. S17. Mechanisms for synergy of chemokine heterodimers.
(**A–D**) Interactions between CCL5, CCL17, CCR4, and CCR5 were detected on the surface of adherent dendritic cells (DCs) using a proximity-ligation assay after the cells were incubated with CCL5, CCL17, or both (all at 6 nM). The proximity ligation signals generated by the direct or indirect interactions between CCL17-CCR4 (**A,** n=3), CCL5-CCR5 (**B,** n=3), CCL5-CCR4 (**C,** n=3), and CCL17-CCR5 (**D,** n=4) were measured. (**E,** n=4) Migration of activated primary mouse T cells was elicited by CCL5, CCL17, or both (all at 6 nM) and compared between cells from wild-type (WT) or CCR5-deficient (*Ccr5$^{-/-}$*) mice, wild-type (WT) mice or cells pretreated with the CCR4-inhibitor C021. (**F**) Binding competition assay; CCL17-Alexa647 (2.5 nM) bound to CCR4-expressing HEK293 transfectants was displaced by unlabeled human CCL17 in presence or absence of CXCL1 (1 nM) (n=6). (**G**) G_i signaling was investigated by determining cAMP levels using Glosensor-HEK293 cells transfected with CCR4 or a mix of CCR4 and CCR5 after stimulation with CCL5 (12.5 nM), CCL17 (125 nM) or a combination of both (shown is one representative experiment at 20 min). Data represent mean±SEM from a number of independent experiments, as indicated. *$p<0.05$, **$p<0.01$, compared to CCL5 and CCL17 combined in the absence of CAN,as analyzed by Mann-Whitney-test (**A–D**) or two-way ANOVA (**E**).
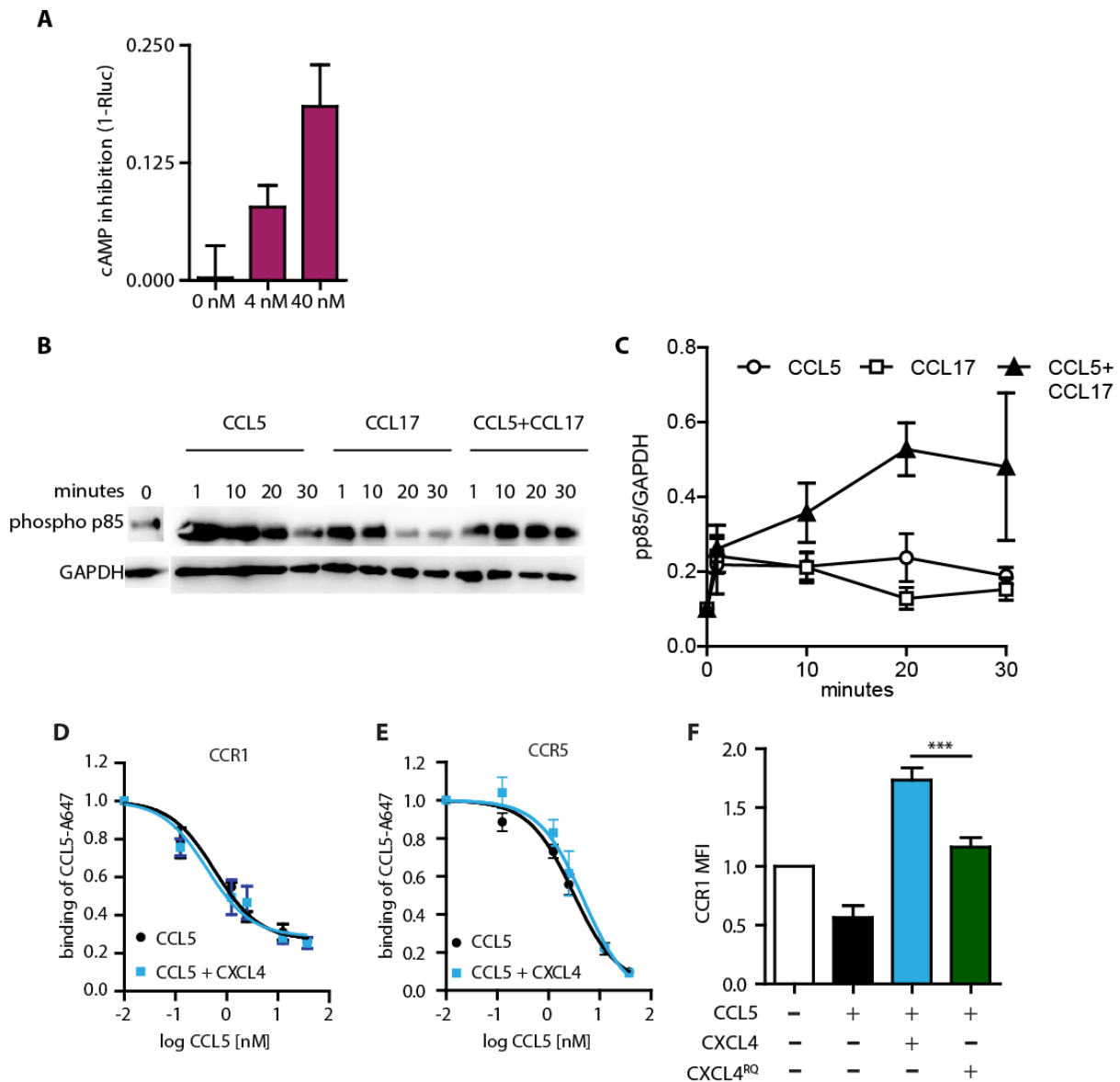
Fig. S18. Effect of heterodimers on signaling pathways, receptor affinity, and internalization.

(**A**) Glosensor HEK293 cells transfected with CCR1 were challenged by indicated concentrations of OPRAH and the reduction of cAMP was recorded after 20 min. (**B, C**) Human CD3/CD28-activated T cells of three donors were stimulated with CCL5 (1 nM) and/or CCL17 (0.1 nM) for the indicated time periods and subsequently lysed. Protein (30 µg) was separated by SDS-PAGE and the phosphorylation of tyrosine 458 in the regulatory subunit p85 of phosphoinositide-3-kinase was detected by specific antibodies relative to GAPDH control. Shown is a representative western blot (**B**) and ratios obtained by densitometry quantification (**C**). (**D, E**) For binding competition assays, CCL5-Alexa647 (2.5 nM) bound to CCR1-expressing (**D**) or CCR5-expressing (**E**) HEK293 transfectants was displaced by unlabeled CCL5 at indicated concentrations in presence or absence of CXCL4 (40 nM) (n=5 and n=3, respectively). (**F**) Carotid arteries were explanted, mounted and perfused with bone marrow-derived leukocytes upon stimulation with either buffer (controls), human CCL5 alone (4 nM), in the presence of human CXCL4 or CXCL4$^{R>Q}$ (both 40 nM). Intensity of CCR1 on adherent cells was quantified with two-photon laser scanning microscopy. Mean fluorescence intensities were standardized to control, Data represent mean±SEM, n>67 cells from two carotid arteries. ***p<0.001, calculated by ANOVA.
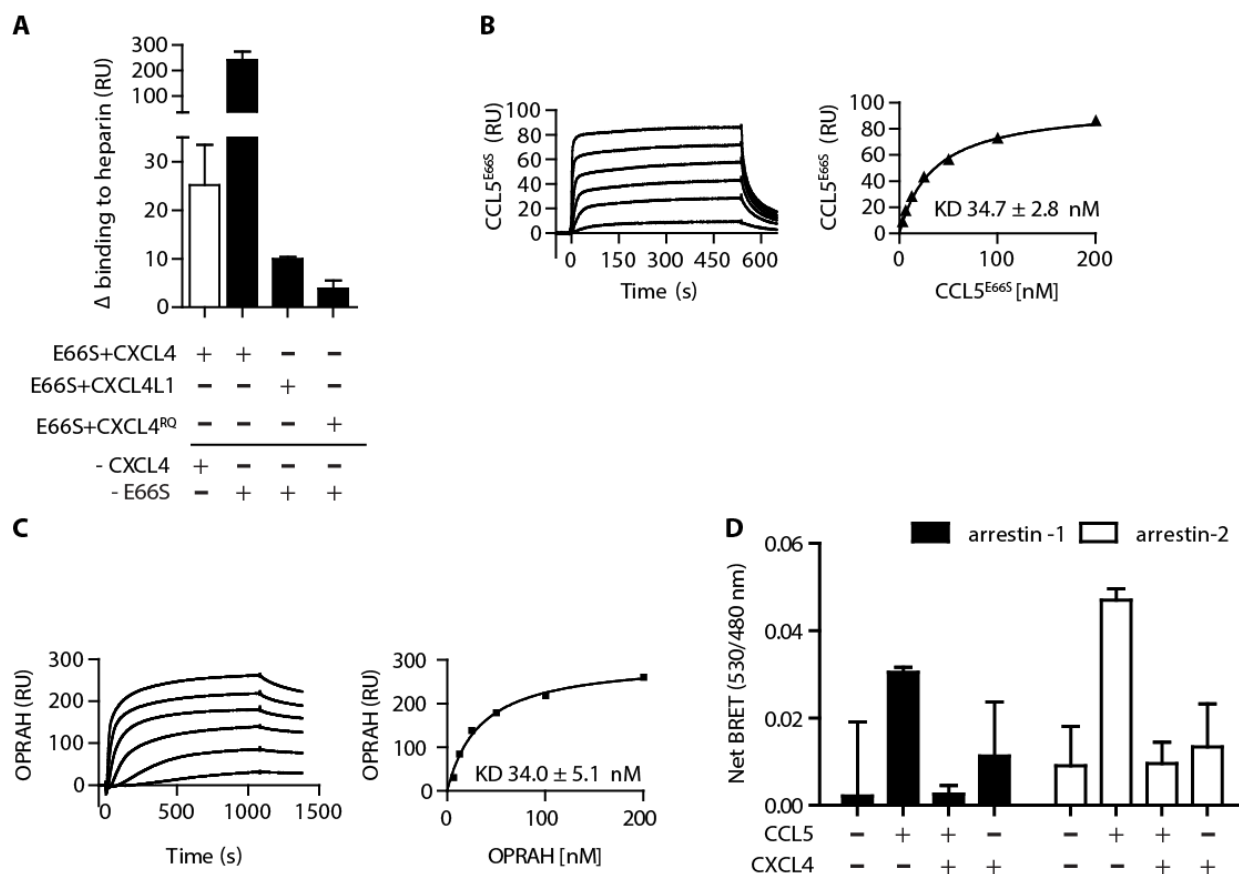
Fig. S19. CCL5-CXCL4 heterodimers bind to heparin and prevent arrestin recruitment.
(**A–C**) The binding of soluble CCL5 with CXCL4 or OPRAH to immobilized enoxaparin, a low molecular weight heparin, was analyzed by SPR. To prevent higher order aggregation and complex binding behavior CCL5^{E66S} was used instead of CCL5. (**A**) The response of CCL5^{E66S} at 50 nM, combined with CXCL4, CXCL4L1 or CXCL4$^{R>Q}$ (all at 100 nM), was assessed at the end of the association (1000 s) and the binding of CXCL4 (white bar) or CCL5^{E66S} (black bars) alone was subtracted, respectively (n=2). (**B**) CCL5^{E66S} or OPRAH (**C**) were perfused over the heparin-conjugated chip at increasing concentrations (at 6.2, 12.5, 25, 50, 100, 200 nM), and association and dissociation were recorded (left panels). Apparent affinities were derived from steady-state analysis (right panel). (**D**) The association of arrestin-1 or arrestin-2 with CCR5 after chemokine stimulation was determined by bioluminescence-initiated resonance energy transfer (BRET) using HEK293 transfectants expressing stably the reporter construct eYFP-fused arrestin-1 or arrestin-2 and transiently transfected with the donor construct CCR5-RlucII or mock. The BRET signal (acceptor/donor ratio 530/480 nm, 1 s acquisition) was recorded by a BRET reader (Tecan Infinity) after addition of the substrate coelenterazine and stimulation with CCL5 (10 nM) and/or CXCL4 (30 nM) for 20 min. Net BRET was calculated by subtracting the BRET signals from mock-transfected cells.
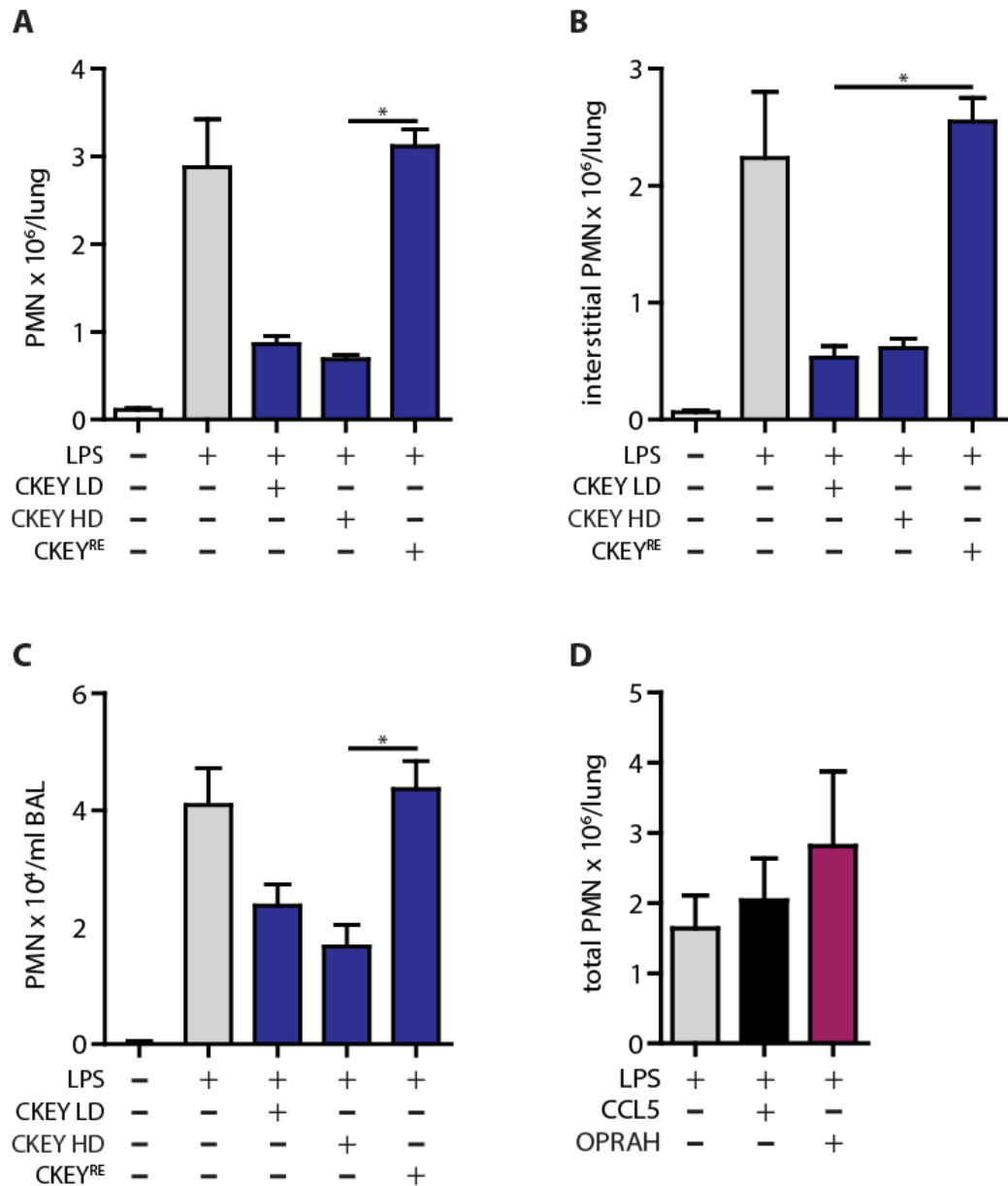
Fig. S20. Relevance of chemokine heterodimer formation in acute lung injury.
(**A–D**) Acute lung injury was induced by LPS inhalation of 10 week old female C57/BL6 mice and 30 minutes before sacrifice a FITC conjugated Ly6G antibody was injected i.v., to discriminate intravascular from interstitial neutrophils. (**A–C,** n=4-10, ctrl=10) CKEY was injected i.v. at low dose (1 mg/kg, LD) or high dose (10 mg/kg, HD), as well as the variant CKEY^{RE} with the substitutions R44A and E26A. Neutrophils were counted by FACS from total lungs (**A**), the interstitial space (**B**) or bronchoalveolar lavage (BAL) fluid (**C**). (**D**) Lethally irradiated female C57/BL6 mice were transplanted at 10 weeks of age with bone marrow from *Ccl5$^{-/-}$Cxcl4$^{-/-}$* mice. Acute lung injury was induced by LPS inhalation and CCL5 (150 µg/kg) or the obligate PF4-RANTES heterodimer (OPRAH, 300 µg/kg) were injected i.v. (n= 3-4). Neutrophils from total lungs were counted. Data represent mean±SEM from the indicated number of mice. *p<0.05, as analyzed by Kruskal-Wallis-test.
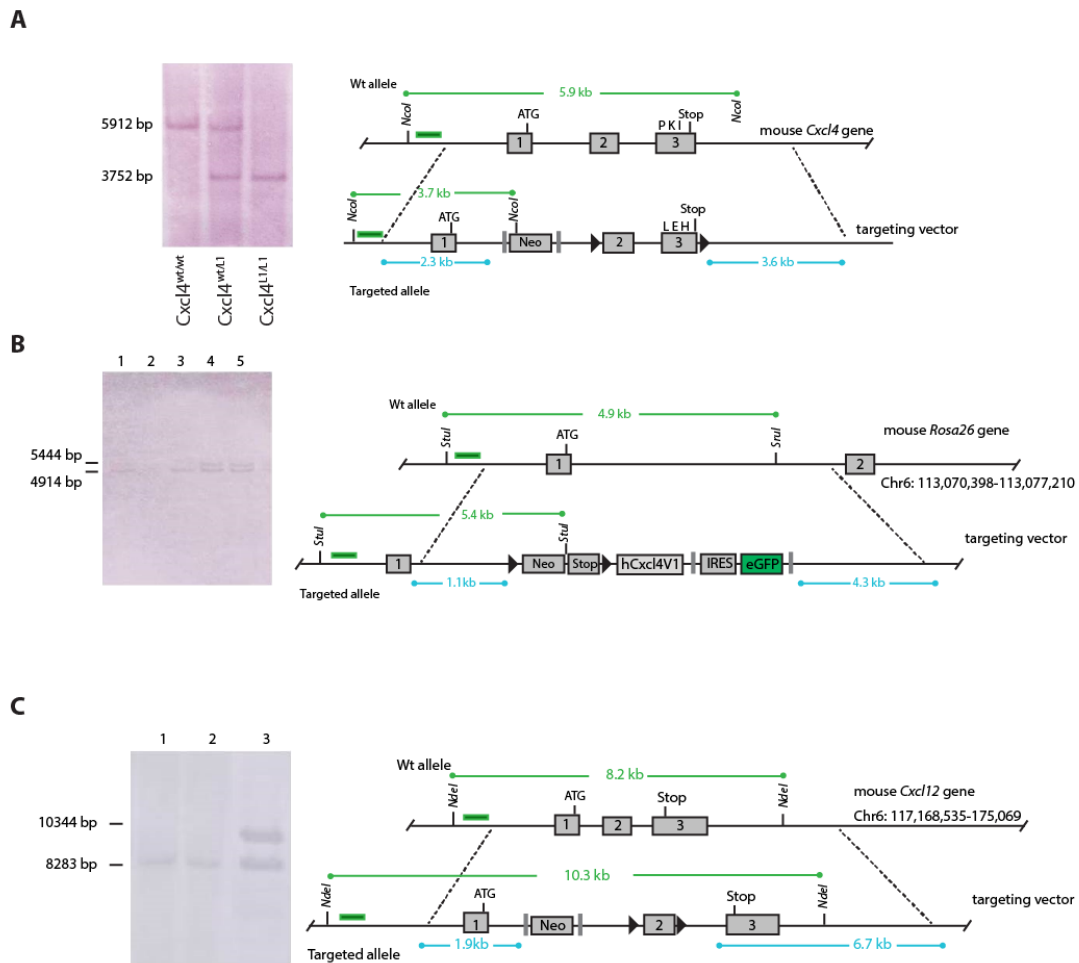
Fig. S21. Generation of mice deficient in *Cxcl4* or *Cxcl12* or carrying *Cxcl4* variants.
(**A–C**) Targeting strategy to generate *Cxcl4l1* knock-in, *Cxcl4* knock-out and *Cxcl12* knock-out mice. The exon-intron structures of the gene loci and the targeting vector (right) and correct targeting as evidenced by southern blotting (left) are shown. Green bars indicate the position of the probe, grey bars indicate flippase recognition target (frt) sites, black triangles indicate loxP sites. (**A**) *Cxcl4$^{L1/L1}$* mice were generated by homologous recombination with a targeting vector of mutated murine *Cxcl4 (Pf4)*, which included a 2.3 kb 5′ homology arm harboring exon 1, intron 1-2 and a frt-flanked neomycin selection cassette (Neo). The 3′ recombination arm spanned 3.6 kb, loxP sites flanked exons 2-3 (the coding part of *Cxcl4* gene) substituting proline P64 by leucine (L), lysine K72 by glutamate (E) and isoleucine I73 by histidine (H) to obtain the murine orthologue of human CXCL4L1. *Cxcl4$^{-/-}$* mice resulted from off-springs of *CreERT2-Cxcl4$^{L1/L1}$* parents after ubiquitous deletion of *Cxcl4* by tamoxifen. Southern blots demonstrated wild-type *Cxcl4$^{wt/wt}$* and correct targeting of heterozygous *Cxcl4$^{wt/L1}$* and homozygous *Cxcl4$^{wt/L1}$*. (**B**) Transgenic *Cxcl4^{tg-L1}* mice were generated by inserting the human *CXCL4L1* gene into the Rosa26 locus. The targeting vector contained a 1.1 kb 5′ arm harboring intron 1-2, a Neo selection and Stop cassette flanked by loxP sites, IRES and eGFP were flanked by frt sites. The 3′ recombination arm spanned 4.3 kb containing intron 1-2. Southern blots demonstrated correctly targeted ES clones (4 and 5). (**C**) Shown is the mouse *Cxcl12* locus and the targeting vector consisting of a 1.9 kb 5′ homology arm including exon 1 and intron 1-2, frt-flanked Neo, loxP-flanked exon 2 and the 3′ recombination arm spanning 6.7 kb. Southern blots show wild-type (1, 2) and correctly targeted heterozygous (3) ES clones. *Cxcl12$^{-/-}$* mice were generated by conditional inactivation of *Cxcl12* by intercrossing *CreERT2* and injecting tamoxifen i.p.
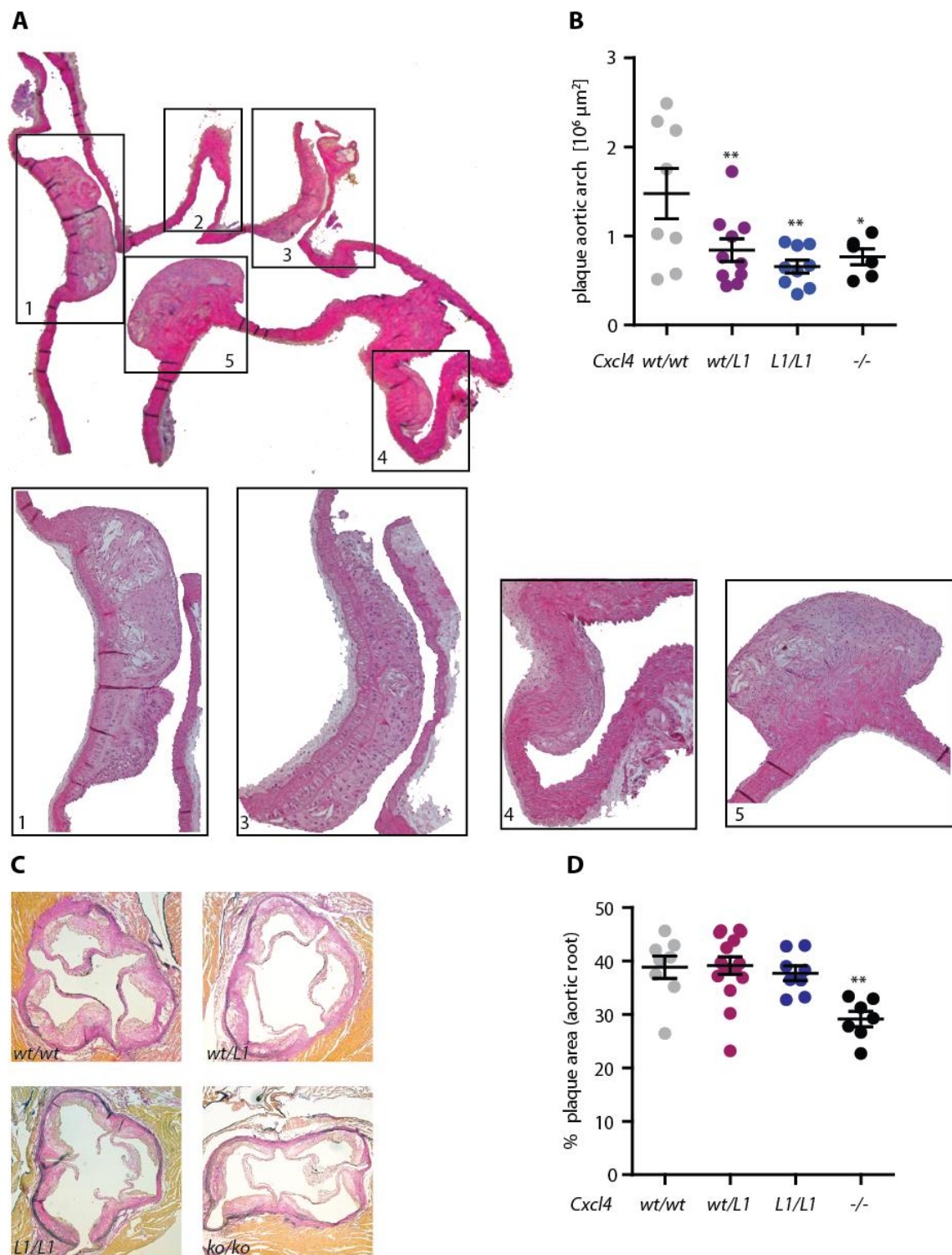
Fig. S22. Analysis of atherosclerotic lesion in mice expressing Cxcl4 or its variant.
(**A**) Overview and zoom-in insets of a longitudinal section through the aortic arch presenting typical sites of plaque development (1: brachiocephalic trunk; 2: left common carotid artery; 3: left subclavian artery; 4: arch; 5: lesser curvature). (**B-D**) $Apoe^{-/-}$ mice homozygous for wild-type Cxcl4 (wt/wt), heterozygous for *Cxcl4* and *Cxcl4l1* (wt/L1), homozygous for *Cxcl4l1* (L1/L1), or deficient for *Cxcl4* and *Cxcl4l1* (-/-) were fed a HFD for 12 weeks. (**C**) Shown are representative aortic root cross-sections after Elastica-van Gieson (EVG) staining. (**D**) Quantification of (**C**). Data represent mean±SEM from the indicated number of mice. *p<0.05, **p<0.01 versus *wt/wt*, as analyzed by one-way ANOVA (**B,D**).
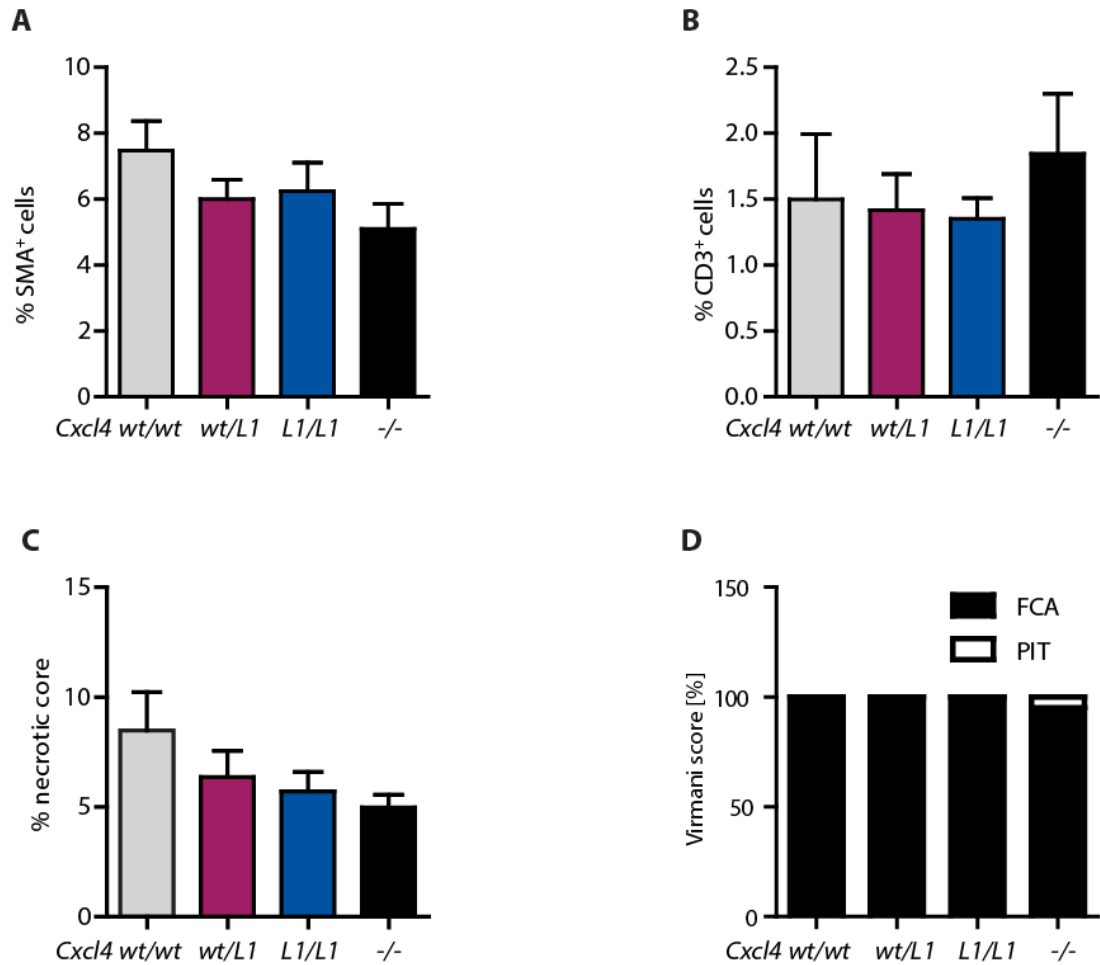
Fig. S23. Composition of aortic root lesions in mice expressing Cxcl4 or its variant.
Apoe^{-/-} mice homozygous for wild-type *Cxcl4* (*wt/wt*), heterozygous for *Cxcl4* and *Cxcl4l1* (*wt/L1*), homozygous for *Cxcl4l1* (*L1/L1*), or deficient for *Cxcl4* and *Cxcl4l1* (*-/-*) were fed a HFD for 12 weeks. Cross-sections of paraffin-embedded roots were analyzed for the content (percentage) of smooth muscle cells by staining smooth muscle-actin (SMA) (**A**), of T cells by staining CD3 (**B**), for necrotic core (**C**) or for staging the plaque phenotype according to the Virmani classification into advanced i.e. fibrous cap atheroma (FCA) or early lesions i.e. pathological intimal thickening (PIT) (**D**). Data represent mean±SEM from the indicated number of mice, as analyzed by Kruksal-Wallis-test (**A–C,** n=6-11).
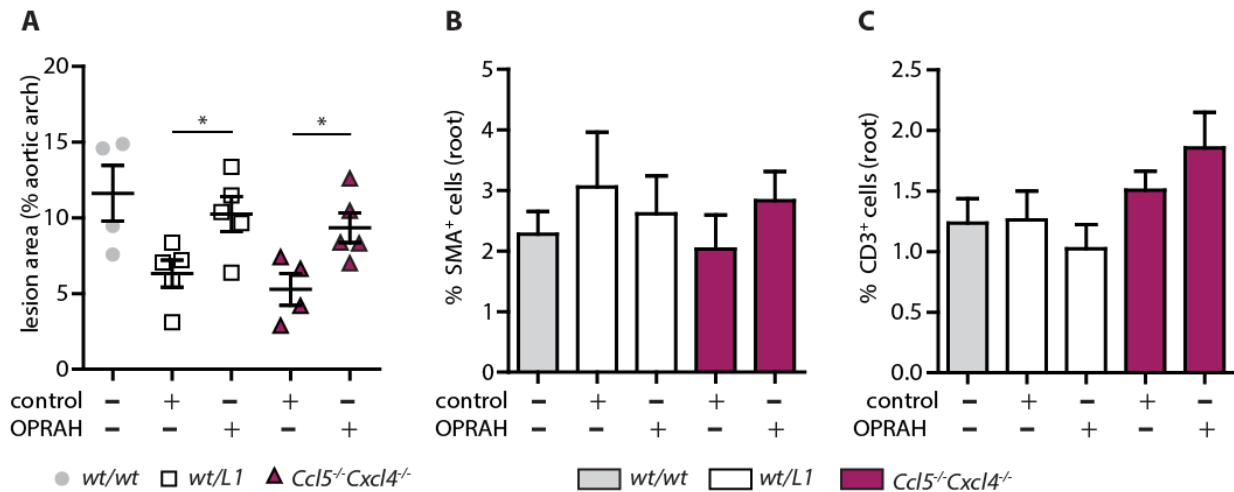
Fig. S24. Obligate chemokine heterodimers mimic natural heterodimers.

Apoe^{-/-} mice, homozygous for wild-type *Cxcl4* (wt/wt), heterozygous for *Cxcl4* and *Cxcl4l1* (*wt/L1*), or deficient for *Cxcl4* and *Ccl5* (*Ccl5*^{-/-}*Cxcl4*^{-/-}) were fed a HFD for 6 weeks. Atherogenesis was exacerbated by injecting i.p. the obligate RANTES-PF4 heterodimer (OPRAH) or saline (control) 3 times a week for 6 weeks (**A, B**, n=5-6 mice). Shown are the lesion size of the aortic arch (**A**), content of SMA+ smooth muscle cells (**B**) and CD3+ T cells (**C**) in aortic root plaques. Data represent mean±SEM. *p<0.05, as analyzed by the Mann-Whitney-test).
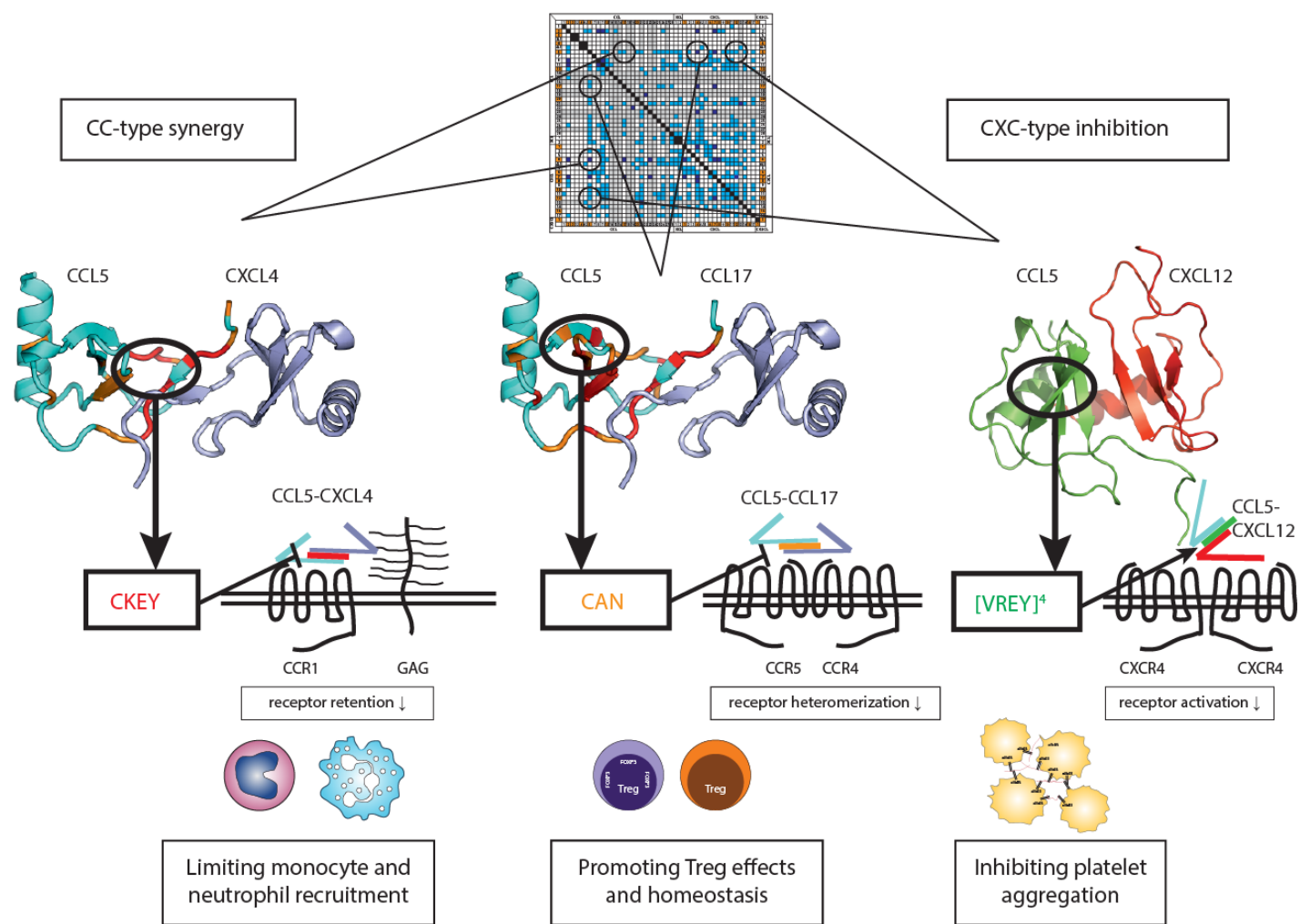
Fig. S25. Summary scheme.
Based on the map derived for the chemokine interactome, paradigmatic chemokine heterodimers were selected. CCL5 interacts with CXCL4 and CCL17 in CC-type but favors a CXC-type interaction with CXCL12. CC-type interactions show synergistic effects, whereas CXC-type interactions are inhibitory. Disrupting heterodimers by specific peptides CKEY (CCL5-CXCL4) or CAN (CCL5-CCl17) blocks inflammatory monocyte/neutrophil recruitment or promotes Treg homeostasis by preventing CCR1 retention (via GAG binding) or CCR5-CCR4 heteromerization at the cell surface, respectively. In contrast, [VREY][4] interacts with CXCL12 to mimic inhibitory effects of CCL5 on CXCR4 activation, and inhibits platelet aggregation.

Supplementary Tables

Table S1. Densitometry analysis of bidirectional immunoligand blotting.

Chemokines immobilized on nitrocellulose membranes are arranged in rows, chemokines added in solution are arranged in columns. Following detection by specific antibodies, the density and area of positive reactions were determined by densitometry, and the ratio relative to the respective positive control is given. Reactions exceeding 5% of the value of the positive control were regarded as positive and are highlighted in green. Means were calculated from 2-4 independent immuno-ligand blots.

	CCL1	CCL2	CCL3	CCL3L1	CCL4	CCL5	CCL7	CCL8	CCL11	CCL13	CCL14	CCL15	CCL16	CCL17	CCL18	CCL19	CCL20	CCL21	CCL22	CCL23	CCL24	CCL25	CCL26	CCL27	CCL28	XCL1	XCL2	CXCL1	CXCL2	CXCL3	CXCL4	CXCL4L1	CXCL5	CXCL6	CXCL7	CXCL8	CXCL9	CXCL10	CXCL11	CXCL12	CXCL13	CXCL14	CXCL16	CXCL17	CX3CL1	
CCL1	x	0.000	0.000	0.000	0.000	0.013	0.000	0.022	0.000	0.000	0.000	0.000	0.000	0.000	0.000	0.000	0.000	0.000	0.000	0.000	0.000	0.000	0.000	0.000	0.015	0.000	0.000	0.001	0.046	0.000	0.000	0.000	0.211	0.000	0.000	0.000	0.000	0.000	0.000	0.000	0.000	0.000	0.000	0.000	0.000	CCL1
CCL2	0.033	x	0.000	0.000	0.000	0.053	0.017	0.056	0.114	0.000	0.000	0.000	0.000	0.000	0.000	0.000	0.000	0.000	0.000	0.000	0.000	0.000	0.015	0.000	0.000	0.000	0.220	0.000	0.000	0.000	0.051	0.000	0.000	0.040	0.019	0.070	0.077	0.000	0.000	0.017	0.000	0.000	0.158	0.000	0.000	CCL2
CCL3	0.000	0.024	x	0.000	0.049	0.007	0.019	0.006	0.000	0.000	0.000	0.000	0.000	0.000	0.000	0.000	0.000	0.000	0.000	0.000	0.000	0.000	0.000	0.000	0.012	0.000	0.000	0.016	0.019	0.000	0.000	0.000	0.017	0.000	0.000	0.000	0.000	0.000	0.000	0.000	0.000	0.000	0.000	0.000	0.000	CCL3
CCL3L1	0.000	0.029	0.000	x	0.036	0.000	0.012	0.028	0.000	0.000	0.000	0.000	0.000	0.000	0.000	0.000	0.000	0.000	0.000	0.000	0.000	0.000	0.000	0.000	0.004	0.000	0.000	0.004	0.046	0.000	0.000	0.000	0.000	0.000	0.000	0.000	0.000	0.000	0.000	0.000	0.000	0.000	0.000	0.000	0.000	CCL3L1
CCL4	0.000	0.000	0.000	0.000	x	0.000	0.014	0.020	0.000	0.000	0.000	0.000	0.000	0.000	0.000	0.000	0.000	0.000	0.000	0.000	0.000	0.000	0.000	0.000	0.007	0.000	0.000	0.000	0.022	0.012	0.000	0.000	0.000	0.000	0.000	0.000	0.000	0.000	0.000	0.000	0.000	0.000	0.000	0.000	0.000	CCL4
CCL4L1	0.003	0.073	0.000	0.000	x	0.000	0.022	0.027	0.000	0.000	0.000	0.000	0.000	0.000	0.000	0.000	0.000	0.000	0.000	0.000	0.000	0.000	0.000	0.000	0.026	0.000	0.191	0.000	0.046	0.044	0.000	0.000	0.000	0.000	0.000	0.000	0.000	0.030	0.053	0.000	0.000	0.000	0.000	0.000	0.000	CCL4L1
CCL5	0.000	0.014	0.000	0.000	0.000	x	0.042	0.004	0.326	0.123	0.000	0.000	0.000	0.287	0.000	0.000	0.000	0.000	0.000	0.000	0.211	0.319	0.268	0.054	0.330	0.111	0.077	0.000	0.000	0.000	0.292	0.000	0.000	0.063	0.038	0.000	0.000	0.000	0.056	0.000	0.000	0.132	0.000	0.000	CCL5
CCL7	0.000	0.048	0.000	0.000	0.000	0.000	x	0.004	0.000	0.000	0.000	0.000	0.000	0.000	0.000	0.000	0.000	0.000	0.000	0.000	0.000	0.000	0.000	0.343	0.000	0.000	0.007	0.000	0.054	0.007	0.000	0.000	0.000	0.000	0.000	0.000	0.000	0.000	0.000	0.000	0.000	0.000	0.000	0.000	CCL7
CCL8	0.000	0.057	0.000	0.000	0.000	0.000	0.019	x	0.008	0.000	0.000	0.000	0.000	0.000	0.000	0.000	0.000	0.000	0.000	0.000	0.000	0.000	0.000	0.099	0.000	0.000	0.000	0.000	0.000	0.008	0.000	0.000	0.029	0.067	0.000	0.000	0.000	0.000	0.000	0.000	0.000	0.159	0.000	0.000	CCL8
CCL11	0.000	0.012	0.000	0.014	0.008	0.020	0.041	0.636	x	0.000	0.000	0.002	0.000	0.000	0.699	0.000	0.000	0.013	0.000	0.000	0.000	0.051	0.065	0.137	0.000	0.047	0.000	0.000	0.009	0.009	0.233	0.027	0.022	0.013	0.017	0.000	0.134	0.000	0.076	0.000	0.000	0.000	0.000	CCL11
CCL13	0.000	0.056	0.000	0.000	0.000	0.267	0.018	0.078	0.435	x	0.000	0.000	0.000	0.000	0.000	0.000	0.000	0.127	0.000	0.000	0.209	0.090	0.000	0.223	0.072	0.000	0.032	0.000	0.037	0.014	0.000	0.033	0.001	0.000	0.033	0.000	0.313	0.188	0.057	0.000	0.317	0.000	CCL13
CCL14	0.000	0.015	0.000	0.000	0.000	0.014	0.000	0.192	0.000	x	0.000	0.000	0.000	0.000	0.000	0.000	0.000	0.000	0.290	0.000	0.000	0.010	0.000	0.000	0.003	0.000	0.000	0.000	0.008	0.019	0.000	0.000	0.000	0.000	0.000	0.000	0.000	0.000	0.000	0.000	0.000	CCL14
CCL15	0.002	0.062	0.000	0.000	0.000	0.000	0.023	0.000	0.000	0.000	0.000	x	0.000	0.000	0.000	0.000	0.000	0.000	0.000	0.000	0.000	0.000	0.006	0.000	0.000	0.000	0.007	0.000	0.000	0.009	0.000	0.000	0.000	0.000	0.000	0.000	0.000	0.000	0.000	0.000	CCL15
CCL16	0.000	0.000	0.000	0.000	0.000	0.094	0.007	0.005	0.000	0.000	0.000	0.000	x	0.000	0.000	0.000	0.000	0.000	0.000	0.000	0.000	0.000	0.000	0.000	0.000	0.000	0.017	0.021	0.000	0.000	0.000	0.000	0.000	0.000	0.000	0.000	0.000	0.000	CCL16
CCL17	0.000	0.000	0.000	0.000	0.000	0.086	0.012	0.006	0.000	0.000	0.000	0.000	0.000	x	0.000	0.000	0.000	0.187	0.000	0.000	0.000	0.088	0.000	0.089	0.000	0.041	0.000	0.000	0.000	0.001	0.000	0.002	0.008	0.000	0.000	0.086	0.000	0.000	0.000	CCL17
CCL18	0.000	0.000	0.000	0.000	0.000	0.005	0.003	0.000	0.000	0.000	0.000	0.000	0.000	0.000	x	0.000	0.000	0.000	0.000	0.000	0.000	0.000	0.025	0.000	0.000	0.005	0.000	0.000	0.028	0.021	0.000	0.000	0.000	0.000	0.000	0.000	0.000	CCL18
CCL19	0.000	0.000	0.000	0.000	0.000	0.017	0.006	0.002	0.000	0.000	0.000	0.000	0.000	0.000	0.000	x	0.000	0.000	0.000	0.000	0.000	0.000	0.000	0.000	0.021	0.000	0.000	0.003	0.000	0.000	0.043	0.014	0.000	0.000	0.000	0.034	0.000	0.000	0.000	CCL19
CCL20	0.000	0.000	0.000	0.000	0.000	0.056	0.002	0.000	0.000	0.000	0.000	0.000	0.000	0.000	0.000	0.000	x	0.000	0.000	0.000	0.000	0.000	0.000	0.000	0.094	0.000	0.063	0.024	0.002	0.000	0.000	0.013	0.228	0.053	0.015	0.000	0.109	0.000	CCL20
CCL21	0.000	0.000	0.000	0.000	0.000	0.192	0.004	0.010	0.000	0.299	0.000	0.000	0.000	0.000	0.000	0.000	0.000	x	0.000	0.000	0.245	0.000	0.072	0.000	0.211	0.029	0.278	0.018	0.051	0.000	0.016	0.085	0.000	0.017	0.003	0.000	0.116	0.150	0.058	0.053	0.019	0.138	0.000	0.203	0.000	CCL21
CCL22	0.000	0.000	0.000	0.000	0.000	0.002	0.001	0.002	0.000	0.000	0.000	0.000	0.000	0.000	0.000	0.000	0.000	0.000	x	0.000	0.000	0.000	0.000	0.000	0.032	0.021	0.000	0.000	0.006	0.000	0.000	0.015	0.024	0.000	0.000	0.000	0.000	0.000	0.000	0.000	CCL22
CCL23	0.000	0.000	0.000	0.000	0.000	0.005	0.002	0.000	0.000	0.000	0.000	0.000	0.000	0.000	0.263	0.000	x	0.000	0.000	0.000	0.000	0.046	0.015	0.000	0.000	0.000	0.010	0.000	0.036	0.049	0.000	0.000	0.000	0.003	0.000	0.000	0.000	CCL23
CCL24	0.000	0.000	0.000	0.000	0.000	0.063	0.000	0.003	0.022	0.000	0.000	0.000	0.000	0.000	0.004	0.000	0.000	x	0.000	0.000	0.000	0.000	0.000	0.038	0.033	0.000	0.000	0.283	0.000	0.000	0.000	0.000	0.000	0.000	0.000	CCL24
CCL25	0.000	0.000	0.000	0.000	0.000	0.000	0.001	0.003	0.000	0.000	0.000	0.000	0.215	0.000	0.000	0.000	0.000	0.000	x	0.000	0.000	0.000	0.022	0.000	0.019	0.006	0.154	0.449	0.003	0.041	0.027	0.000	0.021	0.000	0.253	0.012	0.000	0.000	0.085	0.000	CCL25
CCL26	0.000	0.110	0.000	0.000	0.000	0.263	0.002	0.407	0.030	0.324	0.000	0.000	0.000	0.000	0.000	0.256	0.000	0.000	0.000	0.000	x	0.000	0.192	0.079	0.211	0.000	0.017	0.000	0.282	0.000	0.019	0.011	0.005	0.000	0.112	0.194	0.069	0.248	0.000	0.115	0.000	0.146	0.000	CCL26
CCL27	0.001	0.000	0.000	0.000	0.000	0.060	0.007	0.019	0.000	0.000	0.000	0.000	0.000	0.000	0.000	0.000	0.000	0.000	0.000	0.000	0.000	x	0.000	0.000	0.005	0.000	0.000	0.001	0.002	0.047	0.000	0.000	0.000	0.000	0.000	0.000	CCL27
CCL28	0.012	0.025	0.005	0.016	0.017	0.190	0.020	0.031	0.354	0.379	0.000	0.004	0.011	0.162	0.000	0.000	0.000	0.163	0.000	0.000	0.000	0.113	0.000	x	0.000	0.192	0.000	0.051	0.000	0.391	0.000	0.030	0.000	0.000	0.000	0.021	0.074	0.037	0.070	0.187	0.009	0.000	0.202	0.000	CCL28
XCL1	0.000	0.000	0.000	0.000	0.000	0.062	0.013	0.000	0.098	0.325	0.000	0.000	0.000	0.000	0.000	0.000	0.000	0.167	0.000	0.000	0.341	0.000	0.097	0.000	x	0.000	0.050	0.000	0.052	0.000	0.000	0.016	0.205	0.030	0.014	0.000	0.000	0.000	0.000	0.272	0.000	XCL1
XCL2	0.000	0.000	0.000	0.000	0.000	0.006	0.006	0.002	0.063	0.000	0.000	0.000	0.000	0.000	0.000	0.000	0.000	0.000	0.000	0.000	0.000	0.019	x	0.000	0.000	0.000	0.048	0.000	0.345	0.330	0.000	0.000	0.000	0.000	0.000	CXCL1
CXCL2	0.000	0.000	0.000	0.000	0.000	0.053	0.007	0.094	0.167	0.000	0.000	0.000	0.000	0.000	0.000	0.000	0.000	0.005	0.000	0.000	0.029	0.041	0.000	0.000	0.010	0.098	0.000	0.347	0.059	0.017	0.000	0.000	0.000	0.308	0.089	0.000	0.105	0.000	0.000	CXCL2
CXCL3	0.001	0.000	0.000	0.000	0.000	0.019	0.000	0.004	0.112	0.000	0.000	0.000	0.000	0.000	0.000	0.000	0.000	0.000	0.000	0.000	0.000	0.137	0.000	x	0.009	0.000	0.296	0.116	0.011	0.000	0.000	0.000	0.047	0.000	0.003	0.000	0.000	CXCL3
CXCL4	0.006	0.029	0.000	0.000	0.000	0.034	1.015	0.586	0.000	0.000	0.000	0.000	0.000	0.000	0.000	0.240	0.175	0.000	0.200	0.013	0.118	0.000	x	0.000	0.254	0.011	0.248	0.186	0.161	0.082	0.140	0.000	0.276	0.000	0.512	0.000	CXCL4
CXCL4L1	0.031	0.035	0.000	0.000	0.046	0.004	0.007	0.000	0.032	0.000	0.000	0.009	0.003	0.000	0.000	0.593	0.029	0.076	0.473	0.000	0.146	0.239	0.134	0.225	0.315	0.186	0.000	0.000	x	0.025	0.000	0.024	0.016	0.000	0.341	0.534	0.345	0.419	0.000	0.000	0.000	CXCL4L1
CXCL5	0.005	0.000	0.000	0.000	0.000	0.011	0.023	0.068	0.000	0.000	0.000	0.000	0.000	0.000	0.000	0.000	0.000	0.000	0.287	0.027	0.002	0.005	0.002	0.000	x	0.000	0.000	0.000	0.000	0.013	0.000	0.017	0.000	0.000	0.000	CXCL5
CXCL6	0.004	0.000	0.000	0.000	0.000	0.005	0.223	0.402	0.000	0.000	0.000	0.000	0.000	0.000	0.000	0.000	0.000	0.040	0.000	0.016	0.012	0.000	0.028	x	0.796	0.000	0.000	0.000	0.005	0.000	0.000	0.000	0.000	CXCL6
CXCL7	0.004	0.000	0.000	0.000	0.000	0.098	0.005	0.046	0.013	0.302	0.000	0.000	0.000	0.000	0.196	0.000	0.000	0.071	0.000	0.211	0.000	0.000	0.000	0.008	0.000	0.000	0.005	x	0.000	0.123	0.173	0.079	0.246	0.000	0.162	0.000	0.016	0.000	CXCL7
CXCL8	0.006	0.000	0.000	0.000	0.000	0.003	0.053	0.000	0.000	0.000	0.000	0.000	0.000	0.000	0.000	0.000	0.000	0.009	0.000	0.000	0.000	x	0.000	0.000	0.000	0.000	0.000	0.000	0.000	CXCL8
CXCL9	0.002	0.000	0.000	0.000	0.000	0.178	0.003	0.032	0.062	0.293	0.000	0.000	0.000	0.197	0.000	0.000	0.000	0.115	0.000	0.079	0.000	0.050	0.000	0.221	0.000	0.000	0.000	0.055	0.000	x	0.253	0.070	0.062	0.000	0.102	0.000	0.157	0.000	CXCL9
CXCL10	0.003	0.010	0.000	0.000	0.000	0.101	0.000	0.184	0.551	0.343	0.000	0.000	0.000	0.000	0.000	0.182	0.000	0.000	0.096	0.000	0.221	0.043	0.000	0.042	0.000	0.013	0.000	0.001	0.083	0.015	0.000	0.131	x	0.168	0.114	0.000	0.007	0.000	0.174	0.000	CXCL10
CXCL11	0.000	0.000	0.000	0.000	0.000	0.070	0.006	0.122	0.206	0.104	0.000	0.000	0.000	0.000	0.000	0.000	0.000	0.008	0.000	0.300	0.000	0.058	0.000	0.091	0.000	0.000	0.000	0.002	0.148	0.000	0.021	0.017	0.000	x	0.164	0.000	0.088	0.000	0.000	CXCL11
CXCL12	0.003	0.000	0.000	0.000	0.000	0.100	0.016	0.019	0.000	0.000	0.000	0.000	0.000	0.000	0.000	0.057	0.000	0.000	0.119	0.255	0.024	0.005	0.000	0.052	0.000	0.445	0.000	0.057	0.008	0.000	0.000	0.000	0.169	x	0.000	0.017	0.000	0.000	0.000	CXCL12
CXCL13	0.001	0.000	0.000	0.000	0.000	0.005	0.016	0.031	0.000	0.000	0.000	0.000	0.000	0.000	0.000	0.000	0.024	0.000	0.000	0.005	0.011	0.000	0.019	0.000	0.021	0.011	0.000	0.000	0.000	x	0.000	0.000	0.000	CXCL13
CXCL14	0.002	0.007	0.000	0.000	0.000	0.238	0.001	0.039	0.565	0.581	0.000	0.000	0.000	0.000	0.119	0.000	0.000	0.066	0.000	0.232	0.185	0.000	0.000	0.047	0.000	0.267	0.000	0.144	0.000	0.011	0.000	0.106	0.269	0.052	0.065	0.000	x	0.213	0.000	CXCL14
CXCL16	0.004	0.000	0.000	0.000	0.000	0.000	0.020	0.000	0.000	0.000	0.000	0.000	0.000	0.000	0.000	0.000	0.000	0.000	0.000	0.012	0.000	0.000	0.017	0.007	0.000	0.000	0.000	x	0.000	0.000	CXCL16
CXCL17	0.000	0.000	0.000	0.000	0.000	0.000	0.000	0.000	0.000	0.000	0.000	0.000	0.000	0.000	0.054	0.000	0.000	0.000	0.000	0.000	0.000	0.051	0.000	0.000	0.000	x	0.000	CXCL17
CX3CL1	0.000	0.000	0.000	0.000	0.000	0.000	0.002	0.035	0.000	0.000	0.000	0.000	0.000	0.000	0.000	0.000	0.000	0.000	0.000	0.000	0.000	0.015	0.000	0.000	0.000	0.002	0.000	0.000	0.009	0.005	0.000	0.000	0.000	0.000	0.000	0.000	x	CX3CL1
	CCL1	CCL2	CCL3	CCL3L1	CCL4	CCL5	CCL7	CCL8	CCL11	CCL13	CCL14	CCL15	CCL16	CCL17	CCL18	CCL19	CCL20	CCL21	CCL22	CCL23	CCL24	CCL25	CCL26	CCL27	CCL28	XCL1	XCL2	CXCL1	CXCL2	CXCL3	CXCL4	CXCL4L1	CXCL5	CXCL6	CXCL7	CXCL8	CXCL9	CXCL10	CXCL11	CXCL12	CXCL13	CXCL14	CXCL16	CXCL17	CX3CL1	

Table S2. Kinetic analysis of chemokine binding by SPR.
Biotinylated CCL5, CXCL4, CXCL12 and CCL17 were immobilized on neutravidin-coated C1 sensor chips. Analytes were injected over the 2 flow cells at flow rates and concentrations described in Online Methods. All kinetic rate analyses were performed in running buffer, pH 7.4 at 25°C (n=3). Responses from analyte injections were overlaid with the fit of a 1:1 interaction model to determine on-rates (k_a), off-rates (k_d), and dissociation constants (K_D).

chemokine	k_a (M^{-1}s^{-1}) × 10^4	k_d (s^{-1})× 10^{-4}	K_D (nM)
CCL5 chip			
CCL2	1.5 ± 0.6	15 ± 6.1	95 ± 40
CCL11	286 ± 115	1450 ± 667	51 ± 11
CCL17	169 ± 25	161 ± 35	9.6 ± 1.5
CXCL4	45 ± 19	18 ± 6.4	4.1 ± 1.8
CXCL4$^{R>Q}$	30 ± 17	11 ± 0.1	4.5 ± 2.6
CXCL4^{K50E}	12 ± 0.5	150 ± 4.3	127 ± 3.0
CXCL4L1	0	-	-
CXCL7	11 ± 2.2	30 ± 18	27 ± 16
CXCL10	24 ± 1.5	21 ± 3.2	8.8 ± 1.9
CXCL12	1.6 ± 0.1	94 ± 5.8	578 ± 61
CXCL4 chip			
CCL5	20 ± 14	7.7 ± 2.7	5.2 ± 2.8
CCL5^{E66S}	3.2 ± 0.1	2.2 ± 0.1	6.7 ± 0.5
CCL5^{MT7}	0	-	-
CCL5^{E26A}	9.2 ± 5.2	499 ± 110	678 ± 365
CCL5^{44AANA47}	0	-	-
CXCL7	0	-	-
CXCL8	0.3 ± 0.1	2.9 ± 0.4	105 ± 11
CXCL12	33 ± 9.1	113 ± 28	35 ± 8.6
CXCL12 chip			
CXCL4	2.2 ± 0.7	4.6 ± 2.9	20 ± 7.4
CXCL4L1	10 ± 6.1	12 ± 5.7	13 ± 6.1
CXCL4^{K50E}	23 ± 0.9	279 ± 10	121 ± 3.0
CCL5	4.9 ± 1.2	159 ± 80	298 ± 119
CCL5^{E66S}	42 ± 29	1415 ± 1217	319 ± 60
CCL17 chip			
CCL5	16 ± 3.3	14 ± 2.1	8.6 ± 1.8
CCL5^{E66S}	69 ± 4.8	27 ± 4.5	3.9 ± 0.4
CCL5^{MT7}	0.8 ± 0.2	11 ± 2.2	145 ± 64
CCL5^{E26A}	49 ± 0.8	20 ± 3.9	4.1 ± 0.8
CCL5^{44AANA47}	8.5 ± 1.4	25 ± 2.9	30 ± 5.5

Table S3. Weighted averaging of Δintensity changes and MDS-based in silico modeling.
The changes in resonance intensity (ΔIntensity) of ^{1}H-^{15}N resonances in heteronuclear single quantum coherence spectra of ^{15}N-CCL5^{E66S} in the presence of indicated CXC and CC chemokines were recorded and calculated as 1 minus the ratio presence/absence of any given chemokine. Average ΔIntensity values are shown; "top 10" indicates the average of the 10 resonances showing the greatest reduction in intensity; "all" means the average over all resonances. Free energies (ΔG) for various pairs of chemokines were calculated from molecular dynamics simulations (MDS) of pre-constructed CC-type or CXC-type heterodimers, as indicated. Values assessed using data from 100-130 ns of MD simulation. ΔG values are given in kcal/mol.

	ΔIntensity (top 10)	ΔIntensity (all)	ratio (10/all)	dimer type preferred	ΔG for CC-type	ΔG for CXC-type
CCL5^{E66S}/CCL17	0.85	0.37	2.3	CC		
CCL5/CCL17				CC	-61.3	-45.7
CCL5^{E66S}/CXCL4	0.25	0.11	2.3	CC	-53.2	-40.3
CCL5/CXCL4				CC	-62.6	-44.9
CCL5^{E66S}/CCL2	0.48	0.37	1.3	CC/CXC		
CCL5/CCL2				CC	-56.8	-34.6
CCL5^{E66S}/CXCL12	0.15	0.11	1.4	CXC/CC	-7.9	-44.5
CCL5/CXCL12				CXC	-7.5	-31.5
CXCL4/CXCL12				CXC	-3.0	-67.7
CCL5^{E66S}/CCL3	0.7	0.61	1.1	none		

Table S4. Sequence and origin of peptide inhibitors.

*The synthetic unprotected pro-helical VREY αCOSH peptide was reacted with a template-assembled synthetic protein (TASP) molecule resulting in a 4-helix TASP.

peptide	sequence	configuration	CCL5 origin
CCL5[1-33]	SPYSSDTTPCCFAYIARPLPRAHIKEYFYTSGK	linear	1-33
CKEY	CKEYFYTSGKCSNPAVVFITRC	cyclic	25-45
CKEY[RE]	CK<u>A</u>YFYTSGKCSNPAVVFIT<u>A</u>C	cyclic	25-45
CAN	CKSSNPAVVFVTRKNRQVSANC	cyclic	33-53
[VREY][4]	[TASP]* + 4x [EKKWVREYINSLEMS]	branched	54-68

Table S5. CCL5-derived peptides specifically inhibit heterodimer formation.
Chemokines were biotinylated and immobilized on neutravidin-coated C1 sensor chips. The RU signal of the soluble chemokine was obtained at 50 nM. The inhibition of chemokine heterodimerization by the peptides CCL5[1-33], CKEY, CKEY[RE], CAN, and [VREY][4] was tested at increasing concentrations and is indicated by IC50 values (n=3). Owing to aggregation of peptides, IC50 values > 5.0 μM could not be determined (ND).

peptide inhibitor	ligand (immobilized)	analyte (soluble)	IC50 (μM)
CCL5[1-33]	CCL5	CXCL4	1.7
	CCL17	CCL5	0.24
	CXCL12	CCL5	2.4
CKEY	CCL5	CXCL4	1.9
	CCL17	CCL5	ND
	CXCL12	CCL5	ND
CKEY[RE]	CCL5	CXCL4	ND
CAN	CCL5	CXCL4	ND
	CCL17	CCL5	0.27
	CXCL12	CCL5	ND
[VREY][4]	CCL5	CXCL4	ND
	CCL17	CCL5	ND
	CXCL12	CCL5	2.7

Table S6. Lipid parameters and peripheral blood counts of different CXCL4 genotypes.
Wild-type mice (wt/wt), homozygous $Cxcl4^{L1/L1}$ mice with a CXCL4 knock-out and knock-in of the human variant CXCL4L1, heterozygous $Cxcl4^{L1/+}$ mice and Cxcl4-deficient $Cxcl4^{-/-}$ mice on an $Apoe^{-/-}$ genetic background were fed a high-fat diet for 12 weeks. Lipid parameters, body weight and differential peripheral blood counts were determined using standard methodology. Data represent mean±SEM from 8-15 mice, as analyzed by Kruskal-Wallis-test (ns; not significant).

	CXCL4$^{wt/wt}$	CXCL4$^{wt/L1}$	CXCL4$^{L1/L1}$	CXCL4$^{-/-}$	*P*-value
cholesterol (mg/dl)	1048 ± 202	1088 ± 146	1152 ± 177	1017 ± 88	ns
triglycerides (mg/dl)	394 ± 179	426 ± 144	256 ± 120	379 ± 159	ns
body weight (g)	22.9 ± 1.7	26.1 ± 4.4	25.9 ± 3.1	25.3 ± 2.5	ns
RBC (10^6/µl)	9.1 ± 0.4	8.9 ± 0.6	8.9 ± 0.5	9.5 ± 0.4	ns
WBC (10^3/µl)	4.5 ± 1.4	4.5 ± 1.3	5.3 ± 1.8	4.5 ± 1.5	ns
lymphocytes (10^3/µl)	3.1 ± 1.1	3.2 ± 1.0	4.0 ± 1.3	3.2 ± 1.2	ns
neutrophils (10^3/µl)	1.3 ± 0.7	1.2 ± 0.4	1.1 ± 0.6	1.2 ± 0.4	ns
platelets (10^3/µl)	1019 ± 204	844 ± 242	868 ± 280	937 ± 229	ns

Table S7. Effect of OPRAH on lipid parameters and peripheral blood counts.

Wild-type mice (wt/wt), heterozygous $Cxcl4^{L1/wt}$ mice and $Ccl5^{-/-}Cxcl4^{-/-}$ mice on an $Apoe^{-/-}$ genetic background were fed a high-fat diet for 6 weeks and were treated (i.p.) with vehicle (ctrl) or OPRAH (10 µg, twice a week). Lipid parameters, body weight and differential peripheral blood counts were determined using standard methodology. Data represent mean±SEM from 5-6 mice, as analyzed by Kruskal-Wallis-test (ns; not significant). Dunn's multiple comparison test revealed no significant differences in body weight and platelet counts between relevant treatment groups or when comparing the other groups to wt/wt controls, respectively.

	wt/wt	*Cxcl4*$^{L1/wt}$	*Cxcl4*$^{L1/wt}$	*Ccl5*$^{-/-}$*Cxcl4*$^{-/-}$	*Ccl5*$^{-/-}$ *Cxcl4*$^{-/-}$	*P*-value
treatment	ctrl	ctrl	OPRAH	ctrl	OPRAH	
cholesterol (mg/dl)	1019 ± 182	905 ± 103	969 ± 169	968 ± 124	754 ± 239	ns
triglycerides (mg/dl)	140 ± 50	121 ± 28	105 ± 20	152 ± 56	93 ± 66	ns
body weight (g)	25.2 ± 2.6	23.0 ± 1.9	23.6 ± 2.6	31.7 ± 2.2	31.8 ± 4.6	0.0012
RBC (10^6/µl)	9.1 ± 0.2	8.6 ± 1.2	9.1 ± 0.3	9.1 ± 0.5	8.2 ± 1.1	ns
WBC (10^3/µl)	4.2 ± 0.8	3.7 ± 0.9	3.8 ± 0.8	4.0 ± 0.9	3.6 ± 0.4	ns
lymphocytes (10^3/µl)	3.0 ± 0.6	2.5 ± 0.7	2.7 ± 0.6	2.8 ± 0.9	2.4 ± 0.4	ns
neutrophils (10^3/µl)	1.1 ± 0.2	1.1 ± 0.3	1.0 ± 0.2	1.2 ± 0.3	1.1 ± 0.2	ns
platelets (10^3/µl)	822 ± 97	777 ± 194	821 ± 86	1102 ± 45	1213 ± 319	0.0098

Chemokines and galectins form heterodimers to modulate inflammation

Veit Eckardt[1], Michelle C Miller[2], Xavier Blanchet[1], Rundan Duan[1], Julian Leberzammer[1], Johan Duchene[1] (iD), Oliver Soehnlein[1], Remco TA Megens[1], Anna-Kristin Ludwig[3], Aurelio Dregni[2], Alexander Faussner[1], Kanin Wichapong[4], Hans Ippel[4], Ingrid Dijkgraaf[4], Herbert Kaltner[3], Yvonne Döring[1], Kiril Bidzhekov[1], Tilman M Hackeng[4], Christian Weber[1,4,5,6], Hans-Joachim Gabius[3], Philipp von Hundelshausen[1,5,†,*] (iD) & Kevin H Mayo[2,†]

Abstract

Chemokines and galectins are simultaneously upregulated and mediate leukocyte recruitment during inflammation. Until now, these effector molecules have been considered to function independently. Here, we tested the hypothesis that they form molecular hybrids. By systematically screening chemokines for their ability to bind galectin-1 and galectin-3, we identified several interacting pairs, such as CXCL12 and galectin-3. Based on NMR and MD studies of the CXCL12/galectin-3 heterodimer, we identified contact sites between CXCL12 β-strand 1 and Gal-3 F-face residues. Mutagenesis of galectin-3 residues involved in heterodimer formation resulted in reduced binding to CXCL12, enabling testing of functional activity comparatively. Galectin-3, but not its mutants, inhibited CXCL12-induced chemotaxis of leukocytes and their recruitment into the mouse peritoneum. Moreover, galectin-3 attenuated CXCL12-stimulated signaling via its receptor CXCR4 in a ternary complex with the chemokine and receptor, consistent with our structural model. This first report of heterodimerization between chemokines and galectins reveals a new type of interaction between inflammatory mediators that can underlie a novel immunoregulatory mechanism in inflammation. Thus, further exploration of the chemokine/galectin interactome is warranted.

Introduction

Coordinated trafficking of leukocytes is central to host defense and inflammation. In order to regulate its timing and strategic course of action, various mediators (such as chemokines and adhesion/growth-regulatory galectins) are involved to orchestrate leukocyte recruitment [1–3]. The prototypic CXC chemokine CXCL12 plays a major role in many inflammatory and homeostatic situations. CXCL12 activates the Gi protein-coupled receptor CXCR4 that is expressed by hematopoietic cell types, including T cells, monocytes, and neutrophils, thus promoting their recruitment [4–6]. The CXCL12/CXCR4 axis plays a crucial role in the trafficking of these types of cells in immune homeostasis and in various acute and chronic inflammatory diseases, such as atherosclerosis and rheumatoid arthritis [7–11].

Structurally, chemokines consist of a three-stranded β-sheet and a C-terminal α-helix [12]. In solution, most chemokines form homodimers (CXCL12) or higher-order oligomers. Because of their structural homology, certain CXC and CC chemokines can form heterodimers with altered functionality compared to their homodimer counterparts [13,14]. For example, CXCL12 binds to CCL5 and inhibits its function, whereas CXCL4 enhances CCL5-mediated monocyte recruitment in atherosclerosis [15,16].

In addition to proteins, cell surface glycans convey signals relevant to pathophysiological processes. Their relatively complex and heterogeneous structures are read and translated by various tissue lectins to effect biological functions [17–19]. (β-)Ga(lactoside-binding) lectins (=galectins) are a class of potent cis/trans-acting modulators that function as bridging factors between their carbohydrate recognition domain (CRD) and cell surface glycoconjugates [20,21]. In particular, proto-type galectin-1 (Gal-1) and chimera-type galectin-3 (Gal-3) are involved in inflammatory cell recruitment

[22,23]. Both galectins are upregulated in inflammatory diseases such as atherosclerosis and osteoarthritis that also involve chemokines [24–27].

Structurally, all galectins share a highly conserved β-sandwich fold consisting of a six-stranded β-sheet on one face (S-face or sugar-binding face) and a five-stranded β-sheet on the opposing face (F-face) [28–30]. Gal-3 is unique among galectins, because it has a relatively long N-terminal tail (NT) extending out from its CRD. The NT is relevant to Gal-3 function, self-association, and serine phosphorylation, and it can be proteolytically truncated and fully cleaved from the CRD, thus explaining the term chimera type. Analogous to chemokines, galectins can also form homodimers and oligomers [31,32], as well as galectin/galectin heterodimers [33].

Until now, chemokines and galectins have been investigated as physically separate and functionally independent entities. Here, we test the hypothesis that they can associate as heterodimers with functional consequences, a hitherto unappreciated concept. We first demonstrate by screening that several CC and CXC chemokines can interact with Gal-3 and Gal-1, and then, we focus work on the specific case of CXCL12/Gal-3. Nuclear magnetic resonance (NMR) studies reveal that CXCL12 and Gal-3 form heterodimers and allow for a molecular dynamics (MD) simulation-based structural model to be made. This model is validated by investigating several Gal-3 CRD mutants (engineered by replacing key residues at the interface with CXCL12) that reveal reduced binding to CXCL12. Functionally, wild-type (WT) Gal-3 CRD, but not the mutants, blocks CXCL12-mediated leukocyte migration, indicating relevance of the structurally defined association. Impairing CXCR4 signaling by the CRD is presumably due to its capacity to build a ternary complex with the chemokine and its receptor on the cell surface.

Results

Physical interaction of Gal-3, Gal-3 CRD, and Gal-1 with CC and CXC chemokines

Our initial evidence supporting the new concept for interactions between chemokines and galectins was obtained by using a solid-phase immunoassay with membrane-adsorbed chemokines and biotinylated Gal-3 and Gal-1 in solution. Chemokine-dependent association in the mix was detected with horseradish peroxidase (HRP)-conjugated streptavidin (SA) and chemiluminescence. Figure 1A–D shows an exemplary image and qualitative analysis of a chemokine blot incubated with biotinylated Gal-3. Examination of a comprehensive panel of CC and CXC chemokines with these galectins revealed multiple cases of interaction with a similar binding pattern (Fig 1E). Figure EV1A–D shows an image with qualitative analysis of a chemokine blot incubated with biotinylated Gal-1.

Surface plasmon resonance (SPR) experiments were also performed with these chip-conjugated galectins and soluble chemokines. Excluding artifactual effects from surface adsorption, we found that results from both assays were consistent (Fig EV1E–G). A negative result from the solid-phase assay (e.g., CXCL9 and CXCL11 show no interaction with Gal-3) may be attributed to inactivation and/or inaccessibility of the binding site due to surface adsorption. SPR binding kinetics of CXCL12 with chip-immobilized

Gal-3 allowed us to derive a CXCL12/Gal-3 K_D of 80 nM when Gal-3 was coupled via its sole cysteine (Fig 1F). Immobilized Gal-3 CRD bound CXCL12 with a slightly higher affinity of 34 nM (Fig 1G), suggesting that the NT of Gal-3 is not the site of interaction with CXCL12 and may even interfere with CXCL12 binding due to its transient interactions with the CRD [34]. The affinity of Gal-3 was about 10-fold higher than that of the proto-type (homodimeric) Gal-1, supporting the idea of a galectin-specific interaction (Fig 1H). Lactose, the canonical ligand for the galectin CRD, did not inhibit the interaction between CXCL12 and Gal-3 (Appendix Fig S1A and B). This result indicates that the contact region for the chemokine does not involve the canonical glycan-binding site on the S-face of the CRD, as is the case for pairing of Gal-3 CRD via the NWGR motif (W is central for lactose binding due to C-H/π-interaction) with Bcl-2 family proteins [35]. Besides, unfractionated heparin blocked the binding of Gal-3 CRD to CXCL12 (Appendix Fig S1C), indicating that CXCL12 residues relevant to glycosaminoglycan (GAG) binding contribute to the heterodimer interface.

We then compared the affinity of Gal-3 for CXCL12 with that for a panel of chemokines that showed a robust response to the Gal-3 chip (Figs EV1E and EV2A–F). Whereas CCL17 gave uninterpretable weak responses (Fig EV2C), the other chemokines examined (CCL1, CCL5 E66S, CCL22, CCL26, and CXCL11) gave well-detectable signals with K_D values falling into the range from 7.9 to 99 nM (Fig EV2G). In this experiment, we used the E66S mutant of CCL5 that cannot form higher-order homooligomers, because WT CCL5 did not permit accurate determination of K_D values. For subsequent structural and functional studies, we selected the Gal-3/CXCL12 pair due to its broad tissue distribution, co-expression in diverse organs, and biological relevance (Appendix Fig S2) [36].

In conclusion, Gal-3 interacts with CC and CXC chemokines primarily via its CRD, and without direct involvement of the canonical glycan-binding S-face of the CRD.

Formation of CXCL12/Gal-3 heterodimers

To identify the interacting contact surfaces between CXCL12 and Gal-3, we performed ^{1}H–^{15}N HSQC experiments with ^{15}N-labeled CXCL12 and unlabeled Gal-3 CRD, as well as with ^{15}N-labeled Gal-3 CRD and unlabeled CXCL12. Since CXCL12 itself forms relatively weak homodimers in fast exchange on the chemical shift timescale, the equilibrium between CXCL12 monomers and dimers can be shifted to mostly monomer by lowering the pH [37,38]. Addition of unlabeled Gal-3 CRD to ^{15}N-labeled CXCL12 (and vice versa) resulted in some significant chemical shift changes as shown in the HSQC spectral expansions and chemical shift maps provided in Fig 2A and B. The entire HSQC spectra from which these expansions were made are provided in Appendix Fig S3A and B with some key interacting residues boxed in. Changes in resonance line widths and chemical shifts indicate that binding interactions occur in the intermediate exchange regime on the NMR chemical shift timescale, which in turn suggests that the heterodimer dissociation constant, K_D, falls in the 10^{-6} M range [39], slightly higher than from our SPR measurements. In addition, our HSQC data showed that lactose did not disturb the interaction, consistent with our SPR data (Appendix Fig S1A and B). Chemical shift changes identify regions of inter-protein contacts, as highlighted in orange and red on the structures of CXCL12 (Fig 2C) and Gal-3 CRD (Fig 2D). In support
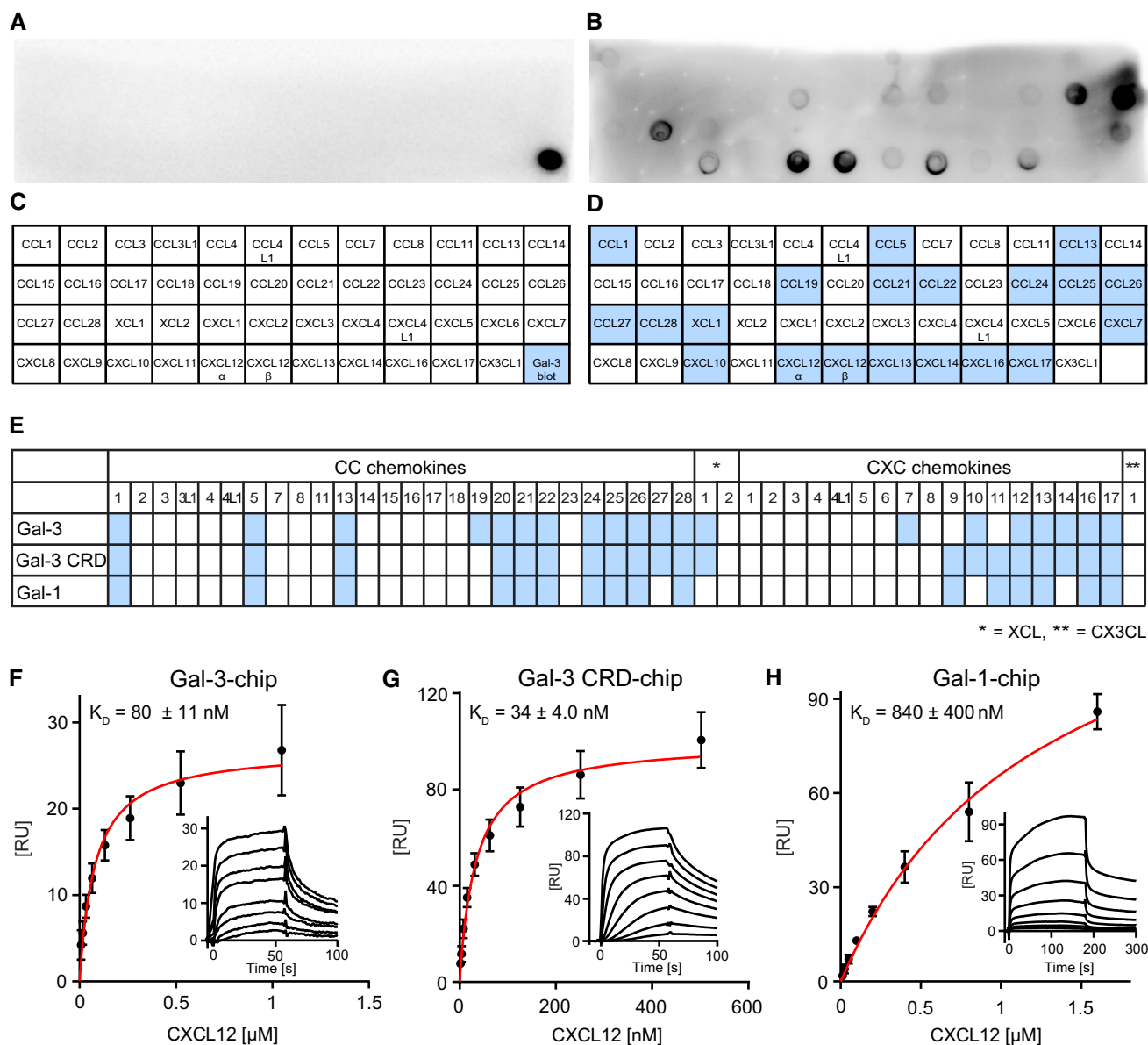
A

B

C

CCL1	CCL2	CCL3	CCL3L1	CCL4	CCL4 L1	CCL5	CCL7	CCL8	CCL11	CCL13	CCL14
CCL15	CCL16	CCL17	CCL18	CCL19	CCL20	CCL21	CCL22	CCL23	CCL24	CCL25	CCL26
CCL27	CCL28	XCL1	XCL2	CXCL1	CXCL2	CXCL3	CXCL4	CXCL4 L1	CXCL5	CXCL6	CXCL7
CXCL8	CXCL9	CXCL10	CXCL11	CXCL12 α	CXCL12 β	CXCL13	CXCL14	CXCL16	CXCL17	CX3CL1	Gal-3 biot

D

CCL1	CCL2	CCL3	CCL3L1	CCL4	CCL4 L1	CCL5	CCL7	CCL8	CCL11	CCL13	CCL14
CCL15	CCL16	CCL17	CCL18	CCL19	CCL20	CCL21	CCL22	CCL23	CCL24	CCL25	CCL26
CCL27	CCL28	XCL1	XCL2	CXCL1	CXCL2	CXCL3	CXCL4	CXCL4 L1	CXCL5	CXCL6	CXCL7
CXCL8	CXCL9	CXCL10	CXCL11	CXCL12 α	CXCL12 β	CXCL13	CXCL14	CXCL16	CXCL17	CX3CL1	

(In panels C and D, binding chemokines are shown in light blue.)

E

	CC chemokines																										*		CXC chemokines																		**
	1	2	3	3L1	4	4L1	5	7	8	11	13	14	15	16	17	18	19	20	21	22	23	24	25	26	27	28	1	2	1	2	3	4	4L1	5	6	7	8	9	10	11	12	13	14	16	17	1
Gal-3																																															
Gal-3 CRD																																															
Gal-1																																															

* = XCL, ** = CX3CL

F Gal-3-chip — $K_D = 80 \pm 11$ nM

G Gal-3 CRD-chip — $K_D = 34 \pm 4.0$ nM

H Gal-1-chip — $K_D = 840 \pm 400$ nM

Figure 1. Physical interaction of Gal-3 and Gal-1 with CC and CXC chemokines.

A–E Chemokine–galectin interactions were detected by using a solid-phase immunoassay. For this, 46 human CC and CXC chemokines were adsorbed on nitrocellulose membranes and the stripes incubated in parallel with (A) TBS or (B) TBS containing biotinylated galectins (the representative image shows a processed membrane tested with labeled Gal-3). Signals had been generated by using SA-HRP and chemiluminescence reagents. (C, D) The blots were subjected to densitometric analysis, and (E) all independent experiments were combined (binding chemokines in light blue, Gal-3: $n = 5$, Gal-3 CRD: $n = 5$, Gal-1: $n = 4$).

F–H For SPR-based experiments, (F) Gal-3 (density 650 RU), (G) Gal-3 CRD (density 1180 RU), and (H) Gal-1 (density 130 RU) were immobilized and increasing concentrations of CXCL12 were passed over the flow cells. The red curve represents a single-site fit to the data. Insets are representative sensorgrams of CXCL12 testing on immobilized galectin. Data represent the mean ± SD from six (F) or three (G and H) independent experiments.

of these NMR data, silver staining of SDS–PAGE gels loaded with CXCL12, the cross-linker BS(PEG)$_5$, and increasing concentrations of Gal-3 CRD exhibited bands at the position expected for the CXCL12/Gal-3 CRD heterodimer (Appendix Fig S4).

Whereas Gal-3 CRD exists as a compact monomer in solution, full-length Gal-3 is characterized by intramolecular dynamics via transient backfolding of the NT onto the CRD F-face and a very weak tendency for self-association, both of which complicate structural interaction analyses [34]. Nevertheless, we assessed CXCL12-induced chemical shift changes in ^{15}N-labeled full-length Gal-3 and found that chemical shifts were overall reduced (Appendix Fig S5). In addition to the residues within the CRD, residues 5-15 near the N-terminus were also chemically shifted (Appendix Fig S5). This may reflect competition of chemokine/galectin heterodimer formation with intramolecular interactions between the NT and CRD [34]. In any event, our ligand blotting, SPR, and cross-linking results show that the NT of Gal-3 is not required for formation of Gal-3/CXCL12 heterodimers (Figs 1E and G, and EV1F, and Appendix Fig S4). Of
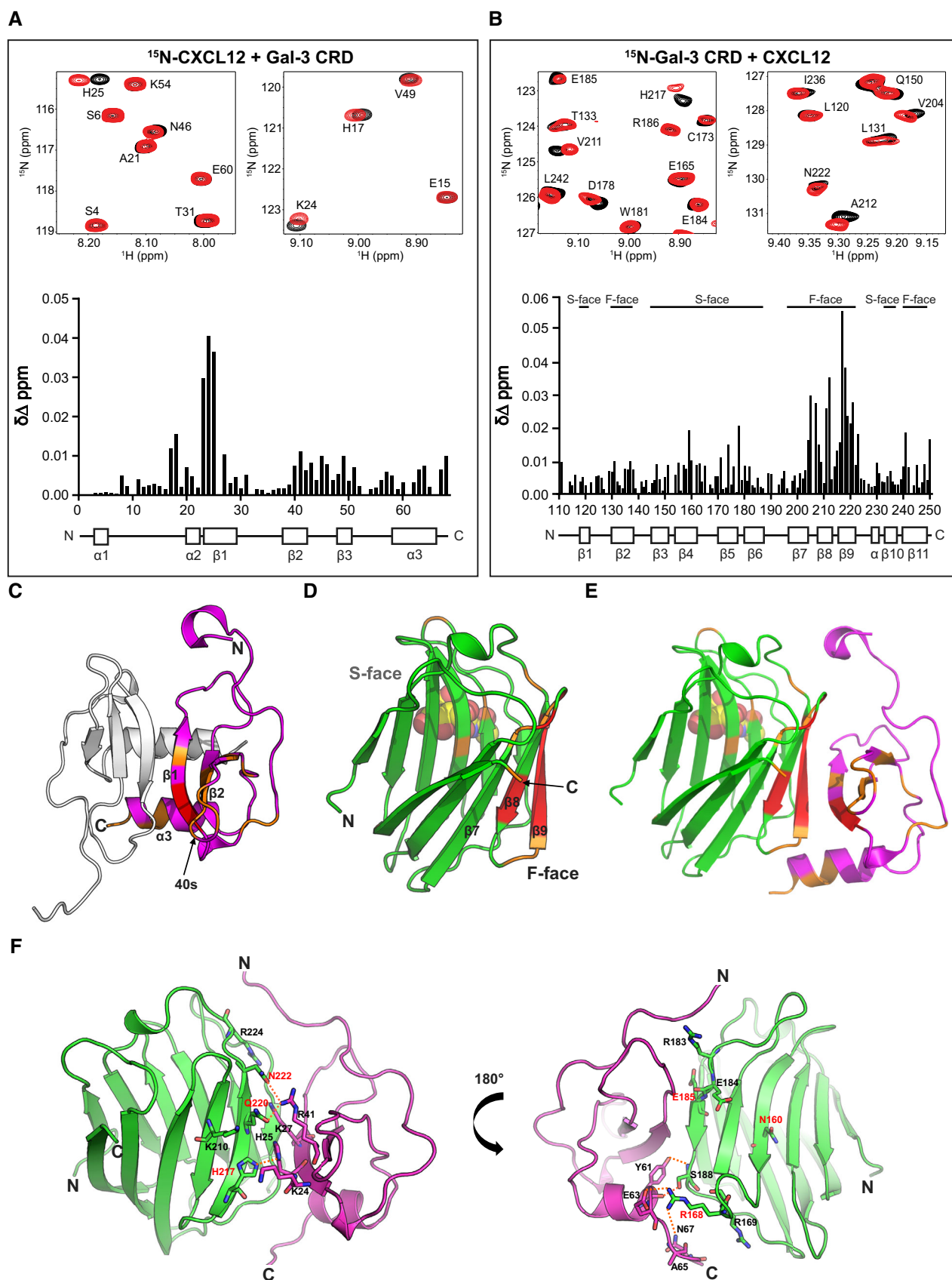
Figure 2.

Figure 2. Formation of the CXCL12/Gal-3 CRD heterodimer.

A, B   Expansions of ^{1}H–^{15}N HSQC spectra are overlaid, and Δδ values are plotted vs. the amino acid sequences, along with secondary structures: (A) 10 μM ^{15}N-enriched CXCL12 alone (black peaks) and in the presence of 330 μM Gal-3 CRD (red peaks; assignments reported by Murphy et al [74]) and (B) 30 μM ^{15}N-enriched Gal-3 CRD alone (black peaks) and in the presence of 500 μM CXCL12 (red peaks; assignments for Gal-3 reported by Ippel et al [34]).

C–E   X-ray crystal structures are depicted (C) for the CXCL12 homodimer (PDB access code 4UAI; monomer in magenta) and (D) for Gal-3 CRD bound with lactose (PDB access code 1A3K; in light green). (E) The energy-minimized structure of the CXCL12/Gal-3 CRD heterodimer was calculated by MD simulations. Residues with the largest Δδ values in HSQC spectra are highlighted in red (2SD-1SD) and orange (1SD-mean).

F   A model structure of the CXCL12/Gal-3 CRD heterodimer interface is shown with Gal-3 CRD in light green, the CXCL12 monomer in magenta, mutated residues in red, and hydrogen bonds as dashed orange lines.

note, analyses of interactions between Gal-1 and CXCL12 are likely hampered by homodimerization of Gal-1 that is favored over heterodimerization (data not shown), thus likely explaining its weaker affinity for CXCL12 compared to Gal-3 (Fig 1F and H).

Having identified mutual sites of interaction on CXCL12 and Gal-3 CRD (Fig 2A–D), we performed MD simulations started after manually docking the Gal-3 CRD to CXCL12 in 10 different rotational orientations that were all consistent with our HSQC data. Appendix Fig S6A shows the resulting heterodimer structures following energy minimization, with complex 6 being the energetically most favorable (−50 kcal/mol). Decomposition analyses of the free binding energies (ΔG) for each residue in the Gal-3 CRD (Appendix Fig S6B) and CXCL12 (Appendix Fig S6C) in complex 6 identify the residue pairing sites (Fig 2). Regions of contact in complex 6 (Fig 2E) correspond best to those identified by NMR (Fig 2A and B). A few specific residue pairings are depicted in Fig 2F. Several amino acids contribute to two major contact sites within the Gal-3 CRD at the strands β6 and β8-9 (CRD F-face), and the loop between β4 and β5. Gal-3 strands β6, β8, and β9 (in particular, residues E185 (β6), H217, Q220, and N222 (β9)) interact with a dominant binding region in the strands β1 and β2 of CXCL12 (in particular, R41 (β2), K27 (β1), and K24 (β1); please see Fig 2F, left panel). In addition, Gal-3 S188 (β6) and residues of the loop between β4 and β5 (i.e., R168 and R169) interact with the CXCL12 helix residues Y61, E63, A65, and N67 to establish a neighboring contact site (Fig 2F, right panel). These HSQC experiments thus revealed that CXCL12 engages in heterodimer formation with the Gal-3 CRD. Since the CRD F-face is located on the opposite side of the lactose-binding β-sheet S-face (Fig 2D), this explains why lactose does not reduce the binding of Gal-3 to CXCL12 and vice versa.

Using complex 6 (Fig 2E and F, Appendix Fig S6A) and decomposition analysis (Appendix Fig S6B and C), we selected several residues at the CXCL12/Gal-3 binding interface, mutated those residues in silico, and performed MD simulations to calculate BFE (Appendix Table S1). Whereas some Gal-3 mutants showed relatively small energetically favorable changes (e.g., K210D, Q220D, Q220E) in binding CXCL12, others showed highly unfavorable energetics (R168A, E185A, H217A, Q220A, Q220K, Q220R, N222A). Several positively charged residues in CXCL12 are located at the interface with Gal-3 (Fig 2F, left panel); Q220 of Gal-3 is one of them, such that introducing a negatively charged residue (i.e., glutamate) at that position (i.e., Q220E) might promote favorable electrostatic interactions and a more negative ΔG value as obtained in silico (Appendix Table S1). On the other hand, N160 lies on the opposing, non-interacting S-face in Gal-3 and is known to contribute to carbohydrate binding (Fig 2F, right panel).

For empirical validation of our model, we used site-directed mutagenesis to produce several mutants and assess effects on

heterodimer formation. Q220E in NMR and N160A in ligand blots and SPR were used as controls. Three Gal-3 CRD mutants (Q220E, Q220K, and H217A) were selected to assess their effects on HSQC spectra of ^{15}N-labeled CXCL12 when examining mixtures. Even though all HSQC spectra look highly similar, analysis of the data could reveal distinct differences. Figure EV3 shows chemical shifts of ^{15}N-labeled CXCL12 with each of these Gal-3 CRD mutants. These maps show the same trends as observed with WT Gal-3 CRD. Although this indicates that WT Gal-3 CRD and its mutants interact with CXCL12 in the same way, the magnitudes of Δδ changes are different. Compared to WT Gal-3, Q220E Δδ values are slightly increased (Fig EV3A), whereas those for Q220K and H217A are decreased (Fig EV3B and C). CXCL12 sequence-averaged Δδ values are 0.0061 ppm for WT Gal-3 CRD, 0.0073 for Q220E, 0.0036 for Q220K, and 0.0048 for H217A. Smaller chemical shift changes usually indicate weaker intermolecular interactions [39]. Here, average Δδ values suggest slightly stronger binding between CXCL12 and Q220E, and weaker binding between CXCL12 and Q220K and H217A. These trends parallel those observed in our MD-based free energy calculations, which yielded ΔG values of −50 kcal/mol for WT Gal-3 CRD, −58 kcal/mol for Q220E, −31 kcal/mol for Q220K, and −38 kcal/mol for H217A (Appendix Table S1).

Densitometric analysis of CXCL12 binding to variants of Gal-3 (Appendix Fig S7A) and Gal-3 CRD (Appendix Fig S7B) demonstrates that residues N222 and E185 are indeed involved in the interaction with CXCL12, whereas N160 is not. Similarly, the affinity of CXCL12 injected over sensor chips with immobilized Gal-3 mutants R168A, E185A, H217A, and Q220K was reduced, whereas the affinity of N160A was not (Appendix Fig S8A–H). In addition, Gal-3 mutant binding to the N-glycans of a common galectin binder, i.e., the glycoprotein asialofetuin (ASF), was only impaired in the case of N160A that showed no significant effect on heterodimer formation (Appendix Fig S8I–L), which supports our findings that CXCL12/Gal-3 heterodimer formation is not significantly affected by glycan binding (Appendix Fig S1A and B).
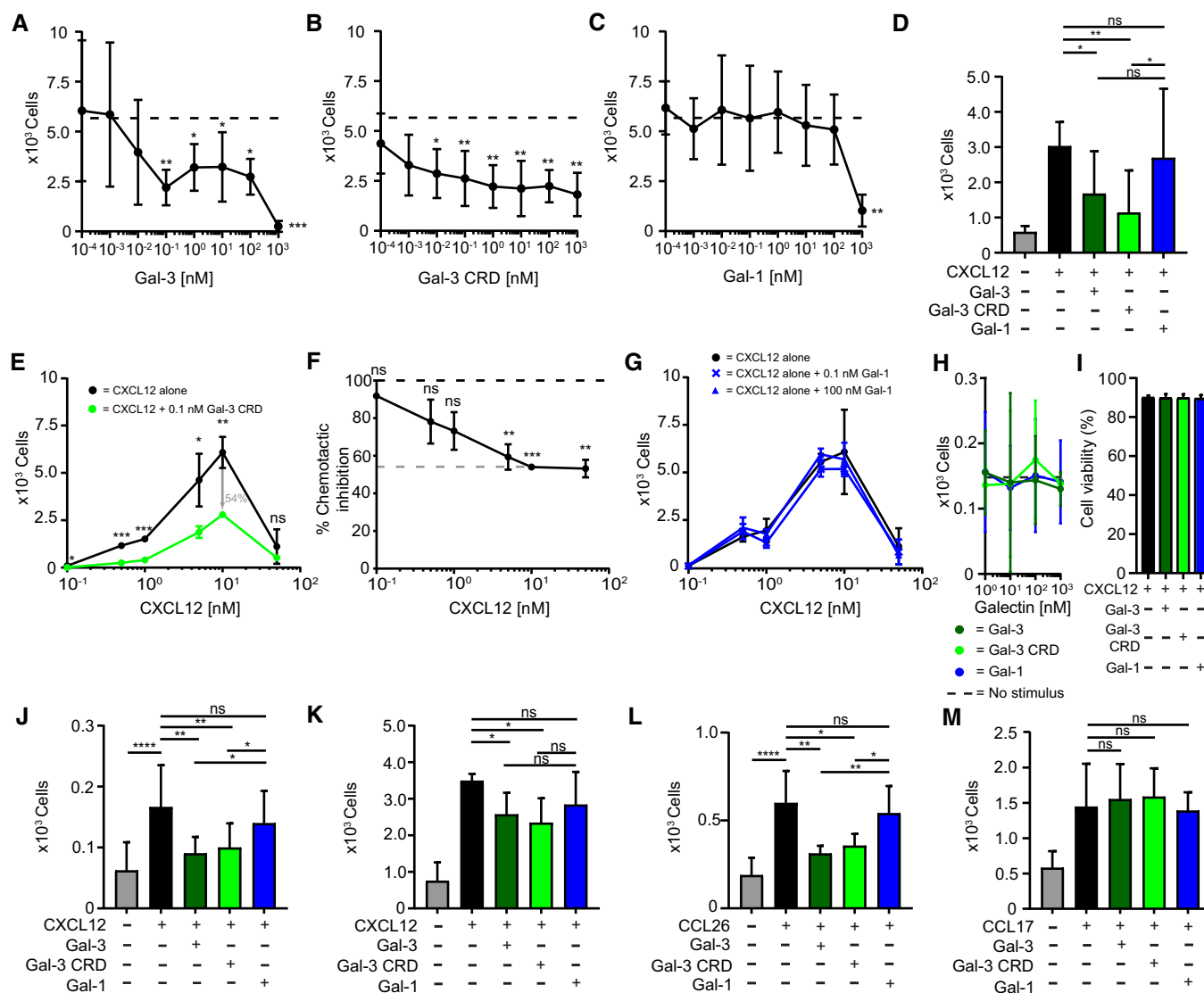
Gal-3-mediated inhibition of CXCL12-induced leukocyte migration

We next investigated the functional consequences of CXCL12:Gal-3 heterodimerization. Initially, we examined whether Gal-3 affects CXCL12-induced migration of Jurkat T cells, and discovered that both Gal-3 and Gal-3 CRD inhibited chemotaxis in a dose-dependent manner (Fig 3A and B). In contrast, Gal-1 only inhibited migration at 1 μM (Fig 3C). These results with Jurkat cells were replicated using primary cells, i.e., activated human CD4$^+$ T cells (Fig 3D). A bell-shaped chemotaxis curve was observed upon increasing the

concentration of CXCL12, with the height of the curve being significantly reduced in the presence of 0.1 nM Gal-3 CRD (Fig 3 E and F). Consistent with our concept, the CXCL12 chemotaxis curve with Gal-1 remained unchanged even in the presence of 100 nM lectin (Fig 3G). Because the affinity of CXCL12 for Gal-1 is lower than that for Gal-3 and Gal-1 has no apparent effect on chemotaxis, we

assumed that chemotactic inhibition resulted from the physical interaction between Gal-3 and CXCL12. Galectins alone at 1 μM had no effect on Jurkat cell migration or viability (Fig 3H and I), consistent with a previous report [40].

Extending the scope of our investigation to other CXCR4-expressing cell types, we found that Gal-3 and Gal-3 CRD also inhibited

Figure 3. Gal-3-mediated inhibition of CXCL12-induced leukocyte migration *in vitro*.

A–C   Jurkat T cells migrated in the presence of 10 nM CXCL12 with increasing concentrations of (A) Gal-3, (B) Gal-3 CRD, and (C) Gal-1 (A–C: $n = 4$).

D   Human CD4^{+} T cells migrated in the presence of 10 nM CXCL12 alone and with 10 nM Gal-3 (dark green), Gal-3 CRD (light green), and Gal-1 (blue, $n = 3$).

E, F   (E) Jurkat T cells migrated to increasing concentrations of CXCL12 alone (black) and CXCL12 in the presence of 0.1 nM of Gal-3 CRD (light green). (F) The inhibitory effect of Gal-3 CRD is shown as percentage of the chemotactic effect of CXCL12 (E, F: $n = 3$).

G   Jurkat T cells were allowed to migrate in the presence of CXCL12 at increasing concentrations alone and with 0.1 nM Gal-1 or 100 nM Gal-1 ($n = 3$).

H   Jurkat T cells did not migrate in the sole presence of 1 nM to 1 μM Gal-3, Gal-3 CRD (both $n = 5$), or Gal-1 ($n = 4$).

I   The viability of Jurkat T cells was assessed after incubation with 1 μM CXCL12 alone and in the presence of Gal-3, Gal-3 CRD, and Gal-1 ($n = 2$).

J, K   (J) THP-1 cells and (K) neutrophils migrated in the presence of 10 nM CXCL12 alone and with 10 nM Gal-3, Gal-3 CRD, and Gal-1 (J, K: $n = 3$).

L   Human eosinophils migrated in the presence of 10 nM CCL26 alone and with 10 nM Gal-3, Gal-3 CRD, and Gal-1 ($n = 3$).

M   CD4^{+} T cells migrated in the presence of 1 nM CCL17 alone and with equimolar concentrations of Gal-3, Gal-3 CRD, and Gal-1 ($n = 4$).

Data information: Cell migration is shown as absolute cell counts. Data represent the mean ± SD from the indicated number of independent experiments each performed in three technical replicates, and these were statistically analyzed by using (A–C, F–G, J) a single sample *t*-test or (D, I, J–M) by an unpaired *t*-test against the effect of the chemokine alone or as indicated (*$P \leq 0.05$, **$P \leq 0.01$, ***$P \leq 0.001$).

CXCL12-induced migration of monocytic THP-1 cells and neutrophils (Fig 3J and K), whereas Gal-1 caused only subtle effects. Supporting the idea of a functional impact from chemokine-Gal-3 interactions, we found that Gal-3 and Gal-3 CRD (both of which interact with CCL26) also inhibit CCL26-mediated migration of human eosinophils (Fig 3L). On the other hand, these galectins have no effect on CCL17-mediated migration of CD4^{+} T cells (Fig 3M), consistent with our observation that Gal-3 and Gal-3 CRD do not interact with CCL17 (Figs 1E, and EV1E and F, and EV2C).

Under physiological conditions, co-injection of Gal-3 and CXCL12 into mice completely abrogated CXCL12-induced intraperitoneal (IP) recruitment of neutrophils (Fig 4A) and classical monocytes (Fig 4B) after 4 h. To find out whether genetic deletion of Gal-3 had an enhancing effect on IP recruitment of classical monocytes post-injection of thioglycolate (TG) broth into the peritoneum, responses in WT and KO mice were analyzed 18 h after stimulation with TG. As Fig 4C documents, (i) TG induces cell recruitment into the peritoneum, (ii) its extent is partially reduced by the CXCR4 antagonist to signal involvement of CXCR4-independent mechanisms, and (iii) Gal-3 absence increases recruitment, pointing to involvement of other chemokines as targets or of CXCR4-independent CXCL12 blocking. TG increased the amount of CXCL12 in the peritoneal lavage (Fig 4D) and reduced CXCR4 expression on classical monocytes (Fig 4E). The TG response was partly dependent on the presence of CXCR4, because pre-injection of the CXCR4 antagonist AMD3465 attenuated the effect (Fig 4C). Therefore, we surmise that these effects are attributable to the absence of CXCL12/Gal-3 interactions in these Gal-3^{−/−} mice.

In addition, we performed antibody-based proximity ligation (PLA, Duolink®), demonstrating that CXCL12 and Gal-3 are in close proximity on cells recruited to the peritoneum after TG injection, and thus allowing for functional interactions under inflammatory conditions (Fig EV4A and B). To further substantiate the formation

of CXCL12/Gal-3 heterodimers *in vivo*, we stained Gal-3 and CXCL12 simultaneously in frozen sections of lymph nodes from WT and CXCL12^{−/−} mice (Fig EV4C and D). Here, we found partial co-localization of Gal-3 and CXCL12 that was primarily detectable at the lymph node capsule where CXCL12-expressing lymphatic endothelial cells come into close proximity with subcapsular sinus macrophages (SSM). Further evidence for close contacts between CXCL12 and Gal-3 *in situ* was obtained by antibody-based PLA staining of lymph nodes extracted from WT and CXCL12^{−/−} mice (Fig EV4E), indicating the potential for CXCL12 and Gal-3 to directly interact under physiological conditions.

To further make the case for this new type of pairing between inflammatory mediators, we found that the weaker interacting Gal-3 mutants E185A and N222A and Gal-3 CRD mutants E185A and N222A did not inhibit CXCL12-mediated chemotaxis up to 100 nM (Fig 5A and B). Similarly, CXCL12-mediated Jurkat cell migration was not inhibited by other weaker binding Gal-3 and Gal-3 CRD mutants, namely R168A, H217A, and Q220K (Fig 5C and D). In contrast, Gal-3 CRD mutant N160A, Gal-3 mutant Q220E, and Gal-3 CRD mutant Q220E (Fig EV3A) that did bind CXCL12 comparable to WT (Appendix Figs S7B, S8B, and Fig EV3A) did have an inhibitory effect (Fig 5C and D).

The observation that variants of Gal-3 at 1 μM inhibited chemotaxis independent of CXCL12, whereas Gal-3 CRD and its mutants E185A and N222A did not completely block cell migration (Fig 5A and B), may be explained by considering that the variants of full-length Gal-3 induce cell aggregation at 1 μM, an effect that was blocked by lactose (Fig 5E). We also performed transmigration assays with lactose (as well as with the disaccharide cellobiose that does not bind galectins) and with cells pre-treated with 1-deoxy-mannojirimycin hydrochloride (DMJ) that reduces the level of galectin-binding ligands on the cell surface by a shift to high-mannose-type N-glycans. As expected, the effect of Gal-3 and Gal-1
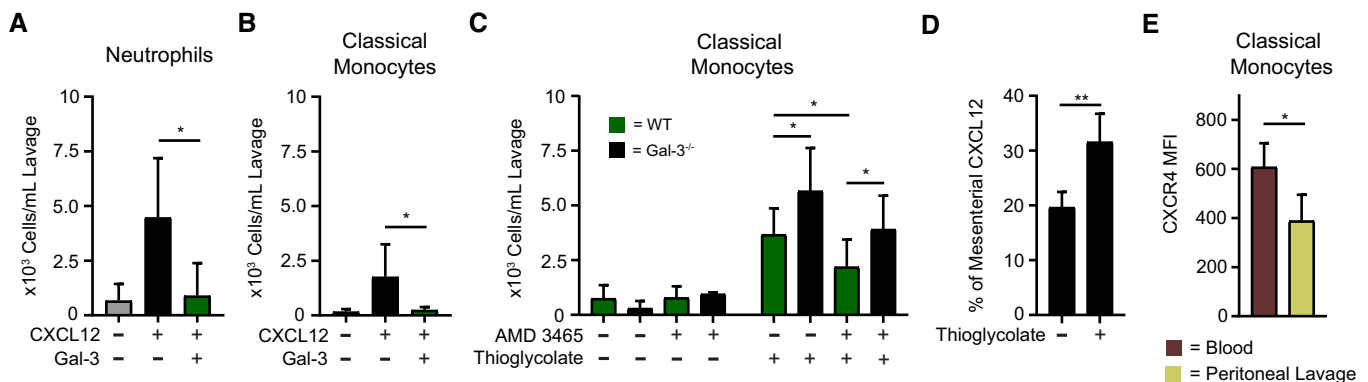
Figure 4. Peritoneal recruitment of leukocytes by CXCL12 in the presence of Gal-3.

A, B The peritoneal recruitment of (A) CD45^{+}/CD115^{−}/Ly6G^{+} neutrophils and (B) CD45^{+}/CD115^{+}/Ly6C^{hi} classical monocytes in C57BL/6J mice was assessed 4 h after intraperitoneal (IP) injection of 500 nM CXCL12 alone (black) and in the presence of 50 nM Gal-3 (dark green; A, B: *n* = 7 mice).

C The peritoneal recruitment of classical monocytes after IP injection of PBS (*n* = 6) or TG in C57BL/6J WT (dark green, *n* = 10 mice) and Gal-3^{−/−} (black, *n* = 5 mice) mice was assessed after 18 h. Where indicated, the mice received an IP injection of CXCR4 antagonist AMD 3465 12 h prior to the experiment.

D The concentration of CXCL12 concentration was determined by ELISA on the peritoneal lavage normalized with levels from the mesenterium (*n* = 4 mice).

E CXCR4 expression levels on Ly6C^{hi} monocytes of the blood and the peritoneal lavage after 18 h of TG stimulation were determined by flow cytometry and indicated as mean fluorescence intensity (MFI) (*n* = 4 mice).

Data information: Cell migration to the peritoneum is shown as cells/ml lavage. Data represent the mean ± SD from the indicated number of mice and were statistically analyzed by using the unpaired *t*-test, as indicated (*$P \leq 0.05$, **$P \leq 0.01$).
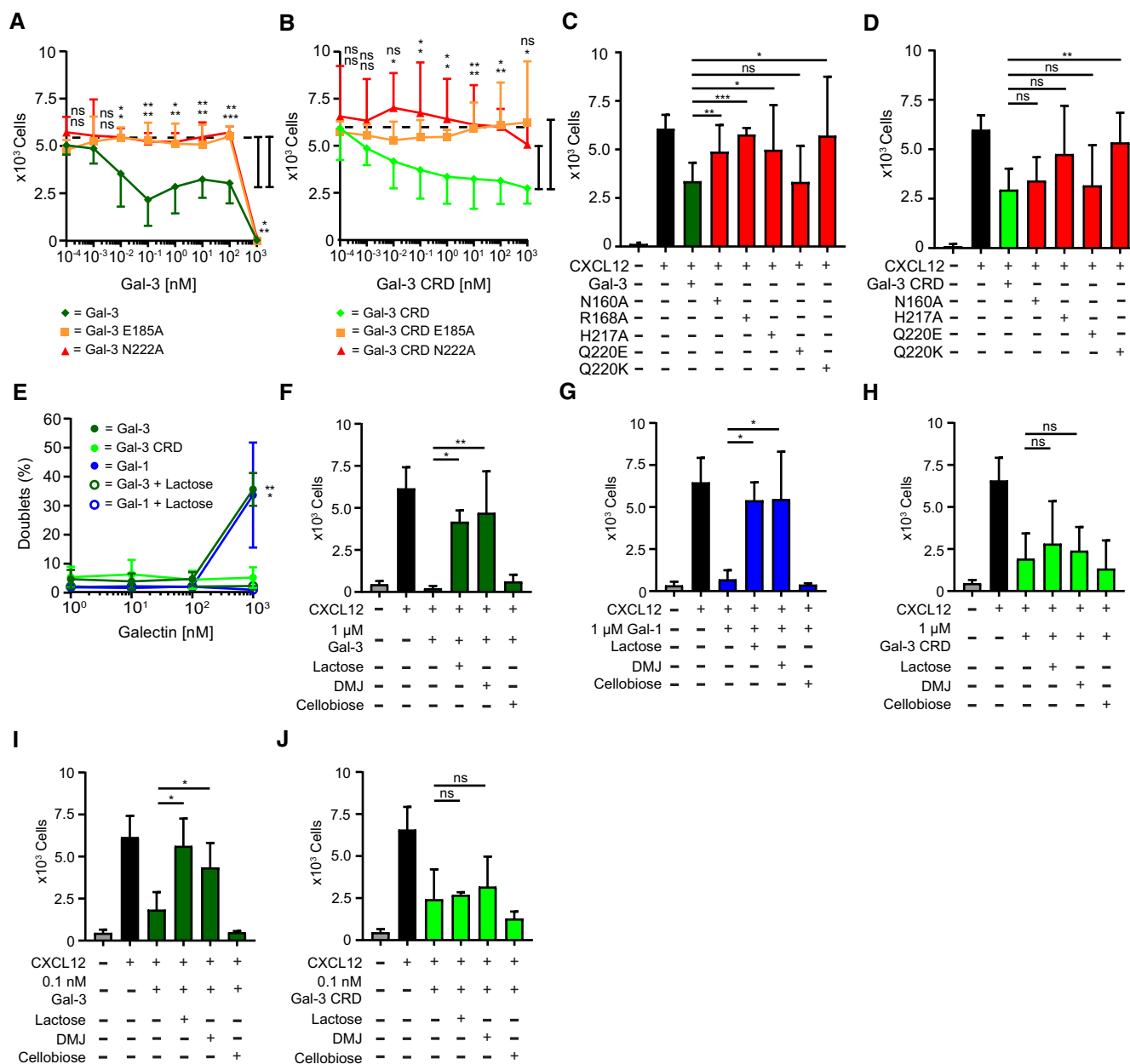
Figure 5. Inhibition of CXCL12-induced leukocyte migration by Gal-3 mutants and the role of galectin/glycan interactions *in vitro*.

A, B Jurkat T cells migrated in the presence of 10 nM CXCL12 with increasing concentrations of E185A (orange, *n* = 4) and N222A (red, *n* = 5) mutants of (A) Gal-3 and (B) Gal-3 CRD.

C, D Jurkat T cells migrated in the presence of 10 nM CXCL12 with 10 nM (C) Gal-3 and (D) Gal-3 CRD mutants as indicated (C, D: *n* = 3).

E Aggregation of Jurkat T cells in the presence of 1 nM to 1 μM Gal-3 and Gal-1 alone and with 70 mM lactose, and Gal-3 CRD, was determined by flow cytometry (*n* = 4).

F–J Jurkat T cells migrated with 10 nM CXCL12 alone and in the presence of (F) 1 μM Gal-3, (G) Gal-1, (H) Gal-3 CRD, and (I) 0.1 nM Gal-3 and (J) Gal-3 CRD in the presence of 70 mM lactose or cellobiose or after treatment of cells with 150 μM DMJ.

Data information: Cell migration is shown as absolute cell counts. Data represent the mean ± SD from the indicated number of independent experiments each performed in three technical replicates, and these were statistically analyzed by using (A, B, E) a single sample *t*-test or (C, D, F–J) by an unpaired *t*-test against the effect of the chemokine alone or as indicated (*$P \leq 0.05$, **$P \leq 0.01$, ***$P \leq 0.001$).

at 1 μM was markedly reduced by the presence of lactose and DMJ (Fig 5F and G), whereas the effect of Gal-3 CRD was unaffected (Fig 5H). Because DMJ alone did not affect CXCL12-induced chemotaxis (Appendix Fig S9A), we assume that abrogation of chemotaxis

at 1 μM galectin concentration was caused by cell aggregation due to galectin oligomerization and cell–cell cross-linking.

Lactose and DMJ have no effect on CXCL12-mediated chemotaxis with Gal-1 (Appendix Fig S9B). However, they do reverse the

inhibitory effect of WT Gal-3 on CXCL12-mediated chemotaxis (Fig 5I). The reason they also do not have an effect with Gal-3 CRD (Fig 5J) is likely due to the presence of the NT in WT Gal-3, which complicates interpretation due to additional and unknown effects at the cell surface. In solution, the Gal-3 NT interacts transiently with the CRD F-face [34], a site of interaction that partially overlaps with the CXCL12 binding site on the lectin. Based on increased line broadening with WT Gal-3 in the presence of lactose, we know that lactose enhances NT binding to the CRD F-face, which results in attenuated CXCL12 binding to the lectin. Because DMJ treatment attenuates binding of galectins to glycans on the cell surface, it may be that some of them are necessary for optimal CXCL12/Gal-3 heterodimer formation and ensuing effects on the cell surface. Furthermore, we found that the small molecule CXCR4 agonist (NUCC-390) induces CXCL12-independent chemotaxis [41] that is unaffected by the presence of Gal-3 or Gal-3 CRD (Appendix Fig S9C).

For insight into the mechanism of Gal-3-mediated inhibition of CXCL12 function, we investigated effects of the galectin on CXCR4-mediated Gi signaling and β-arrestin 2 recruitment to CXCR4, a process that is relevant to chemotaxis [42].

Inhibition of CXCL12-induced CXCR4 signaling by Gal-3 CRD

HEK 293 cells were transfected with CXCR4 and a luciferase-derived intracellular cAMP sensor. As expected, CXCL12 alone reduced cAMP levels reflecting Gi signaling, and Gal-3 CRD inhibited the effect from the chemokine over time (Fig 6A) and in a concentration-dependent manner (Fig 6B). In addition, we transfected HEK 293 cells with *Renilla* sp. luciferase II (RlucII)-conjugated CXCR4 and eYFP–β-arrestin 2 constructs to assess β-arrestin recruitment to the receptor by bioluminescence resonance energy transfer (BRET). CXCL12 caused recruitment of β-arrestin 2 that was prevented by Gal-3 CRD (Fig 6C). Unexpectedly, the effect of Gal-3 CRD was not accompanied by reduced internalization of CXCR4 (Fig 6D), which is mediated by β-arrestin recruitment [42]. However, it has been reported that chemokine receptors may signal in a biased fashion, with β-arrestin recruitment and internalization being uncoupled [42–44].

To confirm that Gal-3 CRD exerts its effect on CXCL12 via CXCR4, we performed cell-binding experiments with CXCL12 and Gal-3 using Jurkat T cells. First, we incubated the cells with CXCL12 and Gal-3, and demonstrated co-localization of the two proteins by an antibody-based PLA (Fig 6E). Next, we incubated the cells with fluorescently labeled Gal-3 CRD and unlabeled CXCL12 in the presence of AMD 3100, a competitive CXCR4 antagonist, and recorded fluorescence intensity by flow cytometry [45]. We found that the signal from the galectin in the presence of the chemokine was inhibited by AMD 3100 (Fig 6F). Furthermore, when we blocked direct binding of Gal-3 CRD to the cell surface with lactose, we observed an increase in the Gal-3 CRD signal upon addition of CXCL12. Once again, this effect was inhibited by AMD 3100 (Fig 6G). In contrast, unlabeled Gal-3 CRD did not displace fluorescently labeled CXCL12 from the cell surface (Fig 6H). Taken together, these findings suggest that Gal-3 CRD interacts with CXCL12, either having an indirect effect on CXCR4 via CXCL12 or directly binding to CXCL12 and CXCR4. Since glycan binding to the Gal-3 CRD is not required for the inhibition

of chemotaxis (Fig 5H and J), the involvement of an additional Gal-3 co-receptor is unlikely.

To test these hypotheses, we performed MD simulations of the CXCL12/Gal-3 CRD heterodimer interacting with CXCR4. Since the structure of CXCL12 bound to CXCR4 has so far not been determined, we superimposed complex 6 of the heterodimer (Fig 2E and F, Appendix Fig S6A) onto the structure of vMIP-II when associated with CXCR4 and removed the docked vMIP-II from the complex. The obtained model was then subjected to energy minimization in the course of a MD run over a period of 50 ns with coordinates and orientation from another monomer of CXCR4 (Fig EV5). The obtained structure illustrates that CXCL12's ligand property is not impaired by the Gal-3 CRD; that is, binding of the CXCL12/Gal-3 CRD heterodimer to CXCR4 is sterically possible. It may even be favored by direct interactions between Gal-3 CRD and CXCR4. This model obtained by MD simulation clearly warrants further investigation. Nonetheless, the experimental and computational lines of evidence converge to exclude galectin-dependent blocking of chemokine–receptor interaction for reducing CXCL12 activity as probed.

Discussion

Chemokines and galectins regulate leukocyte recruitment and can be simultaneously upregulated under inflammatory conditions. In fact, in osteoarthritis, chemokines belong to a set of proteins that are upregulated in a NF-κB-dependent manner by Gal-3 [46]. Building on our discovery that CXC and CC chemokines form heterodimers with functional significance, we established a map of the chemokine interactome that illustrates numerous interactions [15]. Moreover, we recently reported on galectin/galectin heterodimer formation [33]. Due to the functional and structural similarities between chemokines and galectins, we hypothesized that members of both these effector molecule families may themselves interact to form chemokine/galectin heterodimers with functional consequences.

In the present study, we validated this hypothesis by demonstrating that Gal-1 and Gal-3 specifically interact with several chemokines in solid-phase immunoassays and SPR. When comparing the function of interacting and non-interacting chemokines, it is worthwhile to note that some chemokines primarily involved in later stages of inflammation, such as CCL22, CCL24, CCL26, and CXCL12, interact with the galectins, whereas chemokines, such as CCL2, CCL17, or CXCL8, that have been implicated in the initiation of inflammation [11,47–49] do not bind. Therefore, we propose a new concept that chemokine/galectin heterodimers may play a role in later stages of inflammatory processes or chronic inflammation.

Focusing on Gal-3 and CXCL12 that are both often found to be co-expressed and involved in inflammatory processes, we performed HSQC studies that revealed formation of a CXCL12/Gal-3 heterodimer in which Gal-3 binds to CXCL12 via the F-face of its CRD. The opposing glycan-binding S-face and the NT of Gal-3 are not part of the primary interaction domain. NMR analysis of the contact site between CXCL12 and Gal-1 or full-length Gal-3 was impeded by either intramolecular conformational changes or homodimerization. Viewed from the chemokine perspective, the interaction site includes the first β-strand (residues 17–27) and the
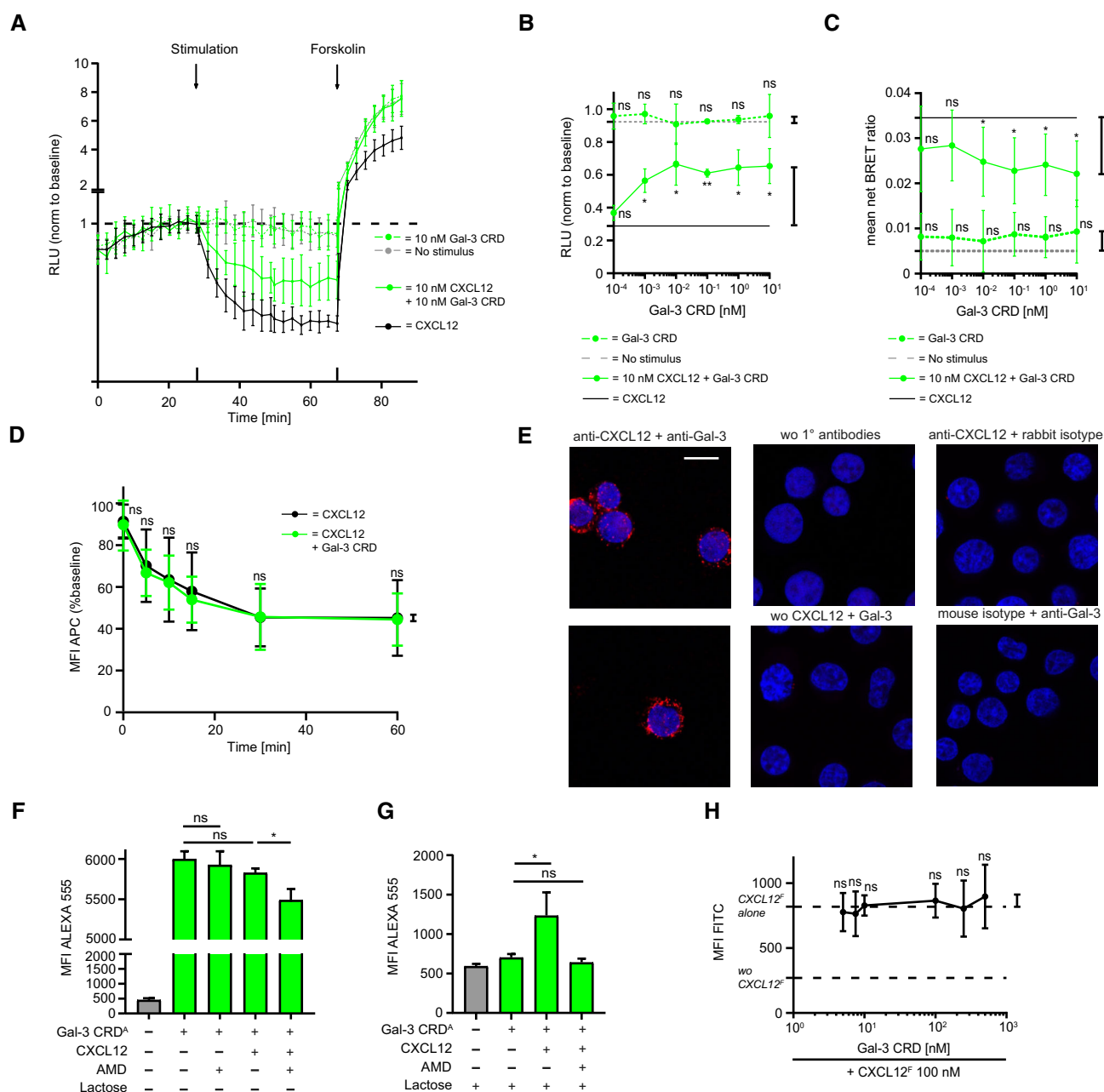
Figure 6. Inhibition of CXCL12-induced CXCR4 signaling by Gal-3 CRD.

A HEK cells transfected with a luminescent cAMP sensor were incubated with 10 nM CXCL12 alone and in the presence of 10 nM Gal-3 CRD followed by stimulation with forskolin, an activator of adenylate cyclase. Results are shown as luminescence relative to baseline (RLU, example of *n* = 3).

B The effect of 10 nM Gal-3 CRD upon stimulation with 10 nM CXCL12 prior to forskolin stimulation was tested. Control experiments were performed as indicated (*n* = 3, four technical replicates).

C HEK cells transfected with a RlucII-conjugated CXCR4 and an eYFP–β-arrestin 2 construct were stimulated with 10 nM CXCL12 alone and in the presence of 10 nM Gal-3 CRD. Control experiments were performed as indicated. Results are given as the net BRET ratio (i.e., ratio of emissions at 535/485 nm minus the ratio of mock cells, *n* = 5, three technical replicates).

D Internalization of CXCR4 with 10 nM CXCL12 alone and in the presence of 10 nM Gal-3 CRD was assessed by incubation with an APC-conjugated anti-CXCR4 antibody (baseline signal = 100%, *n* = 8, two technical replicates).

E 100 nM CXCL12 and Gal-3 were added to Jurkat T cells, and their co-localization was assessed on the cell surface by PLA. Control experiments were performed as indicated (representative example of *n* = 3). White scale bar: 10 μm.

F, G Jurkat T cells were incubated with 100 nM of Gal-3 CRD Alexa Fluor 555 alone, with 10 μM AMD 3100, with 100 nM CXCL12, or with CXCL12 and AMD 3100. Experiments were performed (F) without and (G) in the presence of 70 mM lactose (F, G: *n* = 3, two technical replicates).

H Jurkat T cells were incubated with 100 nM CXCL12 FITC alone and with increasing concentrations of Gal-3 CRD as indicated (*n* = 4, two technical replicates).

Data information: Data represent the mean ± SD of the indicated number of independent experiments and were statistically analyzed by (F, G) unpaired *t*-test or (B–D, H) single sample *t*-test against the effect of the chemokine alone or as indicated (**P* ≤ 0.05, ***P* ≤ 0.01).

C-terminal α-helix (residues 59–68), as well as the second β-strand and 40s loop. Of note, these residues comprise the CXCL12 homodimer interface in the first β-strand and the C-terminal α-helix [50]. Although acidic conditions shift the monomer–dimer equilibrium toward monomer, Gal-3 may interfere with CXCL12 homodimerization and thus affect CXCR4 signaling under more physiological conditions [38,51,52]. Of particular note, the CXCL12/Gal-3 interface contains the GAG-binding motif of CXCL12, which primarily involves the first β-strand and 40s residues. Implying physiological significance, this region is reported as being required for chemokine presentation by endothelial cell GAGs [52,53]. Leading to an anti-chemokine effect, Gal-3 may specifically block this binding, a scenario that may impact on chemokine activity, as an antibody does [54]. The finding that heparin prevents CXCL12 from binding to Gal-3 CRD points into this direction so that interactions of CXCL12 with cognate GAGs and Gal-3 CRD are mutually exclusive. Studying the effect of Gal-3 on CXCL12 activity in a GAG-deficient cell line will be an approach to contribute to answer the arising question on the role of GAGs *in situ* for reducing CXCL12 activity by the galectin.

Here, we have provided initial support for our hypothesis that heterodimer formation affects chemokine function by performing transmigration assays and using a murine model of peritonitis. Whereas Gal-3 inhibited CXCL12-induced chemotaxis, Gal-1 (that exhibited markedly reduced affinity in SPR), the non-interacting chemokine CCL17 and the interaction-deficient mutants Gal-3 R168A, Gal-3 E185A, Gal-3 H217A, Gal-3 Q220K, and Gal-3 N222A had a reduced effect, if any. At this moment, it is puzzling that the effective concentrations of Gal-3 seem unexpectedly low and let it appear that a substantial portion of CXCL12 may not be active. Concerning the first point, should the chemokine be arranged in clusters at high density (presenting multivalency to the lectin), then a gradient of fractional affinity constants could arise with very high affinity for the first step, as documented for Gal-3 CRD association with a nonavalent glycoprotein [55]. Galectins bind to the multivalent glycoprotein asialofetuin with enhanced affinities and a gradient of decreasing binding constants [55]. With respect to low effective chemokine concentrations, although not yet mechanistically fully understood, it appears reasonable to postulate the following: that competition between galectins and GAGs (these glycan chains are discussed as direct or indirect factors for affecting chemokine availability [56]) for the chemokine may have a tangible bearing on CXCL12 activity, as also noted above.

On the cellular level, we showed that Gal-3 CRD affects CXCR4 signaling without interfering with receptor internalization. These results, together with the computational modeling of the ternary complex, suggest that the CXCL12/Gal-3 heterodimer binds CXCR4 rather than preventing the chemokine from interacting with its receptor. The possibility that CXCL12, when associated with the Gal-3 CRD, "may not be as potent as CXCL12 (alone) in triggering intracellular signals" (as suggested by a reviewer) can establish a mechanism toward galectin-mediated reduction of chemokine activity.

The biological functions of extracellular Gal-3 that have so far been described mostly depend on the glycan-binding capacity of its CRD and the formation of aggregates (lattice) with counterreceptors involving the CRD and possibly its NT [57,58]. To give an example from immune regulation, Gal-3 impedes diffusion of the glycosylated cytokine interferon-γ by cross-linking the cytokine with components of the extracellular matrix in a glycan-dependent manner [59]. Thus, Gal-3 can inhibit chemokine effects through both direct and indirect mechanisms. Moreover, Gal-3 induces neutrophil expression of CXCL8 in a glycan-dependent manner. Cleavage of its NT by neutrophil elastase renders the resulting Gal-3 CRD non-functional [60]. Our study has broadened this functional profile by demonstrating that regions of extracellular Gal-3 that are not involved in carbohydrate binding may in fact modulate inflammation. Our observations suggest that the Gal-3 CRD may have an anti-inflammatory role that could be exploited therapeutically. These findings do not exclude S-face-dependent effects of the galectin CRD in a physiological setting. Whether both sites operate simultaneously should prompt further studies. Since homodimeric Gal-3 variants have recently become available [61], this protein and also Gal-1/3 heterodimers offer perspectives on how to resolve this issue and may inspire biomedical efforts.

Since it was shown that CXCL12 and Gal-3 are simultaneously upregulated under chronic inflammatory conditions, proinflammatory Gal-3 may specifically block excessive or persistent inflammation by interfering with CXCL12 activity. Proteolytic Gal-3 truncation to its CRD by matrix metalloproteinases may be a control mechanism that attenuates or resolves inflammation. This assumption inspires the idea that a multimeric Gal-3 CRD construct (with active CRD or a mutant) may efficiently block CXCL12 activity *in situ*, while Gal-1 oligomerization appears to increase aspects of its biomedical activity [62,63]. The interaction of a lectin with a non-glycan counterreceptor, together with such engineering, can thus have a biomedical potential [64]. As a promising target, endothelial cell-derived CXCL12 drives atherosclerosis which underlies coronary heart disease [65,66]. Considering our discovery that Gal-3 is a potential antagonist of CXCL12, the present evidence for chemokine/galectin heterodimerization will prompt further investigation into the inter-family interactome and its pathophysiological relevance. Since Gal-3 fulfills criteria of an alarmin (or damage-associated molecular pattern) and a mediator of autophagy [67,68], the detection of CXCL12 binding will also warrant to explore its capacity to engage in pairing in respective processes.

Materials and Methods

Galectins, chemokines, and asialofetuin

Galectins

Gal-1 and Gal-3 were produced using *Escherichia coli* BL21(DE3) pLysS cells and the pGEMEX-1 expression vector (Promega). Cells were cultured at 37°C until an optical density$_{600}$ value of 0.6–0.8 was reached; then, protein production was induced by 100 μM of IPTG (isopropyl-β-D-thiogalactoside) and cultivation continued at 37°C (Gal-1) or 22°C (Gal-3) for 16 h. Proteins were purified from extracts by affinity chromatography on lactosylated Sepharose 4B as crucial step, and lactose was removed by gel filtration [69]. Isotopic labeling of full-length Gal-3 (residues 1–250) for NMR-spectroscopical analysis was done by using [^{15}N]NH$_4$Cl as medium additive for production at 30°C for 16 h in the presence of 100 μM IPTG [34]. The Gal-3 CRD (residues 108–250) was generated by on-bead collagenase treatment (1 mg/10 mg of protein) for 16 h at 4°C [70].

One-site Gal-3 mutants (N160A, E185A, and N222A) were obtained by mutagenesis of the pGEMEX-1-Gal-3 and pGEX-6P-2-Gal-3 vectors using the QuikChange Mutagenesis Kit (Agilent Technologies, Waldbronn, Germany). All proteins were routinely checked for purity by one- and two-dimensional gel electrophoresis under denaturing conditions and for activity by solid-phase/cell-binding assays.

Chemokines

For the array of the solid-phase immunoassay, chemokines were purchased from PeproTech (Rocky Hill, NJ, USA). WT human CXCL12α was bacterially expressed using a codon-optimized cDNA (Genscript, Piscataway, NJ, USA) as a thioredoxin-His-tagged fusion protein from the pET-32(+) vector with an enterokinase cleavage site at the N-terminus. The plasmid was transformed into *E. coli* BL21(DE3) cells and grown at 37°C in either Luria–Bertani or ^{15}N-enriched Spectra 9 medium (Cambridge Isotope Laboratories, MA, USA). CXCL12α was purified from inclusion bodies. After separation using a HisTrap HP column (GE Healthcare, Chicago, IL, USA), the sample was dialyzed against 50 mM Tris (tris(hydroxymethyl) aminomethane) buffer (pH 8), filtered, and loaded on a Heparin HP column. The bound protein was eluted in 50 mM Tris/2 M NaCl (pH 8) and further dialyzed against 50 mM Tris/2 mM cysteine (pH 8) before cleavage using Enterokinase (Novagen, Merck, Darmstadt, Germany). The cleaved protein was purified using a Mono S 5/50 GL column (GE Healthcare). The fractions containing the protein were pooled, dialyzed against 1% acetic acid, lyophilized, and stored at −20°C until further use. The correct mass of CXCL12α was confirmed by mass spectrometry.

Conjugation of proteins with biotin and fluorescent labels

Fluorescent and biotinylated proteins were prepared with the succinimidyl ester of Alexa Fluor 555 and the N-hydroxysuccinimide ester derivatives of FITC and biotin (all from Thermo Fisher Scientific, Waltham, MA, USA) according to the manufacturer's protocol. The conjugate was separated from the reagent using Sephadex G25 in PD-10 Desalting Columns (GE Healthcare). Preservation of activity was checked by cell signaling, hemagglutination, and binding assays using (neo)glycoproteins as matrix.

Asialofetuin

Desialylation of fetuin from fetal calf serum (Sigma-Aldrich, Taufkirchen, Germany) was performed by hydrolysis in 0.05 N sulfuric acid at 80°C for 1 h, and the product (ASF) was purified by fast protein liquid chromatography on a Superdex 75 column (GE Healthcare).

Cells, cell culture, and cell transfection

Jurkat T cells (clone E6-1, ATCC) and *human monocytic THP-1 cells* (no. ACC-16, DSMZ) were cultured as recommended by the supplier.

Human CD4$^+$ T cells

PBMCs were separated from whole blood by density gradient centrifugation. CD4$^+$ T cells were isolated from PBMCs with the Dynabeads Untouched Human CD4$^+$ T Cells Kit, stimulated with the Dynabeads Human T-Activator CD3/CD28 Kit (both from Invitrogen, Thermo Fisher Scientific) for 3 days, and expanded in the presence of the Dynabeads with 30 U/ml human IL-2 for another 3 days.

Human eosinophils

Whole-blood components were separated by density gradient centrifugation. The erythrocyte pellet was lysed, and eosinophils were isolated with the Eosinophil Isolation Kit in an unlabeled manner (Miltenyi, Bergisch Gladbach, Germany).

Human neutrophils

Neutrophils were separated from whole blood by density gradient centrifugation.

HEK 293 cell transfection for Gi signaling

The sequence of the luciferase-cAMP binding site fusion protein from the pGloSensor-20F vector (Promega) was amplified and ligated into a bicistronic pIRESneo vector (Clontech, Mountain View, CA, USA) to obtain the reporter gene plasmid. The pcDNA5/FRT/TO vector (Invitrogen) was used to express the CXCR4 receptor constructs (cDNA Resource Center, Bloomsburg University, Bloomsburg, PA, USA) [71]. Flp-In T-REx 293 cells (HEK 293, Invitrogen) were first stably transfected with the reporter plasmid using the Flp-In system (Invitrogen) and EcoTransfect (OZ Biosciences, Marseille, France). Stable clones were selected with 1 mg/ml geneticin. A suitable clone was then chosen as host cell line for stable overexpression of the CXCR4 construct using the Flp-In system with 250 μg/ml hygromycin B for selection.

HEK 293 cell transfection for β-arrestin 2 recruitment

HEK 293 cell monolayers at 90% confluency on a 24-well plate were transiently transfected with 0.05 μg/well CXCR4-RlucII construct (Promega) and 0.2 μg/well eYFP–β-arrestin 2 construct or mock plasmid with 1 μl EcoTransfect. After 24 h, the cells were transferred to a black 96-well plate.

Solid-phase immunoassays

100 ng samples of human chemokines or galectins were blotted onto a nitrocellulose membrane, and incubated with 200 nM biotinylated galectins or 120 nM CXCL12 overnight, signals developed with SA-HRP for 1 h, and added enhanced chemiluminescence substrate (Thermo Fisher Scientific). Densitometric analysis of digital records was performed using the program ImageJ.

Cross-linking protein interaction analysis

Galectins were incubated with 1 mM BS3 or BS(PEG)$_5$ cross-linkers (both from Thermo Fisher Scientific) in 20 mM HEPES (pH 8.3) at room temperature. After 10 min, CXCL12 was added and the mixture further incubated for 1 h. The reaction was then stopped by addition of 1 M Tris (pH 8). Samples were analyzed by SDS–PAGE followed by silver staining according to the manufacturer's instructions (Alphalyse, Odense, Denmark).

Surface plasmon resonance measurements

SPR experiments were performed on a Biacore X100 system (GE Healthcare).

Binding experiments

Biotinylated Gal-3 and Gal-1 were immobilized on SA sensor chips at densities specified in the figure legends (Fig EV1E and G). Gal-3 CRD was immobilized using thiol-coupling chemistry on a NeutrA-vidin (Thermo Fisher Scientific)-modified C1 sensor chip at the specified density (Fig EV1F). 100 nM chemokines dissolved in HEPES-buffered saline with EDTA and surfactant P20 (HBS-EP+) were perfused at a flow rate of 30 µl/min for 3 min. The response in resonance units (RU) was recorded 20 s after the end of the injection.

Kinetics experiments

Biotinylated (Gal-1 and Gal-3) and biotin-free (Gal-3, Gal-3 CRD, and mutants) galectins and biotinylated asialofetuin were immobilized on NeutrAvidin or using thiol- or amine-coupling chemistry (Thermo Fisher Scientific) on C1 or SA sensor chips at surface densities specified in the figure legends (Figs 1F–H and EV2A–F, and Appendix Figs S1A–C and S8A–L). CXCL12 and Gal-3 in HBS-EP+ were perfused for 1 min followed by a dissociation phase of 3 and 2 min for the chips with conjugated galectins and the chip presenting the glycoprotein ASF, respectively.

Nuclear magnetic resonance spectroscopy

NMR samples were prepared in 3-mm NMR tubes. Typically, chemokine and galectin samples were buffer-exchanged and concentrated into 20 mM sodium acetate buffer, pH 4.5, and 4.5 mM lactose through five ultracentrifugation steps over Amicon Ultra-4 3-kDa filter devices (Merck, Darmstadt, Germany). Mixtures of CXCL12 and Gal-3 CRD, Gal-3, or Gal-1 at defined molar ratios were prepared from these stock solutions, and 5% (v/v) D_2O was added for field locking, together with a trace of DSS as an internal chemical shift standard. ^1H–^{15}N HSQC experiments with a flip-back pulse and decoupling in the presence of scalar interactions, and nuclear Overhauser effect were recorded at 37°C on Bruker Avance III HD 700- and 850-MHz spectrometers equipped with cryogenically cooled triple resonance inverse probes. Spectra were processed and analyzed using Bruker TopSpin 3.2 and Sparky 3.114 software (T. D. Goddard, D. G. Kneller, SPARKY 3, the University of California, San Francisco, CA, USA). Resonance assignments of CXCL12 and Gal-3 CRD were performed by 2D NOESY and 3D-edited NOESY spectra. Chemical shift differences ($\Delta\delta$) induced upon binding were calculated as follows: $[(\Delta^1H)^2]^{1/2} + [(0.25\Delta^{15}N)^2]^{1/2}$ (in ^1H ppm). ΔIntensity was calculated as follows: $1 - Int_i/Int_0$, where Int_i is the resonance intensity of resonances of CXCL12 or Gal-3 CRD in the presence of the other component, respectively, and Int_0 is the intensity of CXCL12 or Gal-3 CRD resonances in its absence. The same experimental procedure was used for Gal-1 and Gal-3 proteins, as well as for Gal-3 mutants.

Molecular dynamics simulations

The CXCL12/Gal-3 CRD heterodimer was subjected to MD simulations for 50 ns as described except applying Amber 14SB force field with TIP3P water models using Amber16 [72]. MD simulations were performed for 50 ns. Snapshots between 40 and 50 ns were extracted for binding free energy calculation using the MM/GBSA

approach, and the BFE values were approximated from enthalpy values as described [72]. Default parameters were applied for BFE calculation, except using the generalized Born model 8 to compute the free energy of solvation. Ternary complex modeling between CXCL12, Gal-3 CRD, and CXCR4 was performed as described above. PDB access codes are as follows: CXCL12 homodimer (4UAI), Gal-3 CRD (1A3K), vMIP-II bound to CXCR4 (4RWS), and CXCR4 homodimer (3ODU).

Chemotaxis

Transwell migration

Chemotaxis assays were performed in triplicate with the number of independent experiments as stated in each respective figure legend. Chemokines and galectins in 230 µl of RPMI 1640/0.5% BSA were pipetted into the bottom well of a Transwell-96 permeable support (Corning, NY, USA) with 3.0 µm pore size for human granulocytes and 5.0 µm for all other cell types. 10^5 cells in 70 µl were pipetted on top of the filter and allowed to migrate for 2 h for primary cells and 4 h for Jurkat and THP-1 cells. 20 µl of a 0.05 M EDTA solution was added to the bottom well, and the plates were incubated for another 15 min. The number of cells at the bottom of a well was measured by flow cytometry of the cell suspension for 30 s at medium speed (FACSCanto II, BD Biosciences, Franklin Lakes, NJ, USA).

Cell aggregation

Jurkat T cells were incubated with the indicated concentrations of galectins for 4 h and subsequently analyzed by flow cytometry (FACSCANTO II). The forward scatter area (FSC-A) was plotted against the forward scatter width (FSC-W) to discriminate between singlets (low FSC-A, low FSC-W) and doublets/multiplets (high FSC-A, high FSC-W).

Apoptosis

Cell viability was determined by fluorescence-activated cell scanning with the FITC Annexin V Apoptosis Detection Kit with 7-AAD (7-amino-actinomycin D) (BioLegend, San Diego, CA, USA).

Mice

All animal experimental procedures were designed and conducted in agreement with the German Animal Welfare Legislation, and were reviewed and approved by local authorities (Regierung von Oberbayern, Munich, Germany). All mice were housed in IVC units and maintained on a 12-h dark/12-h light cycle. C57BL/6J mice were from Janvier (Le Genest-Saint-Isle, France), and tamoxifen-inducible general Cre-deleter C57BL/6-*Gt(ROSA)26Sor*[tm9(Cre/ESR1)Arte] (CreERT2) mice were from Taconic (TaconicArtemis GmbH, Cologne, Germany) and crossed with CXCL12[flox/flox] mice (on the Apoe$^{-/-}$ background), which were generated as described [15]. CXCL12$^{-/-}$ and WT mice were littermate offsprings from CreERT2$^+$, CXCL12[flox/flox], or CreERT2$^+$CXC12[wt/wt] mice after application of tamoxifen. Mice deficient for *Lgals3* (coding for Gal-3) were from EUCOMM (C57BL/6N-Lgals3tm1a(EUCOMM)Wtsi/H, Strain ID EM:06800) [73].

Murine model of peritonitis

500 nM CXCL12 alone, or in combination with 50 nM Gal-3, in PBS was injected into the peritoneal cavity of C57BL/6J mice (Janvier). To ensure efficacy in this physiological system, the chemokine/galectin molar ratio (10:1) was used. Mice were euthanized after 4 h. HBSS/0.3 mM EDTA/0.06% BSA was first injected into the peritoneal cavity, and then collected.

Peritonitis was induced by IP injection of 0.5 ml of 4% sterile thioglycolate broth. C57BL/6J mice were pre-treated IP with 125 μg of the CXCR4 antagonist AMD3465 (Tocris Bioscience, Bristol, UK) 12 h earlier. The peritoneal lavage was obtained after 18 h.

Cells were stained with a mixture of fluorescent antibodies and analyzed by flow cytometry. Only single cells (FSC-H/FSC-W^{low}) were gated. B cells (B220$^+$) and macrophages (F4/80$^+$) were excluded, and classical monocytes (CD115$^+$/Ly6C^{hi}) and neutrophils (CD115$^-$/Ly6G$^+$) were gated from CD45$^+$ (Appendix Fig S10A). Percentages of leukocyte subsets of untreated and TG-treated mice are indicated (Appendix Fig S10B–H). All antibodies were obtained from eBioscience (Thermo Fisher Scientific).

Proximity ligation assay

Lymph nodes for frozen sections were explanted from C57BL/6 mice. 10^6 Jurkat T cells were incubated with CXCL12 and Gal-3 at 4°C for 1 h, fixed, and mounted onto poly-ʟ-lysine (Sigma-Aldrich)-coated slides. On all samples, sites for non-specific protein binding were blocked and the cells or sections were incubated with 5 μg/ml of a polyclonal goat anti-mouse CXCL12 (Bio-Rad Laboratories, Hercules, CA, USA) and 2.5 μg/ml of a rabbit anti-human Gal-3 (affinity-purified IgG) antibody at 4°C overnight. Samples were incubated with secondary antibodies conjugated to complementary oligonucleotides that were ligated and amplified according to the manufacturer's instructions (all reagents from the Duolink In Situ Red Goat/Rabbit Kit; Sigma-Aldrich). Photomicrographs were taken using a confocal microscope (SP8; Leica, Wetzlar, Germany; magnification × 100, numerical aperture 1.4, oil immersion) and processed with LAS X (Leica) and Huygens software.

CXCR4 signaling

Gi signaling

HEK 293 cells expressing the GloSensor (Promega, Madison, WI, USA) and CXCR4 were cultured in a black 96-well plate (Perkin Elmer, Waltham, MA, USA) for 2–3 days until the cells were confluent. Cells were then incubated with a HBSS/20 mM HEPES/2.5% Luciferin-EF (Promega) solution for 2 h. Luminescence was determined using a plate reader (infinite F2000PRO; Tecan, Männedorf, Switzerland) until steady state was achieved. Forskolin (1 μM) was added 28 min after the stimulus, and the luminescence was recorded.

β-Arrestin 2 recruitment

HEK 293 cells expressing eYFP-β-arrestin 2 and CXCR4 *Renilla* sp. luciferase II (RlucII) were cultured to confluence in a black 96-well plate with 0.5 μg/ml tetracycline used to induce expression. Total fluorescence was determined at 535 nm. Coelenterazine (15 μM) was added, and total luminescence was detected at 485 nm. The stimulus was added, and the BRET ratio (emissions at 535 nm/485 nm) was determined.

Internalization of CXCR4

10^5 Jurkat T cells were incubated with CXCL12 and Gal-3 CRD at 37°C, fixed in 4% PFA, and stained with a monoclonal (12G5) APC-conjugated anti-human CXCR4 antibody (BD Biosciences).

Galectin and CXCL12 binding to T cells

10^5 Jurkat T cells were incubated as stated in the figure legend (Fig 6F–H) for 1 h. Where indicated, cells were pre-incubated with AMD 3100 (Sigma-Aldrich) for 15 min, and experiments were performed in the presence of the compound. Fluorescence signals were recorded by flow cytometry.

Expanded View for this article is available online.

Author contributions

VE designed and performed experiments, analyzed and interpreted results, and wrote the manuscript; MCM, XB, RD, JL, JD, OS, RTAM, A-KL, AD, AF, KW, HI, ID, HK, YD, and KB designed and performed experiments; TMH, H-JG, and CW supervised the study and made critical revisions to the manuscript; PvH and KHM conceived the study, designed experiments, analyzed and interpreted results, wrote the manuscript, and share senior authorship.

Conflict of interest

The authors declare that they have no conflict of interest.

References

1. Cooper D, Iqbal AJ, Gittens BR, Cervone C, Perretti M (2012) The effect of galectins on leukocyte trafficking in inflammation: sweet or sour? *Ann N Y Acad Sci* 1253: 181–192

2. Liu FT, Yang RY, Hsu DK (2012) Galectins in acute and chronic inflammation. *Ann N Y Acad Sci* 1253: 80–91

3. Griffith JW, Sokol CL, Luster AD (2014) Chemokines and chemokine receptors: positioning cells for host defense and immunity. *Annu Rev Immunol* 32: 659–702

4. Eash KJ, Greenbaum AM, Gopalan PK, Link DC (2010) CXCR2 and CXCR4 antagonistically regulate neutrophil trafficking from murine bone marrow. *J Clin Invest* 120: 2423–2431

5. Döring Y, Pawig L, Weber C, Noels H (2014) The CXCL12/CXCR4 chemokine ligand/receptor axis in cardiovascular disease. *Front Physiol* 5: 212

6. Liehn EA, Tuchscheerer N, Kanzler I, Drechsler M, Fraemohs L, Schuh A, Koenen RR, Zander S, Soehnlein O, Hristov M *et al* (2011) Double-edged role of the CXCL12/CXCR4 axis in experimental myocardial infarction. *J Am Coll Cardiol* 58: 2415–2423

7. Martin C, Burdon PC, Bridger G, Gutierrez-Ramos JC, Williams TJ, Rankin SM (2003) Chemokines acting via CXCR2 and CXCR4 control the release of neutrophils from the bone marrow and their return following senescence. *Immunity* 19: 583–593

8. Scimone ML, Felbinger TW, Mazo IB, Stein JV, von Andrian UH, Weninger W (2004) CXCL12 mediates CCR7-independent homing of central memory cells, but not naive T cells, in peripheral lymph nodes. *J Exp Med* 199: 1113–1120

9. Zernecke A, Bot I, Djalali-Talab Y, Shagdarsuren E, Bidzhekov K, Meiler S, Krohn R, Schober A, Sperandio M, Soehnlein O *et al* (2008) Protective role of CXC receptor 4/CXC ligand 12 unveils the importance of neutrophils in atherosclerosis. *Circ Res* 102: 209–217

10. Döring Y, Noels H, van der Vorst EPC, Neideck C, Egea V, Drechsler M, Mandl M, Pawig L, Jansen Y, Schröder K *et al* (2017) Vascular CXCR4 limits atherosclerosis by maintaining arterial integrity: evidence from mouse and human studies. *Circulation* 136: 388–403

11. Nanki T, Hayashida K, El-Gabalawy HS, Suson S, Shi K, Girschick HJ, Yavuz S, Lipsky PE (2000) Stromal cell-derived factor-1-CXC chemokine receptor 4 interactions play a central role in CD4$^+$ T cell accumulation in rheumatoid arthritis synovium. *J Immunol* 165: 6590–6598

12. Fernandez EJ, Lolis E (2002) Structure, function, and inhibition of chemokines. *Annu Rev Pharmacol Toxicol* 42: 469–499

13. Nesmelova IV, Sham Y, Dudek AZ, van Eijk LI, Wu G, Slungaard A, Mortari F, Griffioen AW, Mayo KH (2005) Platelet factor 4 and interleukin-8 CXC chemokine heterodimer formation modulates function at the quaternary structural level. *J Biol Chem* 280: 4948–4958

14. Nesmelova IV, Sham Y, Gao J, Mayo KH (2008) CXC and CC chemokines form mixed heterodimers: association free energies from molecular dynamics simulations and experimental correlations. *J Biol Chem* 283: 24155–24166

15. von Hundelshausen P, Agten SM, Eckardt V, Blanchet X, Schmitt MM, Ippel H, Neideck C, Bidzhekov K, Leberzammer J, Wichapong K *et al* (2017) Chemokine interactome mapping enables tailored intervention in acute and chronic inflammation. *Sci Transl Med* 9: eaah6650

16. Koenen RR, von Hundelshausen P, Nesmelova IV, Zernecke A, Liehn EA, Sarabi A, Kramp BK, Piccinini AM, Paludan SR, Kowalska MA *et al* (2009) Disrupting functional interactions between platelet chemokines inhibits atherosclerosis in hyperlipidemic mice. *Nat Med* 15: 97–103

17. Gabius HJ, Roth J (2017) An introduction to the sugar code. *Histochem Cell Biol* 147: 111–117

18. Gabius HJ (2017) How to crack the sugar code. *Folia Biol (Praha)* 63: 121–131

19. Kaltner H, Gabius HJ (2019) Sensing glycans as biochemical messages by tissue lectins: the sugar code at work in vascular biology. *Thromb Haemost* 119: 517–533

20. Godula K (2018) Following sugar patterns in search of galectin function. *Proc Natl Acad Sci USA* 115: 2548–2550

21. Kaltner H, Toegel S, García Caballero G, Manning JC, Ledeen RW, Gabius HJ (2017) Galectins: their network and roles in immunity/tumor growth control. *Histochem Cell Biol* 147: 239–256

22. Gittens BR, Bodkin JV, Nourshargh S, Perretti M, Cooper D (2017) Galectin-3: a positive regulator of leukocyte recruitment in the inflamed microcirculation. *J Immunol* 198: 4458–4469

23. Auvynet C, Moreno S, Melchy E, Coronado-Martinez I, Montiel JL, Aguilar-Delfin I, Rosenstein Y (2013) Galectin-1 promotes human neutrophil migration. *Glycobiology* 23: 32–42

24. Nachtigal M, Ghaffar A, Mayer EP (2008) Galectin-3 gene inactivation reduces atherosclerotic lesions and adventitial inflammation in ApoE-deficient mice. *Am J Pathol* 172: 247–255

25. Filer A, Bik M, Parsonage GN, Fitton J, Trebilcock E, Howlett K, Cook M, Raza K, Simmons DL, Thomas AM *et al* (2009) Galectin 3 induces a distinctive pattern of cytokine and chemokine production in rheumatoid synovial fibroblasts via selective signaling pathways. *Arthritis Rheum* 60: 1604–1614

26. Toegel S, Weinmann D, André S, Walzer SM, Bilban M, Schmidt S, Chiari C, Windhager R, Krall C, Bennani-Baiti IM *et al* (2016) Galectin-1 couples glycobiology to inflammation in osteoarthritis through the activation of an NF-κB-regulated gene network. *J Immunol* 196: 1910–1921

27. Weinmann D, Schlangen K, André S, Schmidt S, Walzer SM, Kubista B, Windhager R, Toegel S, Gabius HJ (2016) Galectin-3 induces a pro-degradative/inflammatory gene signature in human chondrocytes, teaming up with galectin-1 in osteoarthritis pathogenesis. *Sci Rep* 6: 39112

28. Kamitori S (2018) Three-dimensional structures of galectins. *Trends Glycosci Glycotechnol* 30: SE41–SE50

29. Solís D, Bovin NV, Davis AP, Jimenéz-Barbero J, Romero A, Roy R, Smetana K Jr, Gabius HJ (2015) A guide into glycosciences: how chemistry, biochemistry and biology cooperate to crack the sugar code. *Biochim Biophys Acta* 1850: 186–235

30. Lobsanov YD, Rini JM (1997) Galectin structure. *Trends Glycosci Glycotechnol* 9: 145–154

31. Ahmad N, Gabius HJ, André S, Kaltner H, Sabesan S, Roy R, Liu B, Macaluso F, Brewer CF (2004) Galectin-3 precipitates as a pentamer with synthetic multivalent carbohydrates and forms heterogeneous cross-linked complexes. *J Biol Chem* 279: 10841–10847

32. Kopitz J, Vertésy S, André S, Fiedler S, Schnölzer M, Gabius HJ (2014) Human chimera-type galectin-3: defining the critical tail length for high-affinity glycoprotein/cell surface binding and functional competition with galectin-1 in neuroblastoma cell growth regulation. *Biochimie* 104: 90–99

33. Miller MC, Ludwig AK, Wichapong K, Kaltner H, Kopitz J, Gabius HJ, Mayo KH (2018) Adhesion/growth-regulatory galectins tested in combination: evidence for formation of hybrids as heterodimers. *Biochem J* 475: 1003–1018

34. Ippel H, Miller MC, Vertésy S, Zheng Y, Canada FJ, Suylen D, Umemoto K, Romano C, Hackeng T, Tai G *et al* (2016) Intra- and intermolecular interactions of human galectin-3: assessment by full-assignment-based NMR. *Glycobiology* 26: 888–903

35. Akahani S, Nangia-Makker P, Inohara H, Kim HR, Raz A (1997) Galectin-3: a novel antiapoptotic molecule with a functional BH1 (NWGR) domain of Bcl-2 family. *Cancer Res* 57: 5272–5276

36. Schaum N, Karkanias J, Neff NF, May AP, Quake SR, Wyss-Coray T, Darmanis S, Batson J, Botvinnik O, Chen MB *et al* (2018) Single-cell transcriptomics of 20 mouse organs creates a *Tabula Muris*. *Nature* 562: 367–372

37. Czaplewski LG, McKeating J, Craven CJ, Higgins LD, Appay V, Brown A, Dudgeon T, Howard LA, Meyers T, Owen J *et al* (1999) Identification of amino acid residues critical for aggregation of human CC chemokines macrophage inflammatory protein (MIP)-1α, MIP-1β, and RANTES. Characterization of active disaggregated chemokine variants. *J Biol Chem* 274: 16077–16084

38. Veldkamp CT, Peterson FC, Pelzek AJ, Volkman BF (2005) The monomer-dimer equilibrium of stromal cell-derived factor-1 (CXCL 12) is altered by pH, phosphate, sulfate, and heparin. *Protein Sci* 14: 1071−1081

39. Williamson MP (2013) Using chemical shift perturbation to characterise ligand binding. *Prog Nucl Magn Reson Spectrosc* 73: 1−16

40. Perillo NL, Pace KE, Seilhamer JJ, Baum LG (1995) Apoptosis of T cells mediated by galectin-1. *Nature* 378: 736−739

41. Mishra RK, Shum AK, Platanias LC, Miller RJ, Schiltz GE (2016) Discovery and characterization of novel small-molecule CXCR4 receptor agonists and antagonists. *Sci Rep* 6: 30155

42. Lagane B, Chow KY, Balabanian K, Levoye A, Harriague J, Planchenault T, Baleux F, Gunera-Saad N, Arenzana-Seisdedos F, Bachelerie F (2008) CXCR4 dimerization and β-arrestin-mediated signaling account for the enhanced chemotaxis to CXCL12 in WHIM syndrome. *Blood* 112: 34−44

43. Rajagopal S, Bassoni DL, Campbell JJ, Gerard NP, Gerard C, Wehrman TS (2013) Biased agonism as a mechanism for differential signaling by chemokine receptors. *J Biol Chem* 288: 35039−35048

44. Hitchinson B, Eby JM, Gao X, Guite-Vinet F, Ziarek JJ, Abdelkarim H, Lee Y, Okamoto Y, Shikano S, Majetschak M *et al* (2018) Biased antagonism of CXCR4 avoids antagonist tolerance. *Sci Signal* 11: eaat2214

45. Gerlach LO, Skerlj RT, Bridger GJ, Schwartz TW (2001) Molecular interactions of cyclam and bicyclam non-peptide antagonists with the CXCR4 chemokine receptor. *J Biol Chem* 276: 14153−14160

46. Weinmann D, Kenn M, Schmidt S, Schmidt K, Walzer SM, Kubista B, Windhager R, Schreiner W, Toegel S, Gabius HJ (2018) Galectin-8 induces functional disease markers in human osteoarthritis and cooperates with galectins-1 and -3. *Cell Mol Life Sci* 75: 4187−4205

47. Pope SM, Zimmermann N, Stringer KF, Karow ML, Rothenberg ME (2005) The eotaxin chemokines and CCR3 are fundamental regulators of allergen-induced pulmonary eosinophilia. *J Immunol* 175: 5341−5350

48. Ravensberg AJ, Ricciardolo FL, van Schadewijk A, Rabe KF, Sterk PJ, Hiemstra PS, Mauad T (2005) Eotaxin-2 and eotaxin-3 expression is associated with persistent eosinophilic bronchial inflammation in patients with asthma after allergen challenge. *J Allergy Clin Immunol* 115: 779−785

49. Freeman CM, Stolberg VR, Chiu BC, Lukacs NW, Kunkel SL, Chensue SW (2006) CCR4 participation in Th type 1 (mycobacterial) and Th type 2 (schistosomal) anamnestic pulmonary granulomatous responses. *J Immunol* 177: 4149−4158

50. Veldkamp CT, Seibert C, Peterson FC, De la Cruz NB, Haugner JC III, Basnet H, Sakmar TP, Volkman BF (2008) Structural basis of CXCR4 sulfotyrosine recognition by the chemokine SDF-1/CXCL12. *Sci Signal* 1: ra4

51. Drury LJ, Ziarek JJ, Gravel S, Veldkamp CT, Takekoshi T, Hwang ST, Heveker N, Volkman BF, Dwinell MB (2011) Monomeric and dimeric CXCL12 inhibit metastasis through distinct CXCR4 interactions and signaling pathways. *Proc Natl Acad Sci USA* 108: 17655−17660

52. Ziarek JJ, Veldkamp CT, Zhang F, Murray NJ, Kartz GA, Liang X, Su J, Baker JE, Linhardt RJ, Volkman BF (2013) Heparin oligosaccharides inhibit chemokine (CXC motif) ligand 12 (CXCL12) cardioprotection by binding orthogonal to the dimerization interface, promoting oligomerization, and competing with the chemokine (CXC motif) receptor 4 (CXCR4) N terminus. *J Biol Chem* 288: 737−746

53. Proudfoot AEI, Johnson Z, Bonvin P, Handel TM (2017) Glycosaminoglycan interactions with chemokines add complexity to a complex system. *Pharmaceuticals (Basel)* 10: 70

54. Bonvin P, Gueneau F, Buatois V, Charreton-Galby M, Lasch S, Messmer M, Christen U, Luster AD, Johnson Z, Ferlin W *et al* (2017) Antibody neutralization of CXCL10 *in vivo* is dependent on binding to free and not endothelial-bound chemokine: implications for the design of a new generation of anti-chemokine therapeutic antibodies. *J Biol Chem* 292: 4185−4197

55. Dam TK, Gabius HJ, André S, Kaltner H, Lensch M, Brewer CF (2005) Galectins bind to the multivalent glycoprotein asialofetuin with enhanced affinities and a gradient of decreasing binding constants. *Biochemistry* 44: 12564−12571

56. Graham GJ, Handel TM, Proudfoot AEI (2019) Leukocyte adhesion: reconceptualizing chemokine presentation by glycosaminoglycans. *Trends Immunol* 40: 472−481

57. Newlaczyl AU, Yu LG (2011) Galectin-3: a jack-of-all-trades in cancer. *Cancer Lett* 313: 123−128

58. Flores-Ibarra A, Vertésy S, Medrano FJ, Gabius HJ, Romero A (2018) Crystallization of a human galectin-3 variant with two ordered segments in the shortened N-terminal tail. *Sci Rep* 8: 9835

59. Gordon-Alonso M, Hirsch T, Wildmann C, van der Bruggen P (2017) Galectin-3 captures interferon-γ in the tumor matrix reducing chemokine gradient production and T-cell tumor infiltration. *Nat Commun* 8: 793

60. Nieminen J, St-Pierre C, Sato S (2005) Galectin-3 interacts with naive and primed neutrophils, inducing innate immune responses. *J Leukoc Biol* 78: 1127−1135

61. Ludwig AK, Michalak M, Xiao Q, Gilles U, Medrano FJ, Ma H, FitzGerald FG, Hasley WD, Melendez-Davila A, Liu M *et al* (2019) Design-functionality relationships for adhesion/growth-regulatory galectins. *Proc Natl Acad Sci USA* 116: 2837−2842

62. Vertésy S, Michalak M, Miller MC, Schnölzer M, André S, Kopitz J, Mayo KH, Gabius HJ (2015) Structural significance of galectin design: impairment of homodimer stability by linker insertion and partial reversion by ligand presence. *Protein Eng Des Sel* 28: 199−210

63. Kopitz J, Xiao Q, Ludwig AK, Romero A, Michalak M, Sherman SE, Zhou X, Dazen C, Vertésy S, Kaltner H *et al* (2017) Reaction of a programmable glycan presentation of glycodendrimersomes and cells with engineered human lectins to show the sugar functionality of the cell surface. *Angew Chem Int Ed Engl* 56: 14677−14681

64. Kaltner H, Abad-Rodríguez J, Corfield AP, Kopitz J, Gabius HJ (2019) The sugar code: letters and vocabulary, writers, editors and readers and biosignificance of functional glycan-lectin pairing. *Biochem J* 476: 2623−2655

65. Doring Y, van der Vorst EPC, Duchene J, Jansen Y, Gencer S, Bidzhekov K, Atzler D, Santovito D, Rader DJ, Saleheen D *et al* (2019) CXCL12 derived from endothelial cells promotes atherosclerosis to drive coronary artery disease. *Circulation* 139: 1338−1340

66. Eckardt V, Weber C, von Hundelshausen P (2019) Glycans and glycan-binding proteins in atherosclerosis. *Thromb Haemost* 119: 1265−1273

67. Sato S, St-Pierre C, Bhaumik P, Nieminen J (2009) Galectins in innate immunity: dual functions of host soluble β-galactoside-binding lectins as damage-associated molecular patterns (DAMPs) and as receptors for pathogen-associated molecular patterns (PAMPs). *Immunol Rev* 230: 172−187

68. García Caballero G, Kaltner H, Kutzner TJ, Ludwig AK, Manning JC, Schmidt S, Sinowatz F, Gabius HJ (2020) How galectins have become multifunctional proteins. *Histol Histopathol* https://doi.org/10.14670/HH-18-199

69. Gabius HJ (1990) Influence of type of linkage and spacer on the interaction of β-galactoside-binding proteins with immobilized affinity ligands. *Anal Biochem* 189: 91–94

70. Kübler D, Hung CW, Dam TK, Kopitz J, André S, Kaltner H, Lohr M, Manning JC, He L, Wang H *et al* (2008) Phosphorylated human galectin-3: facile large-scale preparation of active lectin and detection of structural changes by CD spectroscopy. *Biochim Biophys Acta* 1780: 716–722

71. Feierler J, Wirth M, Welte B, Schüssler S, Jochum M, Faussner A (2011) Helix 8 plays a crucial role in bradykinin B_2 receptor trafficking and signaling. *J Biol Chem* 286: 43282–43293

72. Wichapong K, Alard JE, Ortega-Gomez A, Weber C, Hackeng TM, Soehnlein O, Nicolaes GA (2016) Structure-based design of peptidic inhibitors of the interaction between CC chemokine ligand 5 (CCL5) and human neutrophil peptides 1 (HNP1). *J Med Chem* 59: 4289–4301

73. Skarnes WC, Rosen B, West AP, Koutsourakis M, Bushell W, Iyer V, Mujica AO, Thomas M, Harrow J, Cox T *et al* (2011) A conditional knockout resource for the genome-wide study of mouse gene function. *Nature* 474: 337–342

74. Murphy JW, Cho Y, Sachpatzidis A, Fan C, Hodsdon ME, Lolis E (2007) Structural and functional basis of CXCL12 (stromal cell-derived factor-1α) binding to heparin. *J Biol Chem* 282: 10018–10027

Expanded View Figures

Figure EV1. Physical interaction of Gal-3 and Gal-1 with CC and CXC chemokines.

A–D   Chemokines were immobilized on a nitrocellulose membrane and incubated with (A) TBS or (B) TBS containing biotinylated Gal-1. The membranes were then stepwise incubated in solutions with SA-HRP and chemiluminescence reagents. (C, D) The blots were subjected to densitometric analysis.

E–G   Binding of galectins to chemokines was further assessed by immobilizing (E) Gal-3, (F) Gal-3 CRD, and (G) Gal-1 on sensor chips at a density of 700 RU and detecting signals of human chemokines under flow. Signals of the solid-phase assays (Fig 1E) are depicted in light blue (n = 3). Data represent mean $\pm$ SD from three independent experiments.

▶

A

B

C

CCL1	CCL2	CCL3	CCL3L1	CCL4	CCL4 L1	CCL5	CCL7	CCL8	CCL11	CCL13	CCL14
CCL15	CCL16	CCL17	CCL18	CCL19	CCL20	CCL21	CCL22	CCL23	CCL24	CCL25	CCL26
CCL27	CCL28	XCL1	XCL2	CXCL1	CXCL2	CXCL3	CXCL4	CXCL4 L1	CXCL5	CXCL6	CXCL7
CXCL8	CXCL9	CXCL10	CXCL11	CXCL12 α	CXCL12 β	CXCL13	CXCL14	CXCL16	CXCL17	CX3CL1	Gal-3 biot

D

CCL1	CCL2	CCL3	CCL3L1	CCL4	CCL4 L1	CCL5	CCL7	CCL8	CCL11	CCL13	CCL14
CCL15	CCL16	CCL17	CCL18	CCL19	CCL20	CCL21	CCL22	CCL23	CCL24	CCL25	CCL26
CCL27	CCL28	XCL1	XCL2	CXCL1	CXCL2	CXCL3	CXCL4	CXCL4 L1	CXCL5	CXCL6	CXCL7
CXCL8	CXCL9	CXCL10	CXCL11	CXCL12 α	CXCL12 β	CXCL13	CXCL14	CXCL16	CXCL17	CX3CL1	

E

Gal-3

[RU]

F

Gal-3 CRD

[RU]

G

Gal-1

[RU]

CCL   CXC

Figure EV1.

Figure EV2. Heterodimer formation between Gal-3 and chemokines.

A–F For kinetic SPR analyses, Gal-3 was immobilized on sensor chips to a density of 650 RU, and increasing concentrations of (A) CCL1, (B) CCL5E66S, (C) CCL17, (D) CCL22, (E) CCL26, and (F) CXCL11 were passed over the flow cell. Insets show representative sensorgrams of chemokines on Gal-3. Data represent the mean ± SD of three independent experiments.

G K_D values were calculated by fitting signals of steady-state phases vs. the concentration of the chemokine (A–F in red).
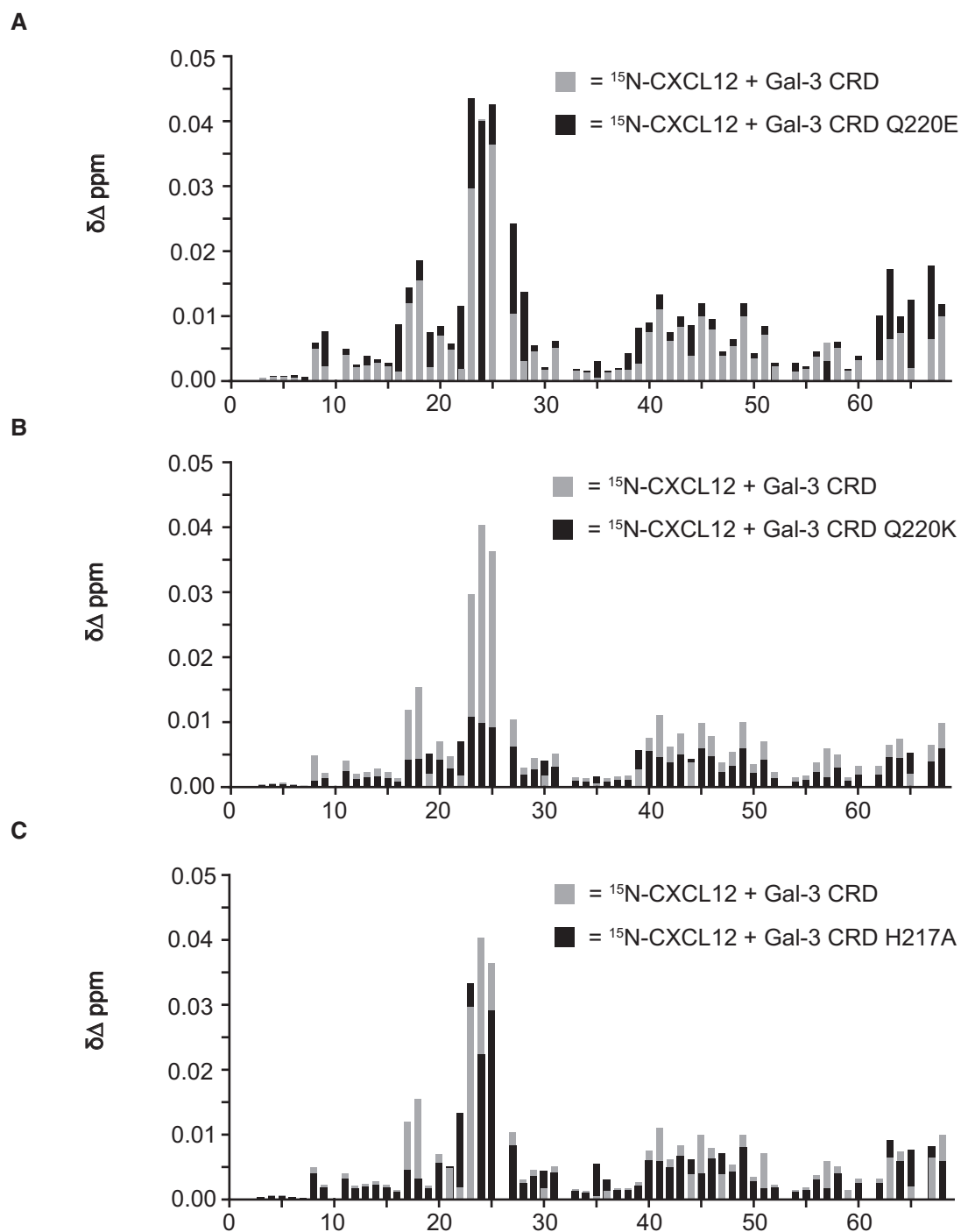
Figure EV3. **¹H–¹⁵N chemical shift maps for ¹⁵N-labeled CXCL12 with WT Gal-3 CRD and its mutants.**

A–C Δδ Values plotted vs. the amino acid sequence of CXCL12 are shown for 30 μM ¹⁵N-enriched CXCL12 in the presence of 500 μM label-free Gal-3 CRD mutants (A) Q220E, (B) Q220K, and (C) H217A (black). The results of the experiment with WT Gal-3 CRD from Fig 2A are overlaid in gray.

Figure EV4. Co-localization of CXCL12 and Gal-3 on cells *in vivo*.

A, B   Proximity of Gal-3 and CXCL12 on cells from peritoneal lavages after injection of (A) PBS or (B) TG was determined by PLA (representative example of n = 3). White scale bar: 10 μm.

C, D   Co-localization of Gal-3 and CXCL12 in frozen sections of lymph nodes from (C) WT and (D) CXCL12$^{-/-}$ mice was determined by immunofluorescence staining using antibodies against Gal-3 and CXCL12 (representative example of n = 3). Scale bar: 40 μm. Arrows indicate subcapsular sinus macrophages (SSM).

E   Co-localization on the same sections was also detected by PLA (representative example of n = 3). Scale bar: 40 μm.
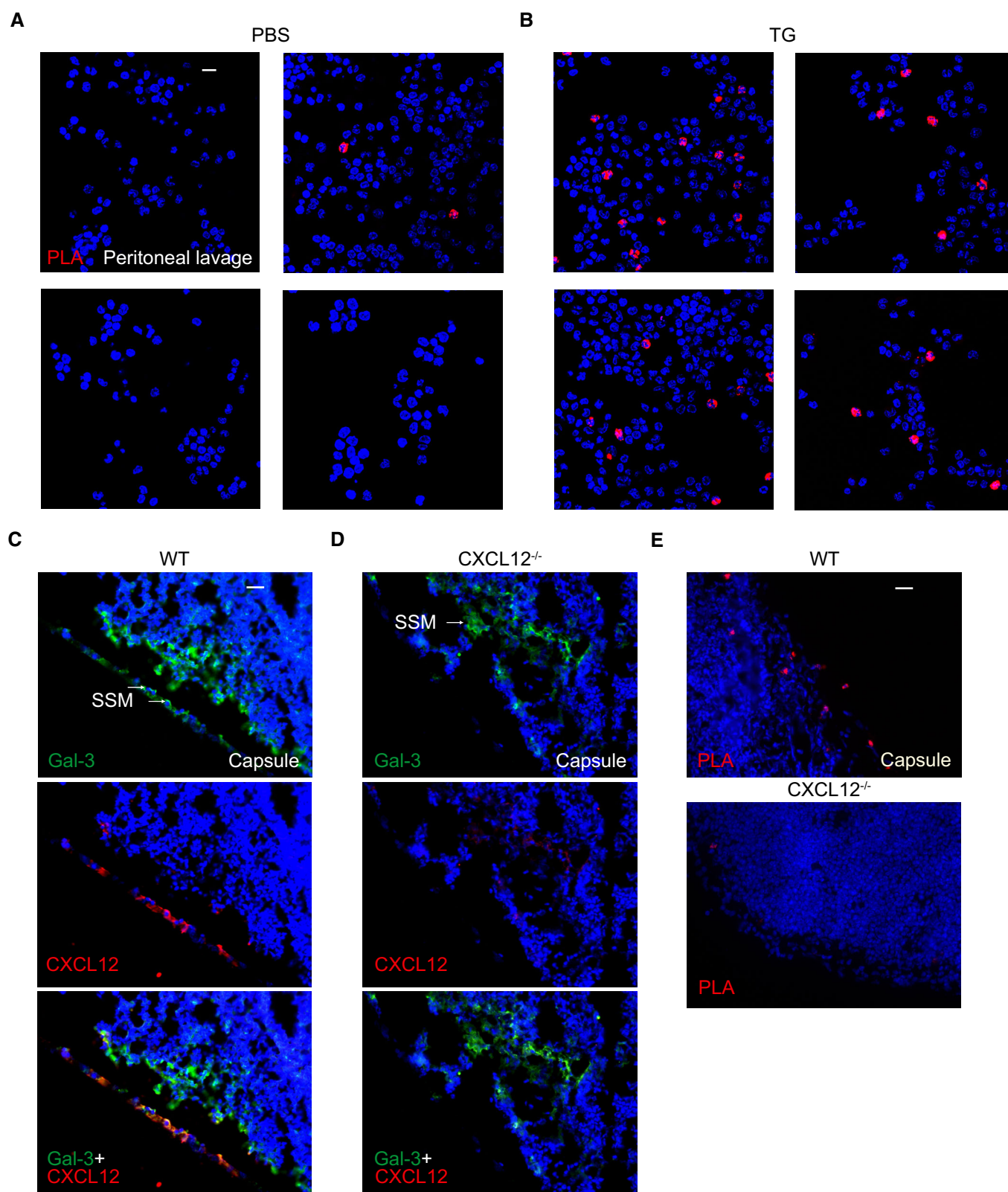
Figure EV4.

134

Figure EV5. MD simulation of a ternary complex between CXCL12, Gal-3 CRD, and CXCR4 in a lipid bilayer environment.

Complex 6 was superimposed onto the viral chemokine antagonist vMIP-II in complex with CXCR4 (PDB access code 4RWS). Subsequently, the viral chemokine antagonist vMIP-II was deleted, and the complex between monomeric CXCR4 in complex with the CXCL12/Gal-3 CRD heterodimer was obtained. This model was refined by energy minimization in the course of MD simulations (50 ns) with coordinates and orientation from another monomer of CXCR4 (CXCR4 as dimer (PDB access code 3ODU), monomers in cyan and yellow, CXCL12 in magenta, and Gal-3 CRD in light green). The inset shows that N180 (Gal-3 CRD) forms H-bonds (dashed red lines) with N97 (CXCR4) and R183 (Gal-3 CRD) can do so with E31 (CXCR4) and with R8 (CXCL12).
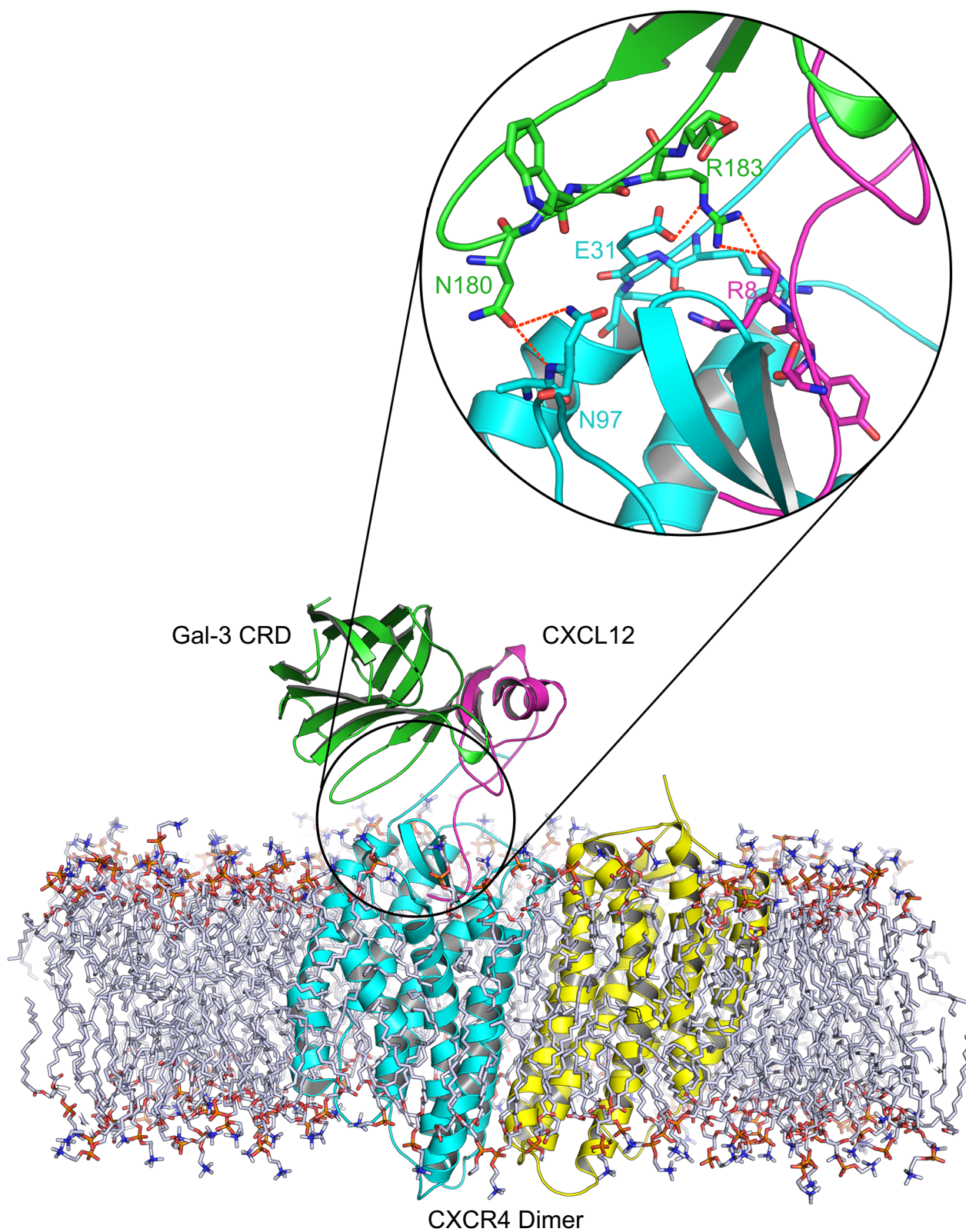
Figure EV5.

Appendix

A new encounter of mediators in inflammation: heterodimer formation between chemokines and galectins

Veit Eckardt,[1] Michelle C. Miller,[2] Xavier Blanchet,[1] Rundan Duan,[1] Julian Leberzammer,[1] Johan Duchene,[1] Oliver Soehnlein,[1] Remco T.A. Megens,[1] Anna-Kristin Ludwig,[3] Aurelio Dregni,[2] Alexander Faussner,[1] Kanin Wichapong,[4] Hans Ippel,[4] Ingrid Dijkgraaf,[4] Herbert Kaltner,[5] Yvonne Doring,[1] Kiril Bidzhekov,[1] Tilman M. Hackeng,[4] Christian Weber,[1,4,5] Hans-Joachim Gabius,[3] Philipp von Hundelshausen,[1,5,*] and Kevin H. Mayo[2,*]

This PDF file includes:

Appendix Figure S1. CXCL12/Gal-3 heterodimer formation in the presence of lactose and heparin.

A-B Gal-3 was immobilized using thiol-coupling on a C1-sensor chip to a density of 650 RU and serial dilutions of CXCL12 were passed over the chip either in the (A) absence or (B) presence of 70 mM lactose (n=3). The K_D values were obtained by fitting the signals of the steady-state phases against the concentration of the chemokine (red) using a single-site model. A representative sensorgram is provided in the inset to each panel.

C For kinetic analysis CXCL12 at increasing concentrations alone or together with heparin (0.5 µg/mL) was passed over the Gal-3 CRD chip (CXCL12 alone in black, and with heparin in purple).

Data information: Insets show exemplary sensorgrams of CXCL12 on immobilized galectin. Data represent the mean ± SD from three independent experiments.
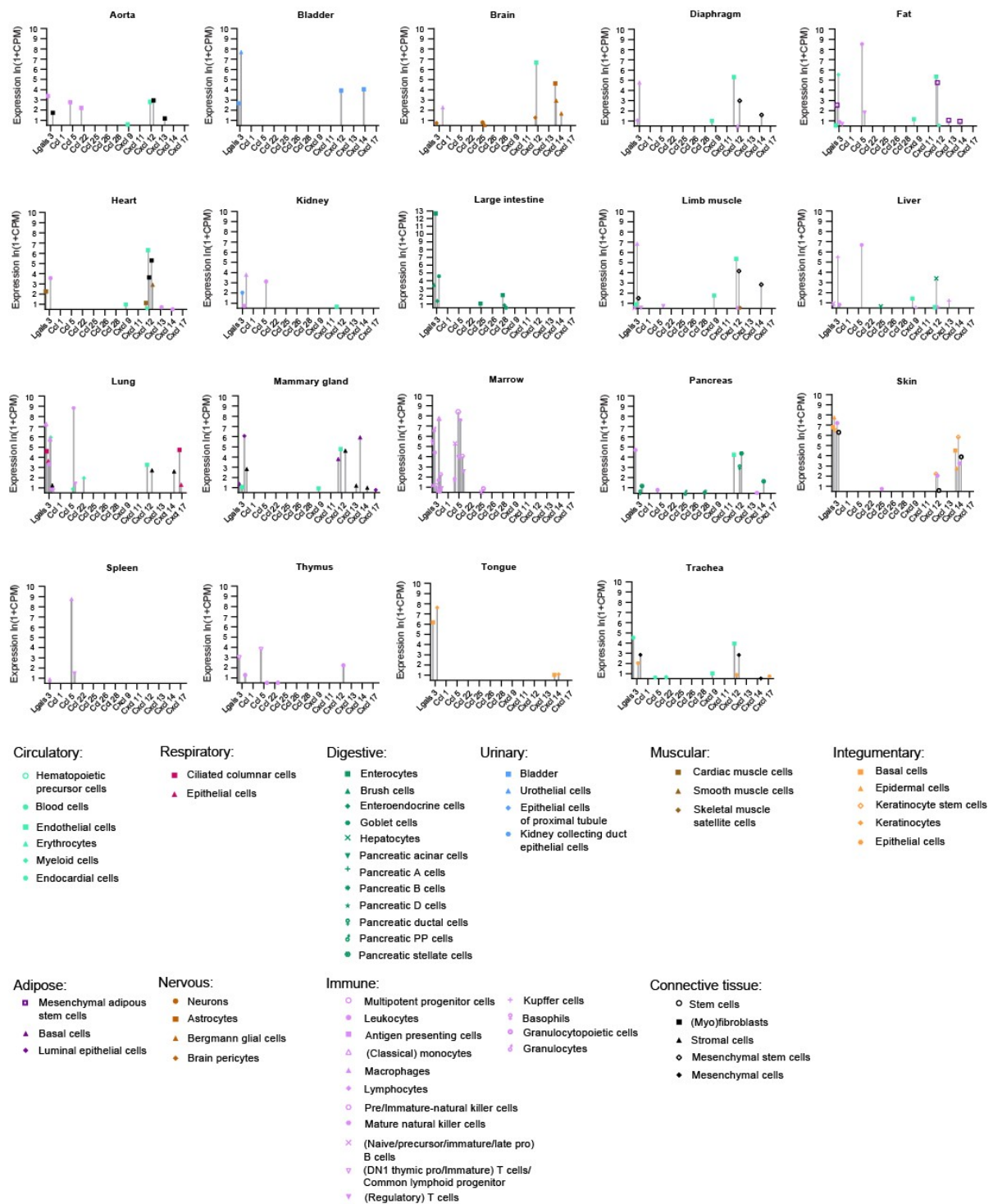
Appendix Figure S2. Co-expression of Gal-3 and chemokines in mouse tissue.
Gene expression data from FACS-based full-length transcript analyses were obtained from
Tabula Muris, a compendium of single cell transcriptome data derived from mouse organs
[36]. The mean gene count expressed as natural logarithm of copies per million (CPM) is
shown.

A ^{15}N-CXCL12 + Gal-3 CRD

B ^{15}N-Gal-3 CRD + CXCL12
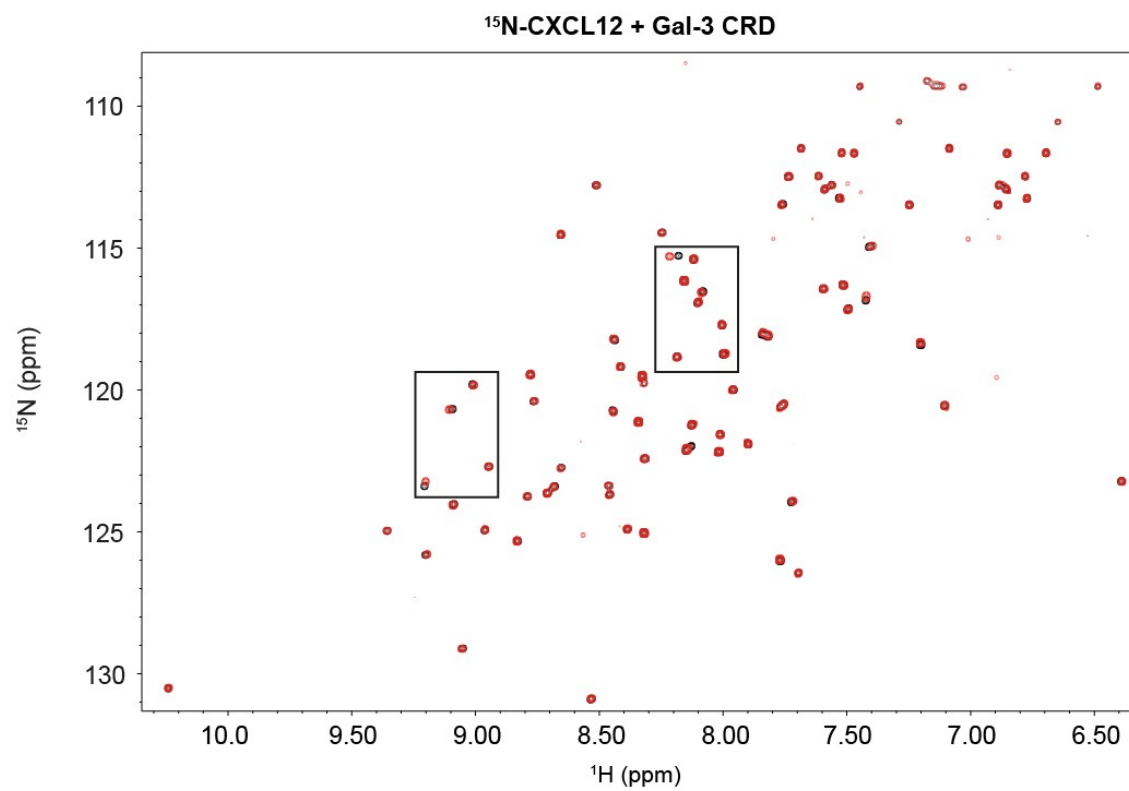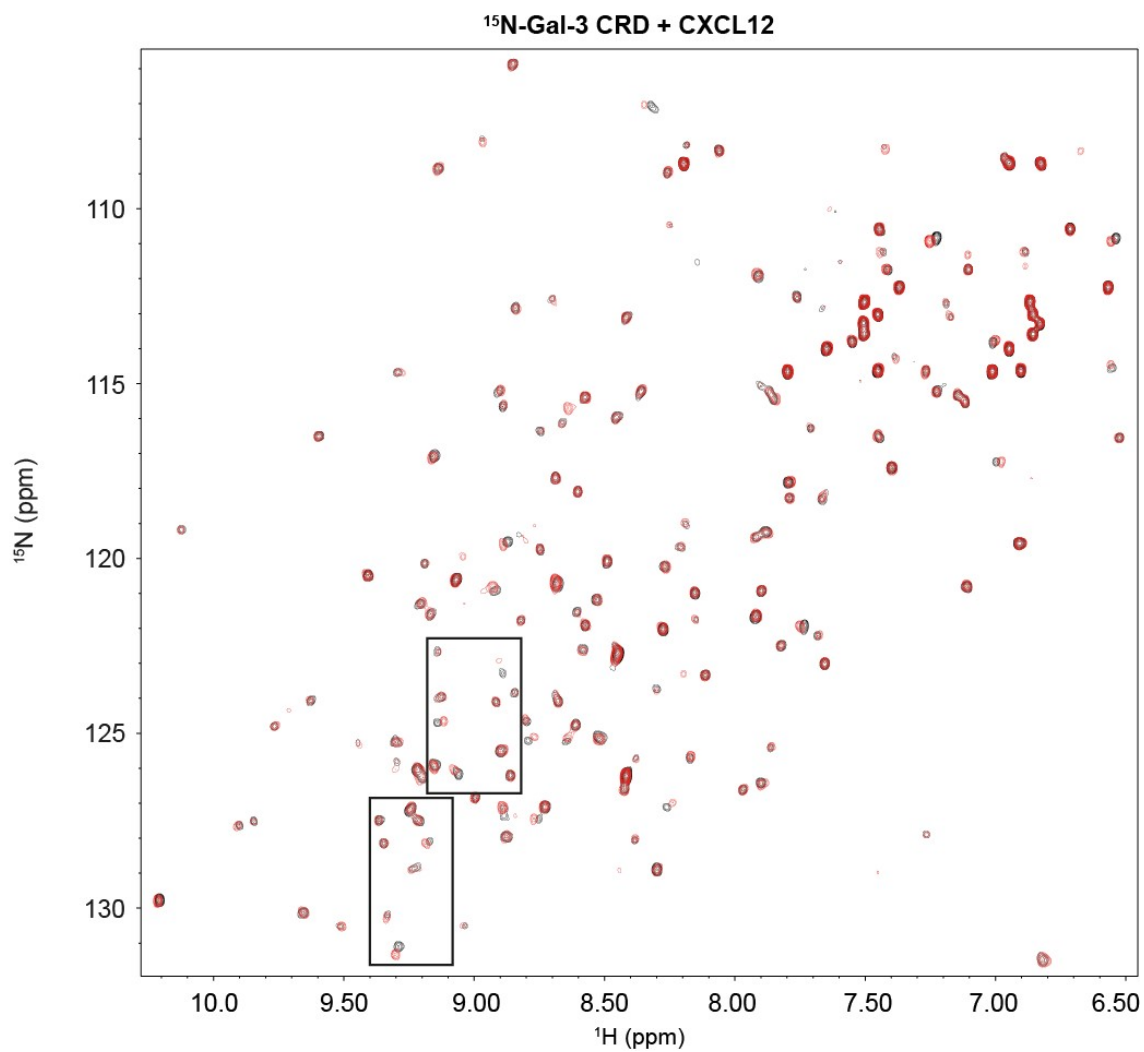
Appendix Figure S3. ^{1}H-^{15}N HSQC spectra of CXCL12 and Gal-3 CRD.

A-B Full ^{1}H-^{15}N HSQC spectra are overlaid depicting (A) 10 µM ^{15}N-enriched CXCL12 alone (black) and in the presence of 330 µM unlabeled Gal-3 CRD (red) and (B) 30 µM ^{15}N-enriched Gal-3 CRD alone (black) and in the presence of 500 µM unlabeled CXCL12 (red). The boxed regions in these spectra are shown in greater detail in Figure 2A and B.
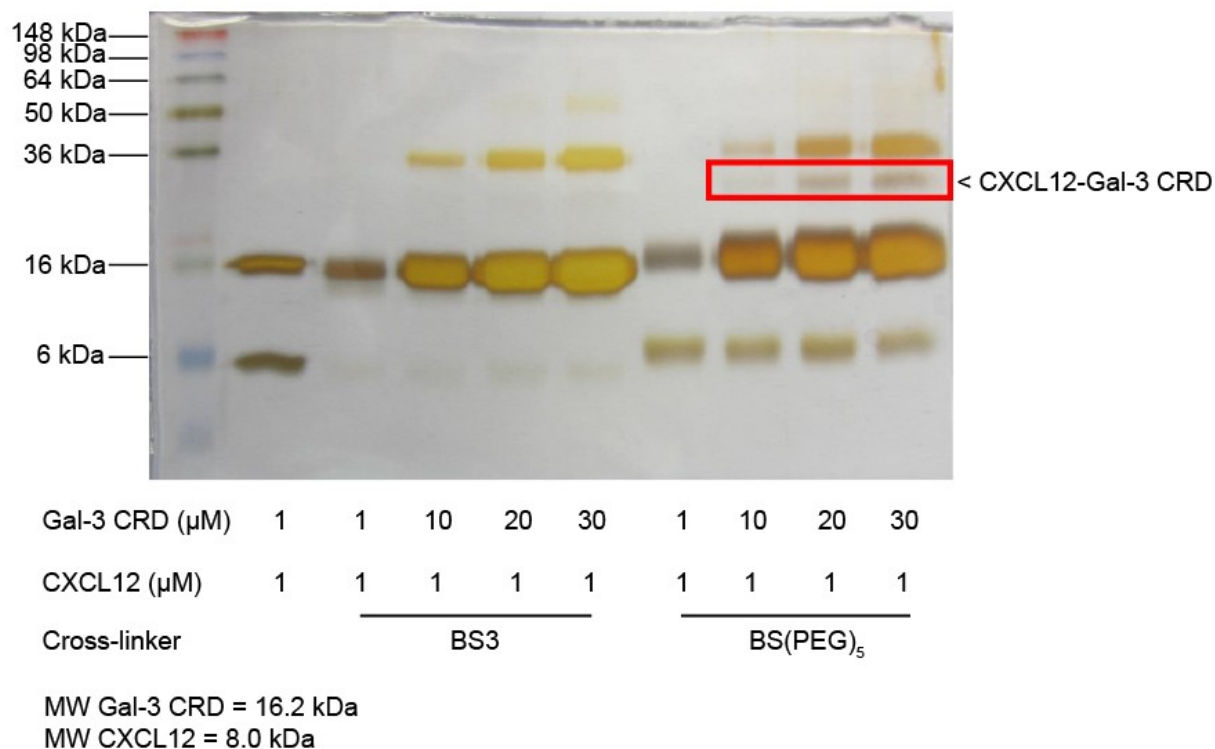
Appendix Figure S4. Cross-linking of CXCL12 and Gal-3 CRD.

CXCL12 and Gal-3 CRD were incubated with cross-linkers BS3 and BS(PEG)$_5$. SDS PAGE and silver staining of the gel were performed. Using increasing concentrations of Gal-3 CRD and the longer BS(PEG)$_5$ linker, bands appeared at the position expected for a molecular weight consistent with that of the CXCL12/Gal-3 CRD heterodimer (red rectangle). This is a representative image of three independent experiments.
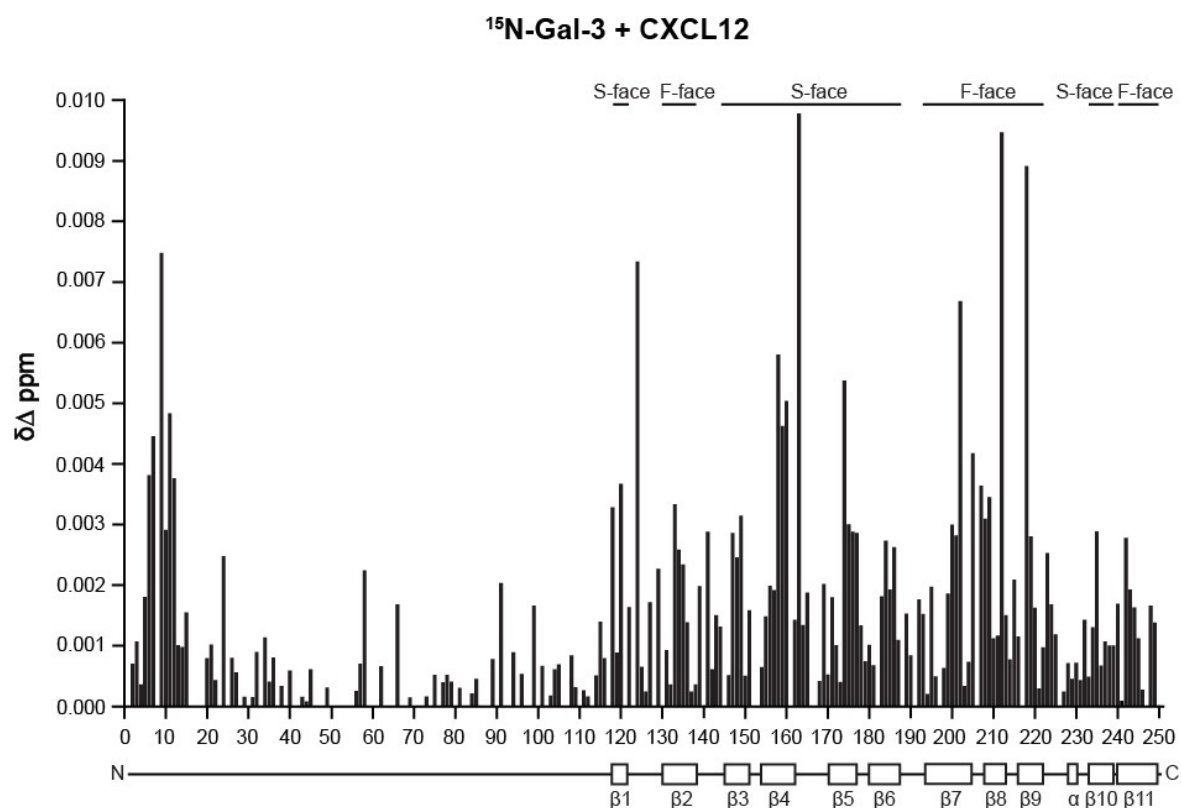
Appendix Figure S5. CXCL12-induced chemical shifts of full-length ^{15}N-labeled Gal-3.
Δδ Values plotted vs. the amino acid sequence and secondary structure of Gal-3 are shown
for 30 μM ^{15}N-enriched Gal-3 in the presence of 500 μM unlabeled CXCL12.

A

Complex 1
ΔG: -11 ± 4.7 kcal/mol

Complex 2
ΔG: -14 ± 5.1 kcal/mol

Complex 3
ΔG: -25 ± 3.7 kcal/mol

Complex 4
ΔG: -28 ± 5.1 kcal/mol

Complex 5
ΔG: -2.8 ± 4.4 kcal/mol

Gal-3 CRD   CXCL12

Complex 6
ΔG: -50 ± 6.6 kcal/mol

Complex 7
ΔG: -19 ± 3.5 kcal/mol

Complex 8
ΔG: -31 ± 5.9 kcal/mol

Complex 9
ΔG: -23 ± 5.0 kcal/mol

Complex 10
ΔG: -8.6 ± 4.1 kcal/mol
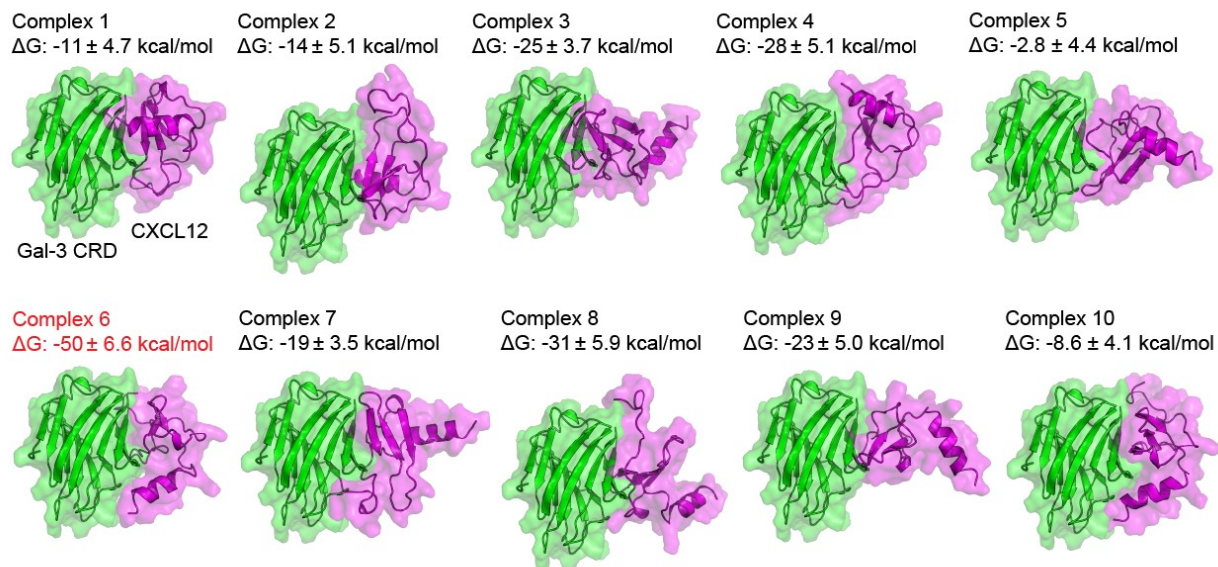
B
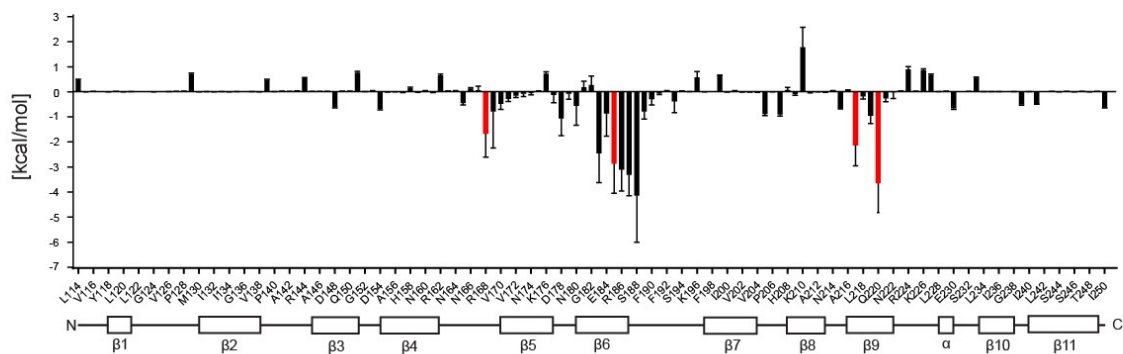
C
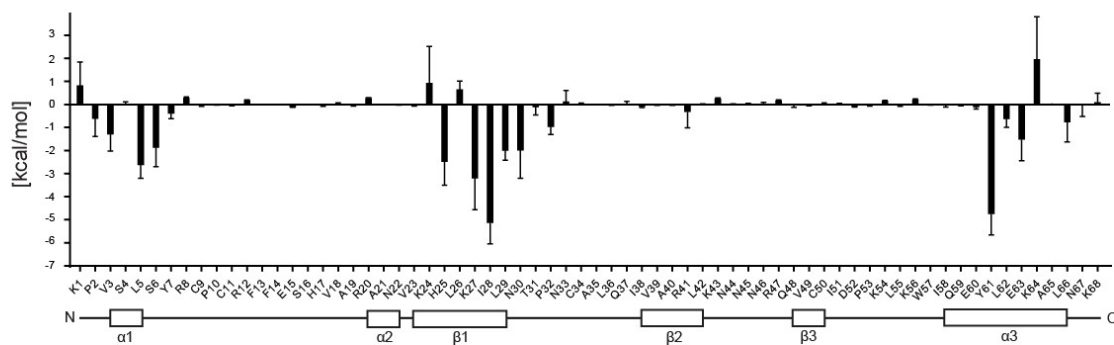
Appendix Figure S6. MD-based energy-minimized structure of the CXCL12/Gal-3 CRD heterodimer.

A   10 Potential structures of the CXCL12/Gal-3 CRD heterodimer consistent with the NMR results (Figure 2A-D, Appendix Figure S3A and B) were modeled and the ΔG values of interaction were calculated. Complex 6 is the thermodynamically most favorable conformation, because its formation generates the largest ΔG value, thus the highest affinity (red).

B-C Decomposition analyses of all residues of (B) Gal-3 CRD and (C) CXCL12 in a CXCL12/Gal-3 CRD heterodimer were performed. Secondary structures are shown below the graph. Sites of amino acid substitutions are highlighted in red.

A
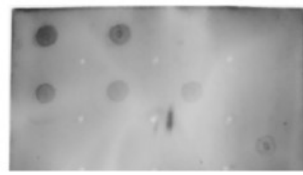
Gal-3	CXCL12 biot		
N160A	E185A	N222A	
CCL2	CCL17	CCL18	CCL5
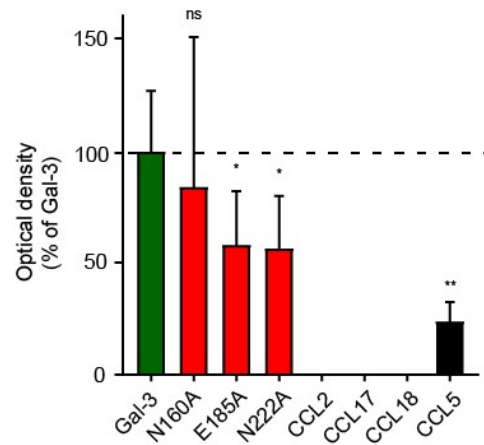
B
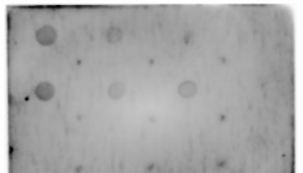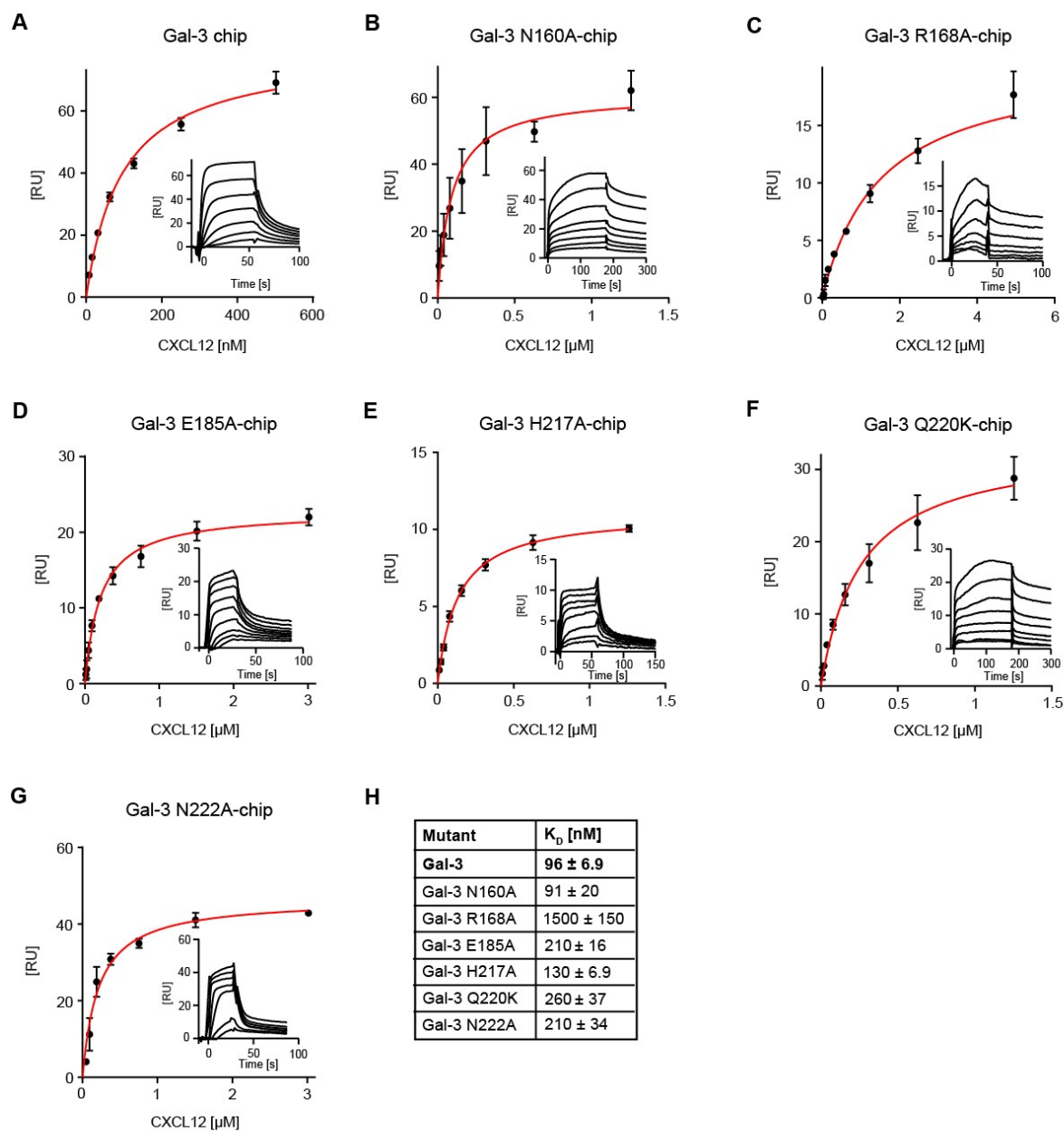

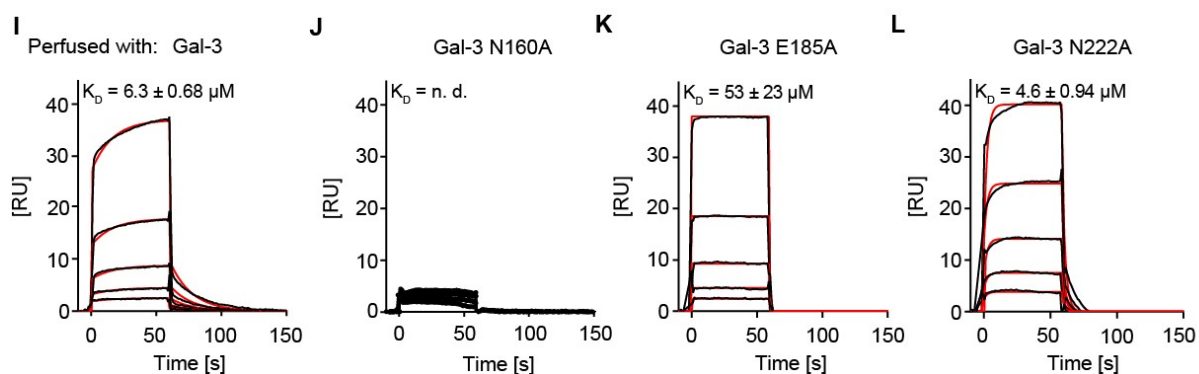| Gal-3 CRD	CXCL12 biot		
CRD N160A	CRD E185A	CRD N222A	
CCL2	CCL17	CCL18	CCL5
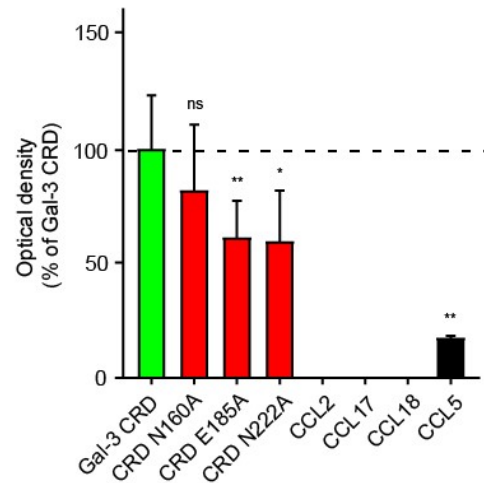
Appendix Figure S7. Binding of CXCL12 to Gal-3, Gal-3 CRD and their mutants.

A-B Membrane blot experiments were performed with (A) Gal-3 and (B) Gal-3 CRD and their mutants immobilized on the membrane and biotinylated CXCL12 in solution, as exemplified on the left in each panel. Chemokines served as negative and positive controls as described [15]. Membranes were subjected to densitometric analysis with values normalized to the galectin, as shown on the right (results of WT Gal-3 and Gal-3 CRD in green and light green respectively, mutants in red).

Data information: Data represent the mean ± SD from three independent experiments and were statistically analyzed against the effect of the galectin by using an unpaired t-test (*=P≤0.05, **=P≤0.01).

| Mutant	K_D [nM]
Gal-3	**96 ± 6.9**
Gal-3 N160A	91 ± 20
Gal-3 R168A	1500 ± 150
Gal-3 E185A	210 ± 16
Gal-3 H217A	130 ± 6.9
Gal-3 Q220K	260 ± 37
Gal-3 N222A	210 ± 34

Appendix Figure S8. Binding kinetics of Gal-3 mutants to CXCL12 and ASF.

A-G For kinetic SPR analysis (A) Gal-3 (density 239 RU), (B) Gal-3 N160A (density 291 RU), (C) Gal-3 R168A (density 160 RU), (D) Gal-3 E185A (density 264 RU), (E) Gal-3 H217A (density 197 RU), (F) Gal-3 Q220K (density 216 RU) and (G) Gal-3 N222A (density 258 RU) were immobilized on sensor chips and increasing concentrations of CXCL12 were passed over the flow cell (A-G: n = 3).

H K_D values were determined by fitting the signals of steady-state phases vs. the concentration of CXCL12 (A-G in red).

I-L The interaction of Gal-3 mutants with glycans was assessed by determining the binding capacity of increasing concentrations of galectin to ASF immobilized at a density of 460 RU on the sensor chip surface (representative example of n = 3). K_D values were obtained by fitting the graphs according to a 1:1 Langmuir interaction model (in red).

Data information: Data represent the mean ± SD from three independent experiments.
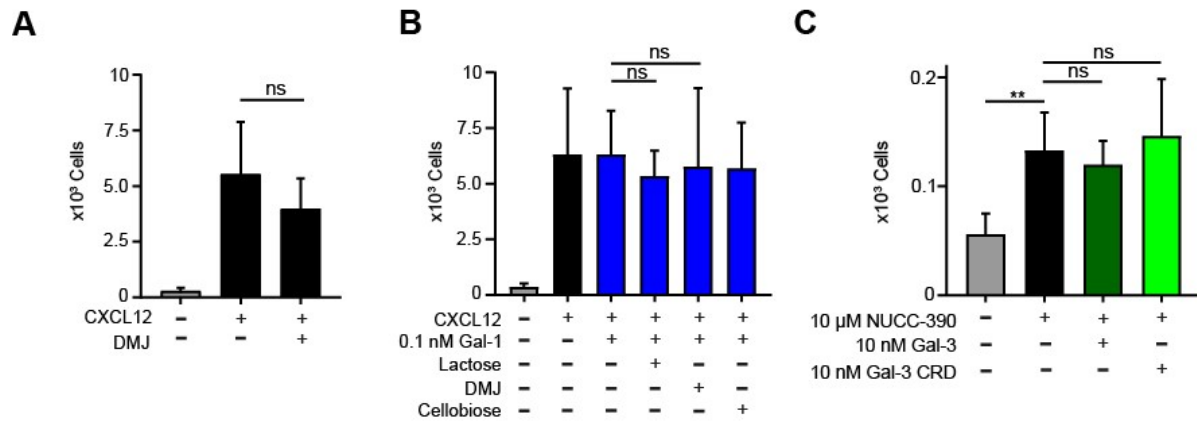
Appendix Figure S9. Effect of DMJ, galectin-mediated glycan binding and NUCC-390 on the chemotaxis of Jurkat T cells.

A   Jurkat T cells migrated to 10 nM CXCL12 alone with and without pretreatment of cells with 150 µM DMJ, an inhibitor of N-linked glycosylation, for 24 hours (n = 3).

B   Jurkat T cells were allowed to migrate in the presence of 10 nM CXCL12 alone or in combination with 0.1 nM Gal-1, 70 mM lactose, DMJ and 70 mM cellobiose (n = 3).

C   Jurkat T cells migrated with 10 µM NUCC-390 (a CXCR4 agonist) and with 10 nM Gal-3 and Gal-3 CRD (n = 3).

Data information: Cell migration is shown as absolute cell count. Data represent the mean ± SD from three independent experiments and were statistically analyzed by using an unpaired t-test as indicated (**=p≤0.01).
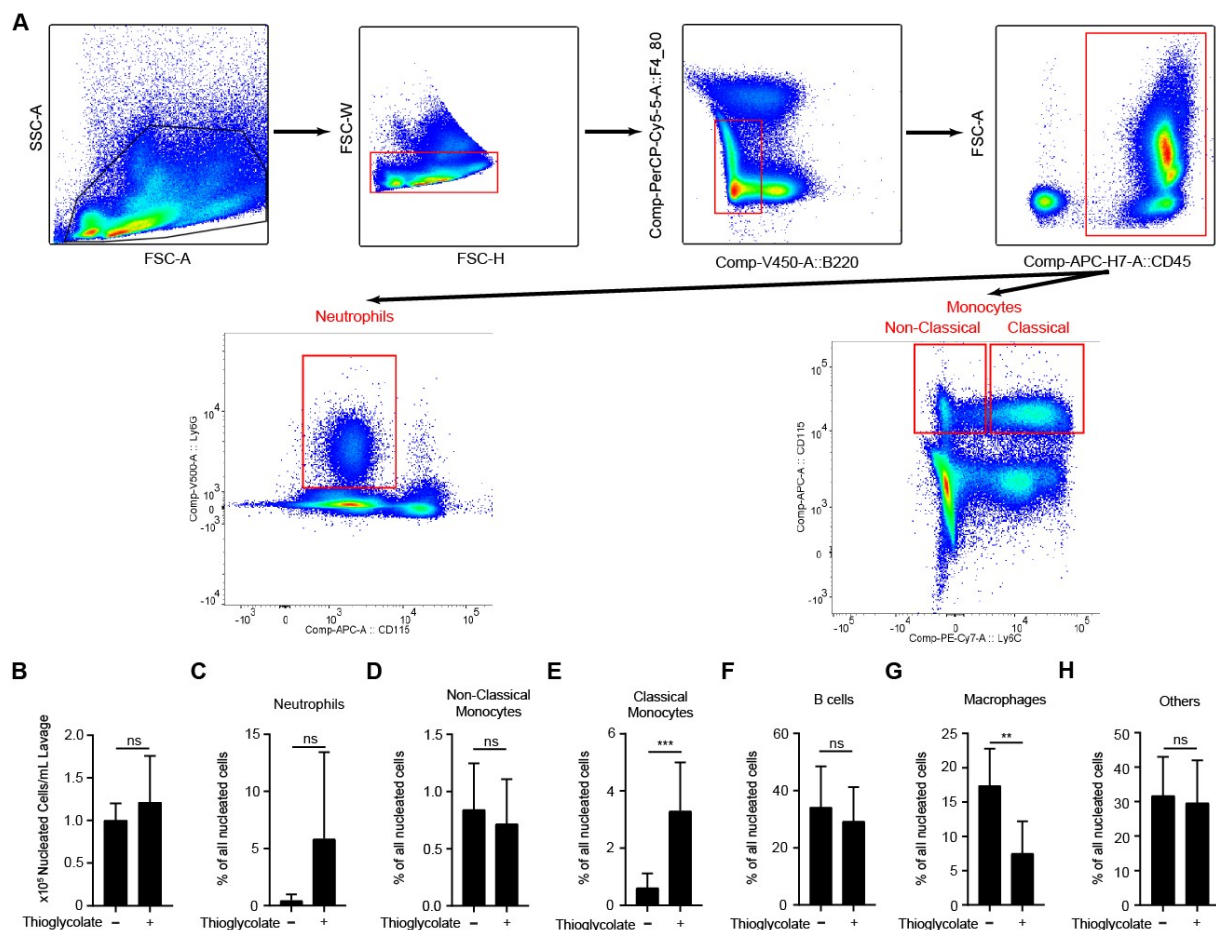
Appendix Figure S10. Analysis of leukocyte subsets from the peritoneal lavage of mice.

A   Sample data from a wild type mouse 18 h after injection of 4% thioglycolate are depicted. Leukocyte singlets were defined as FSC-H high and FSC-W low. Neutrophils, non-classical monocytes and classical monocytes were defined as B220-/F4-80-/CD45+/CD115-/Ly6G+, B220-/F4-80-/CD45+/CD115+/Ly6Clo and B220-/F4-80-/CD45+/CD115+/Ly6Chi respectively.

B-H (B) All leukocytes in the peritoneal lavage and (C-H) percentages of leukocyte subsets of WT mice 18 h after injection with PBS and TG are shown (PBS: n = 6, TG: n = 10).

Mutant	ΔG [kcal/mol]
Gal-3 WT	-50 ± 6.6
N160A	-48 ± 6.4
N160D	-43 ± 8.8
R168A	-33 ± 4.3
R169A	-34 ± 7.0
R183A	-34 ± 5.4
R183D	-51 ± 7.7
R183E	-42 ± 5.8
E184A	-33 ± 5.5
E184N	-42 ± 7.7
E184Q	-40 ± 6.5
E185A	-35 ± 5.7
S188A	-34 ± 7.5
K210A	-53 ± 5.6
K210D	-57 ± 6.8

Mutant	ΔG [kcal/mol]
K210E	-50 ± 6.5
H217A	-38 ± 6.9
H217F	-26 ± 5.6
H217Y	-49 ± 6.4
Q220A	-37 ± 4.4
Q220D	-55 ± 9.5
Q220E	-58 ± 5.4
Q220K	-31 ± 5.8
Q220R	-30 ± 4.4
N222A	-44 ± 7.1
N222D	-37 ± 4.1
N222E	-27 ± 4.7
R224A	-48 ± 6.8
R224D	-35 ± 5.0
R224E	-27 ± 5.8

Appendix Table S1. ΔG of the heterodimer between CXCL12 and Gal-3 CRD and its mutants.

Data from computational analyses of ΔG generated by CXCL12/Gal-3 CRD heterodimerization for WT and mutated Gal-3 CRD are provided. Mutants that were experimentally tested are labeled in color based on ΔG values compared to WT (see also Appendix Fig S6B and C).

15. Acknowledgments